N° d'ordre : 2023ISAL0036

THÈSE de DOCTORAT DE L'INSA LYON,
membre de l'Université de Lyon

École Doctorale N° 160
Électronique, Électrotechnique, Automatique

Spécialité / discipline de doctorat :
Automatique

Soutenue publiquement le 02/06/2023, par :
Hugo FOURNIER

Aeroelastic Reduced-Order Modeling and Active Control of Flexible Aircraft

---

Devant le jury composé de :

VIDAL-SALLE, Emmanuelle	Professeure	INSA-Lyon	Présidente
ALAZARD, Daniel	Professeur	ISAE-Supaero	Rapporteur
LOVERA, Marco	Professore Ordinario	Politecnico Di Milano	Rapporteur
PALACIOS, Rafael	Full Professor	Imperial College London	Examinateur
QUEINNEC, Isabelle	Directrice de recherche CNRS	LAAS-CNRS	Examinatrice
PHAM, Minh Tu	Maître de Conférence HDR	INSA-Lyon	Directeur de thèse
BAKO, Laurent	Maître de Conférence HDR	Ecole Centrale de Lyon	Co-encadrant
MASSIONI, Paolo	Maître de Conférence HDR	INSA-Lyon	Co-encadrant
VERNAY, Robin	Ingénieur	Airbus	Invité

Département FEDORA – INSA Lyon - Ecoles Doctorales

SIGLE	ECOLE DOCTORALE	NOM ET COORDONNEES DU RESPONSABLE
CHIMIE	**CHIMIE DE LYON** **https://www.edchimie-lyon.fr** Sec. : Renée EL MELHEM Bât. Blaise PASCAL, 3e étage secretariat@edchimie-lyon.fr	**M. Stéphane DANIELE** C2P2-CPE LYON-UMR 5265 Bâtiment F308, BP 2077 43 Boulevard du 11 novembre 1918 69616 Villeurbanne **directeur@edchimie-lyon.fr**
E.E.A.	**ÉLECTRONIQUE, ÉLECTROTECHNIQUE, AUTOMATIQUE** **https://edeea.universite-lyon.fr** Sec. : Stéphanie CAUVIN Bâtiment Direction INSA Lyon Tél : 04.72.43.71.70 secretariat.edeea@insa-lyon.fr	**M. Philippe DELACHARTRE** INSA LYON Laboratoire CREATIS Bâtiment Blaise Pascal, 7 avenue Jean Capelle 69621 Villeurbanne CEDEX Tél : 04.72.43.88.63 **philippe.delachartre@insa-lyon.fr**
E2M2	**ÉVOLUTION, ÉCOSYSTÈME, MICROBIOLOGIE, MODÉLISATION** **http://e2m2.universite-lyon.fr** Sec. : Bénédicte LANZA Bât. Atrium, UCB Lyon 1 Tél : 04.72.44.83.62 secretariat.e2m2@univ-lyon1.fr	**Mme Sandrine CHARLES** Université Claude Bernard Lyon 1 UFR Biosciences Bâtiment Mendel 43, boulevard du 11 Novembre 1918 69622 Villeurbanne CEDEX **sandrine.charles@univ-lyon1.fr**
EDISS	**INTERDISCIPLINAIRE SCIENCES-SANTÉ** **http://ediss.universite-lyon.fr** Sec. : Bénédicte LANZA Bât. Atrium, UCB Lyon 1 Tél : 04.72.44.83.62 secretariat.ediss@univ-lyon1.fr	**Mme Sylvie RICARD-BLUM** Institut de Chimie et Biochimie Moléculaires et Supramoléculaires (ICBMS) - UMR 5246 CNRS - Université Lyon 1 Bâtiment Raulin - 2ème étage Nord 43 Boulevard du 11 novembre 1918 69622 Villeurbanne Cedex Tél : +33(0)4 72 44 82 32 **sylvie.ricard-blum@univ-lyon1.fr**
INFOMATHS	**INFORMATIQUE ET MATHÉMATIQUES** **http://edinfomaths.universite-lyon.fr** Sec. : Renée EL MELHEM Bât. Blaise PASCAL, 3e étage Tél : 04.72.43.80.46 infomaths@univ-lyon1.fr	**M. Hamamache KHEDDOUCI** Université Claude Bernard Lyon 1 Bât. Nautibus 43, Boulevard du 11 novembre 1918 69 622 Villeurbanne Cedex France Tél : 04.72.44.83.69 **hamamache.kheddouci@univ-lyon1.fr**
Matériaux	**MATÉRIAUX DE LYON** **http://ed34.universite-lyon.fr** Sec. : Yann DE ORDENANA Tél : 04.72.18.62.44 yann.de-ordenana@ec-lyon.fr	**M. Stéphane BENAYOUN** Ecole Centrale de Lyon Laboratoire LTDS 36 avenue Guy de Collongue 69134 Ecully CEDEX Tél : 04.72.18.64.37 **stephane.benayoun@ec-lyon.fr**
MEGA	**MÉCANIQUE, ÉNERGÉTIQUE, GÉNIE CIVIL, ACOUSTIQUE** **http://edmega.universite-lyon.fr** Sec. : Stéphanie CAUVIN Tél : 04.72.43.71.70 Bâtiment Direction INSA Lyon mega@insa-lyon.fr	**M. Jocelyn BONJOUR** INSA Lyon Laboratoire CETHIL Bâtiment Sadi-Carnot 9, rue de la Physique 69621 Villeurbanne CEDEX **jocelyn.bonjour@insa-lyon.fr**
ScSo	**ScSo*** **https://edsciencessociales.universite-lyon.fr** Sec. : Mélina FAVETON INSA : J.Y. TOUSSAINT Tél : 04.78.69.77.79 melina.faveton@univ-lyon2.fr	**M. Bruno MILLY** Université Lumière Lyon 2 86 Rue Pasteur 69365 Lyon CEDEX 07 **bruno.milly@univ-lyon2.fr**

*ScSo : Histoire, Géographie, Aménagement, Urbanisme, Archéologie, Science politique, Sociologie, Anthropologie

Remerciements

Je veux remercier Michele C. pour avoir cru en moi depuis le début et m'avoir permis de réaliser cette thèse. Bon courage pour la tienne !

Merci à Robin pour tout ce que tu m'as transmis sur des sujets techniques et pratiques. Tu m'as vraiment donné le goût de la recherche en aéronautique, travailler avec toi a été très enrichissant.

Je veux remercier Paolo, Laurent et Minh Tu pour l'excellence, l'assiduité et la disponibilité dont vous avez fait preuve tout au long de ma thèse. Vous m'avez énormément appris pendant ces trois ans, je n'aurais pas fait le quart de mon travail sans vous.

Je veux aussi remercier toute l'équipe charges et aéoélasticité d'Airbus Toulouse pour m'avoir acueilli dans cette famille et ce superbe environnement de travail, j'espère vraiment pouvoir continuer à travailler avec vous dans le futur.

Je tiens aussi à remercier tous les membres du laboratoire Ampère, les quelques mois passés avec vous ont été très gratifiants. J'espère que la bonne ambiance du laboratoire continuera longtemps.

Je souhaite adresser de chaleureux remerciments aux membres du jury de thèse, votre intérêt et votre disponibilité sont précieux et extrêmement appréciés. Je remercie Emanuelle Vidal-Salle de m'avoir fait l'honneur de présider le jury; Daniel Alazard et Marco Lovera pour le temps qu'ils ont passé à la relecture de ce mémoire, et pour l'excellente qualité de leurs commentaires; Isabelle Queinnec pour sa précieuse contribution en mécanique; et enfin Rafael Palacios pour avoir effectué le déplacement pour la soutenance et m'avoir fait profiter de sa préciseuse expérience dans le domaine de l'aéronautique.

Merci aussi à Michele L. pour être moins beau et intelligent que moi, ce réconfort permanent a été décisif pour mener à bien ma thèse.

Enfin, merci à Paola pour ton soutien tout au long de cette thèse !

Contents

List of Figures

List of Tables

Nomenclature and acronyms

General

TAS	=	True airspeed
CAS	=	Calibrated airspeed
VMO	=	maximum operating speed
VD	=	Maximum dive speed
M	=	Mach number
κ	=	Reduced frequency
$\bar{q}$	=	Dynamic pressure
$\boldsymbol{A}, \boldsymbol{B}, \boldsymbol{C}, \boldsymbol{D}$	=	State-space model matrices
$\boldsymbol{x}, \boldsymbol{u}, \boldsymbol{y}$	=	State, input and output vectors
t	=	Continuous time
k	=	Discrete time

Aircraft dynamics modeling (Chapter 2)

b	=	Wing span
S_{ref}	=	Reference surface
AR	=	Aspect ratio
CS	=	Control surfaces
ρ, ρ_0	=	Air density (local and at ground level)
a, a_0	=	Speed of sound (local and at ground level)
P, P_0	=	Air pressure (local and at ground level)
U_{gust}, L_{gust}	=	Gust amplitude and gradient distance
U_{ref}	=	Reference gust velocity
U_σ, L_{turb}	=	Turbulence standard deviation and scale
MTOW	=	Maximum take-off weight
MZFW	=	Maximum zero-fuel weight
MLW	=	Maximum landing weight
Z_{MO}	=	Maximum altitude of operations
F_g, F_{gz}, F_{gm}	=	Flight profile factors
$\mathcal{L}$	=	Lagrangian
q_i	=	Generalized displacements
$\boldsymbol{R_0}$	=	Body axes in inertial frame
$\boldsymbol{\Theta} = \begin{bmatrix} \phi & \theta & \psi \end{bmatrix}^T$	=	Euler angles
$\boldsymbol{D}$	=	Kinematics matrix
$\boldsymbol{Q_t}, \boldsymbol{Q_r}, \boldsymbol{Q_h}$	=	Translational, rotational and elastic generalized forces
$\boldsymbol{u_g}$	=	Displacements in the g-set

$\boldsymbol{x_g}, \boldsymbol{x_h}$	=	Constrained displacements in the g-set and in modal coordinates
$\boldsymbol{\eta}$	=	Generalized elastic coordinates
$m_i, \boldsymbol{J_i}$	=	Mass and inertia of lumped masses
$\boldsymbol{d_i}, \boldsymbol{\phi_i}$	=	Elastic deformation and rotation of lumped masses
$\boldsymbol{V_b}$,$\boldsymbol{\Omega_b}$	=	Translational and rotational velocities of the body frame
$\boldsymbol{L}$	=	Elastic angular momentum
$m, \boldsymbol{J}$	=	Aircraft mass and inertia
$\boldsymbol{g}$	=	Acceleration of gravity
$\boldsymbol{F_{ext}}, \boldsymbol{M_{ext}}$	=	
$\boldsymbol{M_{gg}}, \boldsymbol{B_{gg}}, \boldsymbol{K_{gg}}$	=	Inertia, damping and elastic matrices in the g-set
$\boldsymbol{M_{hh}}, \boldsymbol{B_{hh}}, \boldsymbol{K_{hh}}$	=	Inertia, damping and elastic matrices in modal coordinates
$\boldsymbol{\Phi_{gh}}$	=	Modal matrix
$\boldsymbol{A}(M,k)$	=	Aerodynamic influence matrix
$\boldsymbol{p}$	=	Pressure vector
$\boldsymbol{w}$	=	Downwash
$\boldsymbol{S}$	=	Integration matrix
$\boldsymbol{N}$	=	Splining matrix
$\boldsymbol{D_1}, \boldsymbol{D_2}$	=	Substantial differentiation matrices
ω	=	Angular frequency
$\boldsymbol{v}$	=	Wind velocity
$\boldsymbol{\delta}$	=	Control surfaces deflections
$\boldsymbol{T}$	=	T-matrix for loads computation
α	=	Angle-of-attack
Φ_y	=	Output variable PSD
$\boldsymbol{\rho}^{corr}$	=	Loads correlation factor
$\boldsymbol{\sigma}^{corr}$	=	Correlated loads

System identification (Chapter 3)

n	=	Order of the identified state-space model
$\bar{n}$	=	Number of imposed poles
N_y	=	Number of outputs
N_u	=	Number of inputs
N	=	Number of frequency data samples
$\left[\omega_i,\, \boldsymbol{H}(e^{j\omega_i})\right]_{i=1\ldots N}$	=	Frequency data
$\boldsymbol{V}$, $\boldsymbol{\Sigma}$, $\boldsymbol{W}$	=	Singular value decomposition of a matrix
$\boldsymbol{\mathcal{O}}$	=	Observability matrix
$\hat{\boldsymbol{\mathcal{O}}}$	=	Estimate of the observability matrix
$\overline{\boldsymbol{\mathcal{O}}}$	=	$\hat{\boldsymbol{\mathcal{O}}}$ with first N_y rows truncated
$\underline{\boldsymbol{\mathcal{O}}}$	=	$\hat{\boldsymbol{\mathcal{O}}}$ with last N_y rows truncated
$\mathbb{L}$	=	Loewner matrix
$\mathbb{L}_\sigma$	=	Shifted Loewner matrix

λ_i, $\boldsymbol{p_i}$	=	Pole (eigenvalue) and eigenvector
$\bar{\boldsymbol{\Lambda}}$, $\bar{\boldsymbol{P}}$	=	Matrices of imposed poles and of associated eigenvectors
$\boldsymbol{\Lambda}$, $\boldsymbol{P}$	=	Matrices of free poles and of associated eigenvectors
$\mathcal{D}^{\alpha,\beta}$	=	Set of constrained poles location

Active control design (Chapters 4 and 5)

$\boldsymbol{K}, \boldsymbol{P}$	=	Controller and Augmented plant
$\boldsymbol{G}$	=	Aeroelastic model
$\boldsymbol{u_{com}}$	=	Controlled variable
$\boldsymbol{y_{meas}}$	=	Measured output
$\boldsymbol{T_{\alpha\mapsto\beta}}$	=	Transfer function from generic vector $\boldsymbol{\alpha}$ to $\boldsymbol{\beta}$
$\boldsymbol{H_{act}}, \boldsymbol{H_{sens}}$	=	Actuators and sensors transfer functions
ω_0, ξ	=	Actuators' cutoff frequency and damping ratio
$u_{max}, \dot{u}_{max}$	=	Maximum actuators deflection angle and rate
$\boldsymbol{\tau_{sens}}$	=	Sensors delays
L	=	Lidar measurement distance
k_n	=	Lidar noise coefficient
$\boldsymbol{H_{zu}}, \boldsymbol{H_{zy}}, H_v, \boldsymbol{H_{ref,u}}$, $\boldsymbol{H_{ref,y}}, H^i_{nv}, \boldsymbol{H_{ny}}$	=	H_∞ tunable filters
$\boldsymbol{z_u}, \boldsymbol{z_y}$	=	Exogenous output
$\boldsymbol{w_v}, \boldsymbol{w_{ref,u}}, \boldsymbol{w_{ref,y}}, \boldsymbol{w_{ny}}, \boldsymbol{w_{nv}}$	=	Exogenous input
$\boldsymbol{S_u}, \boldsymbol{S_y}$	=	Input and output sensitivity functions
β_u, β_y	=	Input and output modulus margins
$\boldsymbol{\Delta_u}, \boldsymbol{\Delta_y}$	=	Input and output uncertainties
T	=	MPC output optimization time horizon
T_u	=	MPC input optimization time horizon
$\boldsymbol{u_{min}}, \boldsymbol{u_{max}}, \boldsymbol{y_{min}}, \boldsymbol{y_{max}}$	=	MPC bounds on input and output variables
$\boldsymbol{Q}, \boldsymbol{R}$	=	Matrices defining the MPC L_2 objective
$\boldsymbol{A_K}, \boldsymbol{B_K}, \boldsymbol{C_K}, \boldsymbol{D_K}$	=	State-space matrix functions of LPV controller
$F(\boldsymbol{G}, \boldsymbol{K})$	=	H_∞ objective for AFS
$\boldsymbol{H_{VK}}$	=	Transfer function for approximating Van Karman turbulence
$\boldsymbol{G_f}$	=	Aeroelastic subsystem with only flutter modes

Acronyms

GLA	=	Gust load alleviation
AFS	=	Active flutter suppression
TAS	=	True airspeed
CAS	=	Calibrated airspeed
LTI	=	Linear time-invariant
LPV	=	Linear parameter-varying
HTP	=	Horizontal tail plane
VTP	=	Vertical tail plane
CFD	=	Computational fluid dynamics
AR	=	Aspect ratio
XRF1-HARW	=	XRF1 aircraft model with high aspect ratio wing
GAF	=	Generalized aerodynamic force
DLM	=	Doublet lattice method
FEM	=	Finite-element method
PSD	=	Power spectral density
MIMO	=	Multi-input multi-output
SISO	=	Single-input single-output
SIMO	=	Single-input multi-output
SIDORT	=	System identification with orthogonal eigenvectors
SIDPEV	=	Subspace identification by pseudo-eigenvalue problem
DNOC	=	Direct nonlinear optimization with constraints
SVD	=	Singular value decomposition
LFT	=	Linear fractional transform
LMI	=	Linear matrix inequality
MPC	=	Model predictive control
LQG	=	Linear quadratic gaussian
LQR	=	Linear quadratic regulation

Chapter 1

Introduction

Contents

1.1 Loads and aeroelasticity

The design of an aircraft goes through various steps, from the initial concept to the final certification. Among the different disciplines involved, the loads analysis plays an important role all along the aircraft development, and during its life cycle. The loads are a general concept which can cover different physical phenomena and quantities, introduced in this section. Broadly speaking, loads are forces applied on the airframe, and their study aims at defining the stress environment of the aircraft either in normal operations or in extreme conditions. The loads analysis has different interconnections with the other disciplines. Typically, aerodynamic, structural and control systems engineers provide the inputs to the loads computation, which are then used by the stress analysts to quantify the risk of structural failure and decide whether it is acceptable or not. More loads generally require heavier structures, and affect the overall aircraft design. It is then critical to have a good understanding of them, in order to improve the global performance. A bad knowledge of the loads in an aircraft require important safety margins to cope with the uncertainty, leading to the so-called "conservatism" in design, meaning that more than necessary security precautions are taken. The general framework of the loads computation is called aeroelasticity, the sub-domain of mechanics that takes into account the aircraft structure and the aerodynamics. This section

briefly presents the different types of loads that exist in an aircraft, to introduce the loads due to the wind, that are the first concern of this work.

1.1.1 The causes of loads

Different causes can create loads on the aircraft structure. A first distinction can be made between ground and flight loads. The former are those caused when the aircraft lands and during the maneuvers performed on the ground. The landing gear is designed to withstand the shock generated by the touch down, during the landing, and its study is generally done using nonlinear models. The maneuvers performed on the ground can be of particular importance, as in this phase the wings' weight must be totally supported by the structure, while during a flight the lifting force alleviates this load. Considering the flight loads, two main causes are generally considered. The first includes all the in-flight maneuvers that can be performed by a pilot. For instance, in a positive symmetrical steady maneuver, the elevators are deflected upwards, creating a pitch-up movement which increases the angle-of-attack and increases the lift force applied on the wings. The highest possible cases of vertical acceleration are reached during this maneuver. Similarly, a set of maneuvers is applied to the aircraft during its design phase, to verify that it can withstand extreme loading conditions. The second source of in-flight loads is the wind, and it is the one studied in this work. Extreme cases of gusts or turbulence can generate important loads on the structure. They can have several origins, such as storms and clouds, or can even exist in clear air due to wind shear, jets streams and because of the ground topography [Hoblit 1988]. The wind first applies aerodynamic forces on the lifting surfaces, such as the wings and the horizontal and vertical tail planes, which create structural loads that propagate in the airframe. While the maneuver loads can generally be computed using quasi-steady models, because of the long time constants involved, the wind loads are unsteady due to the relative high frequency of the gust and turbulence disturbances. This implies that several structural modes can be excited, and the full interaction between the aerodynamics and the structure must be considered in the analyses. In addition to the loads, the wind creates discomfort for the passengers and the pilot, and can even lead to injuries when a negative vertical acceleration is suddenly applied to the airplane.

1.1.2 The different natures of loads. Basic certification principles

In addition, the loads can be divided into two categories: the fatigue and the static strength loads. The first one corresponds to loads which, applied continuously throughout the aircraft life cycle, can create damages on the structure, such as cracks or buckling. The fatigue loads are typically computed in normal operational conditions of the aircraft. They have an impact on the aircraft design, by requiring "damage tolerant structures", and on the maintenance. By a precise knowledge of the fatigue loads, we can predict the location and the propagation of an eventual damage, and control it in such a way that it remains safe for the overall structure integrity. The shift from structures designed to stay intact during the full aircraft lifetime to structures

for which the degradation can be forecast and controlled has led to significant performance and safety improvements in aeronautics in the last decades. On the contrary, the static strength loads correspond to extreme events which can occur during the aircraft life, and to which it must survive. More precisely, we distinguish the limit loads, which correspond to the maximum loads expected in service, and the ultimate loads, obtained by applying a safety factor of about 1.5. The general certification philosophy is to demonstrate that the structure can withstand the limit loads without deformation, and the ultimate loads without breaking. A probability of occurrence of about 10^{-5} per flight hour is generally considered for the limit loads, and about 10^{-9} for the ultimate ones. This work mainly focuses on the static strength loads. The active control techniques developed to alleviate them also work in nominal conditions, and could then reduce the fatigue loads if they were always active. However, as will be explained in section 1.2, this should not be the case in real applications.

The different cases of limit loads are described in the official certification documents. To be operated in a region of the world, an aircraft must by certified by the local agencies which issue their own documents. In Europe, the European Union Aviation Safety Agency (EASA) is in charge and the certification documents applicable to large aeroplanes is called the CS-25 [European Aviation Safety Agency (EASA) 2007]. Another agency of importance is the Federal Aviation Administration (FAA) in the United States of America, and their Federal Aviation Requirements (FAR). Only the European CS-25 is considered in this work.

1.1.3 Static and dynamic aeroelasticity

The framework used to study the loads is called aeroelasticity. This discipline of Mechanics dates back to the beginning of the 20-th century, and was formalized in [Bisplinghoff, Ashley, and Halfman 1955a], which is still a work of reference on this subject. Aeroelasticity can be seen as the study of the interaction between aerodynamic and structural forces, as indicated by the name, although the inertial forces play an essential role too. Some important phenomena occurring in an aircraft can only be explained using this theory, and a few of them can be cited hereby. The effectiveness of control surfaces (ailerons, elevators, rudders) is affected by aeroelastic effects, and in certain conditions the controllability of the aircraft can be deteriorated. A phenomenon called "control system reversal" is an extreme case occurring at a certain velocity, in which the deflection of a control surface has no effect on the aircraft motion, and a reversed effect above this velocity. Aeroelastic effects can also influence the aircraft stability, and provoke a structural instability phenomenon called "flutter" that can lead to the destruction of some parts of the airframe. Furthermore, the aeroelasticity strongly affects the loads distribution on the airframe. These effects can be predicted with relatively good accuracy by linear aeroelastic models. Some other effects are of nonlinear nature, such a "buffeting", which causes high-frequency vibrations of some structural parts due to aerodynamic impulses produced by the wake [Bisplinghoff, Ashley, and Halfman 1955a].

Two types of aeroelastic models are used in this work, and rely on different techniques. The static aeroelastic computations are performed assuming that the aircraft is at equilibrium. Historically, a structural Finite-Element Method and a Computational Fluid Dynamics (CFD) computations are performed successively. The former computes the shape of the aircraft deformed by the action of aerodynamic forces, which is in turn used as input to the latter, that must assume a certain aircraft shape to compute the aerodynamic forces. This process is accurate, but extremely time-consuming, and new techniques such as Airbus's α-shift method have been developed to accelerate it. The static aeroelastic model provides the equilibrium loads applied on the aircraft structure, due to the aerodynamic forces (lift and drag) and moments computed at a certain operation point (called trim), composed of the aircraft velocity, climbing angle, altitude, etc. To account for dynamic effects, such as maneuvers and wind, a dynamic aeroelastic model must be used. It will be the base for computing loads, performing simulations, and designing active control solutions. It is defined in details in chapter 2.

The more flexible the aircraft, the more important the aeroelastic effects. The flexibility of an aircraft is defined by the type of materials used, but also by its shape. Typically, long and tapered wings tend to be more flexible, and their deformation due to aerodynamic forces will be higher. From the point of view of an aircraft designer, the flexibility can have pros (better lift-to-drag ratio, lighter structures) and cons (variable wing shape, loss of control effectiveness), and it creates challenges across different disciplines. However, the general trend is to go towards lighter aircraft, with high aspect-ratio wings ("length to width" ratio, defined in section 2.1) and flexible materials. Significant performance improvements could be obtained by such designs, with lower fuel consumption. From a static loads point of view, an increased flexibility means higher structural deformations, hence higher loads. Dynamically, it implies a decrease of the natural structural frequencies, which are more easily excited by external perturbations such as the wind, and which interact more with the flight dynamics and the handling qualities of the aircraft. Finally, an increased flexibility also leads to more unstable aircraft, from an aeroelastic point of view.

1.2 Objectives and methodology

1.2.1 Objectives: load attenuation and stabilization

The general objective of this work is to develop solutions to reduce the loads due to the wind applied to the airframe, with a view to improving the overall aircraft performance, and the passengers comfort. This must be performed in an industrial airplane environment, and the interactions with the other subsystems composing the aircraft must be accounted for, together with the main constraints imposed by the certification documents. This work does not aim at directly interacting with the overall aircraft design, like Multi-Disciplinary Optimization (MDO) does. Instead, by studying some of the new challenges in terms of loads, aeroelastic stability and modeling implied by the next generations of highly efficient aircraft, the focus is on developing new techniques which

can be included in future designs.

The main focus of this work is then the so-called Gust Load Alleviation (GLA), which aims at reducing the loads due to the wind [1]. Intermediary objectives are required to achieve this: the aircraft modeling and the aeroelastic stabilization. The former aims at finding mathematical models used for simulations, control design and analysis. Ideally, they should be simple, accurate, and represent all the physical effects of interest. Of course, no such model exists, and new techniques must be developed and trade-offs must be conducted depending on the application. The aeroelastic stabilization, on the other hand, consists in ensuring that the flutter instability does not occur during nominal operations, with safety margins. Because of their complexity and the influence they have on other related subjects, these intermediary objectives are of primary importance in their own right.

1.2.2 Aeroservoelasticity: active control solutions

The challenges raised by the increased flexibility of aircraft, mentioned in section 1.1.3, have stimulated many active research topics, with the development several new techniques. A review of some existing passive and active techniques will be done in chapters 4 and 5. The active ones have the advantage of not requiring, in general, important modifications of the aircraft structure. They consist in developing laws that use information from the available on-board sensors to control the actuators that affect the elastic behavior of the aircraft. This integration of control laws into the aeroelastic models is called "Aeroservoelasticity". The study of the interaction between flight control systems and the aeroelastic behavior of the aircraft dates back to the early 70's with, for example, [Holloway, Burris, and Johannes 1970] in which the idea of including the classical control laws into the overall aircraft design was proposed. The use of dedicated laws to control aeroelastic models has started to emerge in the same years with [Nissim 1971] and [Sandford, Abel, and Gray 1975]. Aeroservoelasticity gained importance only in the 90's with the development of computers and the so-called fly-by-wire aircraft, where the manual flight controls were replaced by automated systems. In the same period, important progress in automatic control was accomplished, and it profited to active control solutions for aeroelastic systems [Zimmermann 1991]. However, it is only in recent years that active control solutions started being implemented in commercial aircraft, and always with simple laws. The active GLA is implemented in recent aircraft such as Airbus's A380 and A350 by statically deflecting the ailerons to modify the loads distribution along the wing. The active aeroelastic stabilization, called Active Flutter Suppression (AFS) in the literature, is not yet implemented on commercial aircraft.

The development and implementation of active control solutions for loads attenuation and aeroelastic stabilization that would take advantage of the recent developments in control engineering is then a major issue for the next generations of aircraft. Integrated within the general design of new more flexible, lighter aircraft, they can participate in improving its performance

[1] The term "gust loads" is ambiguous, and it is not used in this work.

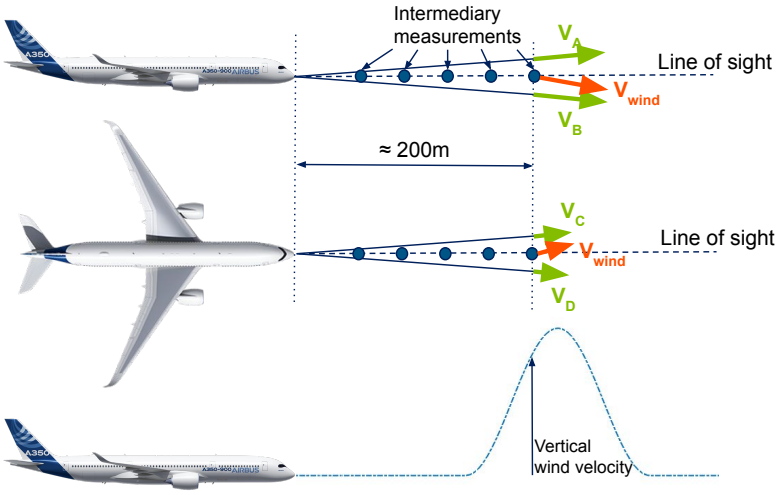

Figure 1.1: Remote measurement of the wind velocity using a lidar

and solving aeroelastic problems in the next generations. New active GLA techniques could also take advantage of the lidar technologies under development. Airborne lidars are sensors which can emit a laser and receive the light scattered by air molecules, or by particles present in the air. By measuring a phase shift caused by Doppler effect, the lidar can deduce the relative velocity of the air at a few hundred of meters ahead of the aircraft, as illustrated in Fig. 1.1. Several laser beams are emitted and the projection of the air velocity onto their directions is measured. This allows the estimation of the wind velocity before it affects the aircraft (see section 4.3 for the detailed wind velocity estimation). The information of the perturbation that will create loads a few tenths of seconds later on the aircraft can be used by feedforward control laws to deflect the actuators with phase advance. Combined with modern control laws, this technology can lead to significant loads attenuation and is studied in detail in this work[2].

Another promising strategy consists in splitting the wing into two different parts, with a hinge connecting them. The external part of the wing, called folding wingtip, can be released in case a high bending moment is estimated or forecast, hence strongly decreasing the lever arm in the inner part of the wing. By doing so, the bending moment at the wing root is instantaneously and a protection in case of extreme loads conditions is ensured. Many challenges are studied for this technology, which is not incompatible with the use of active control techniques for loads alleviation.

1.2.3 Technological readiness of flight control systems

The study of new aeroservoelastic strategies goes hand-in-hand with the technological development of new systems. If a GLA or an AFS system is used for reducing the weight of the structure,

[2]The word lidar is an acronym meaning "light detection and ranging", but is considered a noun in this work and is therefore written without capital letters.

the technology must be reliable enough against failure or malfunction. The choice of the aircraft control architecture must then be done accordingly. It is mostly composed of three elements: actuators, sensors and on-board computers. Actuators include the primary flight control surfaces, which are the ailerons, elevators and rudder. They allow the control of the airplane attitude in three axes, respectively with roll, pitch and yaw rotations. The secondary flight control surfaces are composed of the flaps and slats, which can be deployed at the wing's trailing and leading edge respectively to increase the lift in low-velocity phases such as take-off and landing. Additionally, the spoilers are situated on the top of the wings, and they can be deployed to create drag and negative lift. While these actuators are designed for flight control, their effect on the aeroelastic behavior of the aircraft can be used for GLA and AFS. The control surfaces can be actuated by different mechanisms. Traditionally, they are composed of hydraulic systems which are known for their robustness and the high forces they can generate. However, hydraulic systems suffer from drawbacks, such as the complexity of requiring full hydraulic circuits in the aircraft, generally doubled for redundancy, implying additional weight and maintenance. The presence of the hydraulic fluid is another inconvenience, as its behavior is affected by the temperature, and as it can be subject to leakages [Rosero et al. 2007]. This participates in motivating new actuation technologies, based on electric motors [Derrien 2012]. Compared to hydraulic systems, they would be lighter, less complex, more flexible and with a more precise torque handling, but they also have a lower power density and at the moment, they are less robust. In particular, they are more prone to jamming and can cause fire in case of short circuit [Derrien 2012; Rosero et al. 2007]. Current generations of aircraft (like Airbus A350 XWB or Boeing's B787) include hybrid actuators, in which the power is provided by hydraulic circuits, commanded by electrical systems (while classically the command was mechanical). The fully-electrical actuators for flight control systems are still under development at the time this thesis is being written. While these innovations can make significant design improvements, they have no major influence on the GLA and AFS. The main impact would be the reduced uncertainty of the actuators dynamics (due to hydraulic fluid's temperature) and the improved torque control. A new technology, based on morphing surfaces, could lead to significant advances in aeroservoelasticity. It works by modifying in real-time the shape of the aircraft structure using mechanisms located inside it. For example, morphing ailerons can replace classical rigid ailerons by deflecting continuously the trailing edge of the wing [Pankonien and Inman 2015]. Although most applications are based on such morphing trailing-edge, possibly other parts of the airframe could be actuated this way. Because of the absence of hinge, the continuous deflection along the wing's surface and the absence of fluid's boundary layer separation, this technology is more efficient than classical ailerons [Botez et al. 2018]. In spite of the increased total mass of the mechanism, the drag is strongly reduced [Previtali, Arrieta, and Ermanni 2014; Pankonien and Inman 2015]. Furthermore, this technology offers possibilities for structural optimization and even adaptiveness to local conditions [Botez et al. 2018]. This fact could be used for GLA and AFS to act on the loads distribution and stabilize the wing. Furthermore, control surfaces which are dedicated to GLA could be implemented in the aircraft design in addition to those used for flight control. Systems capable of producing lift in the middle of the wing's chord would avoid the unwanted effects of trainling-edge ailerons, which also create pitching moment

when they are deflected, increasing the wing's torsional moment and requiring a compensation by the elevators. As pointed out in [Previtali, Arrieta, and Ermanni 2014], these "direct-lift" control surfaces could have dedicated objectives, different from the flight control. A study called Smart intelligent aircraft structures (SARISTU) has been carried out by Airbus in the early 2010's, and a new demonstrator project called X-Wing is under development by UpNext, a subsidiary of Airbus. In the present work, only classical ailerons are considered, but the aircraft models described in section 2.1 have fully actuated trailing edges.

Sensors are of primary importance in aeroservoelasticity. Observability and controllability are, mathematically speaking, symmetrical problems of equal importance. However, due to the different system's limitations, the technological challenges are radically different. The main sensors used in airplanes are gyros and accelerometers. They are both very reliable and accurate, with low noise. They can be miniaturized and placed at different parts of the aircraft to obtain a good representation of the aircraft in a large frequency band. From this work's point of view, the accelerometers and gyroscopes suffer from three main limitations. The first is that they provide information about displacements only, and not forces. In order to estimate aeroelastic states and loads, they must be coupled with a structural model, that contains many sources of uncertainties. Estimating the loads is an active research problem, and different sources of information can be needed to obtain a good approximation [Carpenter and Albertani 2015]. Another limitation of the sensors is the delay they create, mainly by centralizing different sources of information in one computer (the intrinsic delay of sensors is low). This can be a source of instability and of performance loss, especially at high frequency. Finally, the third limitation regards the phase delay of the sensors with respect to a wind perturbation. Indeed, at the time the accelerometers and gyroscopes measure the effects of a wind gust onto the aircraft displacements, it might be too late to act. This is due in part to their locations, and to the slow dynamics of the aircraft due to its inertia. The use of probes measuring the angle-of-attack in GLA located at the aircraft nose provides a direct knowledge of the wind velocity disturbance, slightly in advance with respect to the effect on the aircraft structure. The recent developments of lidars goes further by measuring the wind velocity at a distance up to a few hundred of meters ahead of the aircraft as explained in section 1.2.2. These airborne lidar technologies based on the Doppler effect have been actively studied since the 2000's and are still under development. Two main technologies can be distinguished: the coherent and incoherent (also referred to as "direct") Doppler wind lidars [Herbst and Vrancken 2016]. The first type relies on infrared light, which is scattered by aerosols present in the air with size of the order of magnitude of the micron [Banakh, Smalikho, and Werner 2000; Banakh and Smalikho 2013]. The second type uses a near ultraviolet laser which is scattered by air molecules, by the Rayleigh scattering which is more effective at light high frequency (hence shorter wavelength) [Herbst and Vrancken 2016]. Most in-flight test campaigns of airborne Doppler wind lidars have been performed using the UV direct technology. The AWIATOR program [Schmitt et al. 2007], conducted by Airbus in the 2000's, and the DELICAT program [Vrancken et al. 2016], conducted in the 2010's by a European consortium composed of Thales and the DLR among others, were some of the main industrial programs to perform in-flight tests. Airbus UpNext's X-Wing project, already evoked about the morphing ailerons, also plans to implement lidars on the demonstrator.

The IR and UV technologies have different pros and cons: the UV lidars are more accurate (higher spatial resolution) and, because they require only air molecules, they can work at any altitude. The IR lidars can have a higher range with lower spatial resolution and they depend on the presence of aerosols in the air, whose density decreases exponentially with altitude. Furthermore, the UV lidars are affected by the presence of clouds while the IR ones are not. This fact is important for an eventual GLA strategy, for which the availability at any time of the flight is a requirement.

1.2.4 Major issues for active control design and implementation

Assuming that the system's technological advancement meets the objectives for active GLA and AFS, additional considerations must be made to develop a control design methodology. Starting with a rather universal concept, the simplicity of the control laws must be sought, for practical reasons (implementation on on-board computers), and also because clear and simple designs are often associated with robustness. If a complex high-order control law has been designed using a given model, chances are that, unless clear robustness criteria have been included in the synthesis, its performance will be reduced on slightly different models. This concept can be compared to the over-fitting in interpolation theory and machine learning. Robustness is key in aeronautics, and especially for critical systems such as the control laws, which can lead to tragic accidents in case of failure or poor design. Certification documents impose strong rules about this which can lead to conservatism in the aircraft design. However, this is not necessarily inevitable: by demonstrating a good understanding of the physical phenomena and of the uncertainties, this conservatism can be reduced and the door is open to adaptive designs. One important condition for a control strategy to be implemented on industrial airplanes is to be able to prove that it works in any situation, even extreme, that the aircraft is going to encounter during its life. This is at the heart of the certification documents for loads and flutter, and will influence this work in different ways, from the aeroelastic modeling to the control synthesis and post-analysis.

Furthermore, it must be noted that a control strategy is not composed only of a control law. Industrial flight control systems are complex, not because of the functions that compose them (which are generally combinations of gains and low-order transfer functions), but because of their architecture. Their behavior can vary depending on the flight phase, the altitude and velocity conditions, the aircraft configuration, the pilots inputs, the detection of an anomaly, etc. Preliminary studies, such as this work, are not required to account for all these situations; nevertheless, the definition of active GLA or AFS strategies must follow an acceptable logic and ensure compatibility with already existing systems. For instance, one can wonder when a load alleviation law must be activated. By activating it all the time, it would tend to reduce the aircraft handling quality, as the GLA objectives generally go against those of a pilot who wants to perform a maneuver: when trying to increase the aircraft acceleration to make it move, the GLA law tends to minimize it. If it is not operative all the time, then a condition that triggers its activation must be defined, along with the freedom left to the pilot and the flight control laws when the GLA is activated too. The possibility of sensors or actuators failure must also be considered in

the analysis, even in the preliminary study. For example, the lidar sensor can lead to performance gains when it works but if it is not reliable, the overall design of the aircraft may not be improved. With these considerations, we do not claim that all possible problems can be predicted and solved during the control strategy definition, but rather that the law synthesis must be made in a coherent way, as part of a more general design.

Another major challenge for control design is the definition of the aeroelastic model it is based on. Typical industrial state-space models are of very high order, and are incompatible with most control synthesis methods. Tailoring a model to a specific aeroservoelastic problem is a necessity, which requires defining the most important features that must be modeled, by a good understanding of the underlying physics, and using specific methods from dynamics and system identification theories. For GLA, the input/output response of the system must be accurately represented by the model, and the stability must be preserved. For AFS, the necessity to reproduce correctly the aeroelastic modes of the system in addition to the input/output behavior is challenging. The obtained model must be of low order, and the modeling process must preferably not be computationally intensive, to preserve flexibility and the possibility to define multiple models.

1.2.5 Methodology and organization of the manuscript

The general methodology of this work follows the objectives and the different considerations laid down in the previous sections. The main objective consists in defining active GLA laws and will be studied in details in chapter 4. Aeroelastic analyses require the definition of adequate models, and chapter 2 is dedicated to the development of aeroelastic equations based on the XRF1 aircraft concept, developed by Airbus specifically to study the effects of flexibility and to develop aeroservoelastic solutions. The aeroelastic equations cannot be directly used for control synthesis, and chapter 3 describes techniques to identify reduced-order models with different constraints depending on the application. Benefiting from the lessons learned in aerservoelasticity from the GLA study, and from the aeroelastic modeling and identification techniques developed in this work, the problem of AFS is investigated in 5. This logic has driven the PhD thesis whose results are presented in this work. However, it must be noted that the intermediary steps, which have naturally arisen from technical problems and, sometimes, lack of available solutions, have become primary objectives of this work. Their utility exceeds the simple prerequisites for GLA, and extends to other disciplines such as system identification, control and observer syntheses with parameter dependence, among others. The active flutter suppression, for instance, is first motivated by the necessity to use stable models in GLA, but also directly serves the aircraft design in a similar way as the GLA does. Hence, all the chapters contain their own technical advances and can also be considered as independent from one another.

In addition to the general logic followed by this work, the multi-model robust analysis is a common thread linking the different subjects. Inspired by the certification logic consisting in putting the aircraft in all possible extreme conditions, a multi-robust approach is used for control

synthesis and analysis, hence requiring dedicated modeling techniques. While many studies focus on aircraft evolving in one fixed condition, this work investigates a more general aeroelastic model under the form of several linear snapshots at different flight and mass conditions. This multi-model logic is linked to robustness and adaptiveness concepts, which are at the heart of today's challenge in aeroservoelasticity.

This thesis has lead to the publication of two journal papers [Fournier et al. 2022b; Fournier et al. 2023b] and two conference papers [Fournier et al. 2022a; Fournier et al. 2023a].

Chapter 2

Aircraft dynamics modeling

Contents

This chapter describes the framework used to develop the system identification, GLA and AFS techniques exposed in the subsequent chapters. Through the example of the XRF1 concept, a mathematical model of the aircraft and its environment is defined following industrial processes used at Airbus to develop and certify airplanes. No technical novelties are presented in this chapter, which instead lays the foundations of a research approach that intends to solve real-life complex problems by using modern techniques, with the constraints imposed by industry. A comprehensive description of the XRF1 aircraft model is then proposed in section 2.1. Section 2.2 then describes the modeling of the atmospheric environment with an emphasis on the gust and turbulence phenomena. In section 2.3, the aeroelastic modeling process is explained and discussed in view of the techniques described in the literature.

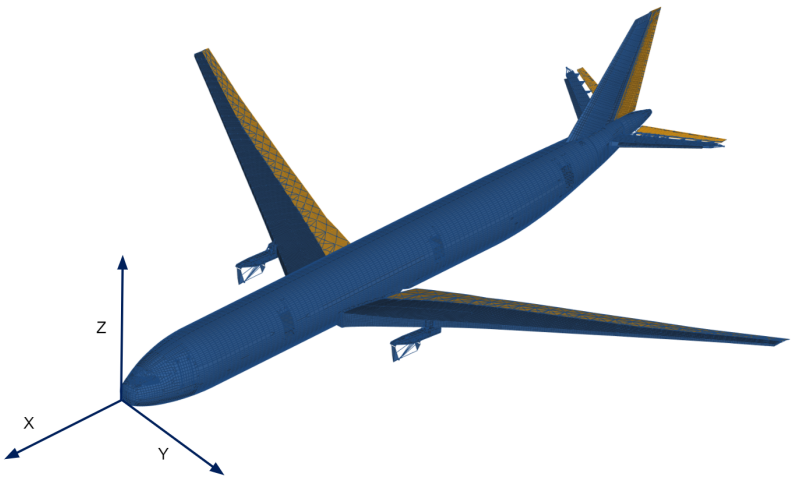

Figure 2.1: 3D view of the XRF1-HARW

2.1 Aircraft modeling

2.1.1 The XRF1 concept

The XRF1 is an aircraft concept developed by Airbus for research purposes. While its general configuration is similar to a long-range commercial aircraft, the wings are more flexible and more tapered. This configuration is very efficient from a global design point of view, as it would lead to a reduced drag compared to current commercial designs. However, the increased wing flexibility creates new challenges in terms of modeling and certification. The interaction between the aerodynamics and the wing structure creates so-called aeroelastic phenomena that will be described in section 2.3. With a highly flexible wing, the structural modes interact more directly with the flight dynamics, and create higher dynamical loads. Furthermore, the vibrations introduced can be slightly damped and even become unstable (flutter phenomenon). The XRF1 concept allows the study of these new challenges and possible solutions such as GLA and AFS, in a realistic large commercial airplane environment.

Several versions of the XRF1 have been issued. In most results and unless stated otherwise, the XRF1-HARW (High Aspect Ratio Wing) version is used in this work. It has been developed through a partnership between Airbus and the University of Michigan (Ann Arbor). As indicated by its name, is has a particularly high Aspect Ratio (AR) of 13, compared to a typical value of 8 in current generations of long-range commercial aircraft. The torsional stiffness of the wings has also been set to a low value to amplify its flexibility and instability. The main characteristics of the XRF1-HARW aircraft are presented in the next section.

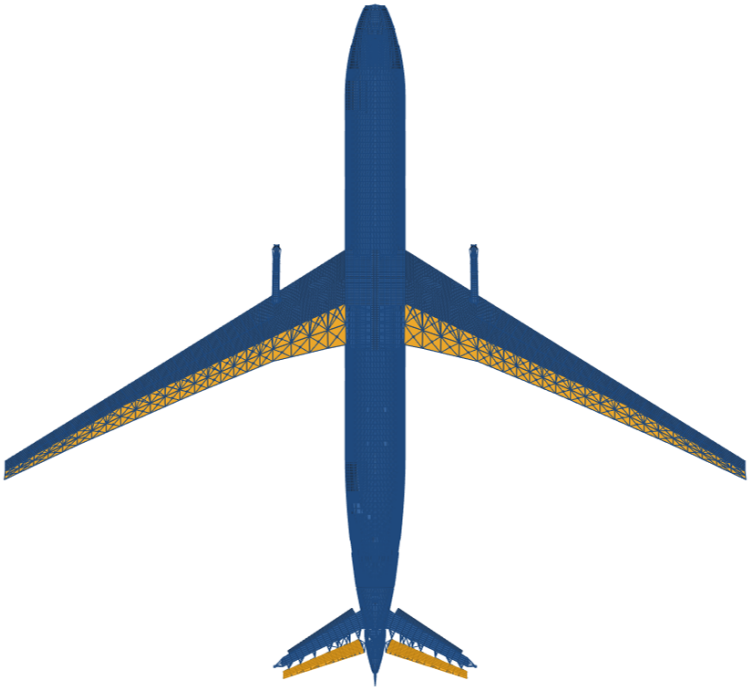

Figure 2.2: View from above of the XRF1-HARW

2.1.2 XRF1-HARW aircraft description

This section presents the main characteristics of the XRF1-HARW aircraft model used in this work, and defines the elementary elements needed for understanding the flight and aeroelastic dynamics. On Fig. 2.1 a 3D view of the XRF1-HARW is shown with the three body axes. The X axis is aligned with the fuselage and goes towards the nose of the aircraft. The Z axis is perpendicular to the X-axis and lies within the symmetry plane of the aircraft. The Y axis completes the others to form an orthogonal basis. Rotations around the X axis, Y axis and Z axis are respectively called roll, pitch and yaw and the corresponding rotation velocities are respectively noted p, q and r. The associated rigid-body dynamics and kinematics will be investigated in section 2.3. The control surfaces (CS) of the XRF1-HARW are made visible in Fig. 2.1 by their yellow color. Ailerons cover the trailing edge of the wing, a pair of elevators are located at the trailing edge of the Horizontal Tail Plane (HTP) and a rudder is positioned on the Vertical Tail Plane (VTP). A view from above of the aircraft is shown on Fig. 2.2, where the 23 pairs of ailerons are clearly seen.

Fig. 2.3 shows a view of the aircraft from the side with the definition of some vectors and angles. We call far-field velocity vector and note $\boldsymbol{V_\infty}$ the velocity of the air relative to the aircraft, assuming no wind. It is only due to the aircraft movement and evolves slowly due to the equilibrium between the aerodynamic forces and the thrust. The angle-of-attack, noted α, is the angle between the opposite of the far-field velocity and the X axis. The climb angle, noted γ, is defined as the angle between the horizon plane and the opposite of the far-field velocity. The total angle-of-attack α_{tot}

Aircraft property	Value
Reference surface (S_{ref})	380 m^2
Wing span (b)	70 m
Wing aspect ratio (AR)	13
Geometrical Mean Chord (GMC)	5.5 m
Mean Aerodynamic Chord (MAC)	7 m
Minimum mass	130.000 kg
Maximum mass	250.000 kg

Table 2.1: Properties of the XRF1-HAR aircraft

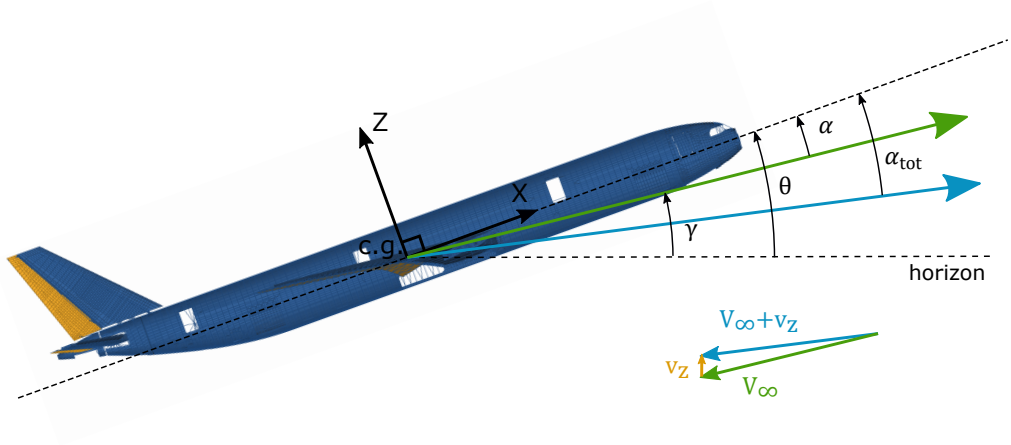

Figure 2.3: Longitudinal angles description

is the angle between the opposite of the air velocity relative to the aircraft (including the vertical wind w_z) and the X axis in the X-Y plane. Finally, θ is considered here as the angle between the horizon and the X-axis, but it will be defined more rigorously in section 2.3.3 with the aircraft kinematics. These constitute the main elements to study the longitudinal dynamics of the aircraft. The sideslip angle is defined similarly to the angle-of-attack, but in the X-Z plane (not shown in the figures.)

Some properties of the XRF1-HARW are presented in the table 2.1. The displayed values are not exact, for confidentiality reasons. The reference surface S_{ref} is the total surface covered by the wings. The wing span b is the distance between the two wing tips. The aspect ratio is defined as AR $= b^2/S_{ref}$. A higher aspect ratio means a more tapered wing. The chord is the distance between the wing's leading and trailing edges. As this distance varies spanwise, more definitions are needed. The GMC is the mean value, and the MAC is a reference value used in aerodynamics computation. The aerodynamic center is arbitrarily located at 30% of the MAC, backward from the leading edge at the wing's root. The minimum and maximum masses of the aircraft are given, the variation being due to the amount of fuel and the payload in the aircraft. More elements about the aircraft mass are exposed below in section 2.1.4.

2.1.3 Flight domain and velocity definitions

The design of an aircraft always includes a flight domain, which defines the velocities and altitudes at which it can fly. It is defined by the missions the aircraft needs to perform, and extreme cases that can occur during a life cycle. The flight domain is an important data in this work, as it defines operational conditions that can be taken as the basis for the study of the aircraft, and for the synthesis of control laws. It also provides a bounded set of conditions which needs to be considered as possible and fully taken into consideration in the analysis of the aircraft with and without GLA or AFS control laws.

Practically, it will be seen in section 2.3 that the loads depend both on the altitude and the velocity. The flight domain then has different implications on the methodology of a GLA law synthesis. First, some objectives can be defined as the maximum loads acceptable in operational and extreme conditions. Then, the synthesis of the GLA law can be performed with an adequately chosen flight point, taking for example conditions that lead to high loads, or even with a set of different flight conditions. The analysis phase must then be performed on the whole flight domain, to ensure that the results are satisfactory in all possible situations the aircraft can face during its life cycle. Concerning the AFS synthesis, one must ensure stability and robustness margins over an augmented flight domain, which helps defining the objectives. The synthesis and analysis must again be performed with full knowledge of the operational and extreme flight conditions. These considerations will be further developed in chapters 4 and 5 dedicated to the GLA and AFS respectively.

Before analyzing the flight domain of the XRF1 aircraft used in this work, some definitions are required. First, different velocities are used in this work and in the loads domain:

- The True Airspeed (TAS) is the velocity norm of the aircraft relative to the surrounding air. The True Airspeed is of particular importance for loads computations as it affects the aerodynamics of the aircraft. The measurement of the static pressure is not enough to determine the True Airspeed of the aircraft, as the knowledge of the local air density is also required.
- The Ground Speed (GS) is the horizontal velocity of the aircraft relative to the Earth's surface. In absence of wind, the ground speed is equal to the True Airspeed. Modern aircraft are generally equipped with Global Positioning Systems (GPS) and Inertial Navigation Systems (INS) that provide a reliable estimation of the Ground Speed. Under the assumption of negligible wind velocity, the True Airspeed can be then used on-board the aircraft.
- The Equivalent Airspeed (EAS) is defined as $\text{TAS}\sqrt{\frac{\rho}{\rho_0}}$ where ρ and ρ_0 are the air density locally and at sea level respectively. It is often used for loads computation as the dynamic pressure can be directly expressed from it regardless of the local air density. The EAS is often used in certification documents.
- The Calibrated Airspeed (CAS) is a modification of the EAS which approximates it, and

sometimes replaces it to define operational and extreme flight conditions because of its simplicity to estimate on-board an aircraft.

Note that the TAS, EAS and CAS are equal at sea level. For the sake of simplicity, only the TAS and CAS will be used in this work, assuming that the former is available on-board the aircraft. The CAS can be obtained as

$$CAS = a_0 \sqrt{5 \left[\left(\frac{\bar{q}}{P_0} + 1 \right)^{2/7} - 1 \right]} \tag{2.1}$$

where the dynamic pressure $\bar{q}$ is defined as

$$\bar{q} = \frac{1}{2} \rho \mathrm{TAS}^2 \tag{2.2}$$

and using results from compressible fluid dynamics, it can be expressed as:

$$\bar{q} = P \left[\left(1 + 0.2 M^2 \right)^{7/2} - 1 \right] \tag{2.3}$$

Here, a_0 is the speed of sound at 15°C, P_0 is the static pressure at sea level, and P is the local static pressure. Finally, we define the Mach number as the ratio of the TAS and the local speed of sound

$$M = \frac{\mathrm{TAS}}{a} \tag{2.4}$$

Furthermore, some values of the velocity are of particular importance for the aircraft design and the loads calculations. They define the different limit velocities for each configuration of the aircraft (airbrakes in or out, flaps and slats in or out, etc). For the sake of clarity, only two of them are mentioned in this work:

- The maximum operating speed VMO is defined as a CAS at which the aircraft operates in normal conditions and a value of 170 m/s is fixed in this work. Similarly a maximum operating Mach number MMO is defined and fixed at 0.86.
- the maximum dive speed VD expressed as a CAS. It represents the maximum possible velocity of the aircraft in case of dive, which is considered as an extreme condition. A value of 190 m/s is used in this work. Similarly a dive Mach number MD is defined and fixed at 0.93.

These velocities have a particular importance for the loads computations. Indeed, as explained above, the CAS is strongly linked to the dynamic pressure. As discussed later in section 2.3, the loads tend to increase with the dynamic pressure although this trend is not automatic when considering unsteady aerodynamics. It can then be assumed in first approximation that the maximum loads occur at the maximum CAS (either VMO in operational conditions or VD in extreme conditions). A verification must be performed at all velocities at the end of an analysis. Because

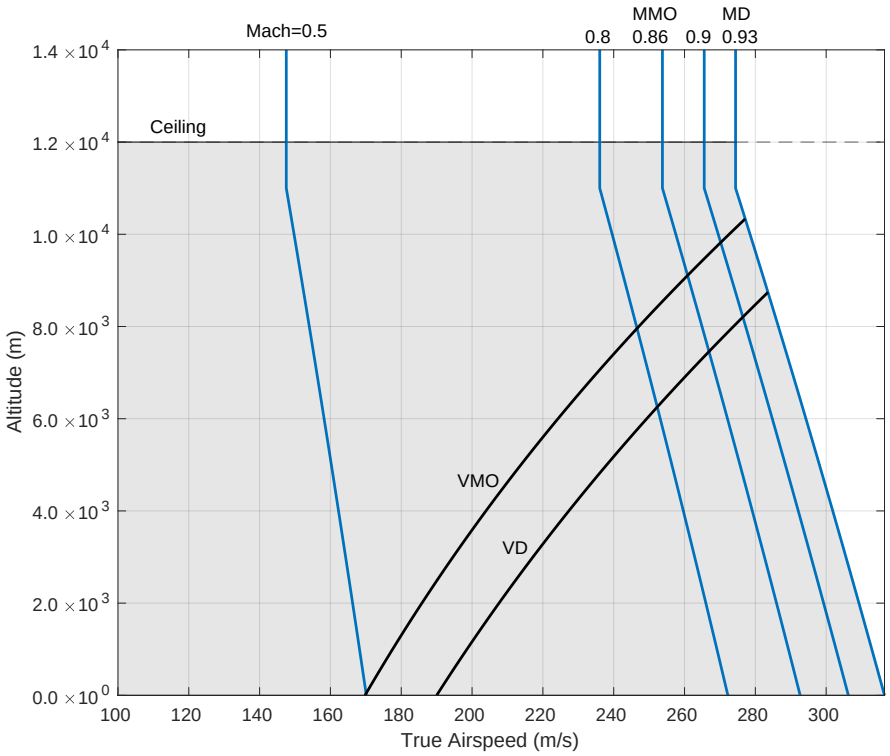

Figure 2.4: Flight domain

the aircraft spends much more time at VMO than at VD, the loads certification requirements are less restrictive at VD, as will be further discussed in chapter 4.

Fig. 2.4 presents a simplified flight domain of the XRF1 aircraft, with the information required for this work. The maximum operation altitude noted Z_{MO} is equal to 12.000 m. The iso-lines corresponding to five values of the Mach number are shown. The iso-lines corresponding to VMO and VD are plotted, recalling that these velocities are expressed as CAS hence cover various conditions of TAS and altitude. Note that at sea level, the TAS corresponds to the CAS.

It can be noted that a flight point can be defined by two parameters. At fixed CAS and altitude, for instance, the value of TAS and Mach number are fixed, and so are the local air density and speed of sound. This is done assuming the U.S. standard atmosphere [Office 1962] that gives the evolution of the temperature with altitude. The air pressure and density are obtained by assuming the air is an ideal gas in hydrostatic equilibrium. When fixing one of the two parameters, for example the CAS, one degree of freedom remains (it can be the altitude or the TAS for example) and will be considered as an uncertain parameters for the design of robust GLA laws in chapter 4.

2.1.4 Mass configurations

The previous section 2.1.3 has explained the boundaries of the aircraft flight domain. This section introduces the definition of the different possible mass configurations of the aircraft. The total weight of the aircraft and the mass distribution can differ from a flight to another, and can vary during the flight itself. Several phenomena can create such mass variations:

- The fuel can represent half of the total mass when the aircraft is fully loaded. During the flight, the fuel will be progressively depleted in the tanks located in the wings, creating important mass variations.
- The fuel density can vary, depending on the supplier and on the local temperature.
- The payload depends on the mission, and so do its mass and distribution inside the aircraft

As will be explained in section 2.3, these variations of mass distribution will have important repercussions on the aircraft dynamics. The moment of inertia and the total mass are directly affected, hence modifying the handling qualities and stability of the aircraft. This is clearly visualized on Fig. 2.5 that shows the mass-center of gravity diagram of the XRF1-HARW. This is a classical representation of the different mass configurations of an aircraft, to understand the

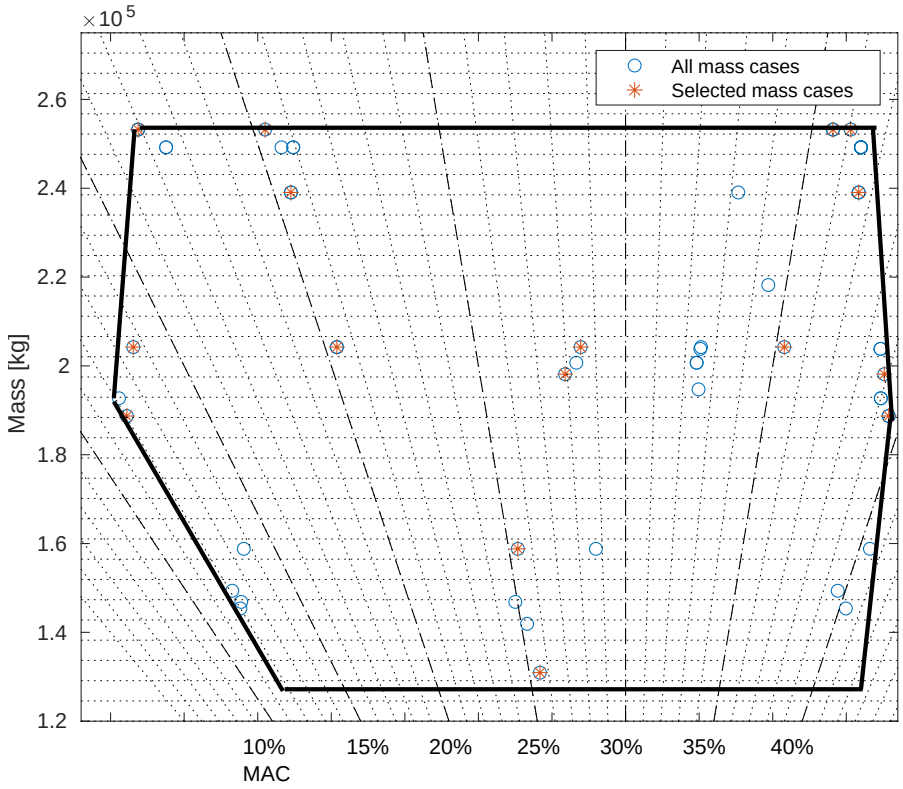

Figure 2.5: Mass-center of gravity diagram of the XRF1-HARW

limits in terms of mass and stability/maneuverability. The y-axis represents the total mass of the aircraft, and the diagonal lines have constant values of the center of gravity position, expressed as a ratio of the Mean Aerodynamic Chord (MAC), backward from the leading edge position. The left part of the diagram then corresponds to a center of gravity closer to aircraft nose and vice versa. The x-axis represents the mass multiplied by the arm (difference between the center of gravity and a point at 30% of the MAC). A mass case situated on the left part is more statically than a point on the right, but less maneuverable. The left limits are typically defined by minimum maneuverability and controllability requirements for landing and the capability to perform prompt avoidance pitch-up maneuvers [Es 2007]. The limits on the right part, in the opposite, are typically defined by stability margins requirements. The study of the loads due to the wind is influenced by thee flight mechanics of the aircraft, hence also by its mass and centering. A lighter aircraft has less inertia, hence a given gust will create a higher load factor. Similarly, an aircraft with a center of gravity situated forward (left on the diagram of Fig. 2.5) is more stable and its dynamic response might be lower than a mass case with a center of gravity located aft. Moreover, the distribution of the mass in the aircraft has a strong influence on the local loads. For example, if the wings fuel tanks are full, the statical wing root loads will be lower because the weight will counterbalance the local lift. The dynamical loads, on the other hand, will be lower because of the local inertia decreasing the local accelerations and displacements.

Some particular values of the mass can be noted, because of their importance in the certification documents. The Operating Weight Empty (OWE) corresponds to the weight of the aircraft without fuel or payload. It corresponds to the bottom limit of the diagram in Fig. 2.5. The Maximum Take-Off Weight (MTOW) is the maximum possible weight of the aircraft authorized at take-off, and corresponds to the upper limit. The Maximum Zero-Fuel Weight (MZFW) is the maximum weight without usable fuel. Its difference with the OWE is the payload mass. Finally, the Maximum Landing Weight (MLW) is the maximum weight authorized for landing.

Similarly to the different flight points mentioned in the previous section 2.1.3, the analysis of the aircraft and the control synthesis shall be performed with the full knowledge of the possible mass variations. Contrarily to the flight point, the mass configuration cannot be defined by a limited number of parameters. For control synthesis, the variations of the mass configuration will be considered as an uncertainty in the robust control syntheses of chapters 4 and 5. Considering the analysis, simulations will be performed with different mass configurations. In Fig. 2.5, a limited number of mass cases (16) have been selected as extreme cases. They should represent as much as possible the maximum loads and most restrictive flutter conditions. For the sake of conciseness, the detail of how these mass cases are selected is not developed in this document.

2.1.5 Flight control systems and limitations

The XRF1-model is equipped with different control surfaces, composed of 23 pairs of ailerons covering the wings' trailing edges, a pair of elevators and a rudder, all commanded by actuators.

All these surfaces can theoretically be used for active control. The high number of ailerons allows the study of different configurations, but using all of them at the same time is unrealistic. We will typically limit the surface covered by the ailerons to one fourth of the total surface. This choice will be further discussed in chapters 4 and 5 for GLA and AFS respectively. In this work a simplified model for the actuators dynamics is proposed, which is the same for all of them. A second-order transfer function between the deflection order and the true deflection is used to model the actuators dynamics:

$$\boldsymbol{H_{act}}(s) = \frac{1}{s^2 + 2\xi\omega_0 s + \omega_0^2} \tag{2.5}$$

where ω_0 and ξ are the actuators' cutoff frequency and damping ratio respectively. The cutoff frequency is typically chosen equal to 4 Hz and the damping ratio to 0.85, the true values will be specified in each results section. This transfer function has an important influence on the GLA and AFS control synthesis. It limits the capability to control the high frequency response of the aircraft. This limit must be studied in view of the frequency content of the variables that must be controlled for a given perturbation (for GLA), or of the frequency of the modes that must be damped (for GLA and AFS). This will be further developed with the study of the aeroelastic transfer functions and Power Spectral Densities (PSD) in section 2.3. In addition, constraints on the actuators' deflection angle and deflection rates are imposed. Typically, a maximum of 30° and 40°/s will be applied. The deflection angle limit is imposed by the system, and it prevents high local changes of direction of the airflow, which would create aerodynamic non-linearities. The maximum deflection rate is also imposed by the system, and acts similarly to the actuator's transfer function, by limiting the high frequencies. Note that these constraints can be seen as a saturation and a rate limiter, which are nonlinear functions. Hence, they cannot be directly imposed in linear robust control synthesis, and they will mainly be used for validation. The actuator's model presented here is simple, but it contains the main limitations of a true system. A significant difference with real-life applications comes from the fact that the behavior of an actuator can vary depending on external conditions. For example, hydraulic actuators (which constitute the majority in today's commercial airplanes) have different dynamics depending on their fluid's temperature. Although this is not directly modeled in this work, the levels of robustness of the control laws should cover this uncertainty.

Different sensors can be included in the XRF1-HARW model. Typically, accelerometers and gyroscopes can measure the acceleration and rotational velocities in the three body axes. They can be placed at the center of gravity, providing important information to understand the aircraft state, or placed anywhere on the structure to estimate the local deformations and loads. Incidence probes measure the total angle of attack, and they are generally located at the front of the fuselage. They are very useful for GLA, as they provide information about the wind disturbance, slightly in advance with respect to the moment they reach the wings. The incidence probes are always redundant to limit the effects of a failure. These sensors are modeled as pure delays that account for the different delays in the data acquisition process. A value of 40 ms is typically used. This value does not deteriorate the GLA performance as long as sufficient levels of robustness

are imposed. Regarding AFS, this delay can make a difference as high-frequency modes are sometimes involved in the flutter phenomenon. Finally, it is assumed in this work that the XRF1-HARW is equipped with a GPS/INS system that provides an accurate estimation of the ground speed, which we consider equal to the true airspeed (no constant wind). Another class of sensors can be used to estimate the loads in real-time. The strain gauges measure the variations in electrical resistance due to local deformations of the aircraft structure, which can be coupled with a structural model of the aircraft to compute the loads. Strain gauges are often used in test flight, in order to validate structural models and check that the loads levels are of the same order as those computed during the design phase. However, many strain gauges are needed to measure the loads, resulting in a heavy and intrusive sensing system. Furthermore, they are very fragile, and they need to be regularly calibrated in order to provide an accurate loads estimation. Other sensors are being developed to estimate the structural loads, such as the inclinometers. They consist of accelerometers located at different locations of the airframe. The relative acceleration vectors allows to deduce geometrically the evolution of the direction of each accelerometer. Since they are fixed to the airframe, the structural deformations can be deduced and coupled to a structural model to estimate the loads. The inclinometers are gaining popularity because of the miniaturization of accelerometers, and because of they do not require calibration.

2.2 Wind models

This section presents the wind models used to compute the loads and to synthesize GLA controllers. As explained in the introductory chapter 1, the strategy employed for GLA in this work is closely related to the aircraft design, aiming at reducing the maximum loads due to the wind. The models used to describe the wind must not necessarily be representative of the average conditions faced by the aircraft, but should rather represent the extreme conditions leading to the maximum loads. It is then natural to adopt the same models which are defined by the official certification documents such as the European CS-25 [European Aviation Safety Agency (EASA) 2007] for large aeroplanes. The paragraph 25.341 provides a definition of a set of wind models that cover different extreme loads cases. Two types of winds are considered:

- Wind gusts are short events of increased wind velocity with a duration ranging from a few tenths of seconds to a few seconds. Several causes can exist, such as the air instability [Oliver 2008] or the presence of large natural or artificial obstacles.
- Turbulence is a sustained increased of the wind velocity that can quickly change direction. It can last several minutes.

The gusts and turbulence define different load conditions for the aircraft by interacting dynamically with it. Exciting certain aeroelastic modes (see section 2.3) can lead to an important transient response of the aircraft. Gusts are designed to simulate short events of variable durations, which

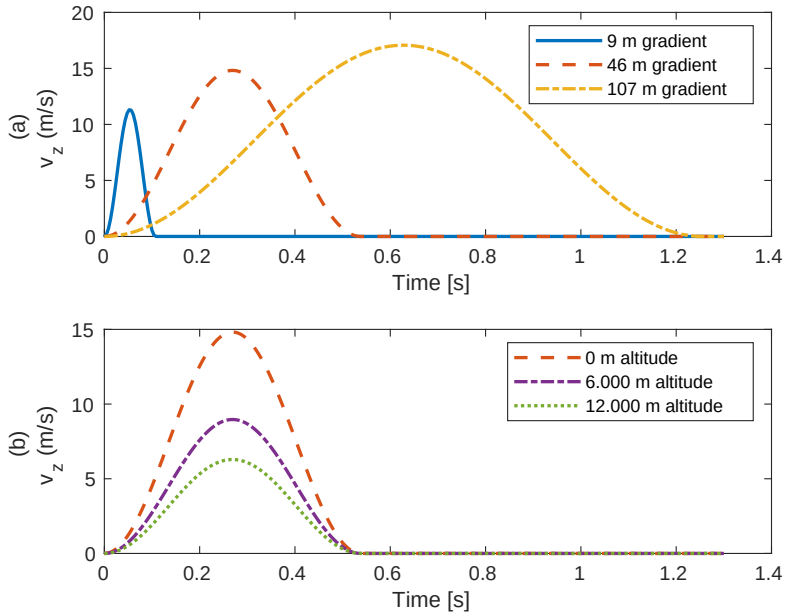

Figure 2.6: Vertical wind velocity of discrete gust profiles of different gradient distances at 0 m altitude (a) and at different altitudes with a 46 m gradient distance (b)

can target specific modes. The turbulence, on the other hand, can last several minutes and statistical effects on the aircraft can be observed.

The wind gust velocity is defined in the CS-25 [European Aviation Safety Agency (EASA) 2007] using the following discrete time gust model (sometimes referred to as $1 - \cos$ model).

$$v_z(t) = \begin{cases} \frac{U_{gust}}{2}\left[1 - \cos\left(\frac{\pi t \text{TAS}}{L_{gust}}\right)\right] & \text{if} \quad 0 \leq t \leq \frac{2L_{gust}}{\text{TAS}} \\ 0 \quad \text{otherwise} \end{cases} \tag{2.6}$$

where t is the time in s. L_{gust} is called the gradient distance in m and defines one half of the gust geometrical length. U_{gust} is the gust amplitude in m/s, which depends on L_{gust} and the altitude h:

$$U_{gust} = U_{ref}\left(\frac{L_{gust}}{107}\right)^{1/6} \tag{2.7}$$

and U_{ref} depends on the altitude as shown in Fig. 2.8 (a). It must be noted that U_{ref} is expressed as an EAS in this definition. The range of gradient distances is generally comprised between 9 m and 107 m. This parameter can vary, and in some circumstances it can excite specific aerolastic modes; these values of L_{gust} are more critical and they should be targeted during load analysis. In Fig. 2.6 time simulations of discrete gusts of various gradient distances (a) and at various altitudes (b) are shown for a TAS of 170 m/s. Short gusts have a lower amplitude but can excite higher frequency modes: due to the aircraft inertia and actuators limitations, they are more difficult to reject.

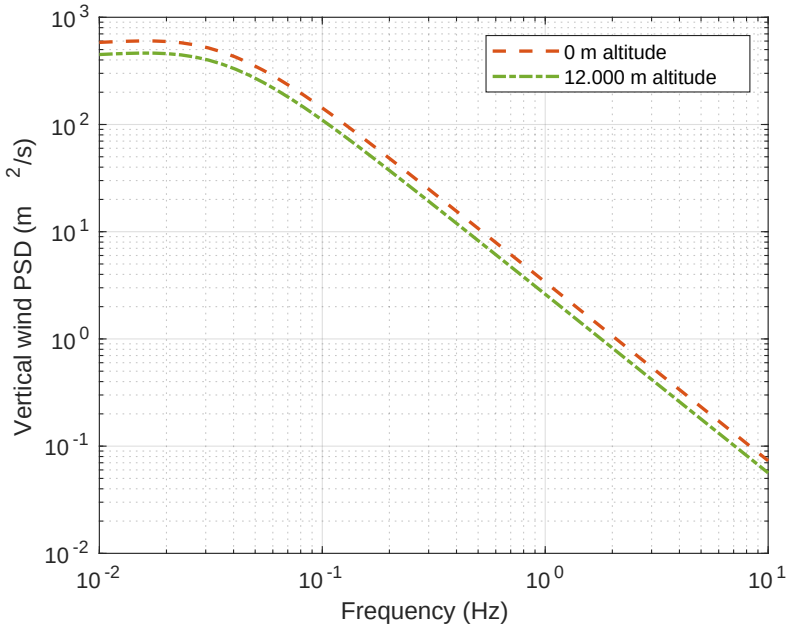

Figure 2.7: Von Kármán turbulence profile of scale length 762 m at 0 m and 12.000 m

The turbulence velocity is defined in the CS-25 as a stochastic process called continuous turbulence. It is characterized by its frequency content through its PSD. In this work, the empirical von Kármán PSD for vertical turbulence [Diederich and Drischler 1957] is used:

$$\Phi_{turb}(\omega) = U_\sigma^2 \frac{L_{turb}}{\pi \mathrm{TAS}} \frac{1 + \frac{8}{3}(1.339\frac{\omega L_{turb}}{\mathrm{TAS}})^2}{[1 + (1.339\frac{\omega L_{turb}}{\mathrm{TAS}})^2]^{11/6}} \tag{2.8}$$

where ω is the angular frequency in rad/s, L_{turb} is the scale of turbulence in m and U_σ is the turbulence standard deviation in m/s that diminishes with altitude as shown on Fig. 2.8 (b). This velocity is defined as a TAS. In Fig. 2.7 the von Kármán PSD is shown with a 762 m scale of turbulence, 170 m/s TAS and amplitudes computed at 0 m and 12.000 m using the equations defined in the European CS-25 [European Aviation Safety Agency (EASA) 2007].

Finally, a correction factor, called flight profile alleviation factor, is applied to the gust and turbulence velocities depending on some characteristics of the aircraft:

$$F_g = \frac{1}{2}(F_{gz} + F_{gm}) \tag{2.9}$$

with

$$F_{gz} = 1 - \frac{Z_{MO}}{76200} \tag{2.10}$$

and

$$F_{gm} = \sqrt{\frac{\mathrm{MZFW}}{\mathrm{MTOW}} \tan\left[\frac{\pi}{4}\frac{\mathrm{MLW}}{\mathrm{MTOW}}\right]} \tag{2.11}$$

where Z_{MO} and the different masses have been defined in sections 2.1.3 and 2.1.4.

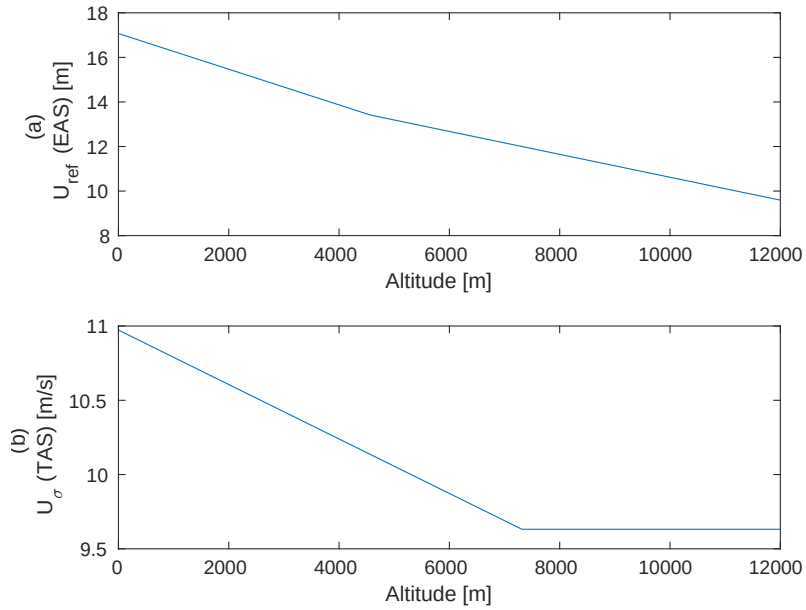

Figure 2.8: Evolution of the reference velocities for gust and turbulence with altitude

The velocities described above are used to compute loads for nominal aircraft speeds, up to VMO. At VD, gust and turbulence velocities used to compute maximum loads are divided by two using the previous definitions.

2.3 Aeroelastic modeling

The following sections describe how the equations of motion of the aircraft are derived and simplified. The objective is to obtain models adapted to active control design, in particular for the GLA described in chapter 4 and the AFS in chapter 5. The former is an active solution to flutter, a purely aeroelastic phenomenon. The latter aims at reducing the structural loads due to the wind, and are then, by essence, of aeroelastic nature. Furthermore, in case of a flexible aircraft, the characteristic frequencies associated to these two mechanisms tend to be lower than for "rigid aircraft". This implies a higher interaction with flight dynamics. The aeroelastic modeling used in this work aims at defining equations of motions of the aircraft that take into account the interaction between the structure and aerodynamics with a high accuracy. At the same time, the aeroelastic modeling should be adapted to control design, for which linear models are often preferred because of the availability of analysis and synthesis tools based on them. Furthermore, the aeroelastic models should be as simple as possible, with the smallest possible state dimension, in order to allow computationally demanding control design techniques such as μ and multi-model syntheses (see chapters 4 and 5).

2.3.1 Context of the aeroelastic modeling

The aeroelastic modeling of aircraft dates back to the middle of the twentieth century, where the equations of flight dynamics started including corrections due to quasi-steady interaction between the rigid motion and aerodynamics (see [Bisplinghoff, Ashley, and Halfman 1955b] and [Etkin 1959]). With the development of computer capabilities, more advanced techniques based on Computational Fluid Dynamics (CFD) methods allowed the modeling of the aerodynamics with better accuracy, taking into account the full aircraft geometry and using nonlinear, unsteady theory that can capture transonic effects. However, performing such accurate aeroelastic simulations is a computationally expensive task. Many applications, including dynamical loads computations, flight dynamics simulations, controller synthesis and stability analysis, require a reduced aeroelastic model that takes less time to evaluate. A popular approach consists in generating time-domain data of the Generalized Aerodynamic Forces (GAF) obtained by CFD computations and derive a nonlinear model that can be coupled with structural dynamics to obtain a reduced aeroelastic model [Lucia, Beran, and Silva 2004]. Several techniques exist, including Volterra theory [Stalford et al. 1987; Jenkins 1989], Proper Orthogonal Decomposition (POD) [Hall, Thomas, and Dowell 2000; Romanowski and Dowell 1995; Kim 1998], Harmonic Balance (HB) method [Thomas, Dowell, and Hall 2002] or more recently neural-network-based models [Huang, Hu, and Zhao 2014]. Specific techniques must be developed to reduce the number of high-fidelity CFD computations that must be performed to generate the time data [Lee-Rausch and Batina 1996; Hall, Thomas, and Dowell 2000]. Using nonlinear models and accurate aerodynamic computations such as CFD is well suited for simulation and analysis. When considering flight dynamics of flexible aircraft, Lagrange equations are generally used and can be simplified by an accurate choice of reference axis. The literature [Waszak and Schmidt 1988; Schmidt and Raney 2001; Reschke 2005] has also often made use of mean axes, with respect to which the linear and angular momenta associated with structural vibrations are zero. The work in [Guimarães Neto et al. 2016] proposed instead a formulation with an arbitrary choice of body axes.

In their original formulation, the methods cited above lead to nonlinear models that can be used for simulations of a large class of aircraft including very flexible aircraft with large aeroelastic deflections [Patil and Hodges 2006; Su and Cesnik 2010]. For controller design, a linear model is often preferred because of the availability of synthesis and analysis tools based on frequency analysis. Gust Load Alleviation (GLA) [Fournier et al. 2022b; Fournier et al. 2022a] and active flutter suppression [Livne 2018] are typical active research topics which are often based on linear models. If a trim equilibrium of the aircraft has been computed using nonlinear techniques, one can make the hypothesis of small displacements and deflections around this point such as done in [Ustinov, Sidoruck, and Goman 2005; Luspay et al. 2019], allowing to define linear structural dynamics of the incremental displacements. By further assuming that the aerodynamics are linear (assuming for instance low angle-of-attack and control surfaces deflections), GAF which are proportional to the modal displacements can be computed using CFD, or faster (but less accurate) techniques such as Doublet Lattice Method (DLM) [Albano and Rodden 1969; Kalman, Rodden, and Giesling 1971], which works in frequency domain, or its time-domain counterpart Unsteady

Lattice Vortex Method (UVLM) [Konstadinopoulos et al. 1985] used for instance in [Hesse and Palacios 2014; Hesse and Palacios 2016]. Both the DLM and UVLM are based on unsteady potential theory that leads to GAF proportional to the modal displacements, hence can easily be coupled with a structural model obtained by built-in Finite Element Method (FEM) for example. Using DLM leads to GAF computed at different frequency values, based on which LTI models can be identified as studied in Chapter 5.

2.3.2 Methodology of aeroelastic modeling

The methodology adopted in this work is to start by defining nonlinear equations of motion of a flexible aircraft, taking into account the aeroelastic interaction and inertial coupling terms. These nonlinear equations are not directly used, and for this reason only the main outline of their derivation is shown in section 2.3.3. These equations allow the definition of a nonlinear equilibrium of the aircraft, and a linearization around it is performed. The linearized equations are reduced by performing a modal analysis and deriving a set of generalized coordinates in section 2.3.4. Section 2.3.5 then defines an aerodynamic model based on linear subsonic unsteady theory, and section 2.3.6 describes how it can be coupled with the structural model to obtain the full aeroelastic dynamics. Section 2.3.7 defines the loads and other outputs of interest based on this aeroelastic model, leading to transfer functions studied in sections 2.3.9, 2.3.10 and 2.3.11, and introducing some metrics used for GLA. Finally, section 2.3.8 studies the stability of the aeroelastic system, introducing the flutter phenomenon and the AFS challenges.

At the end of this chapter, an important question remains open: how to approximate the aeroelastic equations using LTI models? Indeed, the linearity mentioned earlier is related to the input/output relationship: the superposition property applies, allowing the expression of an output as the sum of contributions to different inputs. However, due to the fact that the frequency dependence of the aerodynamic forces is not formalized as a rational function, no representation in the time domain is available. The next chapter 3 is dedicated to this question, by looking at state-space models approximations of the aeroelastic equations.

2.3.3 Equations of motion and trim equilibrium

This section explains the general outline of a method based on Lagrange equations and Finite-Element Method (FEM), inspired from [Waszak and Schmidt 1988], [Guimarães Neto et al. 2016] and [Reschke 2005]. It leads to nonlinear equations of motion of the aircraft, taking into account the inertia couplings, and of course, the influence of the structure flexibility. The main objective of this work is to create models for active control design. For this reason, the nonlinear equations will mostly be used to define an equilibrium, and assuming the increments with respect to it are small, linearized dynamics will be deduced.

The general form of Lagrange's equation can be written as

$$\frac{d}{dt}\left(\frac{\partial \mathcal{L}}{\partial \dot{q}_i}\right) - \frac{\partial \mathcal{L}}{\partial q_i} + \frac{\partial \mathcal{F}}{\partial \dot{q}_i} = Q_i \qquad i = 1 \dots N_p \tag{2.12}$$

where $\mathcal{L} = E_{kin} - E_{pot}$ is the Lagrangian, defined as the difference between the kinetic and potential energies, the q_i are the generalized displacements, the Q_i are the generalized non-conservative forces and N_p is the number of degrees of freedom. $\mathcal{F}$ represents Rayleigh's dissipation function. Typically, the elastic forces will be included in the Lagrangian through the potential energy, while the aerodynamic forces are included in the Q_i and the structural damping in $\mathcal{F}$.

After the definition of body axes attached to the aircraft, the generalized displacements are composed of the translation and attitude coordinates of elements in the body frame, and the so-called generalized elastic coordinates $\boldsymbol{\eta}$. The positions of the body axes are expressed in the inertial frame and noted $\boldsymbol{R_0}$. The attitude is defined by Euler angles with the following convention: the rotation matrix $\boldsymbol{T_b}$ from the inertial frame to the body frame is composed of three rotations around the z-axis, y-axis and x-axis in this order. The respective rotation angles defining the attitude are called bank, elevation and heading angles respectively and noted ϕ, θ and ψ. The rotation matrix from the inertial to the body frame then has the following expression:

$$\boldsymbol{T_b} = \begin{bmatrix} 1 & 0 & 0 \\ 0 & \cos\phi & \sin\phi \\ 0 & -\sin\phi & \cos\phi \end{bmatrix} \begin{bmatrix} \cos\theta & 0 & -\sin\theta \\ 0 & 1 & 0 \\ \sin\theta & 0 & \cos\theta \end{bmatrix} \begin{bmatrix} \cos\psi & \sin\psi & 0 \\ -\sin\psi & \cos\psi & 0 \\ 0 & 0 & 1 \end{bmatrix} \tag{2.13}$$

The translational and rotational velocities of the body frame are expressed in the body coordinates and noted $\boldsymbol{V_b}$ and $\boldsymbol{\Omega_b}$ respectively. The derivatives of the position and attitude are then related to the body velocities by the kinematic equations:

$$\begin{cases} \dot{\boldsymbol{\Theta}} = \boldsymbol{D}^{-1}\boldsymbol{\Omega_b} \\ \dot{\boldsymbol{R}}_{\boldsymbol{0}} = \boldsymbol{T_b}^{-1}\boldsymbol{V_b} \end{cases} \tag{2.14}$$

with

$$\boldsymbol{\Theta} = \begin{bmatrix} \phi & \theta & \psi \end{bmatrix}^T \tag{2.15}$$

and

$$\boldsymbol{D} = \begin{bmatrix} 1 & 0 & -\sin\theta \\ 0 & \cos\phi & \cos\theta\sin\phi \\ 0 & -\sin\phi & \cos\theta\cos\phi \end{bmatrix} \tag{2.16}$$

Using these definitions and conventions, the translational, rotational and elastic equations of

motion are expressed as [Reschke 2005]:

$$\begin{aligned}
&\frac{\partial}{\partial t}\left(\frac{\partial \mathcal{L}}{\partial \boldsymbol{V_b}}\right) + \boldsymbol{\Omega_b} \times \left(\frac{\partial \mathcal{L}}{\partial \boldsymbol{V_b}}\right) - \boldsymbol{T_b}\frac{\partial \mathcal{L}}{\partial \boldsymbol{R_0}} = \boldsymbol{T_b Q_t} \\
&\frac{\partial}{\partial t}\left(\frac{\partial \mathcal{L}}{\partial \boldsymbol{\Omega_b}}\right) + \boldsymbol{V_b} \times \left(\frac{\partial \mathcal{L}}{\partial \boldsymbol{V_b}}\right) + \boldsymbol{\Omega_b} \times \left(\frac{\partial \mathcal{L}}{\partial \boldsymbol{\Omega_b}}\right) - \left(\boldsymbol{D}^T\right)^{-1}\frac{\partial \mathcal{L}}{\partial \boldsymbol{\Theta}} = \left(\boldsymbol{D}^T\right)^{-1}\boldsymbol{Q_r} \\
&\frac{\partial}{\partial t}\left(\frac{\partial \mathcal{L}}{\partial \mathring{\boldsymbol{\eta}}}\right) - \frac{\partial \mathcal{L}}{\partial \boldsymbol{\eta}} = \boldsymbol{Q_h}
\end{aligned} \tag{2.17}$$

where $\mathring{}$ is the time derivative of a vector in fixed body frame and $\times$ is the cross product. The generalized forces $\boldsymbol{Q_t}$, $\boldsymbol{Q_r}$ and $\boldsymbol{Q_h}$ are computed from the derivatives of the virtual work δW_{nc} due to non-conservatives forces:

$$\begin{cases}
\boldsymbol{Q_t} = \frac{\partial(\delta Wnc)}{\partial \boldsymbol{R_0}} \\
\boldsymbol{Q_r} = \frac{\partial(\delta Wnc)}{\partial \boldsymbol{\Theta}} \\
\boldsymbol{Q_h} = \frac{\partial(\delta Wnc)}{\partial \boldsymbol{\eta}}
\end{cases} \tag{2.18}$$

The index "h" is used to indicate matrices associated to these modal coordinates. At this point, the Lagrangian can be decomposed into the different energy components, that include the translational and rotational kinetic energies and the gravity (assumed constant over the airframe). Moreover, we use the important fact that any reference coordinate system that is used to define free vibration mode shapes is a mean axis, meaning that the relative linear and angular momenta due to elastic deformation are zero at every instant [Waszak and Schmidt 1988]. Finally, in order to characterize the elastic displacements $\boldsymbol{\eta}$, each independent structural element of the airframe is considered as a lumped mass m_i with inertia tensor $\boldsymbol{J_i}$. The displacement of a lumped mass is defined by an elastic deformation $\boldsymbol{d_i}$ and a rotation $\boldsymbol{\phi_i}$ in the local reference frame (see [Reschke 2005] for the detailed definition) which are related to the elastic coordinates $\boldsymbol{\eta}$ by a modal transformation. An important assumption is made about the local elastic deformations, which are assumed small with respect to the reference shape. This is typical of the Finite-Element approach, in which the aircraft structure is decomposed into many structural elements. Assuming the elastic displacements are small then does not prevent large deformations of the wing for instance, since the assumption is only local. After a few steps not included in this work for conciseness, the following equations of motion are obtained assuming constant inertia, in which the moments are expressed with respect to the center of gravity:

$$\begin{aligned}
&m\left[\mathring{\boldsymbol{V}}_{\boldsymbol{b}} + \boldsymbol{\Omega_b} \times \boldsymbol{V_b} - \boldsymbol{T_b g}\right] = \boldsymbol{F_{ext}} \\
&\boldsymbol{J\Omega_b} + \boldsymbol{\Omega_b} \times (\boldsymbol{J\Omega_b}) + \mathring{\boldsymbol{p}} + \boldsymbol{\Omega_b} \times \boldsymbol{L} = \boldsymbol{M_{ext}} \\
&\boldsymbol{M_{hh}}\ddot{\boldsymbol{\eta}} + \boldsymbol{B_{hh}}\mathring{\boldsymbol{\eta}} + \boldsymbol{K_{hh}\eta} + \boldsymbol{F_{acc}}(\boldsymbol{\Omega_b}, \boldsymbol{\eta}) + \boldsymbol{F_{coriolis}}(\boldsymbol{\Omega_b}, \mathring{\boldsymbol{\eta}}) + \boldsymbol{F_{centri}}(\boldsymbol{\Omega_b}, \boldsymbol{\eta}) = \boldsymbol{Q_h}
\end{aligned} \tag{2.19}$$

where $\boldsymbol{L}$ is an angular momentum associated to the elastic deformation of the N_p lumped masses:

$$\boldsymbol{L} = \sum_{i=1}^{N_p} m_i \left(\boldsymbol{d_i} \times \mathring{\boldsymbol{d}}_{\boldsymbol{i}}\right) + \sum_{i=1}^{N_p} \boldsymbol{J}_i \mathring{\boldsymbol{\phi}}_{\boldsymbol{i}} \tag{2.20}$$

The first equation of (2.19) represents the translational motion of the aircraft, with no interference of the elastic displacements. m and $\boldsymbol{J}$ are the total mass and inertia of the aircraft and $\boldsymbol{g}$ is the gravity vector in the inertial frame. The second one differs from the rigid-body rotational dynamics (Euler equations) by the terms containing $\boldsymbol{L}$ and its time derivative, indicating the influence of the elastic deformations. Finally, the elastic equation (third) contains a part that depends linearly on the elastic deformation and their derivatives through the generalized inertia, damping and elastic matrices $\boldsymbol{M_{hh}}$, $\boldsymbol{B_{hh}}$ and $\boldsymbol{K_{hh}}$. Additional terms include a part due to the rotational acceleration of the body frame, a Coriolis term and a centrifugal loading term, with different couplings with the body frame rotation. The external forces and moments contained in $\boldsymbol{F_{ext}}$, $\boldsymbol{M_{ext}}$ and $\boldsymbol{Q_h}$ are due to the aerodynamic forces acting on the aircraft, studied in section 2.3.5, and the thrust.

In this form, these equations can be used to study the flight dynamics of a flexible aircraft, for instance, but they are difficult to use for controller design because of the different non-linear terms. We assume the existence of an equilibrium of the equations of motion (2.19), called trim point. This equilibrium involves several parameters which are chosen in such a way that all velocities and accelerations equal zero. Note that an equilibrium with nonzero vertical and lateral velocities (such as an aircraft in climb phase, or in a steady maneuver) is theoretically possible but not considered in this work. It then corresponds to a cruise point, in which, broadly speaking, the aerodynamic drag is counteracted by the thrust, the gravity is equal to the lift by setting the aircraft velocity and angle of attack, the position of the HTP balances the aerodynamic moment, and the wing is statically deformed. Note that the HTP deflection can be controlled with slow-dynamics actuators, and it intervenes in the equations (2.19) in the inertia matrix and the aerodynamic external forces and moments. The true trim point computation involves accurate static aerodynamics simulations based on CFD, and falls outside the scope of this work.

By assuming the aircraft close to a trim point, we can use a perturbation approach in which the displacements slightly differ from their equilibrium value and the dynamics of the increments become linear. Note that the local elastic displacements had already been assumed small with respect to the reference shape. By defining $\tilde{\boldsymbol{V}}_{\boldsymbol{b}}$ (and $\tilde{\boldsymbol{\Omega}}_{\boldsymbol{b}}$) as the difference between the velocity (and angular velocity) and the equilibrium value, and performing a first-order approximation, we obtain the linearized equations of motion:

$$\begin{aligned} &m\dot{\tilde{\boldsymbol{V}}}_{\boldsymbol{b}} = \tilde{\boldsymbol{F}}_{\boldsymbol{ext}} \\ &\boldsymbol{J}\dot{\tilde{\boldsymbol{\Omega}}}_{\boldsymbol{b}} + \sum_{i=1}^{N_p} \boldsymbol{J}_{\boldsymbol{i}}\ddot{\tilde{\boldsymbol{\phi}}}_{\boldsymbol{i}} = \tilde{\boldsymbol{M}}_{\boldsymbol{ext}} \\ &\boldsymbol{M_{hh}}\ddot{\boldsymbol{\eta}} + \boldsymbol{B_{hh}}\dot{\boldsymbol{\eta}} + \boldsymbol{K_{hh}}\boldsymbol{\eta} + \boldsymbol{M_{pb}}\dot{\tilde{\boldsymbol{\Omega}}}_{\boldsymbol{b}} = \boldsymbol{Q_h} \end{aligned} \tag{2.21}$$

The $\boldsymbol{M_{pb}}$ term was initially included in the $\boldsymbol{F_{acc}}$ of Eq. (2.19). It can be seen that the rotational and elastic equation remained coupled in linear form. The $\tilde{\boldsymbol{F}}_{\boldsymbol{ext}}$ and $\tilde{\boldsymbol{M}}_{\boldsymbol{ext}}$ are the forces and moments increments with respect to the equilibrium point. They are due to aerodynamic action only, since no thrust increments are considered. The attitude kinematics are also linearized and

simply relate the angular velocity increments to the derivative of the Euler angles increments as:

$$\dot{\tilde{\Theta}} = \tilde{\Omega}_b \tag{2.22}$$

2.3.4 Inertial and Structural models. Modal Analysis

This section explains how the linearized equations of motion (2.21) are practically obtained to provide a reduced model which can be used for control design and modal analysis. A FEM approach is adopted, using Airbus's Gusto software. It is based on models implemented in Nastran and it uses codes similar to Nastran's "Solution 146" [MSC.Software Corporation 2004], which is dedicated to aeroelastic analysis.

On Fig. 2.1, 2.2 and 2.3, different views of the FEM model of the XRF1-HARW can be seen. It contains structural and inertial elements. The different points which constitute the model are linked by structural elements (such as bars, beams, surfaces, etc) defined by their geometrical properties and materials. The inertial model is composed of several lumped masses that concentrate the mass of the aircraft in a reduced number of points. This inertial model does not coincides, in general, to the structural model. In addition to the FEM model, a reduced set of physical points called g-set is defined by the user. A 3D representation of the set location used in this work is shown on Fig. 2.9. The g-set is considered as the set of physical points of interest, it will be used to compute the different aeroelastic outputs such as the loads and sensors' measurements. From the structural and inertial model, the FEM software is able to define stiffness and inertial matrices $\boldsymbol{K_{gg}}$ and $\boldsymbol{M_{gg}}$. The structural damping information is in general not readily

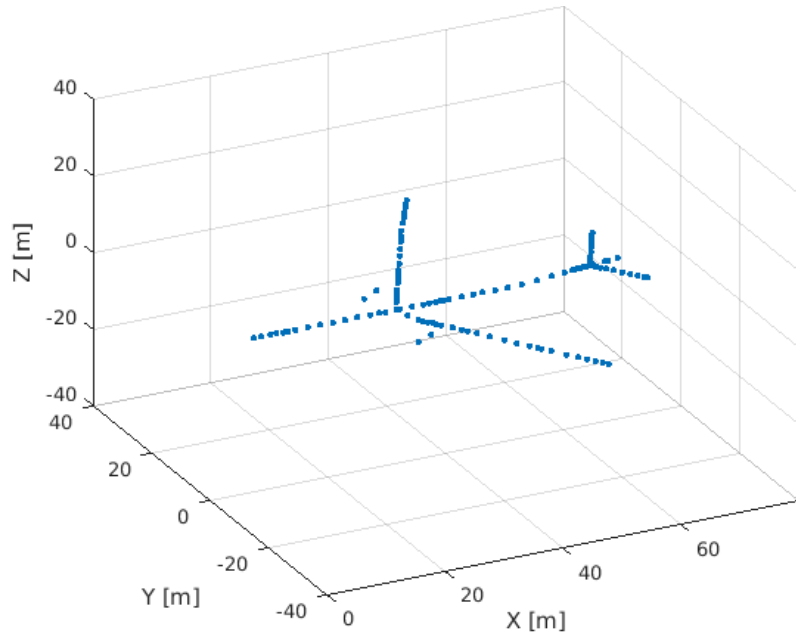

Figure 2.9: Points constituting the g-set

available and the damping matrix $\boldsymbol{B_{gg}}$ cannot be obtained by the FEM model directly. Each point in the g-set has six degrees of freedom. The (linear) equations of motions of the physical g-set is then expressed as:

$$\boldsymbol{M_{gg}}\ddot{\boldsymbol{u}}_{\boldsymbol{g}}(t) + \boldsymbol{B_{gg}}\dot{\boldsymbol{u}}_{\boldsymbol{g}}(t) + \boldsymbol{K_{gg}}\boldsymbol{u_g}(t) = \boldsymbol{q_g}(t) \tag{2.23}$$

where $\boldsymbol{u_g}$ contains the physical translations and rotations of the g-set points, and $\boldsymbol{q_g}$ contains the aerodynamic forces and moments applied on them.

A modal analysis is performed on the matrices $\boldsymbol{K_{gg}}$ and $\boldsymbol{M_{gg}}$ assuming a harmonic excitation aerodynamic force: $\boldsymbol{q_g}(t) = \boldsymbol{Q_g}e^{j\omega t}$. Because of the linearity of Eq. (2.23), the physical displacements have harmonic responses $\boldsymbol{u_g}(t) = \boldsymbol{U_g}(\omega)e^{j\omega t+\phi_g(\omega)}$ with same angular frequency ω. The equation of motion of the physical set becomes, in the frequency domain:

$$\left[-\omega^2\boldsymbol{M_{gg}} + j\omega\boldsymbol{B_{gg}} + \boldsymbol{K_{gg}}\right]\boldsymbol{U_g}(\omega) = \boldsymbol{Q_g}(\omega) \tag{2.24}$$

Normal modes are defined as displacement patterns of free-free structures in absence of damping, and can they be obtained as:

$$\left[-\omega^2\boldsymbol{M_{gg}} + \boldsymbol{K_{gg}}\right]\boldsymbol{U_g} = \boldsymbol{0} \tag{2.25}$$

which is an eigenvalue problem leading to the modal frequencies (eigenvalues) $[\omega_i]_{i=1\ldots N_h}$ and the modal matrix $\boldsymbol{\Phi_{gh}}$ containing the modal shapes (eigenvectors). As $\boldsymbol{M_{gg}}$ and $\boldsymbol{K_{gg}}$ are symmetric, an orthonormal set of eigenvectors can be found. New matrices $\boldsymbol{M_{hh}}$ and $\boldsymbol{K_{hh}}$ are then obtained by transformation using the modal matrices $\boldsymbol{\Phi_{gh}}$ as follows:

$$\boldsymbol{M_{hh}} = \boldsymbol{\Phi_{gh}}^T\boldsymbol{M_{gg}}\boldsymbol{\Phi_{gh}} = \boldsymbol{I}_{N_h} \tag{2.26}$$

where $\boldsymbol{I}_{N_h}$ is the identity matrix of size N_h and

$$\boldsymbol{K_{hh}} = \boldsymbol{\Phi_{gh}}^T\boldsymbol{K_{gg}}\boldsymbol{\Phi_{gh}} = \begin{bmatrix} \omega_1^2 & & \\ & \ddots & \\ & & \omega_{N_h}^2 \end{bmatrix} \tag{2.27}$$

A reduced number of modes N_h can be kept in the analysis, reducing the size of the aeroelastic model. Typically, a frequency threshold is defined based on the problem to investigate, above which the modes are dropped, as the response associated to them becomes very small and does not affect the dynamics of interest. In this work, frequencies above 10 Hz do not create loads or interact with the flight dynamics, and are generally stable. In Fig. 2.10 the shapes of two modes are displayed with an arbitrary exciting force amplitude. They correspond to the first bending (symmetric) and torsion (antisymmetric) modes. Note that these structural modes will be modified by the interaction with aerodynamics as explained in section 2.3.6. By assuming that $\boldsymbol{U_g}(\omega) \approx \boldsymbol{\Phi_{gh}}\boldsymbol{U_h}(\omega)$, this analysis allows the definition of new coordinates called generalized (modal) coordinates [MSC.Software Corporation 2004]. The modal matrix $\boldsymbol{\Phi_{gh}}$ can then be seen as a coordinate transformation matrix, and the equations of motions can be written in the reduced

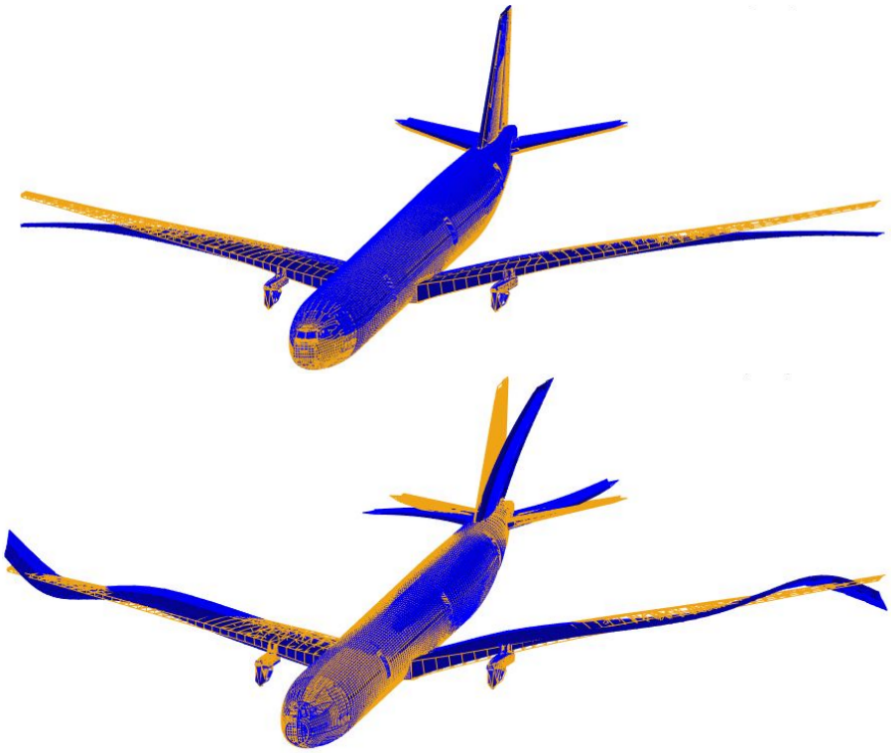

Figure 2.10: First bending (up) and torsion (down) modes shapes of the XRF1-HARW

modal form:

$$\left[-\omega^2 \boldsymbol{M_{hh}} + j\omega \boldsymbol{B_{hh}} + \boldsymbol{K_{hh}}\right] \boldsymbol{U_h}(\omega) = \boldsymbol{Q_h}(\omega) \tag{2.28}$$

It is common to assume that the structural damping matrix $\boldsymbol{B_{hh}}$ in modal coordinates is proportional to the mode frequency, and assumes the following form:

$$\boldsymbol{B_{hh}} = 2\boldsymbol{M_{hh}} \begin{bmatrix} \xi_1\omega_1 & & \\ & \ddots & \\ & & \xi_{N_h}\omega_{N_h} \end{bmatrix} \tag{2.29}$$

where the ξ_i are the damping ratios. In this work, a constant damping ratio is assumed, equal to 0.05 if not stated otherwise. In time domain, the generalized coordinate u_h hence defined includes both rigid-body and elastic modal displacements. Indeed, the aircraft FEM model is free of constraints and then contains intrinsically the six degrees of freedom associated to modal frequencies of zero. The generalized displacement u_h then encompasses both the elastic generalized coordinates $\boldsymbol{\eta}$ and the body displacements defined in the previous section 2.3.3, although the latter are here expressed in a modal frame instead of a body frame.

2.3.5 Unsteady Aerodynamics

This section presents the aerodynamic model used in this work for the computation of the external forces $\boldsymbol{Q_g}$ and $\boldsymbol{Q_h}$ discussed in the previous sections. The full dynamics including the aerodynamic and structural parts will be introduced in the next section 2.3.6.

Different techniques exist for simulating and computing the aerodynamic forces. The unsteady Computational Fluid Dynamics (CFD) is an accurate method that allows the modeling of the nonlinear unsteady aerodynamics around the aircraft thanks to a finite-volume model. It is not fit for the loads computation because of its lack of flexibility and it cannot be introduced into the equations of motion (2.28). In this work, the trim equilibrium is assumed to be known, and only the aerodynamics increments must be computed. These increments are due solely to the wind velocity and the local surface displacements, as the statical contribution is included in the trim computation. Assuming small air downwash (the local deflection of air), which presupposes low wind velocity and surface displacement, it is reasonable to model the aerodynamic forces with a linear dependence on them. Furthermore, the computation of the loads due to the wind is a fundamentally unsteady problem because of the interaction of wind velocities with transient profiles, as explained in section 2.2, with the aircraft dynamics containing several structural modes which can create loads and interact with the flight dynamics. For this reason, methods relying on unsteady aerodynamic theories are required. The Unsteady Vortex Lattice Method (UVLM) [Konstadinopoulos et al. 1985] and Doublet Lattice Method (DLM) [Albano and Rodden 1969] are such techniques, the former being based on a time-dependent description of the forces and the latter is frequency-based. The DLM has the advantage of leading to compact definitions of the aerodynamic forces, and is used for this reason. It is implemented on Nastran's aeroelastic tool and it will be briefly described below.

The DLM method is based on a discretization of the wing and its trail, in so-called aerodynamic panels aligned with the free-stream velocity. Note that this discretization is different from the one used in the FEM model. The base of the DLM method is the expression of the air downwash on the n-th panel as

$$\boldsymbol{w}(x,s) = \frac{1}{8\pi} \sum_{n=1}^{N_{panels}} \iint_{S_n} \boldsymbol{K}(x,\xi;s,\sigma) p(\xi,\sigma) d\xi d\sigma \tag{2.30}$$

where $\boldsymbol{w}(x,s)$ and $p(\xi,\sigma)$ are the downwash and pressure at different spatial coordinates x, s, ξ, σ of aerodynamic panels of surface S_n and N_{panels} is the number of panels. The kernel $\boldsymbol{K}$ describes the link between the pressure applied on a lifting element of the wing to the air deflection anywhere else. Mainly two types of functions are used for the kernel definition: the parabolic dependence was the first used by [Albano and Rodden 1969] with a refinement proposed in [Rodden, Taylor, and Kalman 1972] and a quartic dependence was studied later in [Rodden, Taylor, and McIntosh 1998]. The code used in this work is based on a parabolic kernel described in [Giesing and Kalman 1971].

This computation leads to the so-called Aerodynamic Influence Matrix (AIC) that relates the

downwash $\boldsymbol{w}$ to the pressure vector $\boldsymbol{p}$ containing the pressures on each aerodynamic panel (see [Giesing and Kalman 1971] for the exact discretization):

$$\boldsymbol{w} = \boldsymbol{A}(M, \kappa)\frac{\boldsymbol{p}}{\bar{q}} \tag{2.31}$$

The AIC $\boldsymbol{A}$ is a function of the Mach number and of the reduced frequency $\kappa = \frac{\omega b}{\text{TAS}}$ in which ω is the frequency and b is a reference length. The Mach number and the reduced frequency are important parameters characterizing the airflow. The former has an influence on the compressibility of the fluid. The latter, also called Strouhal number in the fluid mechanics domain, describes the dynamics of the oscillations in a fluid. It is hereby related to the frequency ω that would be imposed by a harmonic wind or surface control input. The dynamic pressure defined in section 2.1.3.

Additionally, the downwash can be related to the structural displacement $\boldsymbol{u_l}$ by the so-called substantial differentiation, which describes the rate of change of a quantity experienced when moving along with the flow:

$$\boldsymbol{w} = [\boldsymbol{D_1} + j\kappa\boldsymbol{D_2}]\,\boldsymbol{u_a} + \frac{\boldsymbol{v^{loc}}}{\text{TAS}} + \boldsymbol{w^{static}} \tag{2.32}$$

where $\boldsymbol{D_1}$ and $\boldsymbol{D_2}$ are the real and imaginary parts of the substantial differentiation matrix. $\boldsymbol{u_a}$ represents the structural displacements of the aerodynamic grid, that does not coincide with the g-set. $\boldsymbol{v^{loc}}$ is the local wind velocity vector and $\boldsymbol{w^{static}}$ is the static part of the downwash, which is not considered in this analysis, as it is included in the trim equilibrium. To understand where this expression comes from, the vertical downwash can be seen as the local angle-of-attack of the airflow on the surface, assuming the TAS is higher than the structural displacement velocity and wind velocity:

$$\alpha = \theta - \frac{\dot{u}_z}{\text{TAS}} + \frac{v_z^{loc}}{\text{TAS}} + \alpha^{static} \tag{2.33}$$

where u_z is local structural vertical displacement, v_z^{loc} is the local vertical wind velocity and α^{static} is the static angle-of-attack. The DLM is performed in the frequency domain, and the time derivative $\frac{b}{\text{TAS}}\frac{d}{dt}$ is replaced by its frequency counterpart $j\kappa = j\frac{\omega b}{\text{TAS}}$. Finally, the aerodynamic forces applied on a grid points are computed by integration of the pressure along the surface:

$$\boldsymbol{Q_a} = \boldsymbol{S}\boldsymbol{p} \tag{2.34}$$

where $\boldsymbol{S}$ is an integration matrix containing the surfaces of panels elements. The aerodynamic force increments (with respect to the equilibrium value) $\tilde{\boldsymbol{Q}}_{\boldsymbol{a}}$ can then be related to the displacements as follows:

$$\tilde{\boldsymbol{Q}}_{\boldsymbol{a}} = \bar{q}\boldsymbol{S}\boldsymbol{A}^{-1}(M, \kappa)\,[\boldsymbol{D_1} + j\kappa\boldsymbol{D_2}]\,\boldsymbol{u_a} + \bar{q}\boldsymbol{S}\boldsymbol{A}^{-1}(M, \kappa)\frac{\boldsymbol{v^{loc}}}{\text{TAS}} \tag{2.35}$$

Note that the control surfaces (CS) are here included in the structural displacements. Practically, the DLM computation is performed at fixed values of the reduced velocity to define the unsteady aerodynamics behavior on the frequency range of interest.

2.3.6 Full Aeroelastic model

The aerodynamic forces defined in the previous section can be included in the equations of motion in generalized modal coordinates (2.28). The first step is to express them in the physical coordinates (g-set). The aerodynamic forces are computed on a set based on the aerodynamic panels, aligned with the airflow, and an interpolation is required to express them in the g-set used for structural and inertial models. This is performed using the so-called splining interpolation theory. Details of its practical implementation in Nastran can be found in [MSC.Software Corporation 2004], and elements of the theory in [Harder and Desmarais 1972; P, McGrew, and Kalman 1972]. The interpolation relates deflections of the structural grid points to the deflections of the aerodynamic grid points. 1D and 2D functions are then defined to interpolate the deflections, using linear and surface splines respectively. Elastic elements are sometimes added to the model to smooth the splines when many points are located closely.

This allows the definition of aerodynamic forces increments in the g-set, which are proportional to the grid displacements and to the wind velocity, as explained in the previous section 2.3.5. Furthermore, we split $\boldsymbol{u_g}$ into the free and constrained structural displacements:

$$\boldsymbol{u_g} = \begin{Bmatrix} \boldsymbol{x_g} \\ \boldsymbol{\delta} \end{Bmatrix} \tag{2.36}$$

where the free displacements $\boldsymbol{\delta}$ include only the control surface deflection angles, which can be used in real-time for active control, and the constrained displacements $\boldsymbol{x_g}$ containing all the elastic displacements. Note that the control surfaces are assumed massless and rotate without damping. The dynamics of the control surface are entirely defined in the transfer function H_{act} defined in Eq. (2.5). Furthermore, the wind contribution in Eq. (2.35) is local, and assumptions must be made in order to obtain a single wind input. It is assumed that the horizontal wind scale is much higher than the aircraft dimensions, in accordance with the Von Kármán model for turbulence, which assumes a 2500 ft scale. Furthermore, the wind velocity is assumed to be constant at a given point of space, or to be more specific, that its time variation is much slower than the aircraft velocity. Based on these two assumptions, the wind velocity on each point of the aircraft can be written as the wind velocity at its nose, delayed by a time $\Delta t = \frac{-d_x}{\mathrm{TAS}}$ where d_x is the position of the local element on the X-axis. After performing the splining between the aerodynamic set and g-set, and making the assumptions on the wind velocity, the aerodynamic forces increments can be expressed in the g-set and split into its different contributions as follows:

$$\boldsymbol{Q_g} = \boldsymbol{N}\tilde{\boldsymbol{Q}}_{\boldsymbol{a}} = \bar{q}\boldsymbol{Q_{gg}}(M,\kappa)\boldsymbol{x_g}(t) + \bar{q}\boldsymbol{Q_{g\delta}}(M,\kappa)\boldsymbol{\delta}(t) + \bar{q}\boldsymbol{Q_{gv}}(M,\kappa)\frac{\boldsymbol{v}(t)}{\mathrm{TAS}} \tag{2.37}$$

where $\boldsymbol{N}$ is the splining matrix, $\boldsymbol{Q_{gg}}$, $\boldsymbol{Q_{g\delta}}$ and $\boldsymbol{Q_{gv}}$ are respectively the aerodynamic forces increments due to elastic displacements of the g-set, the CS deflection and the wind, and $\boldsymbol{v}(t)$ is the wind velocity at the aircraft nose. Note that the delay factor of the wind velocity is included in

the function $\boldsymbol{Q_{gv}}$. The full aeroelastic equation (2.23) can then be written including this element:

$$\boldsymbol{M_{gg}}\ddot{\boldsymbol{x}}_{\boldsymbol{g}}(t) + \boldsymbol{B_{gg}}\dot{\boldsymbol{x}}_{\boldsymbol{g}}(t) + \boldsymbol{K_{gg}}\boldsymbol{x_g}(t) = \bar{q}\boldsymbol{Q_{gg}}(M,\kappa)\boldsymbol{x_g}(t) + \bar{q}\boldsymbol{Q_{g\delta}}(M,\kappa)\boldsymbol{\delta}(t) + \bar{q}\boldsymbol{Q_{gv}}(M,\kappa)\frac{\boldsymbol{v}(t)}{\mathrm{TAS}} \quad (2.38)$$

In the frequency domain, this becomes:

$$\left[-\omega^2\boldsymbol{M_{gg}} + j\omega\boldsymbol{B_{gg}} + \boldsymbol{K_{gg}} - \bar{q}\boldsymbol{Q_{gg}}(M,\kappa)\right]\boldsymbol{X_g}(j\omega) = \bar{q}\boldsymbol{Q_{g\delta}}(M,\kappa)\boldsymbol{\Delta}(j\omega) + \bar{q}\boldsymbol{Q_{gv}}(M,\kappa)\frac{\boldsymbol{V}(j\omega)}{\mathrm{TAS}} \quad (2.39)$$

Where X, $\boldsymbol{\Delta}$ and $\boldsymbol{V}$ are the elastic displacements, CS deflections and wind velocity in the frequency domain. The interaction between the structural, inertial and aerodynamic models can be fully appreciated in the equation. The $\boldsymbol{Q_{gg}}$ term creates an aeroelastic feedback on the system, modifying its dynamics. Physically, the aerodynamics act on the structure and creates displacements increments, which in turn, affects the airflow. As it will be explained in section 2.3.8, the structural modes are modified by the presence of this feedback, and can potentially become unstable. This instability is called "flutter". We stress again that the aerodynamic forces depend of the Mach number and the reduced frequency. The former will be considered constant, and the analysis will be performed at fixed values of the Mach number. The reduced frequency depends on the TAS, which is considered constant in the analysis, similarly to the Mach number. The reduced frequency also depends on the frequency ω, which is assimilated to the oscillatory frequency induced by a harmonic wind or control surface deflection input. Through this dependence, the aerodynamic force increments have their own dynamics. Note that they are computed at discrete values of κ, hence the equation (2.39) does not assume a rational dependence on the frequency. The chapter 3 will be dedicated to identifying a rational model based on these discrete values.

Following the generalization precess introduced in section 2.3.4, the equations of motion can be written in the generalized modal coordinates in which the inertial and structural matrices are diagonal. In time-domain, the equations are written as

$$\boldsymbol{M_{hh}}\ddot{\boldsymbol{x}}_{\boldsymbol{h}}(t) + \boldsymbol{B_{hh}}\dot{\boldsymbol{x}}_{\boldsymbol{h}}(t) + \boldsymbol{K_{hh}}\boldsymbol{x_h}(t) = \bar{q}\boldsymbol{Q_{hh}}(M,\kappa)\boldsymbol{x_h}(t) + \bar{q}\boldsymbol{Q_{h\delta}}(M,\kappa)\boldsymbol{\delta}(t) + \bar{q}\boldsymbol{Q_{hv}}(M,\kappa)\frac{\boldsymbol{v}(t)}{\mathrm{TAS}} \quad (2.40)$$

and in the frequency domain:

$$\left[-\omega^2\boldsymbol{M_{hh}} + j\omega\boldsymbol{B_{hh}} + \boldsymbol{K_{hh}} - \bar{q}\boldsymbol{Q_{hh}}(M,\kappa)\right]\boldsymbol{X_h}(j\omega) = \bar{q}\boldsymbol{Q_{h\delta}}(M,\kappa)\boldsymbol{\Delta}(j\omega) + \bar{q}\boldsymbol{Q_{hv}}(M,\kappa)\frac{\boldsymbol{V}(j\omega)}{\mathrm{TAS}} \quad (2.41)$$

where $\boldsymbol{Q_{hh}} = \boldsymbol{\Phi_{gh}}^T\boldsymbol{Q_{gg}}\boldsymbol{\Phi_{gh}}$, $\boldsymbol{Q_{h\delta}} = \boldsymbol{\Phi_{gh}}^T\boldsymbol{Q_{g\delta}}$ and $\boldsymbol{Q_{hv}} = \boldsymbol{\Phi_{gh}}^T\boldsymbol{Q_{gv}}$ are the aerodynamic forces increments expressed in the generalized coordinates. In Fig. 2.11 two aerodynamic forces

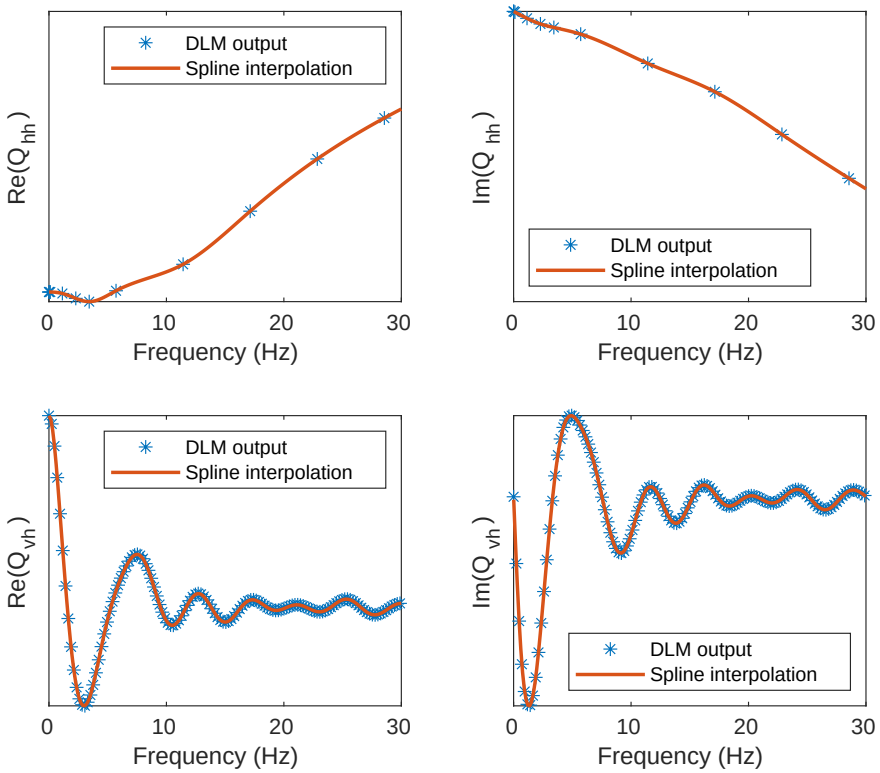

Figure 2.11: Aerodynamic forces computed with DLM at discrete frequency values and interpolation using splines

expressed in the generalized coordinates are shown. The first row corresponds to the a force $\boldsymbol{Q_{hh}}$ describing the aeroelastic feedback from a mode to another, while the second row represents a force $\boldsymbol{Q_{hv}}$ describing the effect of wind onto a mode. It can be seen that the former tend to be more regular than the latter, and the unsteady effects are clearly seen on both by the variation over the frequency. Note that a fixed Mach number and TAS have been set. The DLM is computed at a reduced number of reduced frequencies, which are then interpolated using splines as shown.

Due to the linear assumption, the longitudinal and lateral dynamics are decoupled. The former correspond to the motion of the aircraft symmetrical with respect to the X-Z plane (the only symmetry plane of the aircraft). When all inputs are symmetrical (left and right CS are deflected in a similar way and no wind component in the y direction), only the longitudinal dynamics are excited and the outputs remain symmetrical. On the contrary, the lateral dynamics correspond to anti-symmetrical inputs, with opposite CS deflections on the two wings and only lateral wind. This decoupling is important for GLA, where the main outputs of interest are symmetrical, and the analysis can be restricted to the longitudinal dynamics.

The aeroelastic model depends on the Mach number and on the velocity. One DLM computation must be done for each Mach number, while the velocity can be set directly in the equations without changing the structural and aerodynamics computations. Note that the velocity has an influence through the reduced frequency κ, the wind velocity term and the dynamic pressure $\bar{q}$.

Furthermore, as explained in the section 2.1.4, the aircraft mass configuration can be modified during the flight and depending on the mission. This affects the structural and inertial models, through the matrices $\boldsymbol{M_{hh}}$, $\boldsymbol{B_{hh}}$, $\boldsymbol{K_{hh}}$ and Φ_{gh}. A new FEM computation must be made for each mass case included in the analysis. In the following it will be assumed that the variables implicitly refer to their increment with respect to the trim equilibrium, and the term "increment" will be omitted to avoid cumbersome formulations.

2.3.7 Computation of loads and other outputs of interest

The previous section has presented reduced equations of motion of the system written in the generalized modal coordinates. Working in the modal frame is practical as it allows keeping only a small number of degrees of freedom, representative of the problem that must be analyzed. From given velocity and control surface deflection angles in the frequency domain, the displacements in generalized coordinates can be recovered. The outputs of interest, on the contrary, are physical quantities and must be expressed using the g-set. We define here four types of such interesting quantities: the angular rates around the three body axes, the accelerations in three-directions, the loads, and the angle-of-attack. The computations of these quantities are described below.

Angular rates and translational accelerations

The g-set displacements are expressed as rotations and translations in three directions. From the displacement in generalized coordinates, a multiplication by the modal matrix is performed:

$$\boldsymbol{x_g}(t) = \boldsymbol{\Phi_{gh}}\boldsymbol{x_h}(t) \tag{2.42}$$

Recovering the angular rates and accelerations is then straightforward, by selecting the point of the g-set at which the quantity is computed and taking the time-derivatives as required. In the frequency domain, the derivative is done by multiplying by $j\omega$. The accelerations are generally referred to as load factors, and expressed in "number of $g = 9.81$ m/s^2".

Loads

The loads are a general concept which can cover different definitions. This work investigates the integrated shear force, bending moment and torsional moment which are applied on the aircraft structure, due to aerodynamic forces. They are referred to as external loads because their origin is outside of the aircraft, in opposition to the pressure applied by the fuel in the tanks or the friction that takes place in mechanisms for instance, which are called internal loads. Physically, the aerodynamic pressure leads to deformations of the structure, which in turn creates local loads equal to

$$\boldsymbol{h_g}(t) = \boldsymbol{B_{gg}}\dot{\boldsymbol{x}}_{\boldsymbol{g}}(t) + \boldsymbol{K_{gg}}\boldsymbol{x_g}(t) \tag{2.43}$$

when expressed in time-domain in the g-set coordinates. As explained in section 2.3.4, $\boldsymbol{B_{gg}}$ is in general not known. Using Eq. (2.38), the local loads can be expressed as:

$$\boldsymbol{h_g}(t) = -\boldsymbol{M_{gg}}\ddot{\boldsymbol{x}}_{\boldsymbol{g}}(t) + \bar{q}\boldsymbol{Q_{gg}}(M,\kappa)\boldsymbol{x_g}(t) + \bar{q}\boldsymbol{Q_{g\delta}}(M,\kappa)\boldsymbol{\delta}(t) + \bar{q}\boldsymbol{Q_{gv}}(M,\kappa)\frac{\boldsymbol{v}(t)}{\mathrm{TAS}} \tag{2.44}$$

The shear force, bending moment and torsional moment are obtained by integration of the local loads along the structure. The details of this integration are complex, since they involve many structural elements (beams, bars, membranes, etc) defined in the FEM model, and fall outside the scope of this work. Practically, when considering the discretization into g-set grid, the integrated loads are expressed as a sum of the local loads, which result in the following matrix product:

$$\boldsymbol{y_g^{loads}}(t) = \boldsymbol{T}\boldsymbol{h_g}(t) \tag{2.45}$$

where $\boldsymbol{T}$ is sometimes called the T-matrix. Now the integrated loads at a point of the g-set can be expressed from the displacements in generalized coordinates in the frequency domain:

$$\begin{aligned}\boldsymbol{Y_g^{loads}}(j\omega) = \boldsymbol{T}\Big[\left[\omega^2\left(\boldsymbol{M_{gg}}\boldsymbol{\Phi_{gh}}\right) + \bar{q}\left(\boldsymbol{Q_{gg}}(M,\kappa)\boldsymbol{\Phi_{gh}}\right)\right]\boldsymbol{X_h}(j\omega) \\ +\bar{q}\boldsymbol{Q_{g\delta}}(M,\kappa)\boldsymbol{\Delta}(j\omega) + \bar{q}\boldsymbol{Q_{gv}}(M,\kappa)\frac{\boldsymbol{V}(j\omega)}{\mathrm{TAS}}\Big]\end{aligned} \tag{2.46}$$

One could be tempted to first compute the local loads in the generalized coordinates frame, and then to express them in the g-set by left multiplication by the modal matrix $\boldsymbol{\Phi_{gh}}$. However, the latter is full column rank and can only be used to pass from the g-set to the generalized coordinates, so the loads computation can only be done in the g-set directly.

Although the details of the T-matrix computation are not shown, some elements can be addressed to improve the physical understanding of the integrated loads. By making the assumption that the wings are fixed-free cantilever beams subjected to a uniformly distributed aerodynamic force and moment along it, then the shear force would be zero at the wing tip and increase linearly until reaching the maximum at the root. The bending and torsional moment would follow the same trend, with a quadratic dependence on the span-wise position. This interpretation provides the basic strategy used in GLA: by concentrating the local loads at the inner part of the wing (close to the fuselage), the lever arm is lowered and the integrated bending moment can be reduced everywhere on the wing, and especially at the root, where it is highest.

The loads of interest are the shear force, bending moment and torsional moment in the wing, HTP, VTP and fuselage. Although they can all participate in the aircraft sizing, the most important location is the wing root, where the highest loads are present, requiring important structures to withstand them. The bending moment is of particular interest, and is generally considered the main objective for load alleviation.

Angle-of-attack

The local angle-of-attack can be computed based on its expression in Eq. (2.32). Using the assumptions made at the beginning of this section about the wind velocity, the local angle-of-attack at a point of the g-set is computed in the frequency domain as

$$\alpha_g(j\omega) = [\boldsymbol{D_{1,\theta}} + jkD_{2,z}]\,\boldsymbol{\Phi_{gh}}\boldsymbol{X_h}(j\omega) + \frac{\boldsymbol{v}}{\mathrm{TAS}} e^{\frac{d_x}{\overline{TAS}}j\omega} \tag{2.47}$$

where $\boldsymbol{D_{1,\theta}}$ and $\boldsymbol{D_{2,z}}$ are the rows of D_1 and D_2 associated to the angle-of-attack. Note that d_x is negative following the body axes definition.

The model has been presented in a general framework, but practically, the inputs and outputs considered in the analysis depend on the application. For loads computation and GLA, we will only study the longitudinal aeroelastic dynamics. The wind velocity and the control surfaces inputs are considered, and the main outputs are the loads at the wing root, the angle-of-attack, the vertical acceleration and pitch rate as will be explained in more details in chapter 4. For AFS, both longitudinal and lateral dynamics are considered, and the main objectives concern the stability of the system, hence the only inputs and outputs of interest are those that can be used to create a closed loop. It will be seen in chapter 5 that an option is to consider accelerometers and gyros at different locations of the airframe, and as inputs only the control surface are considered (the wind can be studied as a disturbance of the system but it plays a less important role than in GLA).

This concludes the description of the aeroelastic modeling process used in this work. In the next sections, the main features of the models are analyzed in view of the GLA and AFS control syntheses.

2.3.8 Aerodynamic modes and flutter

The internal stability of the full aeroelastic system defined in Eq. (2.41) comes down to the study of

$$\left[-\omega^2\boldsymbol{M_{hh}} + j\omega\boldsymbol{B_{hh}} + \boldsymbol{K_{hh}} - \bar{q}\boldsymbol{Q_{hh}}(M,\kappa)\right]\boldsymbol{X_h}(j\omega) = 0 \tag{2.48}$$

which is called the flutter equation. At fixed Mach number and velocity, the modal generalized force depends on the frequency ω. $\boldsymbol{Q_{hh}}$ acts as a feedback on the structural model, and the modal analysis described in section 2.3.4 is no more valid in presence of aeroelastic effects. The structural modes are modified by this feedback, and a new modal analysis must be performed based on the closed loop. If the dependence of $\boldsymbol{Q_{hh}}$ on the frequency was rational, the flutter equation could be studied as a Linear Time Invariant (LTI) system, and an eigenvalue analysis could provide information about its stability. This is not the case as from the DLM, the modal generalized force $\boldsymbol{Q_{hh}}$ is evaluated at discrete frequency values. One way to study the stability could then be to estimate a LTI model of $\boldsymbol{Q_{hh}}$ based on the available frequency. However, more direct techniques

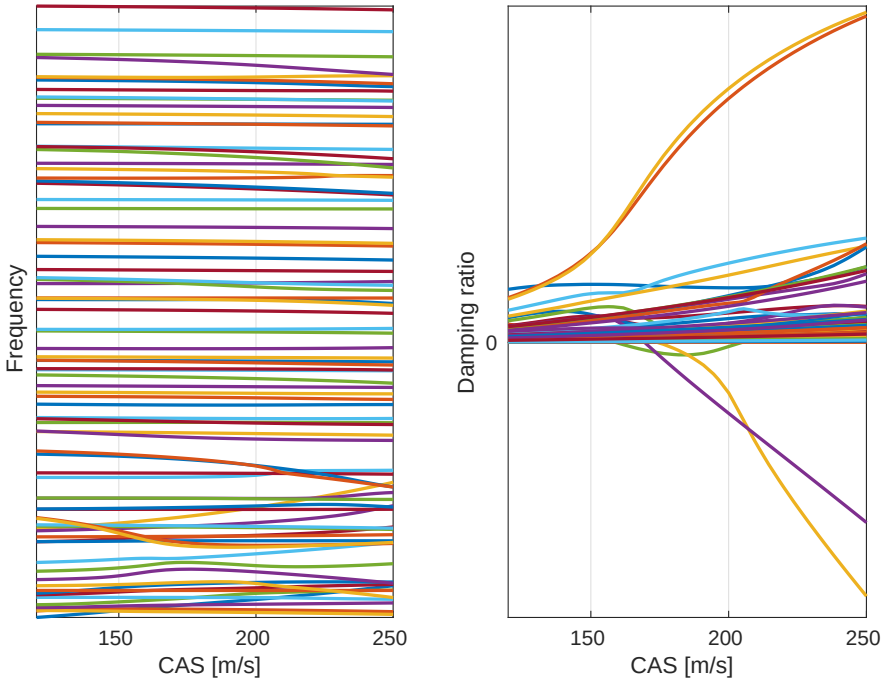

Figure 2.12: Evolution of the aeroelastic modes frequency (left) and damping ratio (right) with increasing CAS

exist, which do not require an intermediary system identification. The so-called "p-k" method [Hassig 1971] is a popular iterative procedure that aims at finding solutions of

$$\left[\frac{\mathrm{TAS}^2}{b^2}\boldsymbol{M_{hh}}\lambda^2 + \boldsymbol{K_{hh}} - \bar{q}\boldsymbol{Q_{hh}}(M,\kappa)\right]\boldsymbol{X_h}(j\omega) = 0 \tag{2.49}$$

at a fixed value of the Mach number M, where λ is an unknown complex number to be found. From an initial estimation of λ called λ_1 the imaginary part is assimilated as an estimate of the reduced frequency k_1:

$$\lambda_1 = \gamma_1 k_1 + j k_1 \tag{2.50}$$

and the generalized modal force $\boldsymbol{Q_{hh}}(M,\kappa)$ is evaluated at $\kappa = \kappa_1$ and the equation (2.49) is solved for λ using this value. This is an eigenvalue problem, which also provides the eigenvector $\bar{X_1}$. The process is iterated until the imaginary part of λ_i gets close to the true reduced frequency κ [Cook 2012]. The procedure is repeated at different values of the velocity. At zero velocity, there are no aeroelastic effects and the aeroelastic modes are the same as the structural modes. After a solution has been found at a certain velocity, it can be used as initial condition to the next velocity. The process is repeated for each mode, initializing λ each time with the structural pole (zero velocity) and converging until the aeroelastic frequency and damping are obtained at each velocity. The eigenvector $\bar{X}$ hence obtained defines the mode's shape. Note that with this technique, the structural damping is assumed to be zero. In Fig. 2.12, the solutions of the p-k method for a Mach number of 0.86 and an empty aircraft are shown in their classical representation. The left part represents the evolution of the modes frequencies with varying CAS, while the right

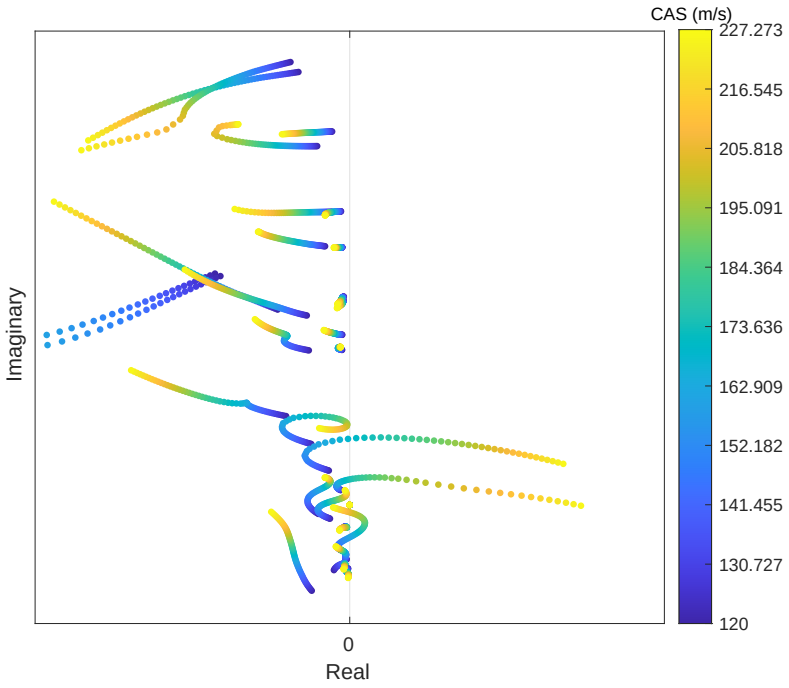

Figure 2.13: Aeroelastic root loci with increasing CAS

part shows the evolution of the damping ratios. When the latter becomes negative, the system is unstable and the associated velocity is called "flutter velocity". It can be seen that three modes are susceptible to become unstable when the velocity increases. The main objective of the AFS studied in chapter 5 is to increase the flutter velocity thanks to the design of a stabilizing control law. Note that the numerical values are not given for confidentiality reasons. In Fig. 2.13, the same results are shown with a different representation: the poles are directly drawn on the complex plane, at different velocities. This representation is more concise, and the evolution of the frequency is clearer, but rate at which the damping ratio increases or decreases with the velocity is more difficult to appreciate. Depending on the results, one configuration or the other will be preferred when studying the AFS.

The p-k procedure described gives information about the evolution of the structural modes with the velocity. The six modes, associated to the rigid dynamics in absence of aeroelastic effects, are not covered by the method. Yet, they are important for the loads analysis. The initially rigid modes (frequency equal to zero) evolve into the so-called "flight dynamics" modes in presence of aerodynamic effects. They are well known in flight dynamics and will not be described in this work, see [Cook 2012] for example. The short-period mode is of particular importance in longitudinal dynamics, with a frequency of about 0.3 Hz, lower than the structural modes that typically start at about 1 Hz for the XRF1-HARW.

Finally, Fig. 2.14 shows flutter results for different torsional stiffness of the wing. In each case, a different FEM model has been defined with an increase or decrease of the torsional stiffness of the wing's spar. For the sake of clarity, only the three modes which are susceptible to become

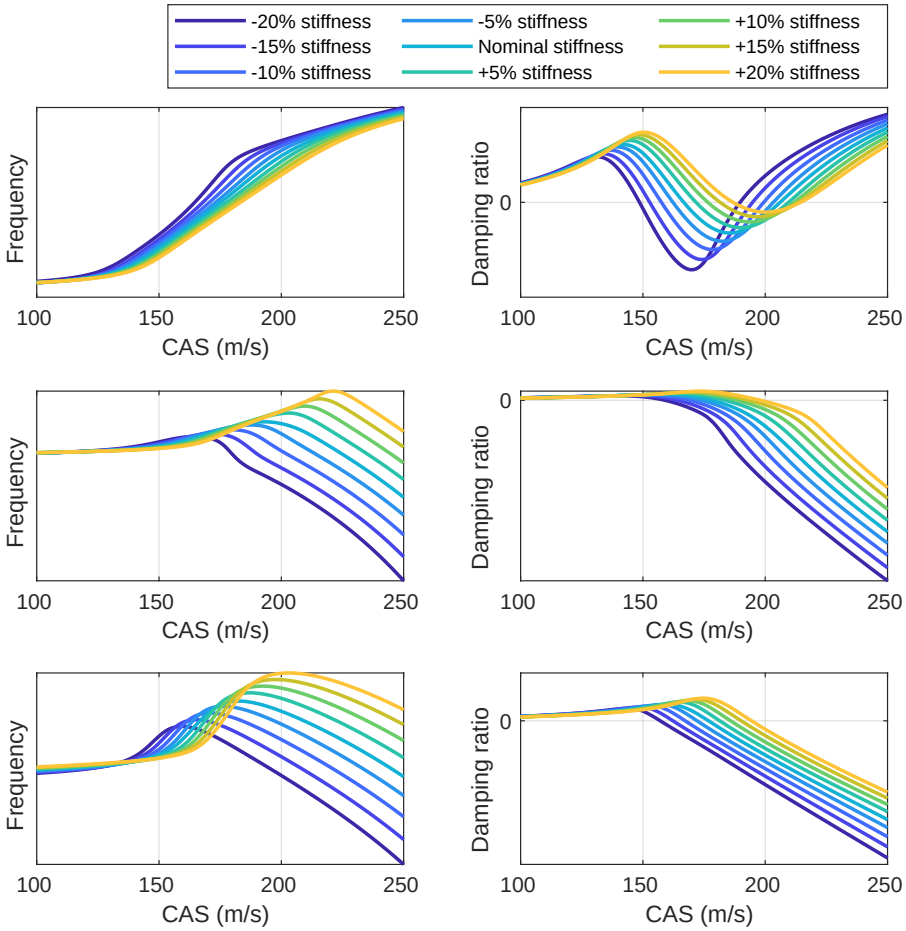

Figure 2.14: Evolution of the aeroelastic modes frequency and damping for different wing torsional stiffness

unstable are shown. It can be seen how increasing the wing's torsional stiffness leads to a better damping of these modes and an increase of the flutter velocity. A stiffness of about -15% will be used in the rest of the work, in order to clearly see the effects of aircraft flexibility on the model. Note that on Fig. 2.14, the first mode becomes unstable then stable again when the velocity increases. The second and third modes become unstable at flutter velocity and the damping only decreases above. The second type of flutter modes, sometimes called "explosive modes", are more problematic as they generally cannot be stabilized at all velocities.

2.3.9 Transfer functions analysis

Combining the equations of motion (2.41) that give the response of the state $\boldsymbol{x_h}$ to wind and control surface inputs, and the outputs equations (2.42), (2.46) and (2.47), we obtain transfer functions which are studied in this section. For the sake of conciseness, only the longitudinal dynamics are shown for their interest for GLA.

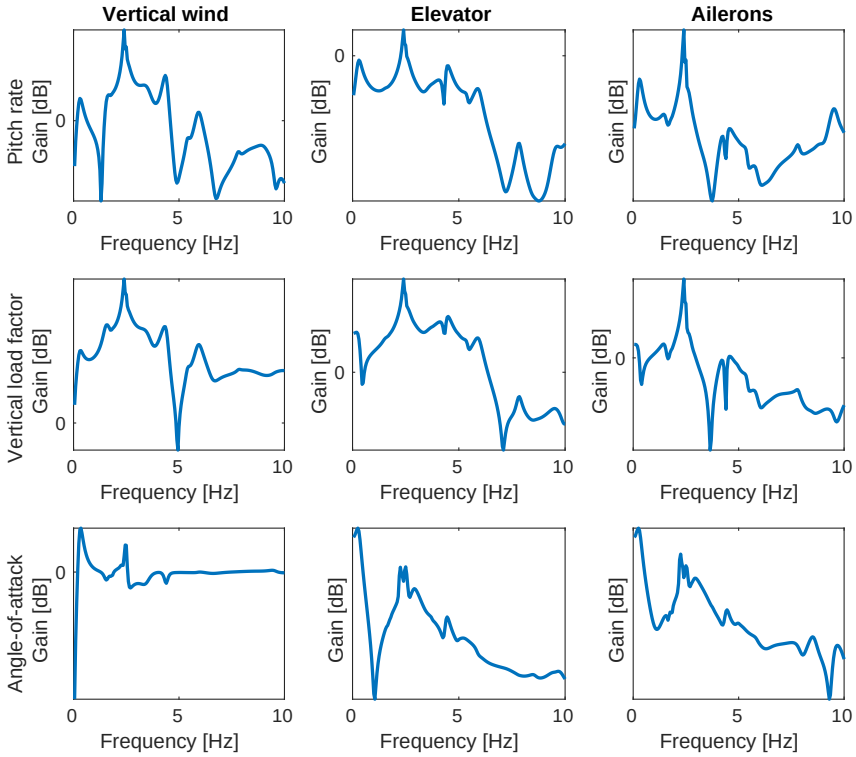

Figure 2.15: Transfer functions of the XRF1-HARW with sensors outputs

The transfer functions gains from the vertical wind velocity (divided by the TAS), an elevator and the innermost aileron to the pitch rate q, vertical load factor n_z and angle-of-attack α are shown on Fig. 2.15. These outputs correspond to the sensors that are mostly used for GLA, in addition to the lidar sensor. The pitch rate and vertical load factor are computed at the center of gravity, while the angle-of-attack is measured in the front part of the fuselage, 6 meters behind the airplane's nose. The computations are done at $M = 0.5$, a fixed CAS = 170 m/s and an empty aircraft. In these conditions, the aircraft is stable with a mode (around 3 Hz) close to instability. As will be explained in section 2.3.10, the response of the aircraft to the wind is low above 5 Hz and negligible above 10 Hz. For this reason the transfer functions are shown up to 10 Hz. This does not mean that no aeroelastic effect can occur beyond: it has been seen in the flutter analysis introduced in section 2.3.8 that instability can occur at high frequency. The influence of the different aeroelastic modes can be seen on the figure: the short period is the first peak located at around 0.3 Hz, then follows the first wing bending peak at around 1 Hz. The peak around 3 Hz corresponds to a flutter mode, close to instability. It can be seen on Fig. 2.15 that the elevators have higher gains than the innermost aileron. This must be contrasted by the fact that the ailerons are of smaller size, and used together they can have higher effect than the elevators. Furthermore, the phase diagrams are not shown for conciseness, but they would reveal that the ailerons have a more direct effect on the vertical load factor. Finally, it can be noted that the angle-of-attack is almost equal to the wind velocity (divided by the TAS) at frequencies higher than 4 Hz, while at lower frequencies the contributions of the rigid body vertical velocity and of

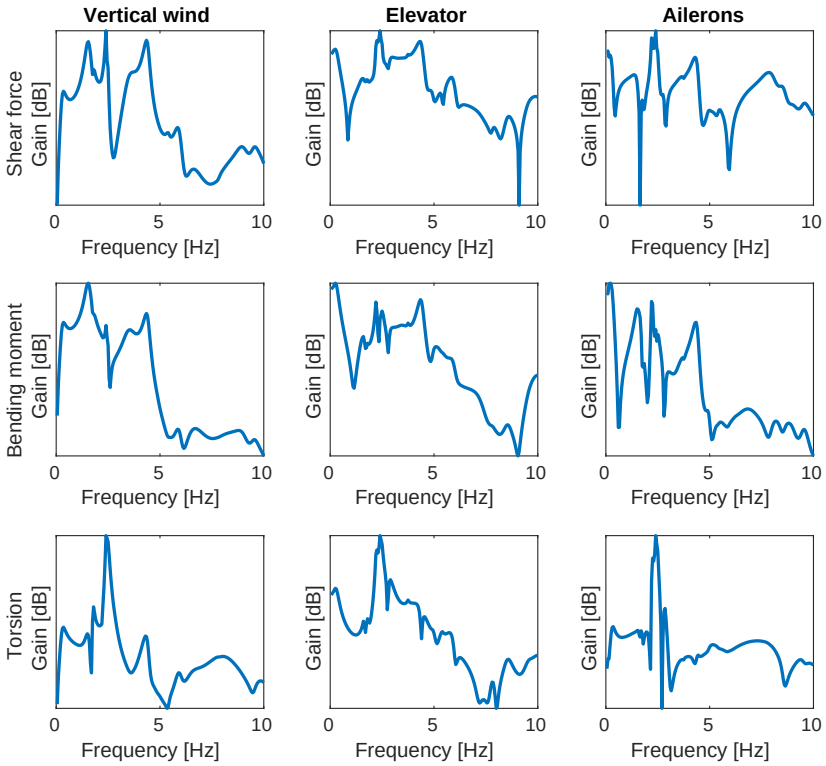

Figure 2.16: Transfer functions of the XRF1-HARW with loads outputs computed at the wing root

the elastic displacements are clearly seen.

The transfer functions gains with three loads outputs are shown in Fig. 2.16, with the same inputs as before. The selected loads are the shear force, bending moment and torsional moment. Again, the elevators have a higher effect than the ailerons due to their size, but less direct. Indeed, the elevators act on the loads through their intermediary effect on the angle-of-attack and the pitch angle. By creating pitch and vertical velocity of the aircraft, the angle-of-attack is modified, affecting directly the local aerodynamic forces applied on the wing, and consequently the loads. The ailerons have a lower influence than the elevators on the aircraft attitude due to the lower lever arm which implies a lower pitching moment. They act on the loads mostly through two different mechanisms. The direct lift created by the ailerons can be used to create a negative force on the wing that partly alleviates the statical lift, hence reducing the total net force. Since only increments are considered hereby, this effect cannot be seen, but it must be kept in mind when deciding the GLA strategy. The second mechanism is by modifying the repartition of the aerodynamic forces on the wing, which has an effect on the lever arm, and the integrated loads at the wing's root are affected. Furthermore, it must be noted that the ailerons action tends to have opposite effects on the bending and torsional moments: by reducing one the other generally increases. These elements will be reviewed in more details in the chapter 4 dedicated to GLA. In Fig. 2.16 it can be seen that the shear force and the bending moment have similar trends, the two variables are correlated. The torsional moment is very sensitive to the mode with low damping

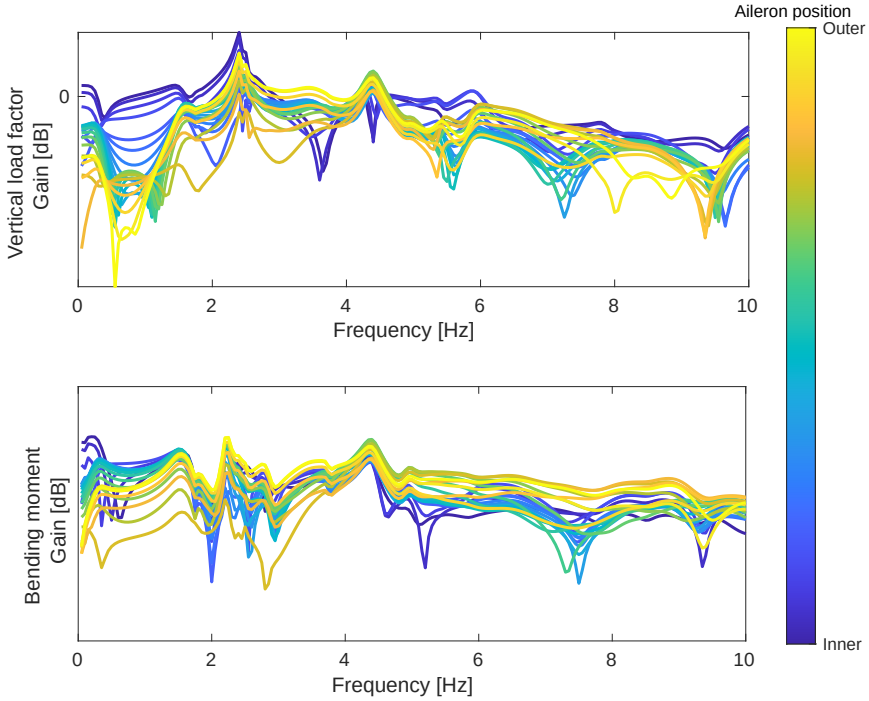

Figure 2.17: Transfer functions of the XRF1-HARW from wind velocity to the vertical load factor and bending moment, with different ailerons inputs

around 4 Hz.

On the previous figures, only one aileron had been considered. In Fig. 2.17, the transfer functions for all ailerons are shown, for a wind velocity input and the vertical load factor and bending moments outputs. This graph is of particular importance for the choice of ailerons used for active control, either for GLA and AFS. The global trend is that the ailerons close to the fuselage are more efficient than those at the wing tips at frequencies up to 1.8 Hz at controlling the vertical load factor. This is in part due to the higher surface of the inner ailerons. This trend is not so clear on the bending moment, where the inner ailerons are efficient at very low frequencies up to 0.3 Hz but not on the critical range around 0.3 Hz and 1 Hz in which most of the loads occur and where the CS limitations are not important. Indeed, both the wind velocity frequency content and the actuators dynamics have a high-frequency roll-off. The three first ailerons have a sensibly different behavior from the others, it can be explained by the presence of the engines situated at the position of the fourth aileron. At high frequency, the outer ailerons are more efficient, and particularly if their relative size are considered. This can have important incidences in GLA and AFS, where the modes with low aeroelastic damping around 3 Hz should be damped (GLA, assuming a stable model) or stabilized (AFS, when increasing the aircraft velocity). The middle ailerons are efficient at controlling the bending moment in all the frequency range of interest. Note that these are important considerations, but not enough to know what ailerons are to be used for GLA and AFS. An approach based on the full model will be studied in chapter 5.

The loads shown so far are those computed at the wing root. In Fig. 2.18, the transfer

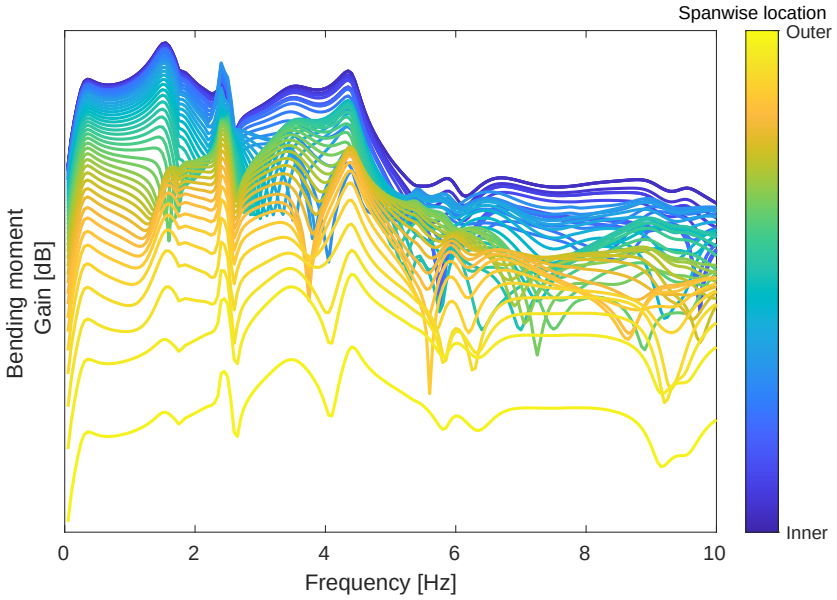

Figure 2.18: Transfer functions of the XRF1-HARW from wind velocity to the bending moment, at different locations along the wing

function for the wind velocity to the bending moment is shown at different locations of the wing. As explained before, the loads are highest at the wing's root, and decrease along the span. That justifies why only the loads at the wing's root are used as criterion for GLA synthesis for example. A verification that the loads are lower at the outer locations is required anyway.

The transfer functions at different flight points and mass configurations are considered. One specificity of this work, as explained in section 1.2.5, is to place the aircraft uncertainty at the heart of the aeroelastic analysis and the active control design. In Fig. 2.19, different transfer functions from the wind velocity to the vertical load factor and bending moment are shown, corresponding to different Mach values (the CAS is still equal to 170 m/s and the airplane is still empty). This figure shows the very important difference between two aeroelastic models computed at different values of the Mach number. Due to compressibility effects, the aerodynamics are very different at low Mach number and in transonic regime. Note that other issues, not studied in this work, can occur in the transonic regime known for its nonlinearities. Fig. 2.19 shows that the wind has a lower effect on the bending moment at $M = 0.5$ than at $M > 0.8$, but this does not mean that the loads are lower. Indeed, as explained in sections 2.1 and 2.2, the aircraft flies at lower altitude at $M = 0.5$, at which the wind intensity is higher.

Finally, the variations of the aeroelastic dynamics due to the mass configuration are studied, at fixed $M = 0.86$. In Fig. 2.20, the 16 mass configurations described in section 2.1.4 are compared using the same transfer functions as before. Again, important variations exist between two configurations. It can be noted that while the Mach number can be known by the aircraft's on-board computer, the mass configuration is more difficult to quantify and parameterized. These variations will hence be considered as uncertainties, in general. In section 3.9.2, a possible parameterization

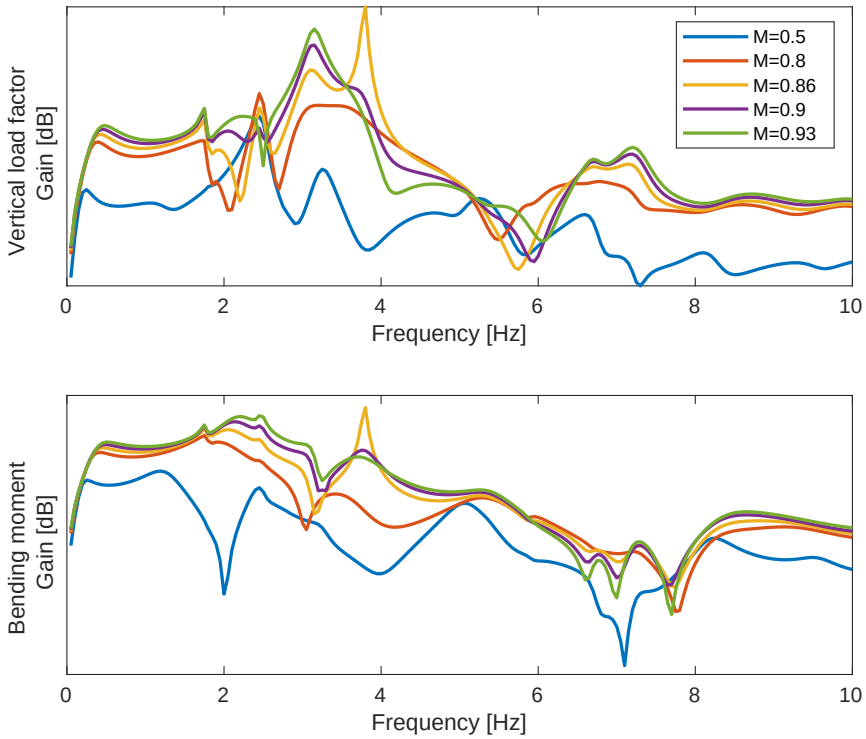

Figure 2.19: Transfer functions of the XRF1-HARW from wind velocity to the vertical load factor and bending moment, at different values of the Mach number

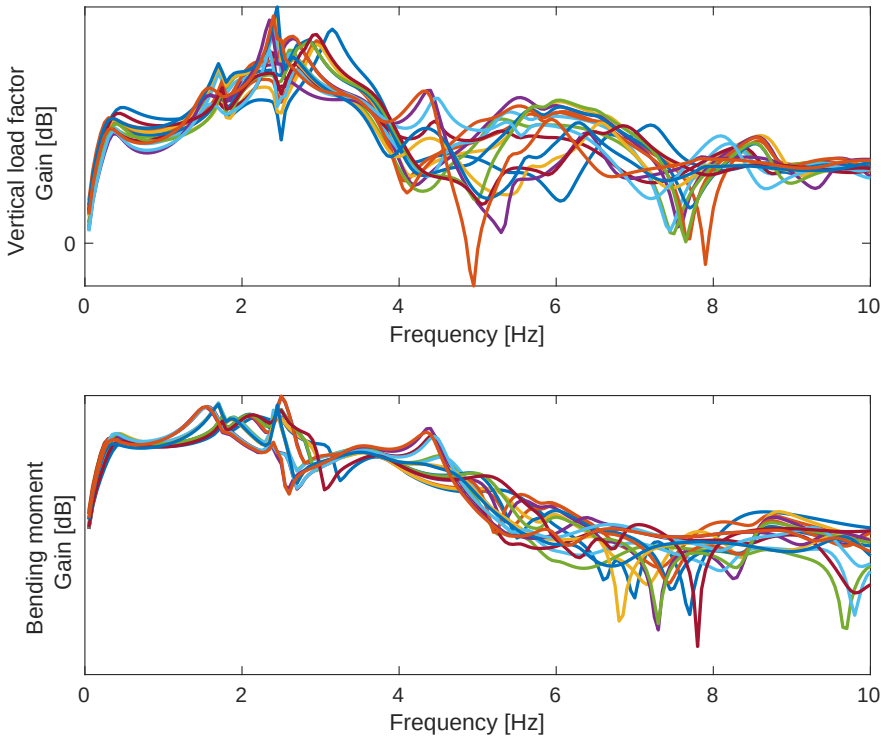

Figure 2.20: Transfer functions of the XRF1-HARW from wind velocity to the vertical load factor and bending moment, for different mass cases

of the mass configuration is investigated.

2.3.10 Frequency response to turbulence

In order to gain insight into the true loads experienced by the aircraft, this section studies the response to a turbulence as defined in 2.2. To this aim, Fig. 2.21 shows the power spectral density of the vertical load factor and the bending moment in response to a von Kármán turbulence with 2500 ft turbulence scale. Knowing the PSD of the turbulence from Eq. (2.8), and the aeroelastic transfer function $H(j\omega)$ from sections 2.3.6 and 2.3.7, the PSD of the output can be computed as:

$$\Phi_y(\omega) = |H(j\omega)|^2 \, \Phi_{turb}(\omega) \tag{2.51}$$

where the absolute value and square are applied element-wise to $H(j\omega)$. Fig. 2.21 shows that with a realistic wind, the frequency content of the load factor and bending moment are almost zero above 5 Hz. Hence, the models used for GLA do not need to be accurate above this frequency. In particular, the aeroelastic modes with frequency above 5 Hz must not be considered. This statement is true if the system is stable. For flutter analysis, all modes can theoretically become unstable, due to the aeroelastic feedback (see section 2.3.8) or to a control law feedback. Finally, note that in Fig. 2.21 two main peaks exist for the bending moment's PSD. The first is due to the short-period mode, and the second to a structural mode. Depending on the Mach number, velocity and mass case, the modes can have different relative influence on the outputs PSD, and this result shall be seen as an illustrative example.

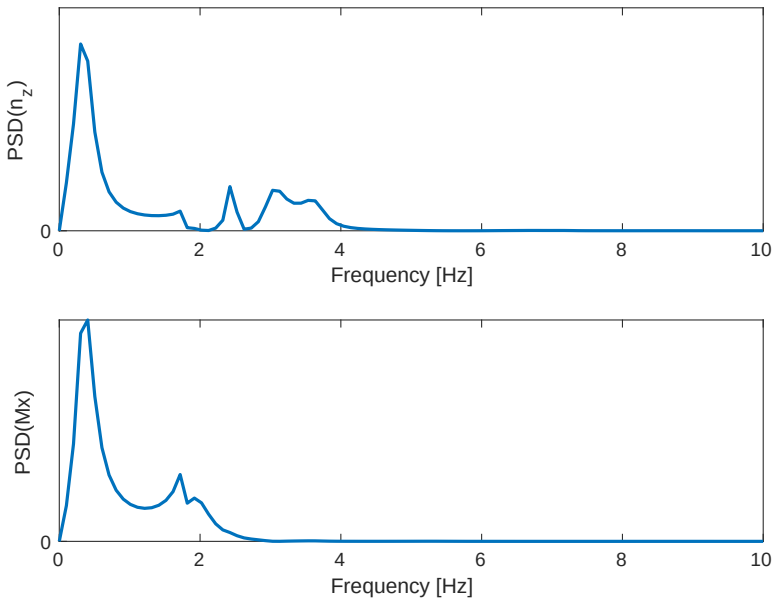

Figure 2.21: Power spectral density of the vertical load factor and bending moment as response to a 2500 ft von Kármán turbulence

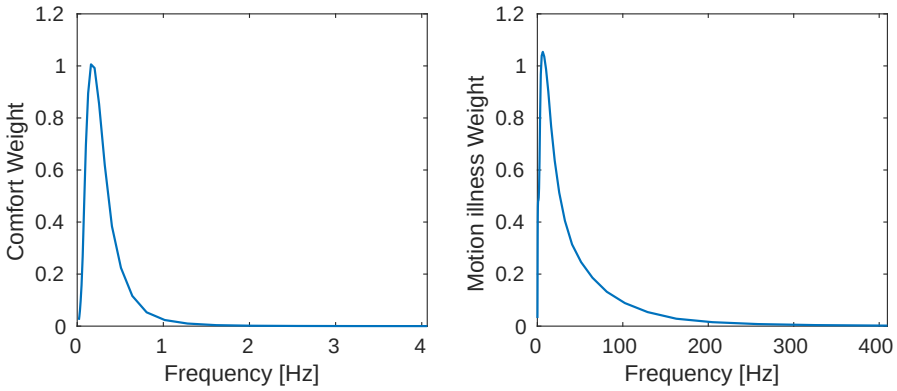

Figure 2.22: Comfort and cinetose frequency weighting according to ISO 2631-1

From a PSD response, the L_2 norm of the time signal y can be computed as:

$$\|y\|_2 = \sqrt{\frac{1}{\pi}\int_0^\infty \Phi_y(\omega)d\omega} \tag{2.52}$$

In case y is a continuous stochastic process with zero mean value, the L_2 norm coincides with the standard deviation. It is the case here, where the output results from the continuous stochastic turbulence with zero mean. This provides the main metric used to quantify turbulent loads, computed in the frequency domain.

Based on the PSD response of the vertical acceleration at a passenger's location, some criteria of comfort and motion illness can be defined. The standard ISO document [*Mechanical vibration and shock — Evaluation of human exposure to whole-body vibration — Part 1: General requirements* 1997] discusses the effects of vibrations on the human body. By neglecting the lateral accelerations, and assuming that a uniform acceleration is applied to the body of the passenger (neglecting the effect of the seat), equivalent comfort and motion sickness accelerations can be obtained by applying frequency weights to the acceleration PSD, as shown in Fig. 2.22. The integration of the integrated PSD then leads to equivalent standard deviations, giving criteria for studying the comfort and motion sickness. The former is associated to low frequencies below 1 Hz, while the latter is created by high-frequency accelerations. An empirical law states that the percentage of passengers who are likely to vomit is proportional to the equivalent acceleration standard deviation (obtained by applying the high-frequency weights) multiplied by the square root of time.

2.3.11 Loads envelopes

The time and frequency responses of an aircraft are computed at a given flight point and mass configuration. It is not straightforward to know which conditions will lead to the higher loads. Considering the velocity (at fixed Mach), it has been explained in section 2.1.3 that, in general, increasing the velocity leads to higher loads. The EAS is particularly meaningful in that sense, as

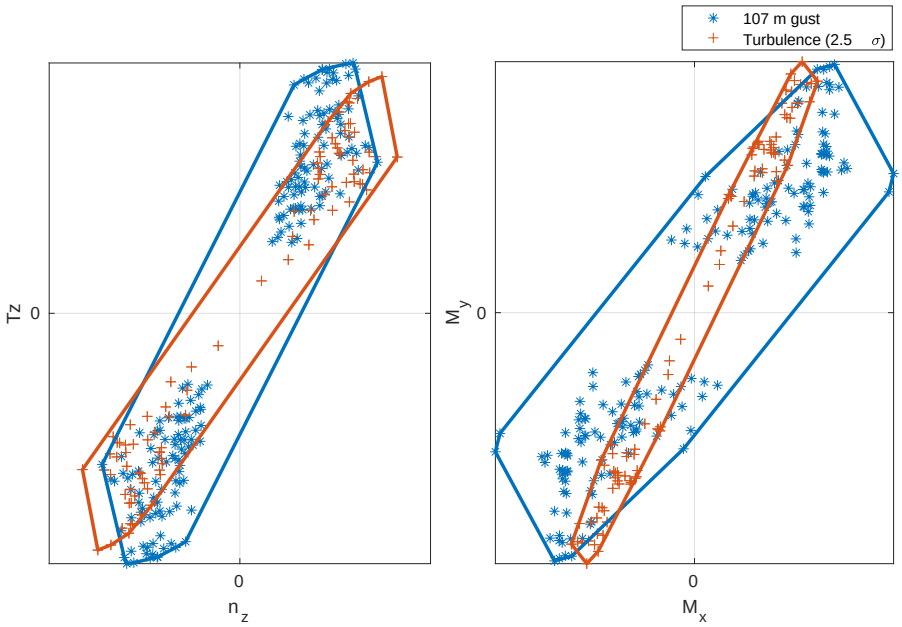

Figure 2.23: Loads envelope for the shear force T_z and vertical load factor n_z (left) and the bending M_x and torsional moment M_y (right), computed at different Mach number and mass configuration

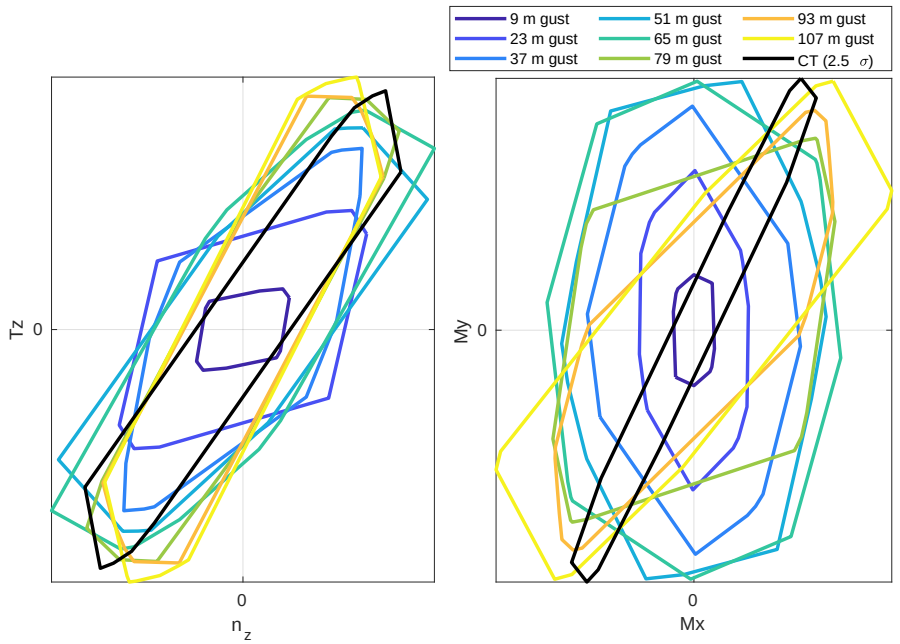

Figure 2.24: Loads envelope obtained with various gust lengths and with continuous turbulence (CT) for the shear force T_z and vertical load factor n_z (left) and the bending M_x and torsional moment M_y (right)

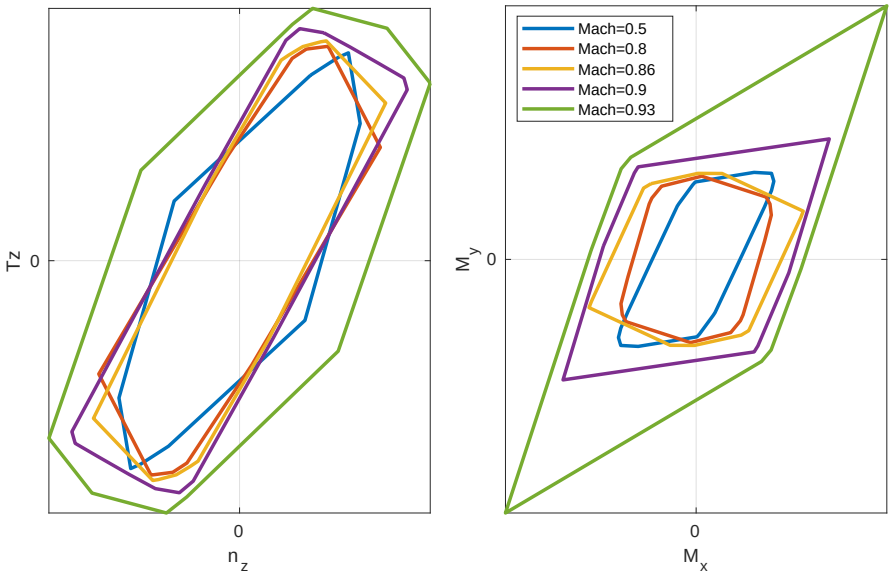

Figure 2.25: Loads envelope obtained at various Mach numbers for the shear force T_z and vertical load factor n_z (left) and the bending M_x and torsional moment M_y (right)

the aerodynamic forces are proportional to its squared value (dynamic pressure), and the CAS is a good approximation of the EAS. For this reason it was decided to work at fixed CAS, taking the highest possible value in the nominal flight envelope. At fixed CAS, the value of the Mach number which leads to the higher loads is not obvious. A higher Mach means a higher altitude hence lower wind velocity (see section 2.2), but the aerodynamics are affected in a non trivial way. Similarly, several mass configurations could in theory lead to the maximum loads. For these reasons, the loads are computed at different values of the Mach number and mass cases, and the results are presented in the so-called correlated loads envelopes. Fig. 2.23 shows an example of correlated load envelopes, one for the couple vertical load factor/shear force at the wing root, and one for the couple bending/torsional moments at the wing root. In the gust case, simulations are performed with positive and negative gusts following the $1 - \cos$ function defined in 2.2. The maximum of each load is computed, and the value of the other load in the couple is used to create a point. The same is done with the minimum value. This representation shows at the same time the maximum positive and minimum negative loads, and the correlation between the loads. For the turbulence case, the computations are performed in the frequency domain. The loads correlations are defined as

$$\rho_{ik}^{corr} = \frac{1}{\pi} \int_0^\infty Re\left(H_i(j\omega) H_k(j\omega)^*\right) \Phi_{turb}(\omega) d\omega \tag{2.53}$$

where H_i and H_k are the frequency transfer functions of the wind to the loads i and k respectively. The square root of the diagonal terms $\sigma_k = \sqrt{\rho_{kk}}$ are the standard deviations of the loads, and correspond to the L_2 norm computed from Eqs. (2.51) and (2.52). The correlated load i corrected by correlation with load k is then expressed as

$$\sigma_{ik}^{corr} = \frac{\rho_{ik}^{corr}}{\sigma_k} \tag{2.54}$$

The points of the loads envelope due to turbulence wind are then defined by coordinates $(2.5\sigma_i, 2.5\sigma_{ki}^{corr})$ or $(2.5\sigma_{ik}^{corr}, 2.5\sigma_k)$. The computations are performed at different values of the Mach number 0.5, 0.8 and 0.86, less or equal to the operational Mach number MMO) and the 16 different mass configurations described in section 2.1.4.

In Fig. 2.24, the correlated loads envelopes are shown for different gust values and for turbulence. It shows that the worst cases of shear force, bending and torsional moment due to a gust are obtained with the longest gust of 107 m. Nevertheless, the turbulent loads are of the same order of magnitude. The maximum load factor is obtained with an intermediary gust of about 65 m gradient. These conclusions are true in absence of control laws only. The (n_z, T_z) and (M_x, M_y) loads couples are correlated for long gust and turbulence, as seen by the oblong shapes of the envelopes.

Finally, Fig. 2.25 shows the comparison of the loads envelopes obtained at different Mach numbers. The values of 0.5, 0.8 and 0.86 correspond to operational values, and the values of 0.9 and 0.93 correspond to extreme cases in which the aircraft dives, with different certification constraints as explained in section 2.1.3. A higher Mach number tends to lead to higher loads, but still of the same order of magnitude as a low Mach number of 0.5. It is then not possible to clearly establish that the strongest loads occur at highest Mach number. The analysis of the worst cases of loads, either in open-loop or with an active control system, should include computations at different Mach numbers in order to be complete.

Chapter 3

System Identification

Contents

3.1 Introduction

3.1.1 Context of aeroelastic reduced order modeling

Aeroelastic models defined in Chapter 2 are linear, in the sense that if y_1 and y_2 are the responses of the model to u_1 and u_2 respectively, then a linear combination of inputs $a_1u_1 + a_2u_2$ leads to a linear combination of outputs of the same form $a_1y_1 + a_2y_2$. However, the DLM method described in section 2.3.5 leads to values of the GAFs at different reduced frequencies, which cannot directly be used by control design techniques or for stability and robustness analysis. Linear Time Invariant (LTI) state-space models can be obtained based on these values, using system identification techniques, and then used for simulation, analysis and control synthesis. The classical approach is to use Roger [Roger 1977] or Karpel [Karpel 1982] approximations that fit a transfer function composed of a second-order polynomial and of delay terms from the GAF data, like in [Waite et al. 2018]. Another popular method is the Eigensystem Realization Algorithm (ERA) [Juang and Pappa 1985] that identifies a state-space model based on time-data, used by several studies on active flutter suppression [Silva and Raveh 2001; Silva 2018; Waite et al. 2018; Waite et al. 2019]. With the assumptions of small displacements around a trim equilibrium and linear aerodynamics, linear aeroelastic models can be obtained with this procedure.

Aeroelastic models obtained by GAF rationalization maintain the physical interpretation of the states, which can be assimilated to modal displacements and aerodynamic delays for example. However, in absence of dedicated methods to reduce their order, these models can be prohibitive for numerically intensive control synthesis techniques. From the author's experience, classical reduction techniques, such as the balanced truncation, [Green 1988], lead to poor approximation of the initial model when the latter is of very high order and numerically ill-conditioned. The current work studies a different strategy, by working directly on identification of the full aeroelastic transfer function, instead of the GAF. The frequency response of the aeroelastic transfer function is first evaluated at different frequencies, and Multi-Input Multi-Output (MIMO) identification algorithms based on this data are used to directly obtain reduced order state-space models. Aerodynamics are modeled by DLM to directly obtain GAF in the frequency domain, and a built-in FEM model is used for structural dynamics. By focusing on the response corresponding to the inputs and outputs of interest, only the main features are modeled, leading to much lower orders than with the classical approach. However, the dependence on the flight parameters (such as Mach and altitude) is lost, and a model must be obtained for each condition separately. The subspace identification is a state-of-the-art set of techniques for estimating a MIMO state-space model from time or frequency data, an overview can be found in [Qin 2006]. The Loewner method [Mayo and Antoulas 2007; Karachalios, Gosea, and Antoulas 2019] is another promising approach, based on rational interpolation theory. In absence of stability constraints, there is no guarantee that these methods will produce models which reflect the stability of the true system, especially when its order is not known in advance. This difficulty, acknowledged in [Kergus et al. 2018] for example, is a typical flaw of the black-box approach, which loses the physical interpretability

of the aeroelastic system whose poles are not exactly modeled. The first step to cope with this issue is to impose stability of the identified model. This is done in this work by using the results of [Miller and De Callafon 2013] based on [Chilali and Gahinet 1996; Lacy and Bernstein 2003], in which a subspace-based identification is proposed with a general set of constraints imposed to the poles, that includes the constraint of stability. The second step to improve the physical interpretability of the models consists in imposing a set of known aeroelastic poles that have been estimated beforehand by p-k method [Hassig 1971] for example, while other poles are left as free parameters to improve the approximation accuracy. With this hybrid method, the objective is to ensure the stability of the mathematical poles that help approximating the true transfer function, while imposing that some poles of interest are correctly modeled, with direct applications in GLA and AFS syntheses, but also in effective aeroelastic simulations. Specific techniques are developed based on the subspace identification and inspired by [Tang, Wu, and Shi 2017], to impose poles with and without constraints on the additional poles.

The contributions of this chapter are the following:

- A low-order identification approach based on the aeroelastic transfer function frequency response, and the comparison of the Loewner method and subspace methods with and without stability constraints.
- The extension of a procedure to impose poles location constraints in the system identification process to the Loewner framework, already existing for subspace methods.
- Novel hybrid identification techniques, in which a part of the poles is imposed and the other part is left as free parameters. The possibility to impose constraints on the free poles is investigated. These methods are validated and compared using data generated from fixed-order random state-space models, before being applied to aeroelastic data obtained from FEM and DLM models.
- The simultaneous identification of multiple state-space models with common matrix $\boldsymbol{C}$ with a modified Loewner method, leading to the definition of polytopic models.

3.1.2 State-space model identification

The objective of this chapter is to identify state-space models that approximate aeroelastic systems defined by the modal displacements dynamics (2.41) and by the expression of the outputs of interests defined by Eq. (2.42), (2.46) and (2.47). The state-space model can be either defined in discrete-time form:

$$\begin{cases} \boldsymbol{x}_{k+1} = \boldsymbol{A}\boldsymbol{x}_k + \boldsymbol{B}\boldsymbol{u}_k \\ \boldsymbol{y}_k = \boldsymbol{C}\boldsymbol{x}_k + \boldsymbol{D}\boldsymbol{u}_k \end{cases} \tag{3.1}$$

where k is the discrete time, or alternatively in continuous-time form:

$$\begin{cases} \dot{\boldsymbol{x}}(t) = \boldsymbol{A}\boldsymbol{x}(t) + \boldsymbol{B}\boldsymbol{u}(t) \\ \boldsymbol{y}(t) = \boldsymbol{C}\boldsymbol{x}(t) + \boldsymbol{D}\boldsymbol{u}(t) \end{cases} \tag{3.2}$$

where t is the continous time. $\boldsymbol{x}$ is the state vector, $\boldsymbol{u}$ and $\boldsymbol{y}$ are respectively the input and output vectors, and the matrices $\boldsymbol{A} \in \mathbb{R}^{n\times n}$, $\boldsymbol{B} \in \mathbb{R}^{n\times N_u}$, $\boldsymbol{C} \in \mathbb{R}^{N_y\times n}$ and $\boldsymbol{D} \in \mathbb{R}^{N_y\times N_u}$ are matrices defining the model.

The choice of the inputs and outputs depends on the application. The outputs of the model can be the variables measured by the aircraft sensors, and the structural loads which are used for GLA only. In some cases all control surfaces inputs will be used, and in others, only a reduced number of them is selected, or the ailerons can even be grouped as to limit the number of independently controlled inputs. The wind is the main disturbance considered in GLA, and is not used in AFS. Considering the choice between a discrete-time or continuous-time model, the latter is generally preferred when the identification techniques allow it. A continuous time model can easily be transformed into a discrete-time model with a selected time step, while the contrary is not always straightforward.

What is meant by "approximating" an aeroelastic system also depends on the problem and the type of identification method used. The main objective is that the transfer function associated to the identified model matches the aeroelastic data. After computing the frequency response $[\boldsymbol{H}(\omega_i)]_{i=1\dots N}$ at N angular frequency values $[\omega_i]_{i=1\dots N}$ using Eq. (2.41), (2.42), (2.46) and (2.47), the identified transfer function $\hat{\boldsymbol{H}}$ must minimize the approximation error:

$$\min_{\boldsymbol{A},\boldsymbol{B},\boldsymbol{C},\boldsymbol{D}} \sum_{i=1}^{N} \left\| \boldsymbol{H}(\omega_i) - \hat{\boldsymbol{H}}(\omega_i) \right\| \tag{3.3}$$

where the transfer function associated to a discrete-time state-space model is expressed as:

$$\hat{\boldsymbol{H}}(\omega) = \boldsymbol{C}\left(e^{j\omega}\boldsymbol{I_n} - \boldsymbol{A}\right)^{-1}\boldsymbol{B} + \boldsymbol{D} \tag{3.4}$$

and for a continuous-time state-space model:

$$\hat{\boldsymbol{H}}(\omega) = \boldsymbol{C}\left(j\omega\boldsymbol{I_n} - \boldsymbol{A}\right)^{-1}\boldsymbol{B} + \boldsymbol{D} \tag{3.5}$$

where $\boldsymbol{I_n}$ is the identity matrix of size n. Depending on the problem studied, different types of norms can be used to define the approximation error. At the same time, the identified models should be of low-order n, leading to a trade-off between complexity and accuracy.

This work also investigates the possibility to constrain the identified model to make its behavior closer to the true physical system. The identification procedures are numerical algorithms, so the existing MIMO identification techniques from frequency data will generally lead to identified poles that differ from the true aeroelastic poles. The most obvious effect comes from the fact that

even when the true system is stable, the identified model can be unstable, hence improper not only for simulations as the time response will diverge, but also for controller synthesis where the stabilization of the system will be a strong, unjustified, additional constraint. Another undesired effect of the bad identification of the aeroelastic poles is the fact that the physical interpretability is lost. For example, when studying the evolution of an unstable pole (flutter) and the design of its active stabilization, one wants to be sure that it is correctly represented by the model. This motivates the development of identification with constraints on the poles location, and with some known aeroelastic poles imposed to the identified state-space model. The poles can be estimated using the p-k method for example, described in section 2.3.8.

Remark 1. *The transfer function associated to a state-space model of order n has the same order n, defined as the order of the polynomial at the denominator. However, from a generic n-th order MIMO rational transfer function with N_u inputs and N_y outputs, a state-space system can be computed but it will have a higher order. It will be equal to $n\min(N_u, N_y)$ if the poles have a simple multiplicity and the residues are full-rank, as explained in more details in appendix A. The direct identification of rational transfer function based on data is then excluded as it would lead to high-order state-space systems.*

Section 3.2 first describes the classical identification by GAF rationalization. In section 3.3 two MIMO identification algorithms based on frequency data are presented: the Loewner interpolation method, and a subspace algorithm. Section 3.4 uses the same subspace framework with additional constraints on the poles location, and section 3.6 investigates methods for imposing known poles to the identified model, with and without constraints on the free poles. Finally section 3.7 presents the results of the validation and comparison of the presented methods on different sets of data. A summary of the techniques presented in this work and their main characteristics can be found in Table 3.1 in the results section, to help the reader keep track of the different methods.

3.2 Identification by GAF rationalization

A classical white-box procedure relies on a rational function approximation (RFA) of the GAFs $\boldsymbol{Q_{hh}}$, $\boldsymbol{Q_{h\delta}}$ and $\boldsymbol{Q_{hv}}$ of Eq. (2.41). Recalling that the GAFs depend on the reduced frequency $\kappa = \frac{\omega b}{\mathrm{TAS}}$, and on the Mach number, they can be assimilated to functions of the Laplace variable $s = j\omega$ at fixed Mach and TAS. A first type of rational approximation is given by the Roger approximation [Roger 1977] of an aerodynamic force matrix by the function:

$$\boldsymbol{F}(s) = \boldsymbol{F_0} + \boldsymbol{F_1}s + \boldsymbol{F_2}s^2 + \sum_{i=1}^{n_\gamma} \frac{\boldsymbol{F_{i+2}}s}{s+\gamma_i} \tag{3.6}$$

where n_γ is an integer parameter, the γ_i are real strictly positive parameters called delay coefficients. These parameters are imposed by the user, a high number of delay coefficients can lead to a better approximation of the aerodynamic force matrices but increase the model's order. The

$(\boldsymbol{F_i})_{i=0...n_\gamma+2}$ are real unknown matrices.

Another commonly used rationalization is the Karpel approximation function [Karpel 1982] of an aerodynamic force matrix by the function:

$$\boldsymbol{F}(s) = \boldsymbol{F_0} + \boldsymbol{F_1}s + \boldsymbol{F_2}s^2 + \boldsymbol{D}[s\boldsymbol{I_{n_\gamma}} - \boldsymbol{R}]^{-1}\boldsymbol{E}s \tag{3.7}$$

where $\boldsymbol{I_{n_\gamma}}$ is the identity matrix of size n_γ, $\boldsymbol{R}$ is a diagonal matrix of delay coefficients $(\gamma_i)_{i=1...n_\gamma}$ imposed by the user, and the matrices $(\boldsymbol{F_i})_{i=0...2}$, $\boldsymbol{D}$ and $\boldsymbol{E}$ are unknown matrices. The Karpel method generally leads to models of lower order than the Roger method.

In both the Roger and the Karpel approximation methods, the unknown parameters are obtained by minimizing the weighted least mean square error:

$$\min \sum_{i=1}^{N_k} \boldsymbol{\Omega_i} \left\| \boldsymbol{Q}(M, \frac{\omega_i b}{\mathrm{TAS}}) - \boldsymbol{F}(j\omega_i) \right\|_F \tag{3.8}$$

where the $(k_i)_{i=1...N_k}$ are the reduced frequencies at which GAF $\boldsymbol{Q}$ is known. The $(\boldsymbol{\Omega_i})_{i=1...N_k}$ are weights fixed by the user. The approximation is performed at a fixed Mach number. Some constraints can be included in the minimization process. For example, imposing that the value of the approximated function equals the true aerodynamic force value at $\kappa = 0$ leads to an improved low-frequency behavior.

The obtained transfer function maintains a physical interpretability, by defining aerodynamic inertia, damping and stiffness through matrices $\boldsymbol{F_2}$, $\boldsymbol{F_1}$ and $\boldsymbol{F_0}$ respectively, and adding aerodynamic delays terms that are always stable. When these rationalized GAFs with the rest of the aeroelastic Eq. (2.41), a state-space model can be obtained, with structured matrices $\boldsymbol{A}$, $\boldsymbol{B}$, $\boldsymbol{C}$ and $\boldsymbol{D}$. The states of this model are composed of the modal displacements, and additional delay states. The main drawback of these methods is the high number of states required to obtain a good approximation of the system's response, leading to ill-conditioned high-order models, better suited to system's analysis and simulations than control synthesis.

3.3 Identification of a MIMO state-space model from frequency data

3.3.1 Subspace identification methods

The idea of subspace methods is to find a realization of some data, namely to define a family of states that mathematically describes the data, without necessarily having a physical interpretation. The term "subspace" comes from the fact that a reduced number of states is wanted, leading to the search of low-dimensional subspaces in which the states evolve. The subspace methods are

efficient techniques that allow the identification of MIMO state-space models from time series composed of the measured outputs and known inputs of a given system. Several variants exist, among which the most famous are the Canonical Variate Analysis (CVA) proposed by [Larimore 1990], the N4SID by [Van Overschee and De Moor 1994], the MOESP by [Verhaegen and Dewilde 1992] and the observer-Kalman filter method (OKID) by [Phan et al. 1992]. While these methods have been developed using different strategies, they rely on similar procedures which all come down the singular value decomposition of a certain matrix with different possible weightings as demonstrated by [Van Overschee and De Moor 1995] and summarized in [Qin 2006]. The subspace methods estimate either the sequence of states of the identified model, or its observability (or similarly the controllability) matrix, leading in both cases to a state-space realization. In the latter case, after arranging the data into Hankel matrices, the influence of the known inputs can be removed by a projection onto the orthogonal space of the input Hankel matrix, leaving only an observability term and a noise term. The latter can be removed under certain assumptions (uncorrelated noise and enough measurements). Allowing to handle noisy data is a strength of the subspace techniques and an improvement compared to the ERA method which does not, in its initial formulation, include noise cancellation. Furthermore, the ERA method requires the known inputs to be impulsive, while the subspace methods apply to any sufficiently exciting sequence of inputs. Following the OKID viewpoint [Phan et al. 1992] and under the assumption of observability, a virtual Kalman filter with arbitrarily high gain can be included in the identification procedure to estimate the states sequence and limit the noise effects, while maintaining the poles in a region that preserves numerical issues from happening. Analogs of these methods can be defined when using frequency data as in the present work. Furthermore, when the data comes from simulations and not from measurements, the absence of noise can lead to very accurate identification. The technique proposed by McKelvey and Ljung in [McKelvey, Akcay, and Ljung 1996], a variant on MOESP, is used in this work to identify fixed-order MIMO state-space models based on frequency data, and will serve as basis for the development of new techniques in sections 3.5 and 3.6. Note that when applied to closed-loop identification, the subspace methods can face additional problems as pointed out in [Qin 2006]. However, the present work only focuses on open-loop identification.

Consider the discrete Laplace transform of the state-space model of Eq. (3.1) that is assumed to model the data:

$$\begin{cases} e^{j\omega}\boldsymbol{X}(j\omega) = \boldsymbol{A}\boldsymbol{X}(j\omega) + \boldsymbol{B}\boldsymbol{U}(j\omega) \\ \boldsymbol{Y}(j\omega) = \boldsymbol{C}\boldsymbol{X}(j\omega) + \boldsymbol{D}\boldsymbol{U}(j\omega) \end{cases} \tag{3.9}$$

where $\boldsymbol{X}$, $\boldsymbol{U}$ and $\boldsymbol{Y}$ are the Laplace or Fourier transforms of the state $\boldsymbol{x}$, input $\boldsymbol{u}$ and output $\boldsymbol{y}$ respectively. A unitary sampling time has been assumed without loss of generality. When considering the frequency response of this system at $q \geq n$ consecutive discrete sampling times, the following equation is obtained assuming that the data have been generated by the state-space

model of Eq. (3.1):

$$\begin{bmatrix} \boldsymbol{H}(\omega) \\ e^{j\omega}\boldsymbol{H}(\omega) \\ \vdots \\ e^{(q-1)j\omega}\boldsymbol{H}(\omega) \end{bmatrix} = \boldsymbol{\mathcal{O}}\boldsymbol{X}^{\boldsymbol{C}}(j\omega) + \boldsymbol{\Gamma} \begin{bmatrix} \boldsymbol{I}_{\boldsymbol{N_u}} \\ e^{j\omega}\boldsymbol{I}_{\boldsymbol{N_u}} \\ \vdots \\ e^{(q-1)j\omega}\boldsymbol{I}_{\boldsymbol{N_u}} \end{bmatrix} \tag{3.10}$$

where $\boldsymbol{H}$ is the impulse response of the system, the compound state matrix is defined as

$$\boldsymbol{X}^{\boldsymbol{C}}(j\omega) = \begin{bmatrix} \boldsymbol{X}^1(j\omega) & \boldsymbol{X}^2(j\omega) & \dots & \boldsymbol{X}^{N_u}(j\omega) \end{bmatrix} \in \mathbb{C}^{n \times N_u} \tag{3.11}$$

where $\boldsymbol{X}^i(j\omega)$ is the response of $\boldsymbol{X}(j\omega)$ to an impulse at input i. The matrix $\boldsymbol{\mathcal{O}}$ is a generalized observability matrix defined as

$$\boldsymbol{\mathcal{O}} = \begin{bmatrix} \boldsymbol{C} \\ \boldsymbol{CA} \\ \vdots \\ \boldsymbol{CA}^{q-1} \end{bmatrix} \in \mathbb{R}^{qN_y \times n} \tag{3.12}$$

The matrix $\boldsymbol{\Gamma}$ is the lower triangular block-Toeplitz matrix associated to the Markov parameters, and is defined as:

$$\boldsymbol{\Gamma} = \begin{bmatrix} \boldsymbol{D} & \boldsymbol{0} & \dots & \dots & \boldsymbol{0} \\ \boldsymbol{CB} & \boldsymbol{D} & \boldsymbol{0} & & \vdots \\ \boldsymbol{CAB} & \boldsymbol{CB} & \boldsymbol{D} & \ddots & \vdots \\ \vdots & \vdots & \vdots & \ddots & \boldsymbol{0} \\ \boldsymbol{CA}^{q-2}\boldsymbol{B} & \boldsymbol{CA}^{q-3}\boldsymbol{B} & \boldsymbol{CA}^{q-4}\boldsymbol{B} & \dots & \boldsymbol{D} \end{bmatrix} \in \mathbb{C}^{qN_y \times qN_u} \tag{3.13}$$

When evaluating Eq. (3.10) at N different frequencies $(\omega_i)_{i=1\dots N}$, the following equation is obtained:

$$\boldsymbol{\mathcal{H}} = \boldsymbol{\mathcal{O}}\boldsymbol{\mathcal{X}}^{\boldsymbol{C}} + \boldsymbol{\Gamma}\boldsymbol{\mathcal{U}} \tag{3.14}$$

with

$$\boldsymbol{\mathcal{X}}^{\boldsymbol{C}} = \begin{bmatrix} \boldsymbol{X}^{\boldsymbol{C}}(j\omega_1) & \boldsymbol{X}^{\boldsymbol{C}}(j\omega_2) & \dots & \boldsymbol{X}^{\boldsymbol{C}}(j\omega_N) \end{bmatrix} \in \mathbb{C}^{n \times N_u N} \tag{3.15}$$

$$\boldsymbol{\mathcal{H}} = \begin{bmatrix} \boldsymbol{H}(\omega_1) & \boldsymbol{H}(\omega_2) & \dots & \boldsymbol{H}(\omega_N) \\ e^{j\omega_1}\boldsymbol{H}(\omega_1) & e^{j\omega_2}\boldsymbol{H}(\omega_2) & \dots & e^{j\omega_N}\boldsymbol{H}(\omega_N) \\ \vdots & \vdots & \ddots & \vdots \\ e^{(q-1)j\omega_1}\boldsymbol{H}(\omega_1) & e^{(q-1)j\omega_2}\boldsymbol{H}(\omega_2) & \dots & e^{(q-1)j\omega_N}\boldsymbol{H}(\omega_N) \end{bmatrix} \in \mathbb{C}^{qN_y \times NN_u} \tag{3.16}$$

and

$$\boldsymbol{\mathcal{U}} = \begin{bmatrix} \boldsymbol{I}_{\boldsymbol{N_u}} & \boldsymbol{I}_{\boldsymbol{N_u}} & \dots & \boldsymbol{I}_{\boldsymbol{N_u}} \\ e^{j\omega_1}\boldsymbol{I}_{\boldsymbol{N_u}} & e^{j\omega_2}\boldsymbol{I}_{\boldsymbol{N_u}} & \dots & e^{j\omega_N}\boldsymbol{I}_{\boldsymbol{N_u}} \\ \vdots & \vdots & \ddots & \vdots \\ e^{(q-1)j\omega_1}\boldsymbol{I}_{\boldsymbol{N_u}} & e^{(q-1)j\omega_2}\boldsymbol{I}_{\boldsymbol{N_u}} & \dots & e^{(q-1)j\omega_N}\boldsymbol{I}_{\boldsymbol{N_u}} \end{bmatrix} \in \mathbb{C}^{qN_u \times NN_u} \tag{3.17}$$

The objective of such a formulation is to obtain from data the value of a generalized observability matrix of the system. This can be achieved by multiplying Eq. (3.14) from the right by an operator $\boldsymbol{\mathcal{U}}^{\perp}$ which projects onto the null space of $\boldsymbol{\mathcal{U}}$. It can be obtained as

$$\boldsymbol{\mathcal{U}}^{\perp} = \boldsymbol{I} - \boldsymbol{\mathcal{U}}^{T}(\boldsymbol{\mathcal{U}}\boldsymbol{\mathcal{U}}^{T})^{-1}\boldsymbol{\mathcal{U}} \tag{3.18}$$

Eq. (3.14) then becomes

$$\boldsymbol{\mathcal{H}}\boldsymbol{\mathcal{U}}^{\perp} = \boldsymbol{\mathcal{O}}\boldsymbol{\mathcal{X}}\boldsymbol{\mathcal{U}}^{\perp} \tag{3.19}$$

An estimated observability matrix can then be obtained by performing a singular value decomposition (SVD) of $\boldsymbol{\mathcal{H}}\boldsymbol{\mathcal{U}}^{\perp}$ and keeping only the right orthogonal vectors associated to the first n singular values, which is, by writing:

$$\boldsymbol{\mathcal{H}}\boldsymbol{\mathcal{U}}^{\perp} = \boldsymbol{V}\boldsymbol{\Sigma}\boldsymbol{W}^{*} \tag{3.20}$$

where $\boldsymbol{\Sigma}$ has the singular values on its diagonal and zeros elsewhere, $\boldsymbol{V}$ and $\boldsymbol{W}$ are unitary matrices ($\boldsymbol{V}\boldsymbol{V}^{*} = \boldsymbol{I}, \boldsymbol{W}\boldsymbol{W}^{*} = \boldsymbol{I}$), the superscript * representing the Hermitian (also called complex conjugate) transpose. The matrix $\hat{\boldsymbol{\mathcal{O}}} \in \mathbb{C}^{qN_y \times n}$ defined as the first n columns of $\boldsymbol{V}$ is then an estimate of the observability matrix of the system. Note that in order to obtain a real estimate of the observability matrix, one must replace $\boldsymbol{\mathcal{H}}$ by $[Re(\boldsymbol{\mathcal{H}}), Im(\boldsymbol{\mathcal{H}})]$ and similarly for $\boldsymbol{\mathcal{U}}$ and $\boldsymbol{\mathcal{X}}$ in Eq. (3.14).

Once an estimate $\hat{\boldsymbol{\mathcal{O}}}$ of the observability matrix for a certain realization of the state-space model has been computed, the corresponding matrix $\boldsymbol{C}$ is obtained as the first N_y rows as seen in the definition of the observability matrix in Eq. (3.12) and the matrix $\boldsymbol{A}$ is obtained as:

$$\boldsymbol{A} = \underline{\boldsymbol{\mathcal{O}}}^{\dagger}\overline{\boldsymbol{\mathcal{O}}} \tag{3.21}$$

where $\underline{\boldsymbol{\mathcal{O}}}$ and $\overline{\boldsymbol{\mathcal{O}}}$ are the matrices obtained by removing the last and first N_y rows of $\hat{\boldsymbol{\mathcal{O}}}$ respectively, and the superscript † denotes the Moore-Penrose pseudo-inverse.

When the matrices $\boldsymbol{A}$ and $\boldsymbol{C}$ are known, the dependence of the state-space's transfer function on matrices $\boldsymbol{B}$ and $\boldsymbol{D}$ is linear, they can be obtained as the solution of the following linear least square problem:

$$\min_{\boldsymbol{B},\boldsymbol{D}} \sum_{i=1}^{N} \left\| \boldsymbol{C}\left[e^{j\omega_i}\boldsymbol{I_N} - \boldsymbol{A}\right]^{-1}\boldsymbol{B} + \boldsymbol{D} - \boldsymbol{H}(\omega_i) \right\|_F^2 \tag{3.22}$$

This problem admits the following solution:

$$\begin{bmatrix} \boldsymbol{B} \\ \boldsymbol{D} \end{bmatrix} = \begin{bmatrix} \boldsymbol{M} \\ \overline{\boldsymbol{M}} \end{bmatrix}^{\dagger} \begin{bmatrix} \boldsymbol{Z} \\ \overline{\boldsymbol{Z}} \end{bmatrix} \tag{3.23}$$

where $\overline{\boldsymbol{M}}$ and $\overline{\boldsymbol{Z}}$ are the complex conjugates of $\boldsymbol{M}$ and $\boldsymbol{Z}$ respectively, which in turn are defined

as

$$\boldsymbol{M} = \begin{bmatrix} \boldsymbol{C}\left[e^{j\omega_1}\boldsymbol{I_N} - \boldsymbol{A}\right]^{-1} & \boldsymbol{I_{N_y}} \\ \vdots & \vdots \\ \boldsymbol{C}\left[e^{j\omega_N}\boldsymbol{I_N} - \boldsymbol{A}\right]^{-1} & \boldsymbol{I_{N_y}} \end{bmatrix} \in \mathbb{C}^{NN_y \times (n+N_y)} \tag{3.24}$$

and

$$\boldsymbol{Z} = \begin{bmatrix} \boldsymbol{H}(\omega_1) \\ \vdots \\ \boldsymbol{H}(\omega_N) \end{bmatrix} \in \mathbb{C}^{NN_y \times N_u} \tag{3.25}$$

With the matrices $\boldsymbol{A}$, $\boldsymbol{B}$, $\boldsymbol{C}$ and $\boldsymbol{D}$ defining the identified discrete-time state-space model with a unitary sampling time.

3.3.2 Loewner method

Another identification approach for MIMO systems, the Loewner method [Mayo and Antoulas 2007; Karachalios, Gosea, and Antoulas 2019], identifies a continuous-time state-space model based on frequency data. This method comes from the field of rational interpolation, and it looks for a state-space which perfectly matches the frequency data, as a first step. A reduction based on singular value decomposition is then performed, leading to a reduced-order model that approximates the data. The Loewner method is well suited to noiseless data.

The objective of the Loewner method is to find a MIMO rational transfer function $\hat{\boldsymbol{H}}(s)$ which interpolates two sets of data along left directions $[\boldsymbol{l_i}]_{i=1\ldots N_l}$ and right directions $[\boldsymbol{r_i}]_{i=1\ldots N_r}$ as follows:

$$\begin{cases} \boldsymbol{l_i}^T \hat{\boldsymbol{H}}(\lambda_i) = \boldsymbol{f_i}^T \\ \hat{\boldsymbol{H}}(\mu_i)\boldsymbol{r_i} = \boldsymbol{g_i} \end{cases} \tag{3.26}$$

In order to identify a state-space model, a particular version of this interpolation problem can be considered, in which the directions $\boldsymbol{r_i}$ and $\boldsymbol{l_i}$ are simply taken as the canonical directions $\boldsymbol{r_1} = \begin{bmatrix} 1 & 0 & \ldots & 0 \end{bmatrix}^T$, $\boldsymbol{r_2} = \begin{bmatrix} 0 & 1 & \ldots & 0 \end{bmatrix}^T$ and so on. The vectors $\boldsymbol{f_i}$ and $\boldsymbol{g_i}$ then correspond to the frequency response of the transfer function used to identify a system. The frequency data $[\boldsymbol{H}(\omega_i)]_{i=1\ldots N}$ are first split in two subsets of data associated to the left ω^l and right ω^r frequency sets:

$$[\omega_i, \boldsymbol{H}(\omega_i)]_{i=1\ldots N} \quad \rightarrow \quad \left[\omega_i^l, \boldsymbol{H}(\omega_i^l)\right]_{i=1\ldots N_l} \cup [\omega_i^r, \boldsymbol{H}(\omega_i^r)]_{i=1\ldots N_r} \tag{3.27}$$

in such a way that $\lambda_i = j\omega_i^l$ and $\mu_i = j\omega_i^r$, and that the vectors $\boldsymbol{f_i}$ and $\boldsymbol{g_i}$ can be stacked into a matrix form:

$$\boldsymbol{F} = \begin{bmatrix} \boldsymbol{f_1}^T \\ \vdots \\ \boldsymbol{f_{N_l N_y}}^T \end{bmatrix} = \begin{bmatrix} \boldsymbol{H}(\omega_1^l) \\ \vdots \\ \boldsymbol{H}(\omega_{N_l}^l) \end{bmatrix} \in \mathbb{C}^{N_l N_y \times N_u} \tag{3.28}$$

and

$$\boldsymbol{G} = \begin{bmatrix} \boldsymbol{g_1} & \dots & \boldsymbol{g_{N_r N_u}} \end{bmatrix} = \begin{bmatrix} \boldsymbol{H}(\omega_1^r) & \dots & \boldsymbol{H}(\omega_{N_r}^r) \end{bmatrix} \in \mathbb{C}^{N_y \times N_r N_u} \tag{3.29}$$

Similarly, the interpolation directions $\boldsymbol{l_i}$ and $\boldsymbol{r_i}$ can be stacked into matrices:

$$\boldsymbol{L} = \begin{bmatrix} \boldsymbol{l_1}^T \\ \vdots \\ \boldsymbol{l_{N_l N_y}}^T \end{bmatrix} = \begin{bmatrix} \boldsymbol{I_{N_y}} \\ \vdots \\ \boldsymbol{I_{N_y}} \end{bmatrix} \in \mathbb{C}^{N_l N_y \times N_y} \tag{3.30}$$

and

$$\boldsymbol{R} = \begin{bmatrix} \boldsymbol{r_1} & \dots & \boldsymbol{r_{N_r N_u}} \end{bmatrix} = \begin{bmatrix} \boldsymbol{I_{N_u}} & \dots & \boldsymbol{I_{N_u}} \end{bmatrix} \in \mathbb{C}^{N_u \times N_r N_u} \tag{3.31}$$

In order to find a function $\hat{\boldsymbol{H}}$ which satisfies the interpolation (3.26), the Loewner matrix is defined as

$$\mathbb{L} = \begin{bmatrix} \frac{\boldsymbol{H}(\omega_1^l) - \boldsymbol{H}(\omega_1^l)}{\omega_1^l - \omega_1^r} & \dots & \frac{\boldsymbol{H}(\omega_1^l) - \boldsymbol{H}(\omega_{N_r}^r)}{\omega_1^l - \omega_{N_r}^r} \\ \vdots & \ddots & \vdots \\ \frac{\boldsymbol{H}(\omega_{N_l}^l) - \boldsymbol{H}(\omega_1^l)}{\omega_{N_l}^l - \omega_1^r} & \dots & \frac{\boldsymbol{H}(\omega_{N_l}^l) - \boldsymbol{H}(\omega_{N_r}^r)}{\omega_{N_l}^l - \omega_{N_r}^r} \end{bmatrix} \in \mathbb{C}^{N_l N_y \times N_r N_u} \tag{3.32}$$

and the shifted Loewner matrix as:

$$\mathbb{L}_\sigma = \begin{bmatrix} \frac{\omega_1^l \boldsymbol{H}(\omega_1^l) - \omega_1^r \boldsymbol{H}(\omega_1^l)}{\omega_1^l - \omega_1^r} & \dots & \frac{\omega_1^l \boldsymbol{H}(\omega_1^l) - \omega_{N_r}^r \boldsymbol{H}(\omega_{N_r}^r)}{\omega_1^l - \omega_{N_r}^r} \\ \vdots & \ddots & \vdots \\ \frac{\omega_{N_l}^l \boldsymbol{H}(\omega_{N_l}^l) - \omega_1^r \boldsymbol{H}(\omega_1^l)}{\omega_{N_l}^l - \omega_1^r} & \dots & \frac{\omega_{N_l}^l \boldsymbol{H}(\omega_{N_l}^l) - \omega_{N_r}^r \boldsymbol{H}(\omega_{N_r}^r)}{\omega_{N_l}^l - \omega_{N_r}^r} \end{bmatrix} \in \mathbb{C}^{N_l N_y \times N_r N_u} \tag{3.33}$$

The main results of the Loewner method is that the quadruple $(\mathbb{L}_\sigma, \mathbb{L}, \boldsymbol{F}, \boldsymbol{G})$ defining the MIMO transfer function

$$\hat{\boldsymbol{H}}(s) = \boldsymbol{G}(\mathbb{L}_\sigma - s\mathbb{L})^{-1}\boldsymbol{F} \tag{3.34}$$

satisfies the interpolation problem (3.26) as long as there exists at least one complex value λ such that $\det(\mathbb{L}_\sigma - \lambda\mathbb{L}) \neq 0$ [Antoulas, Lefteriu, and Ionita 2017]. Another important result is the fact that the Loewner quadruple satisfies the Sylvester equations:

$$\begin{cases} \boldsymbol{M}\mathbb{L} - \mathbb{L}\boldsymbol{\Lambda} = \boldsymbol{F}\boldsymbol{R} - \boldsymbol{L}\boldsymbol{G} \\ \boldsymbol{M}\mathbb{L}_\sigma - \mathbb{L}_\sigma\boldsymbol{\Lambda} = \boldsymbol{M}\boldsymbol{F}\boldsymbol{R} - \boldsymbol{L}\boldsymbol{G}\boldsymbol{\Lambda} \end{cases} \tag{3.35}$$

where the $\boldsymbol{\Lambda}$ and $\boldsymbol{M}$ are diagonal matrices with λ_i and μ_i on their respective diagonals. Although this result is not directly used in the Loewner method for system identification, it can be a useful theoretical result that generalizes the interpolation problem (3.26). For given matrices $\boldsymbol{M}$, $\boldsymbol{\Lambda}$, $\boldsymbol{F}$, $\boldsymbol{G}$, $\boldsymbol{R}$ and $\boldsymbol{L}$ of adequate sizes, the Sylvester equations (3.35) can be seen as an interpolation problem, which admits a unique solution doublet $(\mathbb{L}, \mathbb{L}_\sigma)$ provided that matrices $\boldsymbol{\Lambda}$ and $\boldsymbol{M}$ do not have common eigenvalues.

A reduction of the transfer function obtained with the Loewner method can be performed

using a singular value decomposition of the horizontally appended Loewner and shifted Loewner matrices:

$$\begin{bmatrix} \mathbb{L} & \mathbb{L}_\sigma \end{bmatrix} \approx \boldsymbol{V}\boldsymbol{\Sigma}_{\boldsymbol{l}}\tilde{\boldsymbol{W}}^* \tag{3.36}$$

where only the first n singular values are kept, which will define the order of the identified state-space model. The value of n can be taken as the rank of the Loewner matrix $\mathbb{L}$. In this case, assuming enough data are available, it defines the McMillan degree of the system [Mayo and Antoulas 2007] which is the order of a minimal realization in case the system is causal. Practically, n can be set by the user to identify a reduced-order model. The same is done with the vertically appended matrices:

$$\begin{bmatrix} \mathbb{L} \\ \mathbb{L}_\sigma \end{bmatrix} \approx \tilde{\boldsymbol{V}}\boldsymbol{\Sigma}_{\boldsymbol{r}}\boldsymbol{W}^* \tag{3.37}$$

The following matrices can then be recovered:

$$\boldsymbol{E} = -\boldsymbol{V}^*\mathbb{L}\boldsymbol{W} \tag{3.38}$$

$$\boldsymbol{A} = -\boldsymbol{V}^*\mathbb{L}_\sigma\boldsymbol{W} \tag{3.39}$$

$$\boldsymbol{B} = \boldsymbol{V}^*\boldsymbol{F} \tag{3.40}$$

$$\boldsymbol{C} = \boldsymbol{G}\boldsymbol{W} \tag{3.41}$$

defining the identified continuous-time descriptor state-space model

$$\begin{cases} \boldsymbol{E}\dot{\boldsymbol{x}} = \boldsymbol{A}\boldsymbol{x} + \boldsymbol{B}\boldsymbol{u} \\ \boldsymbol{y} = \boldsymbol{C}\boldsymbol{x} \end{cases} \tag{3.42}$$

As explained in [Antoulas, Lefteriu, and Ionita 2017] the $\boldsymbol{D}$ matrix is incorporated in the other matrices defining the descriptor model, and can be extracted from them. To the author's knowledge, the procedure to recover $\boldsymbol{D}$ has not been accurately described in the literature. We propose a solution in appendix B in the case the system is causal and does not include integrators. Note that by following the procedure presented above, the matrices defining the model are complex. Real matrices are obtained by splitting the frequency response data $\boldsymbol{H}$ into their real and imaginary parts. To the author's knowledge, there is no clear study of the optimal way to split the data into two subsets in the literature.

3.4 MIMO identification with poles locations constraints

3.4.1 Subspace identification with poles locations constraints

The subspace identification algorithm or the Loewner method described in section 3.3 do not ensure the stability of the identified state-space model. Even when the true system is stable, a reduced-order state-space model may contain unstable poles. It will lead to diverging time simulations and

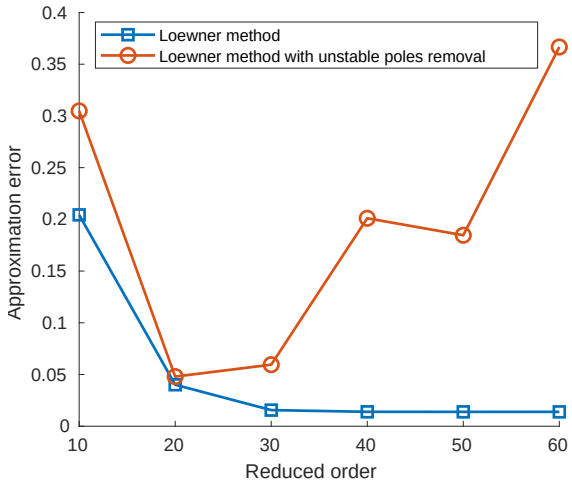

Figure 3.1: Approximation error with and without unstable poles removal using the Loewner method

can cause problems when used for the design of a controller, for instance. For this reason, it is common to simply remove the unstable poles from the identified model as studied in [Köhler 2014]. This post-analysis can lead to a poor approximation capability when the identified model includes a high number of unstable modes. This is illustrated in Fig. 3.1 where aeroelastic data have been approximated by models of variable reduced orders obtained by the Loewner method, with and without removing the unstable poles. It can be seen that for an adequate choice of the model's reduced order (20 here), artificially imposing the stability in post-analysis leads to a satisfactory result. However, when increasing the reduced order, the model contains more artificial unstable poles and removing them causes the approximation error to increase. It is not only sub-optimal, but it also requires a good a-priori knowledge of the system to obtain a good approximation. This limitation motivates the development of dedicated techniques, in which the stability constraint is part of the identification process, and not imposed a-posteriori.

[Lacy and Bernstein 2003] presents an identification algorithm based on subspace methods to impose stability to the state-space model, using convex optimization. The work of [Miller and De Callafon 2013] proposed a state-space identification algorithm based on convex optimization in which the location of the poles are constrained in a similar way as done in [Chilali and Gahinet 1996] for H_∞ synthesis. In this section this technique is presented as an introduction to the methods developed in this work.

Starting from an estimate $\hat{\boldsymbol{\mathcal{O}}}$ of the observability matrix of the system, the objective is to find matrices $\boldsymbol{A}$ and $\boldsymbol{C}$ that generate an observability matrix close to $\hat{\boldsymbol{\mathcal{O}}}$ with eigenvalues of $\boldsymbol{A}$ lying in a region of the following class:

$$\mathcal{D}^{\boldsymbol{\alpha},\boldsymbol{\beta}} = \left\{ z \in \mathbb{C} \,:\, \boldsymbol{\alpha} + \boldsymbol{\beta} z + \boldsymbol{\beta}^T \overline{z} \succeq \mathbf{0} \right\} \tag{3.43}$$

where $\boldsymbol{\alpha}$ is a real symmetric matrix, $\boldsymbol{\beta}$ is a real square matrix, the $\succeq \mathbf{0}$ notation denotes matrix

definite positivity and $\overline{z}$ is the complex conjugate of z. This class includes the unit disk plane and the left half plane to ensure stability of discrete-time and continuous-time systems respectively.

It is shown in [Chilali and Gahinet 1996] that the eigenvalues of a matrix $\boldsymbol{A} \in \mathbb{C}^{n\times n}$ lie within a region $\mathcal{D}^{\boldsymbol{\alpha},\boldsymbol{\beta}}$ defined in Eq. (3.43) if and only if there exists a matrix $\boldsymbol{P} \in \mathbb{R}^{n\times n}$ such that $\boldsymbol{P} = \boldsymbol{P}^T \succ \boldsymbol{0}$ and

$$\boldsymbol{\alpha} \otimes \boldsymbol{P} + \boldsymbol{\beta} \otimes \boldsymbol{AP} + \boldsymbol{\beta}^T \otimes (\boldsymbol{AP})^T \succeq \boldsymbol{0} \tag{3.44}$$

where the $\otimes$ symbol denotes the Kronecker product. A matrix $\boldsymbol{A}$ can be obtained by the following optimization problem:

$$\min_{\boldsymbol{A},\boldsymbol{P}} \left\| \underline{\boldsymbol{\mathcal{O}}}\boldsymbol{AP} - \overline{\boldsymbol{\mathcal{O}}}\boldsymbol{P} \right\|_F \tag{3.45}$$

$$\text{subject to} \begin{cases} \boldsymbol{\alpha} \otimes \boldsymbol{P} + \boldsymbol{\beta} \otimes \boldsymbol{AP} + \boldsymbol{\beta}^T \otimes (\boldsymbol{AP})^T \succeq \boldsymbol{0} \\ \boldsymbol{P} = \boldsymbol{P}^T \succ \boldsymbol{0} \end{cases} \tag{3.46}$$

The cost function and the inequality constraint contain a non-convex term $\boldsymbol{AP}$ which can be removed by defining the variable $\boldsymbol{Q} = \boldsymbol{AP}$, leading to the following convex formulation:

$$\min_{\boldsymbol{Q},\boldsymbol{P}} \left\| \underline{\boldsymbol{\mathcal{O}}}\boldsymbol{Q} - \overline{\boldsymbol{\mathcal{O}}}\boldsymbol{P} \right\|_F \tag{3.47}$$

$$\text{subject to} \begin{cases} \boldsymbol{\alpha} \otimes \boldsymbol{P} + \boldsymbol{\beta} \otimes \boldsymbol{Q} + \boldsymbol{\beta}^T \otimes \boldsymbol{Q}^T \succeq \boldsymbol{0} \\ \boldsymbol{P} = \boldsymbol{P}^T \succ \boldsymbol{0} \end{cases} \tag{3.48}$$

An additional constraints such as $tr(\boldsymbol{P})$ is added to avoid solutions of arbitrarily low norm. The idea behind this formulation is to modify the unconstrained problem, in which the matrix $\boldsymbol{A}$ was obtained in Eq. (3.21) using a least-square problem, by a problem with constraints in which the matrix $\boldsymbol{A}$ is found by approximating the unconstrained solution. The change of variable then leads to an optimization problem which can be solved efficiently using convex optimization techniques. We can then compute $\boldsymbol{A} = \boldsymbol{QP}^{-1}$ as $\boldsymbol{P}$ is positive definite. The matrix $\boldsymbol{C}$ is then obtained as the first N_y rows of $\hat{\boldsymbol{\mathcal{O}}}$, and the matrices $\boldsymbol{B}$ and $\boldsymbol{D}$ can be calculated similarly as in Eq. (3.22).

3.4.2 Loewner method with poles locations constraints

To the author's knowledge, there is no example in the literature of methods imposing stability with the Loewner system identification. Instead, the unstable are generally simply removed after the identification process, or a procedure such as the one described in [Köhler 2014] can be applied to find the closest stable state-space system in the RH_2 or RH_∞ sense. In any case, the stability is applied in post-analysis, and this can lead to a loss of modeling accuracy compare to an identification process which includes stability constraints, such as the one described in section 3.4.1 with a subspace method. This section proposes a similar procedure to apply stability in the Loewner framework.

By looking at the subspace identification method with constraints on the poles, the function to minimize can be re-written assuming that the matrix $\underline{\boldsymbol{\mathcal{O}}}$ is full column rank and for $\boldsymbol{P}$ invertible:

$$\underset{\boldsymbol{A}}{\operatorname{argmin}} \left\| \underline{\boldsymbol{\mathcal{O}}} \boldsymbol{A} \boldsymbol{P} - \overline{\boldsymbol{\mathcal{O}}} \boldsymbol{P} \right\|_F = \underset{\boldsymbol{A}}{\operatorname{argmin}} \left\| \boldsymbol{A} \boldsymbol{P} - \underline{\boldsymbol{\mathcal{O}}}^{\dagger} \overline{\boldsymbol{\mathcal{O}}} \boldsymbol{P} \right\|_F = \underline{\boldsymbol{\mathcal{O}}}^{\dagger} \overline{\boldsymbol{\mathcal{O}}} \tag{3.49}$$

This implies that, in this case, the matrix $\boldsymbol{A}$ is simply found as the one that minimizes the error with the "ideal" matrix $\underline{\boldsymbol{\mathcal{O}}}^{\dagger} \overline{\boldsymbol{\mathcal{O}}}$ which is the one obtained with the subspace algorithm presented in section 3.3.1, in absence of poles location constraints. Note that the estimate of the observability matrix, $\hat{\boldsymbol{\mathcal{O}}}$, is full column rank if the reduced model order n is lower than rank($\boldsymbol{\mathcal{H}} \boldsymbol{\mathcal{U}}^{\perp}$). $\underline{\boldsymbol{\mathcal{O}}}$ is obtained by removing the last N_y rows from $\hat{\boldsymbol{\mathcal{O}}}$, and is therefore also an estimate of the observability matrix. It is then full column rank when the arbitrary q is higher than $n+1$.

As a consequence, a similar procedure can be applied to identify a stable state-space using the Loewner method. First, the matrices $\boldsymbol{A_0}$, $\boldsymbol{B_0}$, $\boldsymbol{C_0}$ and $\boldsymbol{D_0}$ are obtained with the Loewner method without poles location constraints. Then, a matrix $\boldsymbol{A}$ is found by solving

$$\min_{\boldsymbol{A}, \boldsymbol{P}} \left\| \boldsymbol{A} \boldsymbol{P} - \boldsymbol{A_0} \boldsymbol{P} \right\|_F \tag{3.50}$$

$$\text{subject to} \begin{cases} \boldsymbol{\alpha} \otimes \boldsymbol{P} + \boldsymbol{\beta} \otimes \boldsymbol{A} \boldsymbol{P} + \boldsymbol{\beta}^T \otimes (\boldsymbol{A} \boldsymbol{P})^T \succeq \boldsymbol{0} \\ \boldsymbol{P} = \boldsymbol{P}^T \succ \boldsymbol{0} \end{cases} \tag{3.51}$$

where the matrix parameters $\boldsymbol{\alpha}$ and $\boldsymbol{\beta}$ define constraints $\mathcal{D}^{\boldsymbol{\alpha}, \boldsymbol{\beta}}$ of the continuous poles. The matrices $\boldsymbol{C}$ is then equal to $\boldsymbol{C_0}$, and the matrices $\boldsymbol{B}$ and $\boldsymbol{D}$ can be obtained by similar procedure as described in Eq. (3.22), changing the $e^{j\omega}$ into $j\omega$ to deal with continuous-time data.

3.5 MIMO identification with imposed poles

This section presents a new approach for the hybrid identification of a state-space model, where some poles are imposed and the remaining poles are free parameters. A method to obtain a state-space model whose poles are all known beforehand is described [Tang, Wu, and Shi 2017]. We generalize this procedure to the case in which some poles are unknown, in order to give additional degrees of freedom to the identification, and better fit to the frequency data. Moreover, in most real-life applications, a small portion of the true system's poles is known, like in the aeroelastic equations presented in section 3.1.2. An alternative to this method is obtained by working on the parameters defining the MIMO transfer function. This presents two main disadvantages: first, this involves operations on polynomials, that present numerical issues when the order increases. Secondly, by fixing the transfer function order to n, the associated state-space model will be of order $\min(nN_y, nN_u)$ with n distinct poles (under some assumptions detailed in appendix A). For this reason, the transfer function approach will not be applied in the results section.

We start by estimating an observability matrix $\hat{\mathcal{O}}$ using the subspace algorithm described in

section 3.3.1. We assume that the poles of the system have an algebraic multiplicity of 1. We first impose some poles $(\bar{\lambda_i})_{i=1...\bar{n}}$ and compute the associated eigenvectors $\bar{\boldsymbol{p_i}}$ by noting that:

$$\hat{\boldsymbol{\mathcal{O}}}\bar{\boldsymbol{p_i}} = \begin{bmatrix} \boldsymbol{C}\bar{\boldsymbol{p_i}} \\ \boldsymbol{C}\boldsymbol{A}\bar{\boldsymbol{p_i}} \\ \vdots \\ \boldsymbol{C}\boldsymbol{A}^{n-1}\bar{\boldsymbol{p_i}} \end{bmatrix} = \begin{bmatrix} \boldsymbol{C} \\ \bar{\lambda_i}\boldsymbol{C} \\ \vdots \\ \bar{\lambda_i}^{n-1}\boldsymbol{C} \end{bmatrix} \bar{\boldsymbol{p_i}} \tag{3.52}$$

For each pole $\bar{\lambda_i}$ a corresponding eigenvector can be found as $\bar{\boldsymbol{p_i}} \in \ker(\tilde{\boldsymbol{\mathcal{O}}})$ where ker refers to the null space of a matrix and

$$\tilde{\boldsymbol{\mathcal{O}}} = \hat{\boldsymbol{\mathcal{O}}} - \begin{bmatrix} \boldsymbol{C} \\ \bar{\lambda_i}\boldsymbol{C} \\ \vdots \\ \bar{\lambda_i}^{n-1}\boldsymbol{C} \end{bmatrix} \tag{3.53}$$

When all the $\bar{n}$ column eigenvectors $\bar{\boldsymbol{p_i}}$ have been obtained, they can be assembled into a matrix $\bar{\boldsymbol{P}}$ such that the matrix $\boldsymbol{A}$ verifies

$$\boldsymbol{A}\begin{bmatrix} \bar{\boldsymbol{P}} & \boldsymbol{P} \end{bmatrix} = \begin{bmatrix} \bar{\boldsymbol{\Lambda}} & 0 \\ 0 & \boldsymbol{\Lambda} \end{bmatrix} \begin{bmatrix} \bar{\boldsymbol{P}} & \boldsymbol{P} \end{bmatrix} \tag{3.54}$$

where $\bar{\boldsymbol{P}}$ and $\bar{\boldsymbol{\Lambda}}$ are known. The objective is to find the unknown eigenvalues λ_i and their associated eigenvectors $\boldsymbol{p_i}$ that best approximate the data and such that $\begin{bmatrix} \bar{\boldsymbol{P}} & \boldsymbol{P} \end{bmatrix}$ is invertible.

There is no guarantee that a family of $\bar{n}$ independent vectors $\bar{\boldsymbol{p_i}}$ can be found in the null space of $\tilde{\boldsymbol{\mathcal{O}}}$, whose dimension can be zero. Vectors $\bar{\boldsymbol{p_i}}$ such that $\tilde{\boldsymbol{\mathcal{O}}}\bar{\boldsymbol{p_i}} \approx \boldsymbol{0}$ can be obtained by the singular value decomposition of $\tilde{\boldsymbol{\mathcal{O}}} = \boldsymbol{V}\boldsymbol{\Sigma}\boldsymbol{W}^*$ and taking the last column of $\boldsymbol{W}$, that is the right vector associated to the minimum singular value. No mention is done in [Tang, Wu, and Shi 2017] of why the matrix composed of the eigenvectors $\bar{\boldsymbol{p_i}}$ should be invertible but for each pole $\bar{\lambda_i}$, if the last column of $\boldsymbol{W}$ does not make the rank of $\boldsymbol{P}$ increase, then the previous column can be used instead and so on, until the assembled matrix has full rank.

By making the assumption that the column vectors $\boldsymbol{p_i}$ that compose the matrix $\boldsymbol{P}$ are orthogonal to the previously imposed $\bar{\boldsymbol{p_i}}$, we can find the remaining eigenvectors $\boldsymbol{p_i}$ by decomposing them on a basis of the orthogonal subspace to $\text{span}([\bar{\boldsymbol{p_i}}]_{i=1...\bar{n}})$. We first obtain such a basis by finding $\boldsymbol{e_i} \in \ker(\bar{\boldsymbol{P}}^*)$, by singular value decomposition for example, taking $\boldsymbol{e_i}$ as right column vectors corresponding to singular values equal to zero. Note that this basis is orthogonal. Since $\bar{\boldsymbol{P}}$ is of rank $\bar{n}$ and $\bar{\boldsymbol{P}} \in \boldsymbol{C}^{n\times\bar{n}}$, there exist exactly $n-\bar{n}$ singular values of $\bar{\boldsymbol{P}}^*$ equal to zero. We look for the coefficients k_{ij} which verify

$$\boldsymbol{p_j} = \sum_{i=1}^{n-\bar{n}} k_{ij}\boldsymbol{e_i} \tag{3.55}$$

which is, by assembling the vectors $\boldsymbol{e_i}$ and the coefficients k_{ij} into matrices $\boldsymbol{E}$ and $\boldsymbol{K}$,

$$\boldsymbol{P} = \boldsymbol{E}\boldsymbol{K} \tag{3.56}$$

with $\boldsymbol{E} \in \mathbb{C}^{n\times(n-\bar{n})}$ and $\boldsymbol{K} \in \mathbb{C}^{(n-\bar{n})\times(n-\bar{n})}$. We then recall from section 3.3 that $\underline{\boldsymbol{\mathcal{O}}}\boldsymbol{A} = \overline{\boldsymbol{\mathcal{O}}}$ hence, after right multiplying by the eigenvector $\boldsymbol{p_j} = \boldsymbol{E}\boldsymbol{k_j}$, it results in solving the generalized eigenvalues problem

$$\overline{\boldsymbol{\mathcal{O}}}\boldsymbol{E}\boldsymbol{k_j} = \lambda_j \underline{\boldsymbol{\mathcal{O}}}\boldsymbol{E}\boldsymbol{k_j} \qquad j = 1 \dots n-\bar{n} \tag{3.57}$$

where the $\boldsymbol{k_j}$ are columns of $\boldsymbol{K}$. Since $\underline{\boldsymbol{\mathcal{O}}}$ is full-column-rank, from Sylvester inequality $\text{rank}(\underline{\boldsymbol{\mathcal{O}}}\boldsymbol{E}) = \text{rank}(\boldsymbol{E}) = n - \bar{n}$. Hence, this comes down to an eigenvalue problem:

$$[\underline{\boldsymbol{\mathcal{O}}}\boldsymbol{E}]^{\dagger}\,\overline{\boldsymbol{\mathcal{O}}}\boldsymbol{E}\boldsymbol{k_j} = \lambda_j \boldsymbol{k_j} \qquad j = 1 \dots n-\bar{n} \tag{3.58}$$

the pseudo-eigenvectors $\boldsymbol{p_j}$ are then recovered as $\boldsymbol{p_j} = \boldsymbol{E}\boldsymbol{k_j}$. The matrix $\begin{bmatrix}\bar{\boldsymbol{P}} & \boldsymbol{P}\end{bmatrix}$ is invertible because both $\bar{\boldsymbol{P}}$ and $\boldsymbol{P}$ are full rank and satisfy an the orthogonality constraint. The matrix $\boldsymbol{A}$ can then be computed with Eq. (3.54), the matrix $\boldsymbol{C}$ is obtained as the first N_y rows of $\hat{\boldsymbol{\mathcal{O}}}$, and the matrices $\boldsymbol{B}$ and $\boldsymbol{D}$ can be calculated similarly as in Eq. (3.22). This method will be referred to as the System Identification with Orthogonal eigenvectors (SIDORT) method.

3.6 MIMO identification with imposed poles and locations constraints

3.6.1 Subspace identification by Pseudo-Eigenvalue problem (SIDPEV)

If the assumption of orthogonality of the unknown eigenvectors is dropped, the matrix $\boldsymbol{P}$ of the generalized eigenvalue problem (3.57) can be obtained by a non-convex optimization. We first obtain the eigenvectors $\bar{\boldsymbol{P}}$ associated to the imposed poles in a similar way as done in section 3.5. The matrix $\boldsymbol{P}$ associated to the unknown eigenvectors can then be obtained iteratively, by solving the following optimization for each unknown eigenvector successively:

$$\text{For } i = 1 \dots n-\bar{n} \tag{3.59}$$

$$\min_{\boldsymbol{p_i},\lambda_i} \left\| \underline{\boldsymbol{\mathcal{O}}}^{\dagger}\overline{\boldsymbol{\mathcal{O}}}\boldsymbol{p_i} - \lambda_i \boldsymbol{p_i} \right\|_2 \tag{3.60}$$

$$\text{s.t.} \begin{cases} \text{rank}(\begin{bmatrix}\bar{\boldsymbol{P}} & \boldsymbol{P_i}\end{bmatrix}) = \bar{n} + i \\ \lambda_i \in \mathcal{D}^{\boldsymbol{\alpha},\boldsymbol{\beta}} \\ \|\boldsymbol{p_i}\| = 1 \end{cases} \tag{3.61}$$

where $\boldsymbol{P_i} \in \mathbb{C}^{n\times i}$ is the matrix containing the first i eigenvectors computed so far, including the unknown vector $\boldsymbol{p_i}$, and the sets $\mathcal{D}^{\boldsymbol{\alpha},\boldsymbol{\beta}}$ have been defined in section 3.4. A constraint $\|\boldsymbol{p_i}\| = 1$

is added to avoid trivial solutions. This optimization problem can be approximated by a Bilinear Matrix Inequality problem by relaxing the rank constraint into a constraint of the type $[\bar{\boldsymbol{P}}\,\boldsymbol{P_i}]^*[\bar{\boldsymbol{P}}\,\boldsymbol{P_i}] \succ \boldsymbol{0}$. Otherwise, the problem can be solved by a nonlinear optimization with constraint method, such as the interior-point method [Byrd, Hribar, and Nocedal 1999; Waltz et al. 2006], with the nonlinear rank constraint expressed as a positive lower bound on the matrix minimum singular value for example. The latter option is preferred for its robustness. It can be seen that the gradient of the objective function with respect to the variables is easily computed. Furthermore, each eigenvalue/eigenvector pair is computed independently, so each optimization problem has a low number of variables which makes the method not too computationally intensive.

3.6.2 Direct Nonlinear Optimization with Constraints (DNOC)

The methods exposed previously aim at decomposing the general problem of state space model identification with imposed poles and constraints on the unknown poles in a way that limits the computational cost. By doing so, errors due to over-constraining hypotheses or to suboptimal solutions can accumulate and increase the approximation error. Another strategy consists in solving the different steps simultaneously by a single optimization.

A direct identification of a state space model with imposed poles and constraints on the unknown poles can be obtained by looking for the identified model in its modal canonical form and solving the following non-convex optimization problem with constraints:

$$\min_{\substack{\lambda_i,\boldsymbol{B},\boldsymbol{C},\boldsymbol{D}\\ i=1\ldots n-\bar{n}}} \sum_{k=1}^{N} \left\| \boldsymbol{C}\left[e^{j\omega_k}\boldsymbol{I_n} - \boldsymbol{A}(\lambda)\right]^{-1}\boldsymbol{B} + \boldsymbol{D} - \boldsymbol{H}(\omega_k)\right\|_F^2 \tag{3.62}$$

$$\text{s.t. } \lambda_i \in \mathcal{D}^{\boldsymbol{\alpha},\boldsymbol{\beta}} \tag{3.63}$$

with

$$\boldsymbol{A}(\lambda) = \begin{bmatrix} \boldsymbol{\Psi}(\bar{\lambda}_1) & & & & & \\ & \ddots & & & 0 & \\ & & \boldsymbol{\Psi}(\bar{\lambda}_{\bar{n}}) & & & \\ & & & \boldsymbol{\Psi}(\lambda_1) & & \\ & 0 & & & \ddots & \\ & & & & & \boldsymbol{\Psi}(\lambda_{n-\bar{n}}) \end{bmatrix} \tag{3.64}$$

and

$$\bar{\boldsymbol{\Psi}}(\lambda) = \begin{bmatrix} Re(\bar{\lambda}) & Im(\bar{\lambda}) \\ -Im(\bar{\lambda}) & Re(\bar{\lambda}) \end{bmatrix} \tag{3.65}$$

The matrices $\boldsymbol{A}$, $\boldsymbol{B}$, $\boldsymbol{C}$ and $\boldsymbol{D}$ are obtained simultaneously, by an interior-point algorithm [Byrd, Hribar, and Nocedal 1999; Waltz et al. 2006] for example. The computational cost is expected to be higher than with the other methods described above, because of the high number of variables

and the non-convexity of the optimization. Because of the non-convex nature of the problem, solvers such as the interior-point method do not guarantee the convergence to a global minimum.

For example, with the above formulation and when only the poles stability is wanted, the free poles must lie within the complex unit circle, and can be parameterized by the modulus and angle, with a constraint on the former. The search space can be reduced to the half plane by looking only to positive imaginary values, and adding the complex conjugate in the matrix $\boldsymbol{A}$. If a continuous-time model is desired, the poles can be parameterized by their real and imaginary values, imposing the former to have negative values. The search space can also be reduced, by considering poles with frequency not higher than the maximum data frequency. After experimenting with the two approaches, the discrete-time formulation has proved more efficient and will be used in the results section. Note that this nonlinear optimization problem with constraints can be transformed into an unconstrained problem in some cases. In the case of stability of a discrete-time model, the modulus of the unknown poles can be taken as the output of a bijective function $f : \mathbb{R} \to [0, 1]$ such as the sigmoid function. Using initial conditions from the result of a numerically simpler algorithm (like the SIDPEV described in section 3.6.1) is not advised, as it can correspond to a local minimum. Rather, random initial conditions close to unity are preferred in this work.

3.7 Numerical Results: identification with imposed and constrained poles

3.7.1 Validation scenarios

The methods described in this paper will be tested in different conditions in the next sections. The objectives that are expected to be fulfilled by the results are the following:

1. Compare the ability to identify a MIMO model of the subspace and the Loewner methods
2. Evaluate the capability to approximate a high-order MIMO model with a variable reduced order model
3. Compare the computational time needed by the different methods to identify models based on the same data
4. Verify that the methods of sections 3.5 and 3.6 can exactly impose some known poles

In order to satisfy these objectives, we study two scenarios. In the first one, the so-called "test data" are generated from a fixed-order MIMO state-space model defined by random matrices $\boldsymbol{B}$, $\boldsymbol{C}$ and $\boldsymbol{D}$ and a matrix $\boldsymbol{A}$ with conjugated poles on its diagonal. The poles have a constant damping ratio and regularly spaced frequencies. Each pole is simple (algebraic multiplicity equal to one), and we impose the 40% poles of lowest frequencies when the identification technique allows it.

Identification method	Reference section	Continuous/ discrete time	Numerical operations	Imposed poles	Constrained free poles	Approximation error	Computational time
Subspace	3.3.1	Discrete	Linear algebra	No	No	Very low	Few seconds
Loewner	3.3.2	Continuous	Linear algebra	No	No	Very low	Few seconds
Stable subspace	3.4	Discrete	Convex optimization	No	Yes	Very low	Few seconds
SIDORT	3.5	Discrete	Linear algebra	Yes	No	High	Few seconds
SIDPEV	3.6.1	Discrete	Nonlinear optimization	Yes	Yes	Low	Minutes/hours
DNOC	3.6.2	Discrete	Nonlinear optimization	Yes	Yes	Low	Hours

Table 3.1: Summary of the different identification methods

We define models of variable order that can be stable or unstable in order to study the methods presented above in a broad range of situations. In the second scenario, the methods are applied to aeroelastic data generated using FEM and DLM models as described in section 3.1.2. This is the primary intended objective of this work, but in this situation, the model used to generate data is fixed. The underlying aeroelastic model can be considered of infinite order because the aerodynamic forces are not rational functions of the frequency. The imposed modes associated to the aeroelastic data are all stable.

The main metric used in the results is the normalized approximation error of the frequency response, defined by

$$error_{response} = \sqrt{\frac{\sum_{k=1}^{N_f} \left\| \boldsymbol{H^{true}}(\omega_k) - \boldsymbol{H^{ident}}(\omega_k) \right\|_F^2}{\sum_{k=1}^{N_f} \left\| \boldsymbol{H^{true}}(\omega_k) \right\|_F^2}} \tag{3.66}$$

where $\boldsymbol{H^{true}}$ and $\boldsymbol{H^{ident}}$ are the true and identified transfer functions respectively, N_f is the number of data points.

The state-space model used to generate the test data in section 3.7.2 has 7 outputs and 11 inputs. It contains poles with the same damping ratio of 0.1 and frequencies linearly ranging from 0.1 Hz to 5 Hz. The frequency data is computed at 200 different frequencies, linearly ranging from 0 Hz to 10 Hz. The aeroelastic data are obtained from a XRF1-HARW model. The aeroelastic data response is obtained at Mach 0.85 and altitude 9000 m (from which the density is obtained using the standard atmosphere model), and the aircraft is empty (no fuel and no payload) with a center of gravity position at about 25% of the mean aerodynamic chord, aft of the leading edge. Only the longitudinal dynamics are considered. The aeroelastic data include 7 outputs (pitch angle, pitch velocity, vertical load factor, shear force, bending moment and torsional moment at wing root) and 25 inputs (one pair of elevators and 24 pairs of ailerons). The frequency response is computed at 300 different frequencies linearly ranging from 0 Hz to 10 Hz. Initially 80 structural modes are included in the FEM model, in addition to the 6 rigid modes. The number of longitudinal modes with frequency below 10 Hz is about 20. Seven pairs of conjugated aeroelastic poles are imposed in addition to an integrator, when the method allows it. They are chosen as those contributing the most to the transfer function of the considered input/output pairs. Note that the aeroelastic response is normalized before being used by the different identification algorithms, in such a way that all inputs and outputs have approximately the same weight in the identification process.

In the nonlinear subspace method (SIDPEV) defined in 3.6.1, minimum singular values of 10^{-7} are accepted in the nonlinear constraint definition. Up to 10 runs with different initializations are performed for each optimization as long as the objective function has not reached a threshold of 10^{-7}. A maximum of 1000 function evaluations is set for the direct method defined in 3.6.2. Both methods are implemented using an interior-point algorithm [Byrd, Hribar, and Nocedal 1999; Waltz et al. 2006] in which the gradient of the objective function with respect to the parameters is computed and supplied.

A summary of the different methods investigated in this work is shown in Table 3.1. Their accuracy and computational time are given to give an approximate order of magnitude. For example, to identify a 60th order reduced model with 11 inputs and 7 outputs, the SIDPEV method takes about 16 minutes, the DNOC 2 hours, and the other methods between 5 and 20 seconds. The computational complexity will be studied more accurately in the following results. Note that the stable Loewner method described in section 3.4.2 is not studied in the results for the sake of conciseness, as it is similar to the stable subspace method.

3.7.2 Results with test data (first scenario)

In this section, the first scenario described in sections 3.7.1 is tested. In Fig. 3.2, the amplitude of the transfer function associated to a pair of input/output of the true test data is shown in solid line. On the left part of the figure, the different identification techniques presented in this paper

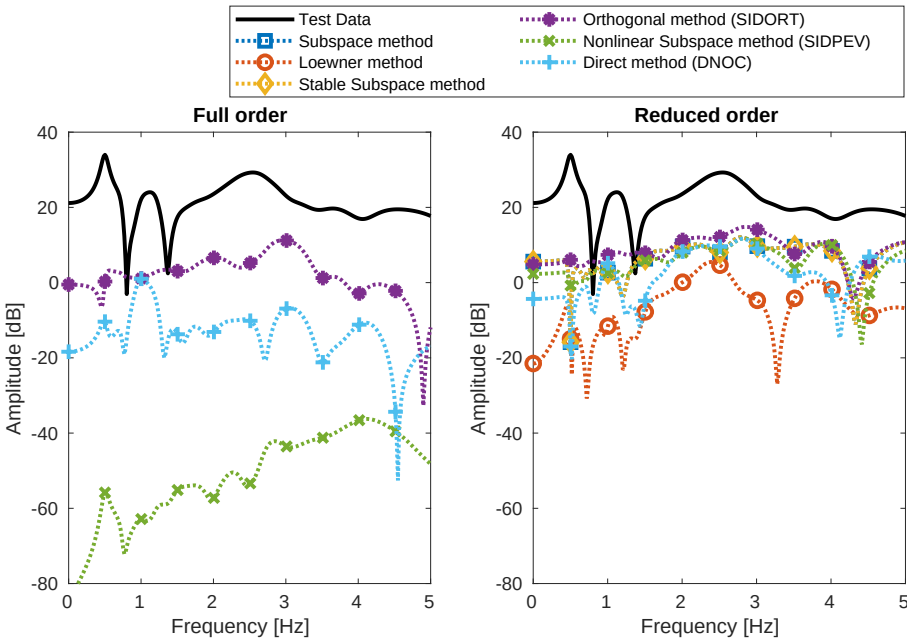

Figure 3.2: Amplitude of the test data (solid line) and of the approximation errors with different methods (dotted line) with 40th-order (left, same as the state-space model used to generate test data) and 30-th order (right) models

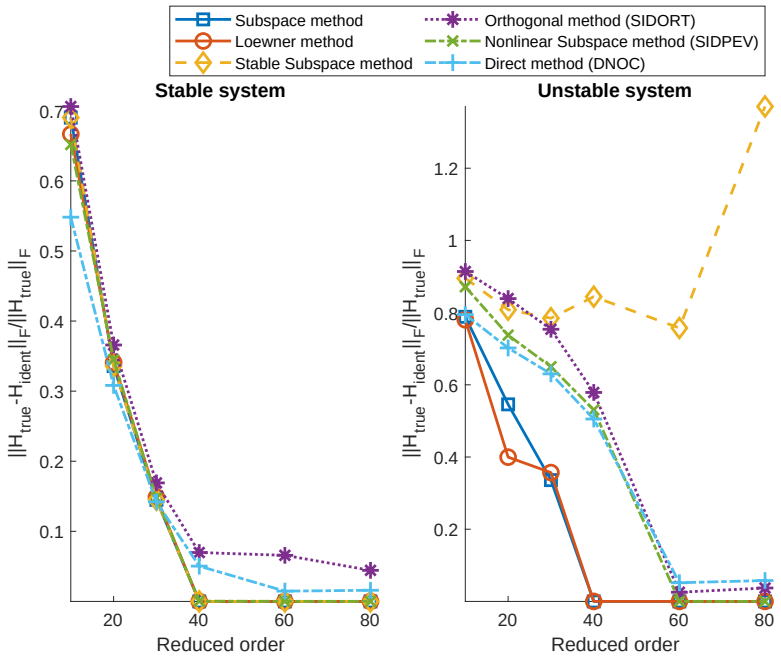

Figure 3.3: Approximation error with models of different reduced orders (the test data are generated using a 40th order model), in case all poles are stable (left) and half of the poles are unstable (right)

are applied to obtain models of the same order as the model used to generate the test data (40), and the amplitude of the difference between the test data and the identified frequency response is shown in dotted line. Note the difference between the dotted lines, which represent approximation errors, and the solid line, which is reported to show the response from the data. The lines that are not represented are below the figure's window, we consider that in this case the approximation is perfect. It results from this figure that the Loewner and subspace methods (with and without stability constraint) approximate the underlying system's response with very high accuracy when the order matches. The SIDPEV method leads to a very low error, while the SIDORT and DNOC methods identify the model with a non-zero error, that remains very low when compared to the true response. When looking at the bode diagram with models of reduced order 30 on the right part of Fig. 3.2, the difference between the different methods is less significant, only the Loewner method leads to a better approximation of the test data.

This trend is further investigated in Fig. 3.3 in which the normalized approximation error defined in Eq. (3.66) is compared for the different presented methods, with variable reduced order and test data generated using a 40-th order state-space model. In the left part, the test data are obtained from a stable model, hence the stability constraints included in some methods (stable subspace, SIDPEV and DNOC) are not expected to increase the approximation error. It can be seen that the Loewner method, the subspace algorithms (with and without stability constraint) and the SIDPEV method have the same trend, with a decreasing approximation error as the reduced order increases, and close to zero when the order of the underlying model is reached. This validates the SIDPEV method, in which nonlinear optimization issues (such as local minimum)

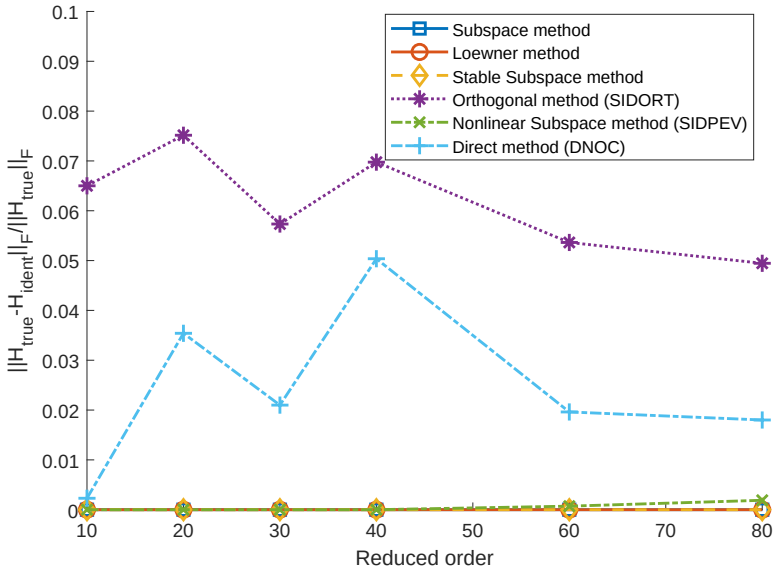

Figure 3.4: Approximation error with models of the same order as the state-space model used to generate test data

do not seem to alter the results. The direct optimization method DNOC is more efficient at low reduced order, but does not perfectly approximate the transfer function response at full order and above. Note that this method is greatly affected by the number of iterations of the nonlinear optimization. For the sake of applicability, it is limited to 1000 but theoretically with a higher computational time, lower errors would be obtained at full order and above. Finally, the SIDORT method has a slightly higher error, due to the additional constraint of orthogonality between the identified and the imposed poles. The SIDORT method is validated by this experience as it leads to errors comparable to the well-established subspace and Loewner method at reduced-order. On the right part of Fig. 3.3, the same experience is done with test data generated from a state-space model with half of the poles unstable. The Loewner and unconstrained subspace methods lead to results similar to the stable case. The SIDPEV and DNOC methods have stability constraints in the free poles location, which expectedly leads to an increased approximation error. In the case of SIDPEV and DNOC, the model eventually approximates the true test data with good accuracy with a reduced order of 60 and above. In the case of the stable subspace, the constraints are stronger than with SIDPEV and DNOC as no pole is imposed, hence all poles of the identified model are stable. This explains the higher errors obtained with the stable subspace method, and illustrates how imposing unstable poles can improve the approximation when the free poles must be stable. Finally the SIDORT leads to approximation errors similar to the methods with constrained poles.

Fig. 3.4 further investigates the case in which the identified models are of the same order as the state-space model that generates the test data. For different values of this order, the capability of the presented methods to approximate the frequency response is evaluated. This aims at verifying that no numerical issue arise when the order increases. Indeed, not only this causes the matrices'

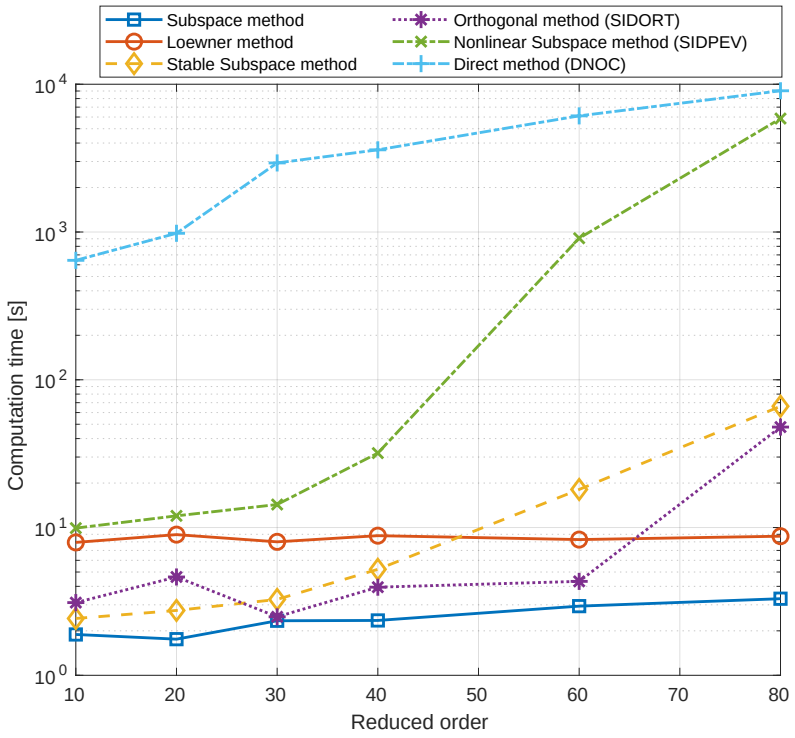

Figure 3.5: Computation time of the identification techniques

size (such as the observability matrix) to increase, but also the number of variables in the SIDPEV and DNOC. In Fig. 3.4 the Loewner and subspace (with and without stability constraint) methods lead to very low approximation error, regardless of the order. Considering the SIDPEV method, the error remains very low, although a slight increase seems to start at order 80. In the range of reduced orders of interest for this work, no numerical issue exist with the SIDPEV method. Similarly, the error obtained with the SIDORT method remains low at high orders, and even tends to decrease.

To conclude the comparison and validation of the presented methods on the test data, the computation time is studied. On Fig. 3.5, the time needed to perform the identification is shown with the different methods. The DNOC method, that relies on a nonlinear optimization with constraints and a high number of parameters, leads to the highest computation time. It lasts more than one hour when the reduced order is higher than 40. Note that by increasing the maximum number of iterations, this time would increase and the approximation error would be lower at higher orders. The SIDPEV method starts having computational time comparable to the DNOC when the order approaches 80. The other techniques are much faster, as seen on Fig. 3.5. Up to the order 40, the computation time is lower than 40 s for all techniques except the DNOC. The Loewner method is slightly slower than the subspace methods. The convex optimization used in the stable subspace method proves its efficiency compared to nonlinear optimization-based algorithm, in terms of computational time. Finally, the SIDORT method manages to perform a hybrid identification with some imposed poles in a relatively short time. For the sake of conciseness, the

influence of the number of inputs and outputs is not shown in these results. A quick consideration can be made concerning the unconstrained subspace Loewner methods, assuming that the most time-consuming operation is the SVD. In both cases, the decomposition is performed on matrices ($\mathcal{H}\mathcal{U}^{\perp}$ for the subspace method and $\begin{bmatrix}\mathbb{L} & \mathbb{L}_{\sigma}\end{bmatrix}$ for the Loewner method) which scale linearly with N_y and N_u in number of rows and columns respectively. The SVD having a time complexity of $\mathcal{O}(\min(mn^2, m^2n))$ with m and n the number of rows and columns of the matrix to decompose, the time complexity of the unconstrained algorithm approximately follows $\mathcal{O}(\min(N_y N_u^2, N_y^2 N_u))$.

3.7.3 Results with aeroelastic data (second scenario)

This section presents the second scenario in which the true data come from an aeroelastic model described in section 3.1.2 with additional details in sections 3.7.1. Contrary to the test data used in the previous section, the aeroelastic data are not generated by a finite-order transfer function or state-space model, hence the objective is to approximate it with the best accuracy possible.

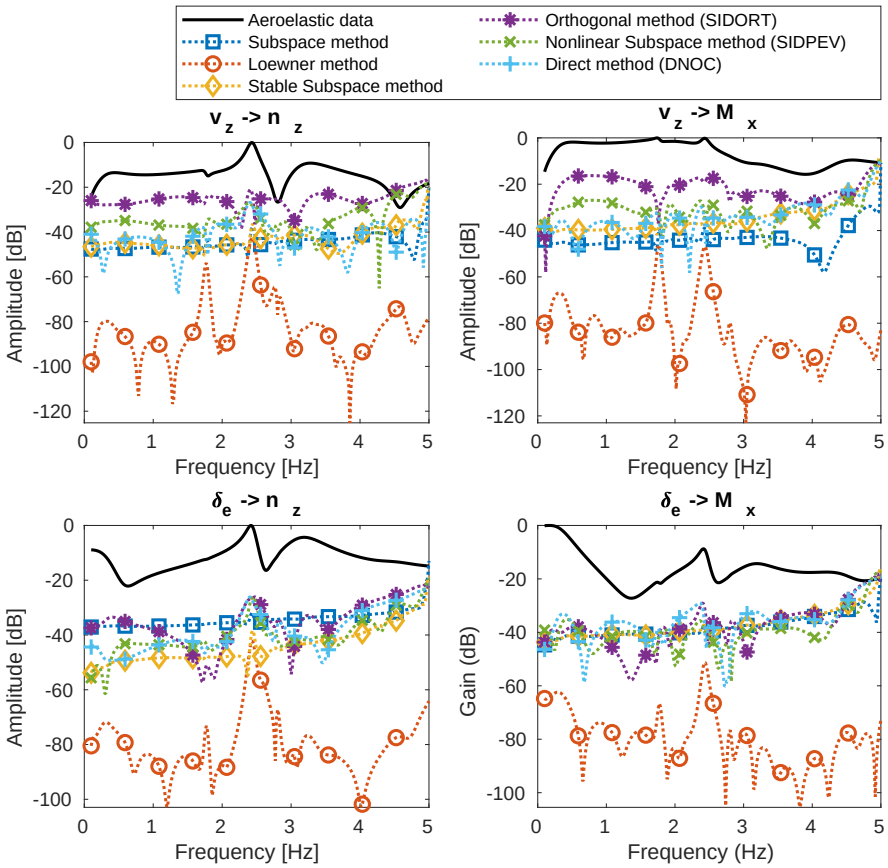

Figure 3.6: Amplitude of the aeroelastic data (solid line) and of the approximation errors with different methods (dotted line) with 40-th order models, from vertical wind velocity (v_z) and elevator deflection (δ_e) inputs to vertical load factor (n_z) and wing root bending moment (M_x) outputs

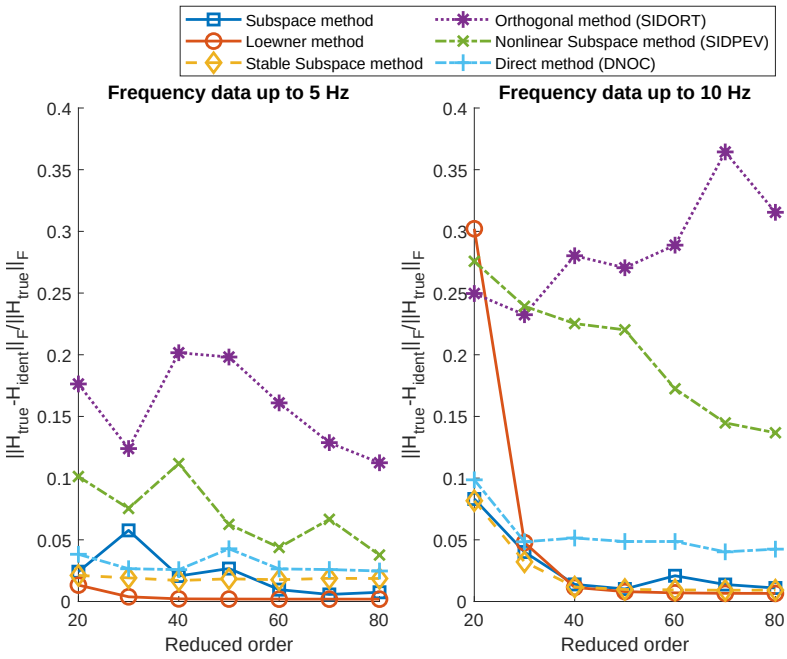

Figure 3.7: Approximation error with models of different reduced orders, with aeroelastic data up to 5 Hz (left) and 10 Hz (right)

Furthermore, as explained in section 3.1.2, the poles that we wish to impose are not perfectly known, they result from an estimation using the p-k method.

In Fig. 3.6, the amplitude of the aeroelastic transfer function from the wind velocity and elevator deflection to the vertical load factor and wing root bending moment is shown in solid line, for frequencies ranging from 0 Hz to 5 Hz. All values are normalized. Similarly to the previous section, the different identification methods defined in this work are compared and the amplitudes of the difference between the 40-th order identified models and the true frequency data are plotted in dotted lines. All methods lead to errors that are significantly lower than the true response. The Loewner method is by far the most accurate, and performs better than the subspace method in this situation. The stable subspace method with stability constraint leads to an error comparable to the subspace method obtained without constraints. When imposing some aeroelastic poles, the SIDPEV and DNOC methods lead to a good approximation of the aeroelastic transfer function, while the SIDORT method is slightly less accurate.

More complete results are presented on the left part of Fig. 3.7, where the normalized errors of Eq. (3.66) are computed with models of different reduced orders. The global trend is a reduction of the error when the reduced-order increases. Some methods, such as the stable subspace method and the DNOC, show an error that does not decrease when the order increases. It can also be noted that the methods relying on nonlinear optimization (SIDPEV and DNOC) show relatively continuous results. Although a proper analysis would be needed to confirm it, this tends to show that they always converge to satisfactory results. A final observation concerns the SIDORT method, for which the best results are obtained at order 30, a higher order leads to a higher

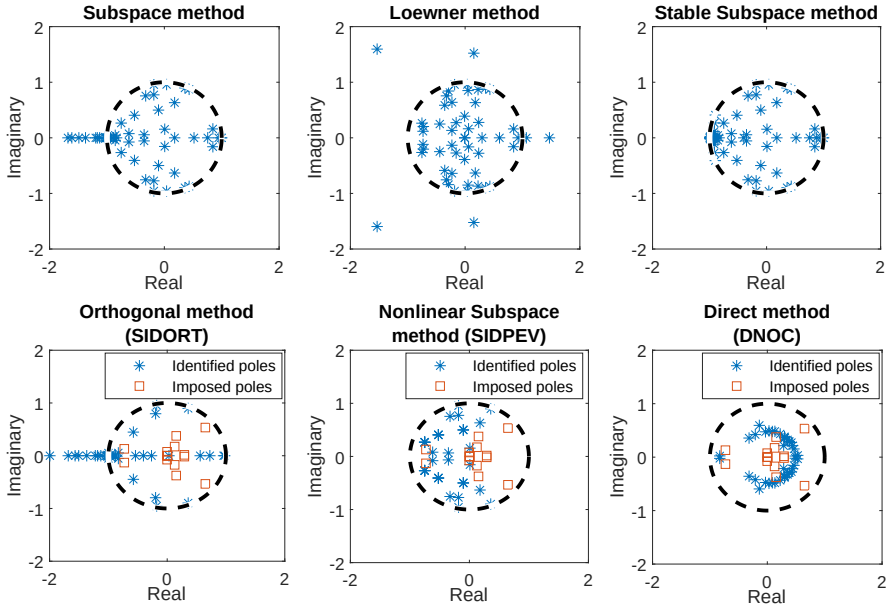

Figure 3.8: Poles of the identified models obtained by different techniques and imposed poles when applicable

error. Although no numerical issue has been detected with the analysis of the previous section, this shows that the reduced order should be chosen with care when using this method, requiring a prior knowledge of the approximative underlying system's order. The right part of Fig. 3.7 shows the same analysis, but performed with data up to 10 Hz instead of 5 Hz. This increases the complexity of the system, as more modes are involved in the frequency response. Note that the number of imposed poles is the same as in the previous case. It can be seen that the methods require a higher order to converge to the asymptotic error. In this case, the advantage of the Loewner method is less marked, and the stable subspace method still leads to a low error while imposing stability. The SIDPEV method still leads to a low error, that decreases when the order increases. The SIDORT method is less accurate in this case, and the error tends to increase with the order, confirming the fact that the reduced order should be chosen adequately.

Finally, an illustration of the poles locations using the different methods is provided in Fig. 3.8. These correspond to the discrete-time poles, which are stable when they are located within the unit disk. In case the identified model is continuous (Loewner method only), the poles λ_i are converted to their discrete-time counterpart $e^{T_s\lambda_i}$. It can be seen that the stability is correctly imposed by the stable subspace, SIDPEV and DNOC methods, while the Loewner, subspace and SIDORT methods lead to unstable poles as no constraint is put on them. The pairs of imposed poles are shown for the techniques that impose them. It can be seen that the DNOC method identifies poles with an almost constant modulus, this could correspond to a sub-optimal result from the nonlinear identification.

3.7.4 Conclusions of the identification techniques comparison

In this work, reduced order modeling techniques intended for aeroelastic systems have been presented and tested. The full aeroelastic transfer function corresponding to certain inputs and outputs of interest is identified based on its frequency response. The Loewner method has been applied and compared to a subspace algorithm, in which the possibility to apply constraints on the poles have been studied. Furthermore, in order to improve the physical interpretability of the identified models, dedicated techniques have been developed specifically for this work to impose a set of a-priori known poles that can be stable or unstable. These methods have been compared through different scenarios, starting from stable and unstable models of various orders, to finally be applied to aeroelastic data in which case the imposed poles have been computed by p-k method beforehand.

It results from this work that the different methods described are valid over the range of reduced orders studied (up to 80). The transfer function response is systematically approximated with an error that remains at least one order of magnitude below the true value, provided the reduced order is high enough. The different constraints (poles location, imposed poles) are successfully applied by the relevant methods.

A first comparison can be performed between McKelvey subspace algorithm and the Loewner interpolation method, when no constraint is applied to the identified models. The Loewner method is slightly slower than the subspace algorithm, but is more efficient at approximating a system with a reduced order. This has been verified using data generated with a fixed-order random state-space model and with an aeroelastic model. Another advantage of the Loewner method is that it leads to a continuous-time model, that can more easily be transformed into a discrete-time state-space of any sampling time if needed. Although not shown in this work for the sake of conciseness, similar conclusions can be drawn with different numbers of inputs and outputs. Furthermore, the stable subspace algorithm based on [Miller and De Callafon 2013] is able to approximate a transfer function within an error comparable to the McKelvey subspace algorithm and with a similar computational time within the reduced order range considered in this work, whilst ensuring stability. It can hence be applied to obtain models used in simulations and control synthesis without the classical instability issues obtained with the Loewner and subspace methods.

A second comparison concerns the different techniques defined for imposing some poles of the system, with and without constraints on the remaining poles. The SIDORT method adds very little complexity to the McKelvey algorithm as mainly eigenvalue problems and SVD decomposition concerning matrices of low sizes are concerned in the additional step. However, it suffers from two main limitations: the first is the hypothesis of orthogonality between the eigenvectors associated with the imposed poles and those associated with the free poles respectively. The second is the fact that it does not impose stability of the remaining poles. It approximates the data with good accuracy but lower than the other techniques presented in the current work. When applied to the aeroelastic data, the error does not seem to systematically decrease as the reduced order increases.

It can also be noted that it cannot perfectly approximate the data when the reduced order is the same as the data-generating model's order, due to the conservative orthogonality constraint. In comparison, the SIDPEV method leads to lower approximation errors both with the test and the aeroelastic data, and although it relies on a nonlinear optimization with constraints that requires multiple runs with different initial conditions, its computational time remains low at orders lower than or equal to 40. Moreover, with an appropriate initialization, it seems to always converges to a satisfactory solution. Finally, the DNOC method relies on an direct optimization to find the state-space matrices of the reduced order model with constraints on the poles. Because of the high number of variables, this method requires high computational times, but eventually converges to solutions with good approximation accuracy. It can be noted that when the complexity of the system increases (higher order or in case of the aeroelastic data on a broader frequency range), the number of iterations required to converge increases. For practical use, when poles must be imposed to the identified model, the SIDPEV method seems the most appropriate.

Some remarks about the limits of this study can be formulated to prepare future works. Concerning the choice of working with frequency response of the full aeroelastic transfer function, it must be noted that a different identification must be performed for each mass configuration and aerodynamic (Mach number, altitude), with no possibility of using a common structure. A second remark concerns the complexity of the algorithms. In this work only models of limited sizes evaluated on relatively low amounts of data have been considered, and numerical issues such as memory limitations could happen with bigger systems. Finally, while efforts have been done to improve the convergence of the DNOC algorithm, different optimization schemes could be studied in order to promote convergence to better solutions in shorter times.

3.8 Identification by pole-residue decomposition

This section presents a different strategy, that takes advantage of the reduced-order estimation capability of black-box identification methods such as the Loewner method, while accurately imposing the aeroelastic poles. It starts by identifying a reliable, potentially high-order, state-space model using GAF RFA for example, as described in section 3.2. The idea is to keep the part of the model associated to the poles of interest, and to reduce the rest. It is done by performing a pole-residues decomposition of the full-order aeroelastic state-space model's transfer function obtained in section 3.2, assuming that each pole is simple:

$$\boldsymbol{H}(s) = \sum_{i=1}^{n} \frac{\boldsymbol{R_i}}{s - \lambda_i} \tag{3.67}$$

where the $\boldsymbol{R_i} \in \mathbb{C}^{N_y \times N_u}$ are matrices called residues associated to the poles λ_i. By putting the aeroelastic state-space system in the basis in which the matrix $\boldsymbol{A}$ is diagonal (which is possible because the poles are assumed to be of multiplicity 1), the $\boldsymbol{R_i}$ would be the product of a column of $\boldsymbol{C}$ and a row of $\boldsymbol{B}$, which shows that their rank is equal to 1. However, as the matrix $\boldsymbol{A}$ is of

very high order, its diagonalization is not numerically efficient. An effective solution to compute the residues is to evaluate the transfer function $(s-\lambda_i)\boldsymbol{H}(s)$ at $s=\lambda_i$, which directly gives the value of $\boldsymbol{R_i}$. Efficient ways of computing the frequency response of a transfer function of high order are required to do so, like for example with Matlab's *freqresp* function.

Only the aeroelastic poles of interest are computed with the identification procedure proposed in this section. In particular, only the poles in the frequency range of interest can be computed to reduce the order of the final system. By using the fact that the transfer function has real coefficients, it can be written as:

$$\boldsymbol{H}(s) = \sum_{k=1}^{\bar{n}} \left(\frac{\boldsymbol{R_k}}{s-\lambda_k} + \frac{\overline{\boldsymbol{R_k}}}{s-\overline{\lambda_k}} \right) + \boldsymbol{H_{diff}}(s) \tag{3.68}$$

where $\boldsymbol{H_{diff}}(s)$ is the difference between the full transfer function and the part we wish to impose. The idea of this methodology is to perform a model reduction of $\boldsymbol{H_{diff}}$, by approximating it with a reduced-order state-space model. This is done here by evaluating its frequency response, and using it to identify a reduced model by the Loewner method. Note that this new model must be stable, assuming that we have included all the unstable modes in the selected set. The final reduced order state-space model with imposed poles then has the following transfer function

$$\boldsymbol{H^{ROM}}(s) = \sum_{k=1}^{\bar{n}} \left(\frac{\boldsymbol{R_k}}{s-\lambda_k} + \frac{\overline{\boldsymbol{R_k}}}{s-\overline{\lambda_k}} \right) + \boldsymbol{H_{diff}^{ROM}}(s) \tag{3.69}$$

where $\boldsymbol{H_{diff}^{ROM}}$ has been identified with the Loewner method with imposed stability. Each subsystem associated with a selected aeroelastic pole λ_k can be put in a state-space form of order 2, and the full Reduced-Order Model (ROM) state-space with imposed poles can be obtained with block-diagonal matrix $\boldsymbol{A}$ composed of state matrices of each subsystem, and the associated $\boldsymbol{B}$ and $\boldsymbol{C}$ matrices are obtained by concatenation. This method has the advantage of linearly decoupling the part of the system associated with the imposed poles from the part that is reduced. Furthermore, not only does it ensure that the selected poles are accurately represented in the model, but also that they affect the transfer function in a similar way as in the reliable model defined in the first step of the procedure.

Fig. 3.9 illustrates an example of the identification techniques with residues. The conditions are the same as the second validation scenario described in section 3.7.1, in which aeroelastic data up to 5 Hz and 10 Hz are studied. The figure shows the approximation errors obtained with several reduced orders, with and without stability constraints. The results obtained with the DNOC are also shown for comparison. It results that the approximation accuracy is better with the residues methods than the DNOC, for data up to 5 Hz, and similar with data up to 10 Hz with high orders. The computational cost is much lower than the DNOC, as the most time-consuming task is the identification of a high-order model by GAFs RFA, which takes about two minutes, regardless of the final reduced model order. The identification of the difference part $\boldsymbol{H_{diff}^{ROM}}$ takes a few tenths of seconds at maximum, depending on whether stability constraints are included or not

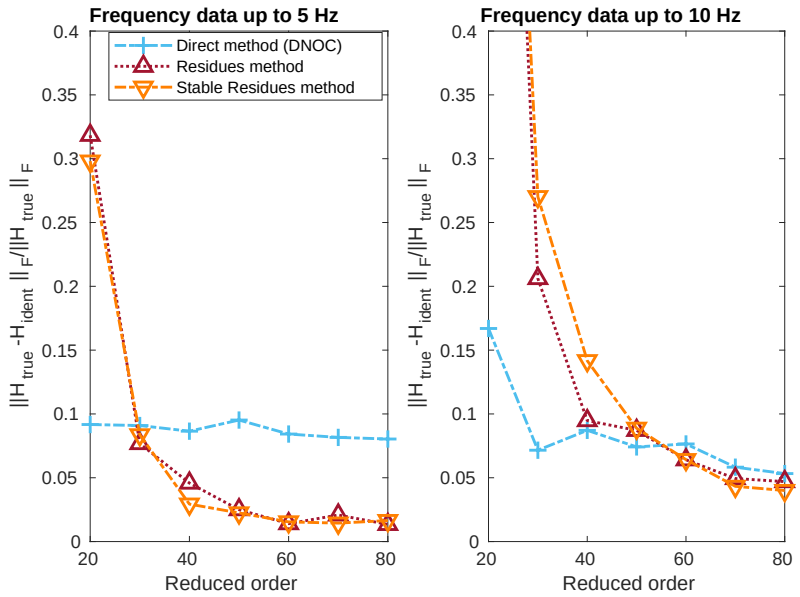

Figure 3.9: Approximation error with models of different reduced orders, with aeroelastic data up to 5 Hz (left) and 10 Hz (right)

(see Fig. 3.5 for more details). When a good accuracy is required, with imposed poles and eventual stability constraints, the method with pole-residue decomposition described in this section then outperforms the others. The fact that the accuracy is lower with low orders can be explained by the lower number of degrees of freedom with this technique, compared to the others. Indeed, at 20-th order for instance, since 16 poles are already imposed, only a 4-th order model can be computed to fit to the data. The residues associated to the imposed poles are fixed for the residues method, while they are free with the other methods. Finally, it can be noted that the presence of stability constraints has a small influence on the approximation accuracy. In conclusion, the identification method based on pole-residue decomposition is the most accurate and the fastest when high accuracy is needed, but it requires the prior identification of a reliable rational model and its pole-residue decomposition, which lead to a more cumbersome overall procedure.

3.9 Parametric identification

3.9.1 Review of some existing techniques

Instead of identifying one state-space model for each flight point and mass configuration, it can be useful to have one single Linear Parametrically Varying (LPV) model. At fixed values of the parameters, the model is LTI, and the matrices defining the LTI model have a dependence on the parameters. Such models can be used for flexible simulations and analysis, allowing to easily modify the value of the TAS or Mach number for example, or for control design, requiring a synthesis method adapted to the model structure. Several approaches exist with different dependence

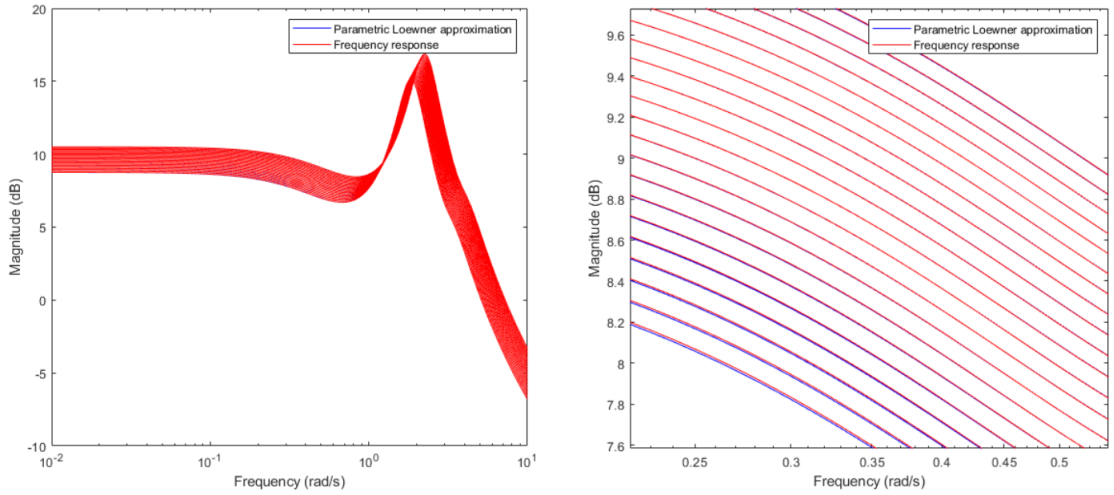

Figure 3.10: Parametric identification of a simple parameterized state-space model (general view on the left, zoom on the right)

of the model on the parameters. Subspace methods have been successfully applied to affine LPV model identification, in which the state-space matrices have affine dependence on potentially several parameters. This is done in [Verdult and Verhaegen 2002] where an identification based on a single experiment is performed, and in [Lovera and Mercere 2007] based on multiple experiments. In [Kergus, Demourant, and Poussot-Vassal 2020], a subspace method using frequency data and Linear Matrix Inequalities (LMI) constraints on the poles is proposed with the same parametric dependence, which can be extended to the polynomial case. The identification of Linear Fractional Transform (LFT) LPV models has been proposed in [Lee and Poolla 1999]. Such models can be used to design robust and adaptive controllers based on μ synthesis. The Loewner method has also been extended to parameterized identification, such as in [Antoulas, Ionita, and Lefteriu 2012] where the parameter is treated as a second frequency variable, resulting in a rational dependence of the identified transfer function. In [Xiao et al. 2019], the Loewner framework is also used, exploiting transfer functions expressed in barycentric form, and leading to polynomial dependence on the parameter. This technique is illustrated in Fig. 3.10 where it has been applied to a simple 8-th order state-space system with 4-th order polynomial dependence. The same orders are used to define the identified model. It demonstrates the possibility to accurately identify a LPV model using this method based on the Loewner framework, in a very simplified case (low dimensions and order, the latter being known in advance). Note that as pointed out in [Verdult and Verhaegen 2002], these parametric identification require defining matrices of very large sizes, that generally contain all the data, leading to memory issues.

3.9.2 Polytopic identification with Loewner method

This section presents another type of model parameterization based on polytopic representation of the following form

$$\begin{cases} \dot{\boldsymbol{x}} = \boldsymbol{A}(\boldsymbol{\theta}) + \boldsymbol{B}(\boldsymbol{\theta})\boldsymbol{u} \\ \boldsymbol{y} = \boldsymbol{C}\boldsymbol{x} \end{cases} \tag{3.70}$$

where the matrices $\boldsymbol{A}(\boldsymbol{\theta})$ and $\boldsymbol{B}(\boldsymbol{\theta})$ are convex combinations of r generating matrices:

$$\begin{bmatrix} \boldsymbol{A}(\boldsymbol{\theta}) & \boldsymbol{B}(\boldsymbol{\theta}) \end{bmatrix} = \sum_{i=1}^{r} \theta_i \begin{bmatrix} \boldsymbol{A_i} & \boldsymbol{B_i} \end{bmatrix} \tag{3.71}$$

with $\boldsymbol{\theta} \in \mathbb{R}^r$ is parameter such that $0 \leq \theta_i \leq 1$ and $\sum_{i=1}^{r} \theta_i = 1$. This class of parameterized models has several attributes which make it interesting for aeroelastic modeling and controller synthesis. First, there exist control synthesis techniques relying on semi-definite programs to design robust or adaptive controllers based on polytopic models such as [Silva Campos, Nguyen, and Palhares 2016] or [Kothare, Balakrishnan, and Morari 1996], similarly to the μ-synthesis with LFT models. Another interesting advantage is the fact that no explicit definition of the parameter is needed. Indeed, a polytopic model is defined based on the vertices, which are the state-space models defined by matrices $(\boldsymbol{A_i}, \boldsymbol{B_i}, \boldsymbol{C})$. In cases in which the uncertainty is not easily defined by a reduced number of parameters, it allows to define a parameterized model based on a set of data obtained at different points. This is the case of the dependence on the mass configuration, which, contrarily to the TAS and Mach dependence for example, cannot be directly defined by a single parameter. However, there is no guarantee that once vertices have been obtained, the resulting polytopic uncertainty makes sense from a physical point of view.

The objective of the polytopic identification is to identify the vertices of the model, using the frequency responses $(\boldsymbol{H_i})_{i=1\ldots r}$. Each vertex must have the following state-space representation

$$\begin{cases} \dot{\boldsymbol{x}} = \boldsymbol{A_i}\boldsymbol{x} + \boldsymbol{B_i}\boldsymbol{u} \\ \boldsymbol{y} = \boldsymbol{C}\boldsymbol{x} \end{cases} \qquad i = 1 \ldots r \tag{3.72}$$

the main difficulty is to obtain a common $\boldsymbol{C}$ matrix for all vertices. This is an important assumption for most controller or observer design based on such models, as this implies that the states must have a common "meaning". A simultaneous identification of the different models is then needed.

This can be achieved within the Loewner framework. Recall that a single state-space model of the form of Eq. (3.72) can be obtained using data $\boldsymbol{H_i}$ by defining large-size matrices $\mathbb{L}_i$, $\mathbb{L}_{\sigma,i}$, $\boldsymbol{G_i}$, $\boldsymbol{F_i}$ which are then reduced in a way that conserves the data contained in the Loewner pencil

$[\mathbb{L}_i, \mathbb{L}_{\sigma,i}]$. The matrices $\boldsymbol{X_i}$ and $\boldsymbol{Y_i}$ are defined by the Singular Value Decompositions (SVD):

$$\begin{bmatrix} \mathbb{L}_i \\ \mathbb{L}_{\sigma,i} \end{bmatrix} \approx \tilde{\boldsymbol{Y}} \boldsymbol{\Sigma_r} \boldsymbol{X_i}^* \tag{3.73}$$

$$\begin{bmatrix} \mathbb{L}_i & \mathbb{L}_{\sigma,i} \end{bmatrix} \approx \boldsymbol{Y_i} \boldsymbol{\Sigma_l} \tilde{\boldsymbol{X}}^* \tag{3.74}$$

where the "$\approx$" symbol means that only the first n singular values are kept, n being fixed by the user or taken as the McMillan degree equal to $\text{rank}(\mathbb{L}_{\sigma,i})$. Note that the matrices $\tilde{\boldsymbol{X}}$, $\tilde{\boldsymbol{Y}}$, $\boldsymbol{\Sigma_r}$ and $\boldsymbol{\Sigma_l}$ are not used, and economy-size SVD can be performed. The state-space matrices of a single model are defined as:

$$\boldsymbol{E_i} = -\boldsymbol{Y_i}^* \mathbb{L}_i \boldsymbol{X_i} \tag{3.75}$$
$$\boldsymbol{A_i} = -\boldsymbol{Y_i}^* \mathbb{L}_{\sigma,i} \boldsymbol{X_i} \tag{3.76}$$
$$\boldsymbol{B_i} = \boldsymbol{Y_i}^* \boldsymbol{F_i} \tag{3.77}$$
$$\boldsymbol{C_i} = \boldsymbol{G_i} \boldsymbol{X_i} \tag{3.78}$$
$$\tag{3.79}$$

To perform a simultaneous identification, the right and left reduction are performed in a different way. The right reduction matrix $\boldsymbol{X_{sim}}$ is computed in such a way that the matrix $\boldsymbol{C}$ is the same for all systems. To this aim, an augmented vertical Loewner pencil is obtained by concatenation and the matrix $\boldsymbol{X_{sim}}$ is obtained as:

$$\begin{bmatrix} \mathbb{L}_1 & \dots & \mathbb{L}_r \\ \mathbb{L}_{\sigma,1} & \dots & \mathbb{L}_{\sigma,r} \end{bmatrix} \approx \tilde{\boldsymbol{Y}} \boldsymbol{\Sigma_{sim}} \boldsymbol{X_{sim}}^* \tag{3.80}$$

Regarding the left reduction, it is performed similarly to the single-model case, and the polytopic system is defined as

$$\boldsymbol{E_i} = -\boldsymbol{Y_i}^* \mathbb{L}_i \boldsymbol{X_{sim}} \tag{3.81}$$
$$\boldsymbol{A_i} = -\boldsymbol{Y_i}^* \mathbb{L}_{\sigma,i} \boldsymbol{X_{sim}} \tag{3.82}$$
$$\boldsymbol{B_i} = \boldsymbol{Y_i}^* \boldsymbol{F_i} \tag{3.83}$$
$$\boldsymbol{C} = \begin{bmatrix} \boldsymbol{G_1} & \dots & \boldsymbol{G_r} \end{bmatrix} \boldsymbol{X_{sim}} \tag{3.84}$$
$$\tag{3.85}$$

If the reduced order is taken lower or equal to the highest McMillan degrees of all single models, the matrix $\boldsymbol{E_i}$ hence obtained are invertible and a model of the form of Eq. (3.70) is obtained. Note that this technique requires higher orders than for a single model identification. It also requires to know in advance that the different data sets are obtained at different operating points. Indeed, if all the data was mixed without "labels" indicating which part is associated to each model, then the procedure described above would not be possible as it requires to first perform independent identification processes for each operating point.

3.9.3 Numerical results of polytopic identification

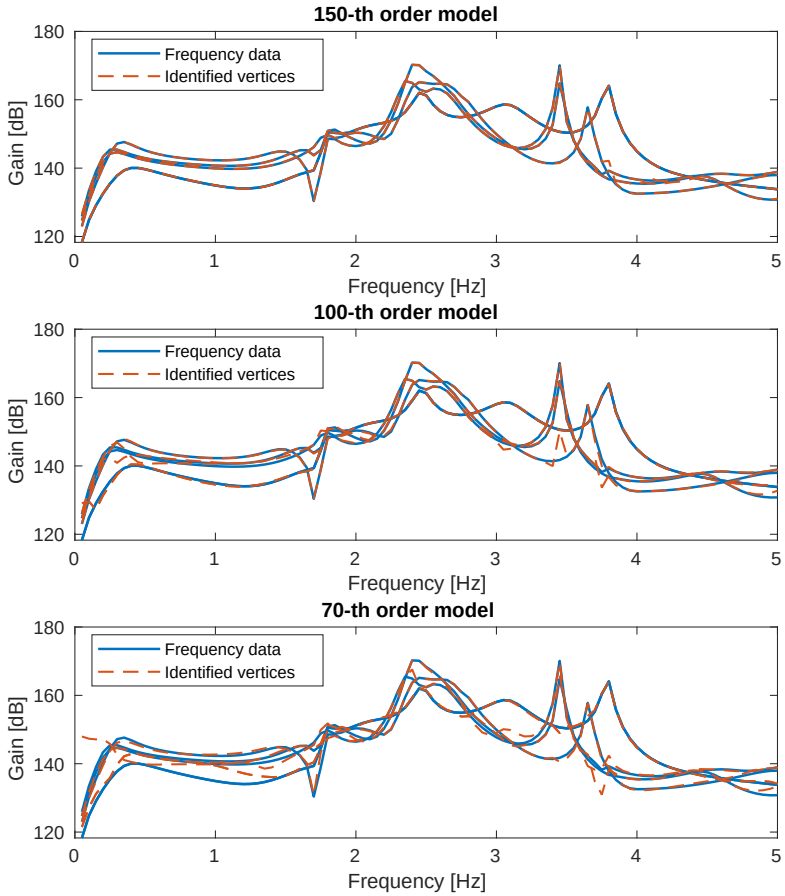

Figure 3.11: Identification of a 150-th order polytopic model using four sets of aeroelastic data

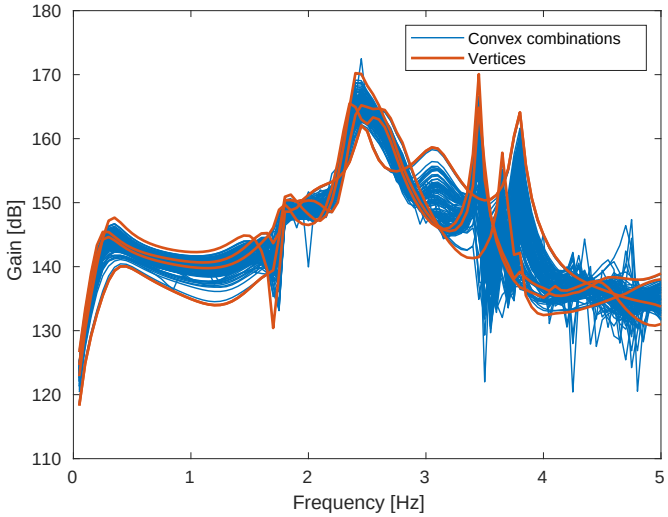

Figure 3.12: Frequency response of 100 models randomly taken in the polytopic uncertainty defined by four vertices

The polytopic identification technique is validated using aeroelastic data up to 5Hz, with 4 inputs (vertical wind velocity, symmetric elevator deflection, and symmetric deflections of two groups of ailerons) and 6 outputs (pitch rate, vertical load factor, angle of attack, and shear, bending and torsion at the wing root). Four models corresponding to different mass configurations are identified simultaneously, at the same Mach number 0.86 and 9000 m altitude.

In Fig. 3.11 models of different orders are identified. The 150-th and 100-th order models almost perfectly match the frequency data. The 70-th order model approximates the data with a low error. If independent identifications had been performed with the Loewner method on each set of data, a similar error would have been obtained with a reduced order of 40 approximately. With an order of 70, the polytopic identification successfully uses the correlations between the various sets of data to define states that explain the different models simultaneously.

Finally, Fig. 3.12 shows the frequency response of 100 models generated from these four vertices according to Eq. (3.70) and (3.71).

Chapter 4

Active Gust Load Alleviation with Lidar

Contents

This chapter focuses on the main initial objective of this work, namely the reduction of loads created by wind gust and turbulence on the airplane structure, using active control techniques. The different concepts related to the aeroelastic loads and the elements of aircraft modeling have been described in chapter 2, and different techniques for identifying low-order state-space models have been studied in chapter 3. These developments have paved the way for the efficient design of model-based controllers using modern, computationally intensive techniques such as μ-synthesis, multi-model H_2/H_∞ synthesis or model-predictive control in order to actively reduce the loads on an aircraft. The lidar sensor can play a major role in the future of active gust load alleviation thanks to its capability to anticipate the gust perturbations, hence giving more time to the controllers to attenuate their effect on the aircraft. This chapter provides answers to some questions raised by the potential use of this sensor.

4.1 Introduction to Gust Load Alleviation

4.1.1 State-of-the-art

The design of an aircraft is a multi-disciplinary process aiming at reducing the required fuel consumption for a given payload and range. It can be improved in different ways, by improving the engines efficiency or reducing the mass of the aeroplane whilst maintaining its overall capabilities. Using new lighter materials, but also in a less straightforward way reducing the maximum loads the aircraft must be able to withstand are the means to reduce the mass. For example, the wing spar is a heavy element, designed to resist to the maximum bending moment and shear force that will be created during the aircraft life cycle. One of the load sizing cases for the wing is the strong turbulence or gust. With an adequate control law that uses the elevators, ailerons, and possibly other control surfaces dedicated to GLA [Moulin and Karpel 2007], this load level can be strongly reduced, leading to significant mass savings and so to an overall performance improvement. Active gust load alleviation has been successfully implemented since the 1970s with the Lockheed L-1011 with a mass-saving objective, and more recently on the Airbus A380 and the Boeing 787 [Regan and Jutte 2012] for instance. By deflecting the ailerons symmetrically upwards when a vertical gust is detected, the lift is locally reduced and concentrated in the innermost part of the wings, which reduces the integrated loads at the wing root. Another simple strategy for active gust load alleviation (GLA) would consist in turning the plane towards the wind direction to reduce its influence, by use of the elevators.

Active gust load alleviation will most likely gain importance in the future generations of aircraft. The autonomy of the aircraft electric flight control system (EFCS) at the expense of the pilot's freedom to maneuver in flight will allow more efficient load alleviation control laws by reducing the risk of a detrimental pilot input and by coordinating the flight control and gust alleviation

systems. Furthermore, many new aircraft concepts choose to increase the wing aspect ratio and to reduce its structural weight to enhance aircraft energy efficiency. This increases airframe flexibility, leading to aeroelastic modes frequencies that approach the flight dynamics frequencies, creating flight dynamics-aeroelastic interactions (see [Chang, Hodges, and Patil 2008] and [Silvestre and Paglione 2008] for example). The recent development of lidar sensors [Herbst and Vrancken 2016; Rabadan et al. 2010] that can measure the vertical and lateral wind several hundreds of meters ahead of the aircraft allows new perspectives for gust load alleviation, by anticipating the response of the aircraft to the incoming wind perturbation. With the availability of computational capabilities, this motivates the development of more complex gust alleviation techniques, based on a full automation of the aircraft and taking advantage of its complete aeroelastic dynamics. While the active gust load alleviation laws implemented on the current generation of aircraft only allow to statically reduce the loads, more complex control techniques could attenuate the full dynamical response of the aircraft when it faces a wind gust or a turbulence, improving the passenger's comfort and reducing the loads in a broader frequency range.

The most straightforward method for active gust load alleviation of flexible aircraft is feedback control [Fonte, Ricci, and Mantegazza 2015; Che, Gregory, and Cao 2012; Stanford 2019; Mokrani et al. 2019] also broadly used in flight control [Luspay et al. 2019; Ustinov, Sidoruck, and Goman 2005]. It is based on the aircraft measured outputs, typically the pitch rate, yaw rate and vertical load factor obtained from gyroscopes and accelerometers. Feedback control allows a direct design of the closed loop poles, ensuring stability and robustness to the system uncertainties, without depending on the exact knowledge of the aircraft system. In order to improve the loads reduction, a feedforward controller that directly uses the measurement of the wind perturbation can be used in addition to feedback control [Alam, Hromcik, and Hanis 2015; Wildschek et al. 2010; Magar et al. 2017] or it can be used alone [Zhao, Yue, and Hu 2016; Li, Wang, and Ronch 2016; Wildschek et al. 2006]. A perfect feedforward controller can theoretically be obtained by direct inversion of the system's dynamics, but this is generally impossible due to actuator limitations, and the resulting controller would be very sensitive to system uncertainties. [Caverly et al. 2017] has used such a technique in addition to a linear controller and a disturbance observer for the gust load alleviation of a flexible aircraft. [Wang et al. 2019] has developed a method based on dynamics inversion with state estimation while ensuring robustness to system's uncertainties. Both of these methods work with a nonlinear model of the aircraft. A promising alternative is the employment of adaptive control, in which the system's dynamics are constantly estimated and the control is adapted accordingly. It generally relies on a finite-impulse response (FIR) model of the controller [Zeng et al. 2010; Wildschek et al. 2006; Wildschek et al. 2007; Zhao, Yue, and Hu 2016; Li, Wang, and Ronch 2016; Wang, Li, and Ronch 2015].

Developments in the last decades [Herbst and Vrancken 2016; Rabadan et al. 2010] such as Airbus AWIATOR program [Schmitt et al. 2007] or DLR's DELICAT program [Vrancken et al. 2016], thanks to which airborne lidar sensors emit a laser and measure the light scattered by air molecules, create new opportunities in gust load alleviation by not only diminishing the effects of wind but also preventing them. While simple controller structures are commonly used for

feedback control, finding a controller structure that takes the wind predictions as input is not straightforward. Model predictive control (MPC) methods that perform an online optimization can be used, they have been applied to gust load alleviation [Haghighat, Liu, and Martins 2012; Giesseler et al. 2012] and maneuver load alleviation [Freitas Virgilio Pereira et al. 2019; Gaulocher, Roos, and Cumer 2007]. More complex strategies based on wavelet decomposition of the lidar signal have been used in order to map the signal onto the different actuators depending on the frequency and the amplitude of the gust [Fezans and Joos 2017; Fezans, Schwithal, and Fischenberg 2017]. In absence of lidar measurement, the future states of the system cannot be predicted, and [Vuillemin, Martin, and Poussot-Vassal 2021] have developed a MPC technique in which optimal control values are computed assuming the future wind velocity belongs to a discrete set. The optimization aims at minimizing the worst case among those possible wind profiles, which can be taken as different $1-\cos$ gusts for example, providing robustness with respect to the wind velocity input. MPC techniques can be very efficient thanks to the online optimization, which computes the ideal values of controlled variables according to a model and a criterion to be minimized on a future time horizon. However, they suffer from two main drawbacks. The first is that they require the aircraft onboard computer to perform heavy computations, which is not in line with today's technological development and regulations. The second drawback is the absence of robustness, in the classical MPC formulation. Some techniques have been developed to ensure robustness within the MPC framework, and [Morari and Lee 1999] reviews some of them. Using a polytopic model as described in section 3.9.2, one can perform an online optimization based on Linear Matrix Inequalities (LMI) to compute the control variables value, as in [Kothare, Balakrishnan, and Morari 1996] or [Zhang, Wang, and Wang 2014]. A limitation of these techniques is the important computational required to solve LMIs based on multiple models. Furthermore, they lead to controlled signals that are proportional to the states at a given time, losing the nonlinear aspect of the classical MPC method.

The H_∞ and μ-syntheses [Doyle, A, and Tannenbaum 2009; Skogestad 1996; Vidyasagar and Kimura 1986] provide a frame in which one can perform a multi-objective optimization based on multiple sensors measurements including the lidar, while ensuring compliance with robustness constraints and system's limitations. Unlike MPC, closed loop stability and robustness can be imposed with these methods, and the on-line computational cost is much lower because the controllers are obtained off-line. Already used for robust GLA with classical sensors [Zeng, Kukreja, and Moulin 2012; Cook, Palacios, and Goulart 2013; Ferrier et al. 2018], the application of H_∞ to lidar-based GLA has been proposed in [Khalil and Fezans 2019] where the additional loads reduction obtained with a noiseless lidar was assessed on a simple sailplane model including two elastic modes, without robustness constraints.

4.1.2 Active Gust Load Alleviation: objectives and constraints

The main objective of active GLA, as the name suggests, is to reduce the loads due to the wind using the available sensors' measurements by using the aircraft control surfaces. This can be broken

down into different sub-objectives: the first is the reduction of the maximum absolute value of the structural loads (shear force, bending moment, torsional moment) at different locations of the aircraft structure (wings, fuselage, HTP and VTP) in worst case scenarios. The worst case scenarios, already mentioned in section 2.1, will be clearly defined in section 4.2.4. The GLA laws implemented on current generations of aircraft focus on this objective, by reducing the maximum positive value of the bending moment. A second sub-objective is to attenuate the dynamical response of the aircraft at different frequencies, reducing the structural vibrations, stabilizing the aircraft, and improving the passengers comfort. The ability of the pilot to correctly read the flight data and to command the aircraft are also affected by the cockpit's vibrations, and the replacement of traditional analogical controls by digital touchscreens in future generations of aircraft amplifies the need to attenuate the high-frequency effects of turbulence. The dynamical load factor (acceleration) plays an important role in the comfort and motion sickness, as explained in section 2.3.7, and is strongly correlated with loads (ex: vertical load factor and wing bending moment). These objectives then roughly come down to reducing the PSD (see section 2.3.10) of the loads and load factors as response to extreme winds, in worst case flight conditions. A diminution of the highest peak of the PSDs lead to a decrease of the maximum loads, and attenuating the higher-frequency peaks suppresses the structural vibrations. The main constraints in achieving these objectives are the control surfaces and sensors limitations, described in section 2.1.5. The mathematical models used to define these limitations are kept simple, and described in the different applications studied in this work.

4.2 Strategy for active Gust Load Alleviation

This section presents the methodology employed in this work for the design of a GLA strategy.

4.2.1 Control complexity

This work always seeks simplicity in the control strategy, to favor practical implementation of GLA in the future. Several elements participate in the control simplicity. First, simple control laws should be favored: low-order functions, using a minimum number of inputs and outputs are preferred. Simple gains from selected measurements to some meaningful control surface would be ideal to this effect. However, the gain in performance of using state-space models with multiple inputs and outputs make them attractive. Their order should then be as low as possible if it does not lead to a significant loss of performance. Preferring simple control laws has several impacts on the overall GLA strategy design. It makes the closed loop analysis easier: when a low number of inputs/outputs combinations are used, simple SISO analyses can be conducted, looking at Bode diagrams for instance and computing classical gain and phase margins. Another example is the constrained MPC, which cannot be expressed in a closed form, making the closed loop analysis more complicated. Furthermore, high-order laws are generally associated to more important hid-

den dynamics. For instance, a high-order state-space model has many states whose values are not directly measured, and do not have a physical interpretation. It is therefore not straightforward to guarantee that they will not have detrimental effects on the closed loop dynamics in certain conditions. Another effect of using simple control laws is the easier implementability on onboard computers. Today's computers can easily handle gains and low-order SISO transfer functions, and could in the near future allow the implementation of low-order MIMO state-space models. Online optimization, as done with MPC, and nonlinear control laws could require additional decades to be certified and implemented on commercial aircraft. Finally, simple control laws tend to be more robust than complicated ones. The latter will more naturally give optimal solutions to a given problem, similarly to an interpolation with more degrees of freedom than data points, leading to over-fitting. While it is not true that high-order controllers are systematically less robust, they require more effort by the control designer to obtain similar level of robustness.

Another aspect affecting the complexity of the GLA strategy regards the number of sensors and actuators used. In addition to increasing the complexity of the control laws, using more control surfaces has an impact on the aircraft design. Indeed, in addition to the ailerons, elevators and rudder needed for the flight control of the aircraft, other control surfaces could be added in future designs, specifically for GLA. With its 23 pairs of ailerons, the XRF1-HARW model used in this work allows the study of different configurations with more actuators than in a classical aircraft. Looking for the ailerons that maximize the load alleviation performance allows finding effective configurations, in which a small number of control surfaces are dedicated exclusively to GLA. In the results presented in this work, different control laws of various complexity are compared. Considering the ailerons configuration, 8 out of the 23 pairs are used, situated in the middle of the wing (positions 7 to 14 span-wise from the wing root). This choice is partly motivated by Fig. 2.17 of chapter 2, where the effectiveness of the different ailerons was compared. Other studies have been conducted based on closed loop performance, and are not shown in this work for the sake of conciseness. The 8 ailerons are split into two groups of 4, to reduce the number of controlled variables. Considering the measured variables used by GLA controllers, the pitch velocity and vertical acceleration at the center of gravity have proved to provide sufficient observability of the relevant aeroelastic modes. The use of inclinometers, which allow the estimation the structural loads, has not led to performance improvements according to the author's experience, and has therefore be dropped. In addition, the lidar and angle-of-attack sensors provide information on the wind perturbations, and are of major importance for GLA.

4.2.2 Choice of the targeted loads

Ideally, the shear force, bending moment and torsional moment at different locations of the wing, fuselage, HTP and VTP, should be reduced simultaneously thanks to the GLA law. However, this strategy might be counterproductive because a control surface deflection can decrease a certain load and increase another. Furthermore, in order to improve the overall aircraft design, some loads are more meaningful than others. The wing root bending moment is generally considered in GLA

as the main load to minimize, because of the high mass that could be saved by reducing it. As explained in the GLA objectives described in section 4.1.2, the vertical load factor is also of great importance in GLA for the impact it has on the passengers comfort and on the overall aircraft motion. The priority is then given to the wing root bending moment and the vertical load factor, and the other loads are considered secondary: they must be minimized if possible, but not if it has a detrimental effect on the main loads reduction.

The case of the wing root bending and torsional moments is of particular interest in the GLA analysis, because the reductions of these two loads are generally incompatible. This can be physically explained by the fact that an upward aileron deflection locally decreases the lift, hence reducing the shear force and bending moment, but at the same time decreases the wing camber, creating a pitching moment that increases the wing torsion. It is then necessary to conduct a tradeoff between the wing bending moment reduction and the cost it has in terms of torsional moment increase. While the torsional moment may not be included in the controller design objectives, the closed loop post-analysis and simulations should always verify that its value is acceptable. On the contrary, the diminutions of the shear force, bending moment and load factor are globally compatible.

4.2.3 Synthesis and validation models

The synthesis of controllers and the post-analysis and simulations require the use of aeroelastic models of the aircraft. They are obtained with techniques developed in chapter 3. The reduced-order aeroelastic modeling can be considered a part of the controller synthesis. Indeed, depending on the application, the user can decide that losing modeling accuracy in part of the frequency range can be acceptable if it leads to a reduced order for instance. After all, the H_∞ methods described in appendix D consist in playing with the model to create an augmented plant with the desired frequency response, and this process actually starts with the system identification, where the model can already be shaped in view of the control objectives. In the case of GLA, the accurate aeroelastic poles location is not particularly meaningful, contrarily to the AFS case studied in chapter 5. The accuracy of the input/output frequency response approximation is the main figure of merit for the models used in GLA synthesis. In order to reduce the order of the state-space models, a specific frequency range is selected, between approximatively 0.1 Hz and 5 Hz. At higher frequencies, the effect of the wind is considered negligible, as seen on the PSD responses studied in section 2.3.10 and due to the high-frequency roll-off of the wind dynamics, clearly seen on the Von Kármán turbulence profile of Fig. 2.7. The upper frequency limit of the range of interest could also be lowered, arguing that the actuator's dynamics start rolling-off at about 1 Hz, and consequently frequencies higher than about 3 Hz are difficult to control. At frequencies lower than 0.1 Hz, the wind has no effect on the loads, and other controllers are specifically designed to control the aircraft altitude and attitude in this range. Additional considerations regarding the interaction of GLA with flight control are discussed in section 4.2.5. The dynamics of interest for GLA are then mainly due to the flight dynamics aeroelastic modes (the short-period mode in

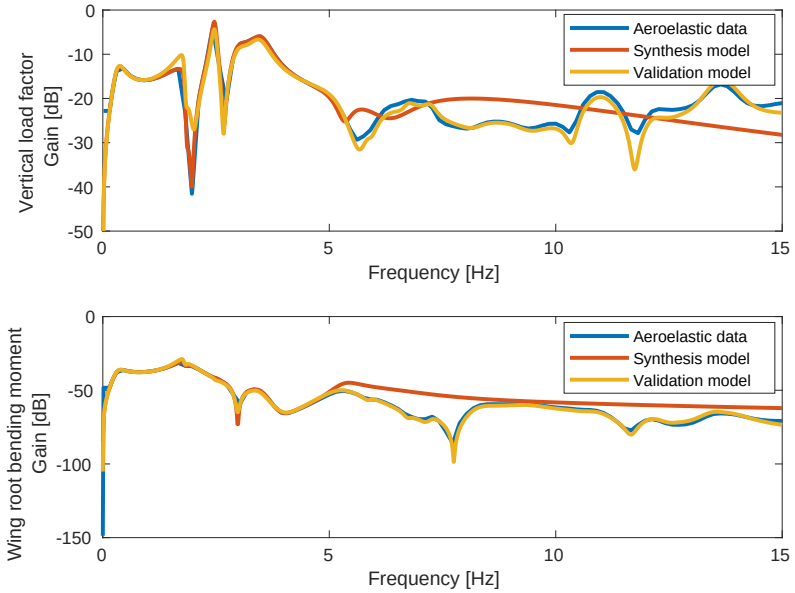

Figure 4.1: Comparison of input/output frequency response data with wind velocity input obtained with aeroelastic equations, synthesis model (40-th order with Loewner method) and validation model (GAF rationalization with Roger method). Numerical values are normalized

longitudinal dynamics) and the first structural modes, the peak response to a wind gust being generally strongly influenced by the first wing bending mode at about 1 Hz. A further reduction in the aeroelastic model used for synthesis is obtained by splitting the longitudinal and lateral dynamics. This work focuses on the former, as the longitudinal loads have a higher impact on the aircraft design than the lateral loads. Following the considerations discussed in section 4.2.2, the priority is given to the wing bending moment and the load factor, but also the torsional moment. These quantities are described by the longitudinal dynamics of the aircraft, and to simplify the analysis, the lateral dynamics will not be studied in this chapter. Note that this will not be the case of the AFS analysis of chapter 5, in which both longitudinal and lateral dynamics are considered. The Loewner method, described in section 3.3.2, is used to identify the synthesis models.

When a controller has been obtained, a post-analysis of the closed loop and simulations must be conducted. In this case, the previous considerations for model reduction are not always valid. Since, in this work, the validation phase requires lower computational resources than the synthesis phase, higher order models can be used with better accuracy in a broader frequency range. This allows the verification that the GLA controllers are correctly designed to work with a model closer to the reality, and not only with a specific reduced model. For example, the controller must guarantee that the high-frequency closed loop poles are stable, with robustness margins, which could not be seen with the synthesis models described above. The method based on aerodynamic forces rationalization by Roger approximation, described in section 3.2, is selected because of the good accuracy of the frequency response and the preservation of some physical quantities, such as the aeroelastic poles location. Fig. 4.1 shows the transfer function from the wind velocity to the vertical load factor and the wing root bending moment directly using the equations of sections

2.3.7 and 2.3.6, compared to the synthesis and validation models. The validation model is of order 1200. The synthesis model is of order 40 and has been identified with data up to 5 Hz, at Mach 0.86 and CAS= 170 m/s. Fig. 4.1 shows that both models are accurate up to 5 Hz, but the validation model maintains a good accuracy up to 15 Hz, and is slightly less accurate than the synthesis model at low frequencies.

When using linear control methods such as the H_∞ framework, the actuators and sensors dynamics included in the augmented plant must be linear too. In post-analysis simulations, nonlinearities can be added to study the effects of actuators saturations and rate limitations.

4.2.4 Choice of the flight conditions

The aeroelastic models obtained in chapter 2 depend on two flight parameters and on the mass configuration. The Mach number and the calibrated airspeed (CAS) are selected to define the flight conditions, following considerations made in section 2.1.3. The Mach number has an important effect on the aerodynamic computation, by modifying the compressible fluid mechanics. The CAS has a direct influence on the aerodynamic forces, which are proportional to its squared value at fixed Mach in first approximation (assuming $\bar{q} \approx \text{CAS}^2$ and neglecting the unsteady effects, see Eq. (2.35)). The GLA strategy developed in this work follows the general ideas of official certification documents for commercial aircraft, such as the European CS-25 [European Aviation Safety Agency (EASA) 2007]. The conditions leading to the worse case that can possibly happen in an aircraft lifetime are selected. While some studies are performed at fixed Mach, CAS and mass configuration for the sake of clarity, some syntheses and closed loop analyses are performed using different aeroelastic models. In this case, the CAS is fixed at a value imposed by the certifications, considering that lower values lead to lower loads (see section 2.1.3 for more details). Different mass configurations and values of the Mach number are considered, as there is no clear indication that one case leads to the highest loads. This strategy goes in the direction of practical industrial implementation of controllers in commercial aircraft.

4.2.5 Interaction with the flight control laws

The integration of a GLA controller into a flight control system is an important topic when considering a possible implementation on future commercial aircraft. This work mainly focuses on the aspects related to load alleviation, and the techniques that enable it, and considers the interaction with flight control in a very simplified way. Future works could take over this study and consider the GLA from a systems-oriented point of view, studying in more details the interaction with the flight control laws existing in a commercial aircraft. A first consideration can be discussed regarding the altitude keeping. This task is carried out in commercial aircraft by the pilot, who can act on the stick to give a vertical load factor order n_z^{pilot}, which serves as an output reference to the longitudinal flight control law, based on a feedback loop using the elevators as actuators. The pilot

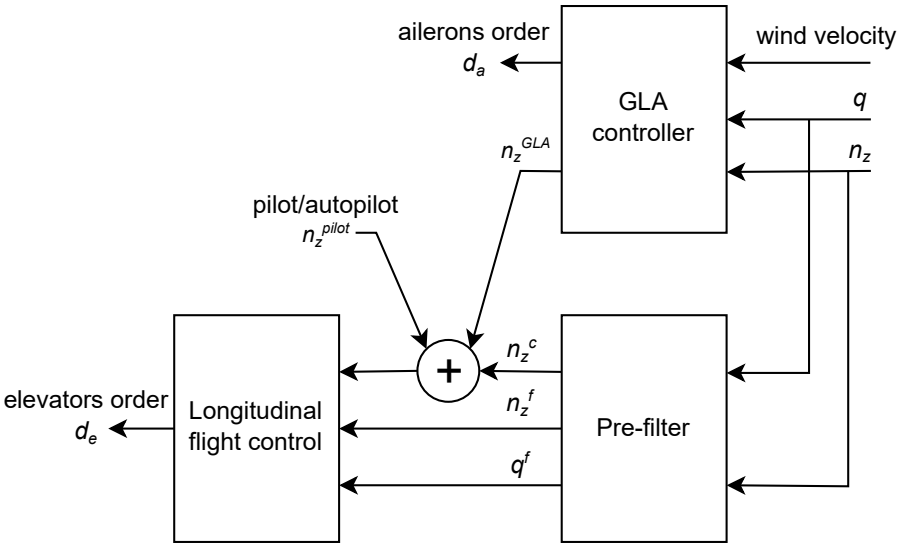

Figure 4.2: Controller architecture with flight control

can be replaced by an autopilot, which automatically computes a vertical load factor reference to follow a given trajectory. The longitudinal control law also uses the measured pitch rate, to improve the aircraft stability and to provide its adequate maneuverability. Additionally, a filter computes a pre-order n_z^c which adds to the pilot order. This works proposes a simple integration of the GLA law into this architecture, as illustrated on Fig. 4.2. The vertical load factor and the pitch rate are used as input, in addition to the wind velocity which can be estimated using the angle-of-attack probe and possible lidar measurements. A direct order is sent to the ailerons, while a reference load factor is computed and added to the pre-order and to the pilot order. A second aspect regards the activation logic of the GLA controller. The question of when to activate it, and how the pilot order could be affected, is open and can be studied in future works. This works makes the assumption that the GLA controller takes over the aircraft commands when it is activated, and that the pilot cannot give orders. It implies that the GLA system is activated in extreme cases, but no considerations on how to trigger it are expressed. While no strict limits are imposed, a gust encounter should not lead to vertical deviations higher than 50 m. As the low-frequency dynamics of the synthesis models are not well represented, no altitude keeping objectives are defined during the GLA synthesis, which does not uses the altitude as input. The vertical deviation is then only checked afterwards, in post analysis.

4.2.6 Maximum load alleviation imposed by certification documents

The certification documents limit the maximum possible loads alleviation that can be obtained using a GLA system. This limit relies on the fact that, although the maximum loads can be reduced, there is a probability that the GLA system fails and special conditions apply in this case. In the CS-25 document [European Aviation Safety Agency (EASA) 2007], the paragraph 25.302 and appendix K define limitations to the use of any system affecting "structural performance",

such as the GLA. It states that in case the GLA system fails (and the GLA orders are equal to zero), the loads should be lower than the ultimate loads divided by a safety factor SF:

$$\mathcal{L}_{failure} \leq \frac{1}{SF}\mathcal{L}_{ultimate} = \frac{1.5}{SF}\mathcal{L}_{limit} \tag{4.1}$$

recalling that the ultimate loads are the limit loads multiplied by 1.5. Now, if a GLA system is used, the limit loads are those obtained in absence of GLA multiplied by an alleviation factor:

$$\mathcal{L}_{limit} = (1 - f_{GLA})\mathcal{L}_{failure} \tag{4.2}$$

resulting in

$$f_{GLA} \leq 1 - \frac{2}{3}SF \tag{4.3}$$

The safety factor depends on the probability of the GLA system to be in failure mode, at any time. If the probability is lower than 10^{-5}, the safety factor should be equal to one. In this case, the loads cannot be attenuated by more than a third ($f_{GLA} = 33\%$). Any further attenuation would have no effect on the aircraft design. If the probability is higher than 10^{-5}, then the safety factor is higher than one, and the maximum possible loads alleviation having an effect on the aircraft design is lower than a third. These considerations are taken into account during the GLA design: when loads attenuations are much higher than a third, it is worth considering reducing the control effort and increasing the closed loop robustness, or reducing the number of control surfaces used.

Remark 2. *This limit affects the total loads, defined as the sum of the equilibrium value and the increment value. Most results studied in this work regard only the latter.*

4.2.7 Presentation of the GLA study

Based on the control design techniques used in the literature for active GLA with or without lidar, which have been presented in section 4.1.1, the main retained direction is robust control. The H_∞ framework has several advantages, such as the closed loop robustness, the possibility to obtain simple controllers, the ease of lidar implementation into this framework, and the flexibility in the control objectives definition. The MPC is also studied because of the optimal performance it can theoretically provide.

This chapter is organized as follows. Section 4.3 describes the process of estimating the wind velocity using a lidar. Section 4.4 then reviews a simplified version of the GLA method implemented on current generations of aircraft, consisting in statically deflecting the ailerons upwards to decrease the local lift and alleviate the wing bending moment. Section 4.5 introduces a first robust GLA implementation based on the H_∞ and μ-syntheses, and some lidar sensitivity studies are carried out concerning the optimal measurement distance and the effect of noise and offset. Several types of closed loop robustness are analyzed, and the capability to reduce several loads at the same time is assessed. Finally, section 4.6 studies another robust approach, based on multi-model H_2/H_∞ synthesis. It focuses on the capability of reducing the maximum loads that can be faced

by an aircraft in different flight and mass conditions, thanks to the synthesis of controllers using several aeroelastic models simultaneously. Section 4.7 then studies an MPC approach for GLA control synthesis, with or without lidar. An ideal adaptive variation of the MPC is also proposed for comparison, in which the aeroelastic model used for the online optimization is always adapted to the current flight conditions and mass configurations. Finally, an overall comparison of these different control strategies for GLA is carried out in section 4.8 using multi-model post-analysis tools based on correlated loads envelopes.

4.3 Wind velocity estimation from lidar measurements

The lidar plays an important role for turbulence detection and GLA. This section describes the nature of the lidar measurements and how they can be used to estimate the wind velocity ahead of the aircraft. Fig. 4.3 sums up the different elements of this description, following the model used in this work. The lidar, located at the nose of the aircraft (point A_0), sends four laser beams in different directions forming a cone shape that can be considered as rigidly connected to the structural points located at A_0. The measurement are performed at the vertices of the cone's base, called A_1 to A_4, which lie in a plane perpendicular to the X-axis at a distance L_{lidar} of the nose. At each point A_i, the wind has a velocity vector called $\boldsymbol{V_{w/A_i}}$. By Doppler effect, the lidar measures the orthogonal projection of the relative velocity between the air at each point A_i and the point A_0 on the A_0A_i line:

$$V_i = -\left(\boldsymbol{V_{w/A_i}} - \boldsymbol{V_{A_0}}\right) \cdot \frac{\boldsymbol{A_0A_i}}{\|\boldsymbol{A_0A_i}\|} \tag{4.4}$$

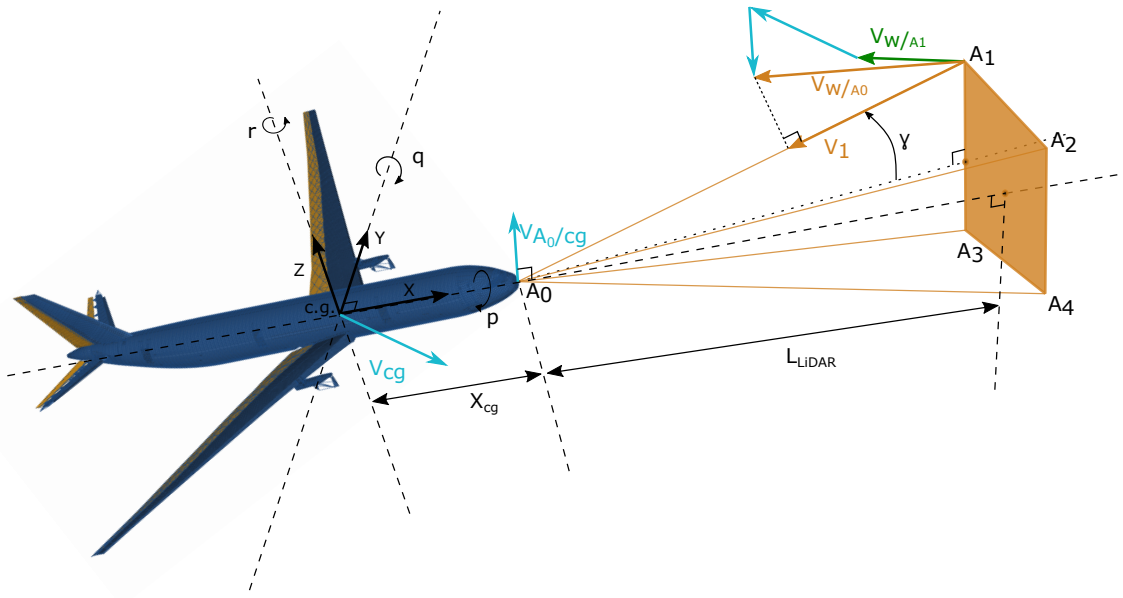

Figure 4.3: Description of the lidar measurements

where V_i is the lidar measurement, $\boldsymbol{V_{A_0}}$ is the velocity vector of the structural points A_0, $\boldsymbol{A_0A_i}$ is the geometrical vector from A_0 to A_i and "$\cdot$" is the dot product. Note that the delay due to the light traveling to points A_i and back to A_0 is negligible. By calling γ the half aperture angle of the cone, supposed to have a squared base, the vector $\boldsymbol{A_0A_i}$ has the following coordinates in the body frame:

$$\frac{\boldsymbol{A_0A_i}}{\|\boldsymbol{A_0A_i}\|} = \begin{Bmatrix} \sqrt{\cos^2\gamma - \sin^2\gamma} \\ \pm\sin\gamma \\ \pm\sin\gamma \end{Bmatrix}_b \tag{4.5}$$

with different signs for the four points. The velocity of the point A_0 can be obtained by the aeroelastic model (2.41), but it is not directly measured. We split it in two parts:

$$\boldsymbol{V_{A_0}} = \boldsymbol{V_{A_0/c.g.}} + \boldsymbol{V_{c.g.}} \tag{4.6}$$

where $\boldsymbol{V_{A_0/c.g.}}$ is the relative velocity of A_0 with respect to the center of gravity and we assume hereby that the fuselage is rigid and that the center of gravity is located on the X-axis:

$$\boldsymbol{V_{A_0/c.g.}} \approx \begin{Bmatrix} p \\ q \\ r \end{Bmatrix}_b \times \begin{Bmatrix} X_{cg} \\ 0 \\ 0 \end{Bmatrix}_b = \begin{Bmatrix} 0 \\ rX_{cg} \\ -qX_{cg} \end{Bmatrix}_b \tag{4.7}$$

where $\times$ is the cross product. This gives an approximation of the relative velocity of A_0 with respect to the center of gravity that includes the angular velocity, which are measured by the aircraft. This does not mean that the effects of flexibility are totally neglected, as the value of the rotation rates are influenced by the aeroelastic effects. Finally, expressed in body axes, the relative velocity of the wind at A_i with respect to the center of gravity is expressed as

$$\boldsymbol{V_{w/A_i}} - \boldsymbol{V_{x.g.}} = \begin{Bmatrix} v_{x,i} - V_x \\ v_{y,i} - V_y \\ v_{z,i} - V_z \end{Bmatrix}_b \tag{4.8}$$

where $v_{x,i}$, $v_{y,i}$ and $v_{z,i}$ are the components of the wind velocity at point A_i, and V_x, V_y and V_z are the components of the center of gravity velocity, in the body frame. Combining the previous equations, the lidar measurements are approximated as

$$V_i = \sqrt{\cos^2\gamma - \sin^2\gamma}\,(V_x - v_{x,i}) \pm \sin\gamma\,(V_y + rX_{cg} - v_{y,i}) \pm \sin\gamma\,(V_z - qX_{cg} - v_{z,i}) \tag{4.9}$$

If we assume that the aircraft velocity is known and that the wind velocity is the same at each location A_i, the three unknowns v_x, v_y and v_z can be obtained by solving this system of four

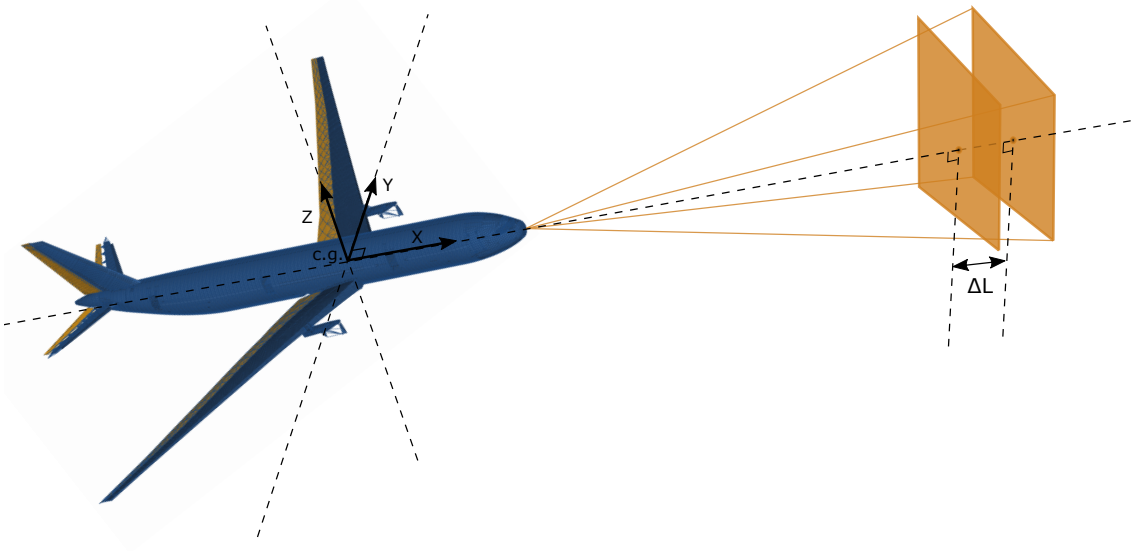

Figure 4.4: Description of the lidar delay due to measurement acquisition

equations:

$$\begin{Bmatrix} v_x \\ v_y \\ v_z \end{Bmatrix}_b = \begin{Bmatrix} V_x \\ V_y + rX_{cg} \\ V_z - qX_{cg} \end{Bmatrix}_b - \begin{bmatrix} \sqrt{\cos^2\gamma - \sin^2\gamma} & +\sin\gamma & +\sin\gamma \\ \sqrt{\cos^2\gamma - \sin^2\gamma} & -\sin\gamma & +\sin\gamma \\ \sqrt{\cos^2\gamma - \sin^2\gamma} & +\sin\gamma & -\sin\gamma \\ \sqrt{\cos^2\gamma - \sin^2\gamma} & -\sin\gamma & -\sin\gamma \end{bmatrix}^{\dagger} \begin{Bmatrix} V_1 \\ V_2 \\ V_3 \\ V_4 \end{Bmatrix} \tag{4.10}$$

where $\boldsymbol{A}^{\dagger}$ is the left pseudo-inverse of a generic matrix $\boldsymbol{A}$. A few remarks can be made:

Remark 3. *Eq.* (4.10) *does not depend on the measurement length* L_{lidar}*. The relative velocity of the points* A_i *and the air when the cone rotates around its vertex and swipes different directions does not have any effect on the measurement, because of the way the lidar works.*

Remark 4. *The roll motion of the aircraft does not have a direct effect on the lidar measurement.*

Remark 5. *An error on the measurements* V_i *would have a* $\frac{1}{\sin\gamma}$ *effect on the* v_y *and* v_z *estimations, while it would have a (lower)* $\frac{1}{\cos\gamma}$ *effect on the* v_x *estimation.*

Finally, one must account for a delay in the wind velocity acquisition. As illustrated in Fig. 4.4, instead of measuring instantaneously the wind velocity, the lidar performs a continuous measurement on a distance ΔL traveled by the airplane, and the actual velocities V_1 to V_4 correspond to average values on this distance. The process described in Eq. (4.10) then estimates the mean value of the wind velocity in the volume that separates the two squares by a distance ΔL. This can be modeled as a time delay $\frac{\Delta L}{TAS}$ in the wind velocity data acquisition, of the order of a few hundredths of seconds.

4.4 GLA by static ailerons deflection

The current generation of aircraft already implements load alleviation functions. They generally consist in static upward deflections of ailerons when high-velocity winds are detected, and static elevators deflections to counteract the induced pitching moment. The objective is not to stabilize the aircraft and attenuate the aeroelastic response, as done in this work, but rather to protect the wing from too high maximum positive bending moments. Indeed, the total bending moment is the sum of a steady term included in the equilibrium defined in section 2.3.3 and of a dynamic increment. During cruise, the steady term is positive because the lift on the wings is higher than their weights, resulting in a positive net force. By deflecting the ailerons upward, the objective is then to reduce this force and limit the maximum positive bending moment. Note that this strategy also tends to increase the torsional moment of the wing, similarly to what has been observed before. This section studies this strategy, in order to provide a comparison with the techniques developed in this work. Moreover, the static ailerons deflection technique has been implemented on commercial aircraft with relatively low aspect ratio. Implementing it on the flexible XRF1-HARW, which presents a high aspect ratio and a low torsional stiffness, also allows the study of the effects of flexibility on this technique.

Time simulations of the response to a 107 m discrete gust are shown in Fig. 4.5, comparing the case without GLA and the case in which the ailerons are statically deflected upwards, with the flight control law active. They are performed at Mach 0.5 with an empty aircraft, at CAS=VMO= 170 m/s. At $t = 0$ s, a 15° upward deflection of the ailerons is ordered. The actuators dynamics and rate limit lead to a short setting time before reaching the desired angle. The same two groups of ailerons, used for robust dynamic GLA and defined in section 4.2.1, are selected here. A static downward increment of elevators deflection is commanded in order to compensate the pitch rate created by the ailerons. The compensation can be computed thanks to the relative values of the moment coefficients $C_{m_{\delta a}}$ and $C_{m_{\delta e}}$ of the ailerons and elevators respectively. Moreover, the flight control law gives an additional order to the elevator in order to bring the vertical load factor to zero. After about 10 s, it can be seen that the pitch rate and vertical load factor are equal to zero, and the aircraft is then in a new equilibrium. When setting the ailerons angles, the elevators do not provide enough degrees of freedom to maintain all the variables at zero in this new equilibrium, and a new positive value of the angle-of-attack is obtained, hence creating a positive lift which compensates the total vertical force created by the ailerons and the elevators. A vertical velocity is associated to this new state, as seen in Fig. 4.5 (h) with a linear increase of the altitude, and a positive climb angle, as seen on the pitch angle response (g). Considering the loads, the main objective of reducing the steady value of the root bending moment is reached, as seen on 4.5 (d) with a negative increment. The natural consequence of this is an increase of the equilibrium value of the torsional moment (i). At 10 s, after the aircraft has reached its new equilibrium, it is struck by a 107 m gust. The bending and torsional moment caused by the wind are simply translated compared to the case without GLA. The vertical load factor response is nearly the same in the new equilibrium with static deflections as in the case without controller. The increase of the pitch

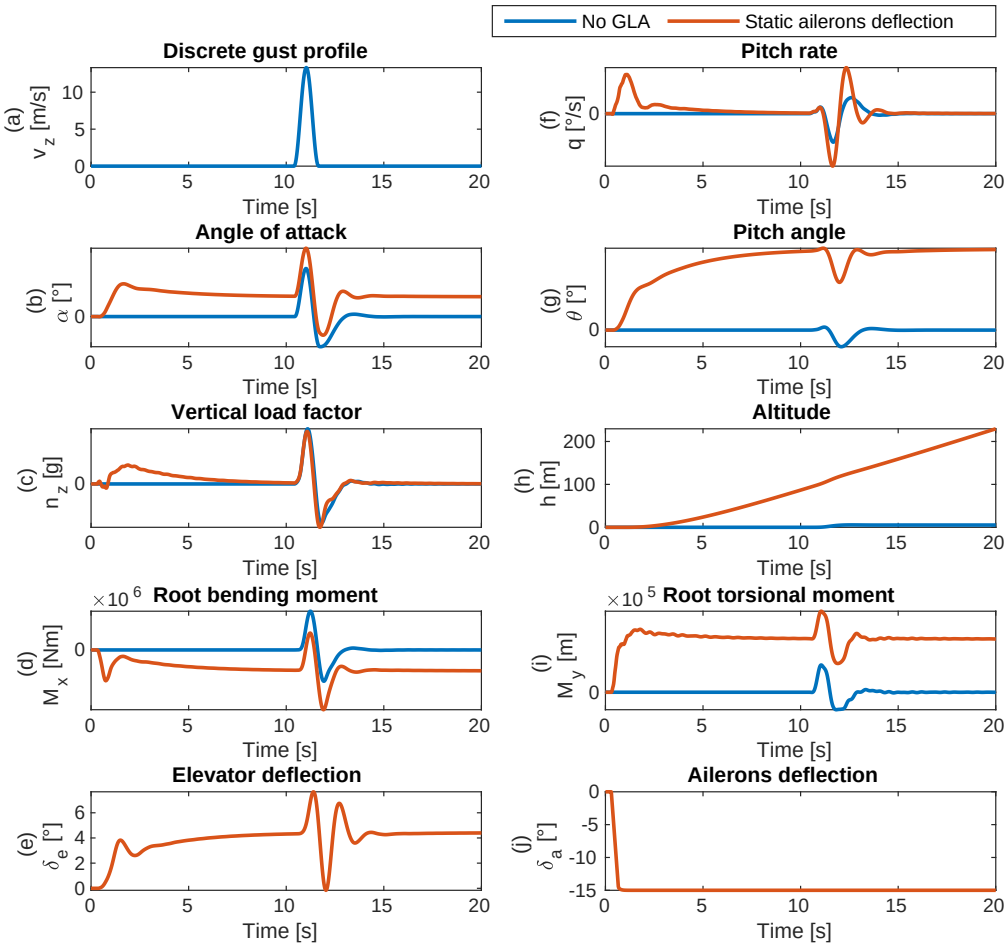

Figure 4.5: Time response to a 107 m discrete gust with static ailerons deflections and flight control law, in comparison to case without GLA

rate response, is mainly due to the presence of the flight control law. The case in which only this law is present has been simulated and is not shown for the sake of conciseness.

The limits of this approach can be appreciated in Fig. 4.5. The transient response to the gust is not affected by the static deflection, and the vertical load factor response is unaffected. Only the positive bending moment is reduced, while there is a risk of increasing the negative values if a high ailerons deflection angle is selected. Furthermore, in case an aeroelastic mode presents a low damping ratio, the resulting sustained oscillations would not be suppressed. Finally, an important modification of the trajectory can be noted, with a 200 m increase of the altitude in only 20 seconds. This could limit the maximum acceptable ailerons deflection, hence reducing the loads attenuation.

The time simulations shown in Fig. 4.5 assume that the gust reaches the aircraft when it is already in equilibrium. It is also of interest to understand what happens if the gust occurs in the transient phase, shortly after the ailerons have started deploying. Fig. 4.6 shows the results of

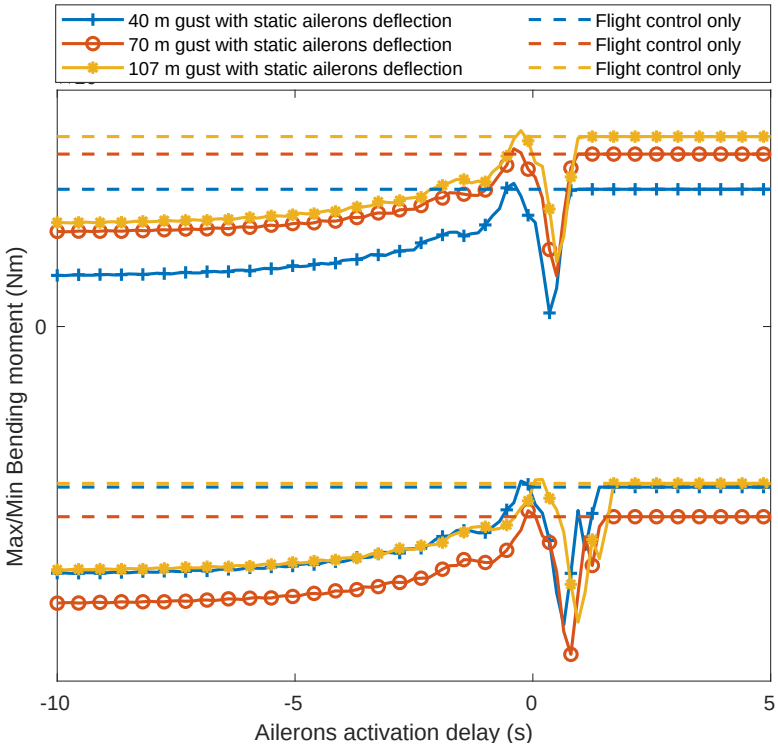

Figure 4.6: Maximum and minimum bending moment in response to positive discrete gusts for various activation delays of the ailerons deflections

several simulations performed with different delays of the ailerons activation, and for three positive discrete gusts of 40 m, 70 m and 107 m. An empty aircraft flying at Mach 0.5 is considered here. A delay of 0 s means that the deflection order is sent to the ailerons at the moment the discrete gusts starts growing on the nose of the aircraft. A negative delay means the order has been sent before the gust has arrived, and vice versa. The curves on the upper part of Fig. 4.6 are the maximum bending moments in each simulation, and those on the lower part are the minima. The dashed lines are the minimum and maximum bending moments obtained in absence of ailerons deflection (in all cases the flight control law is activated). The left asymptote of the full-line curves are associated to the case the equilibrium has been reached before the gust occurs. Due to the relatively low gains of the flight control law, the aircraft takes time to reach a new equilibrium after the ailerons and elevators are deflected, which can result in a loss of total bending moment reduction, as seen on the left part of the figure. The interaction of the transient response due to the ailerons and the gust, for delays between 0 s and 2 s, is of particular interest. When the GLA order is given at the exact moment the gust reaches the aircraft nose, the bending moment reduction is low. On the opposite, a high bending moment reduction is obtained for a particular timing of ailerons activation, starting about 1 s after the gust strikes the aircraft nose. Minimum (negative) bending moments approximately follow the same trend. This optimal timing could be of interest if an isolated gust were to occur, without prior wind triggering the GLA system. This is, however, purely theoretical as the results are valid for a specific gust profile, that is not likely to occur in real life. What this analysis really shows is that the deflections of ailerons for GLA should

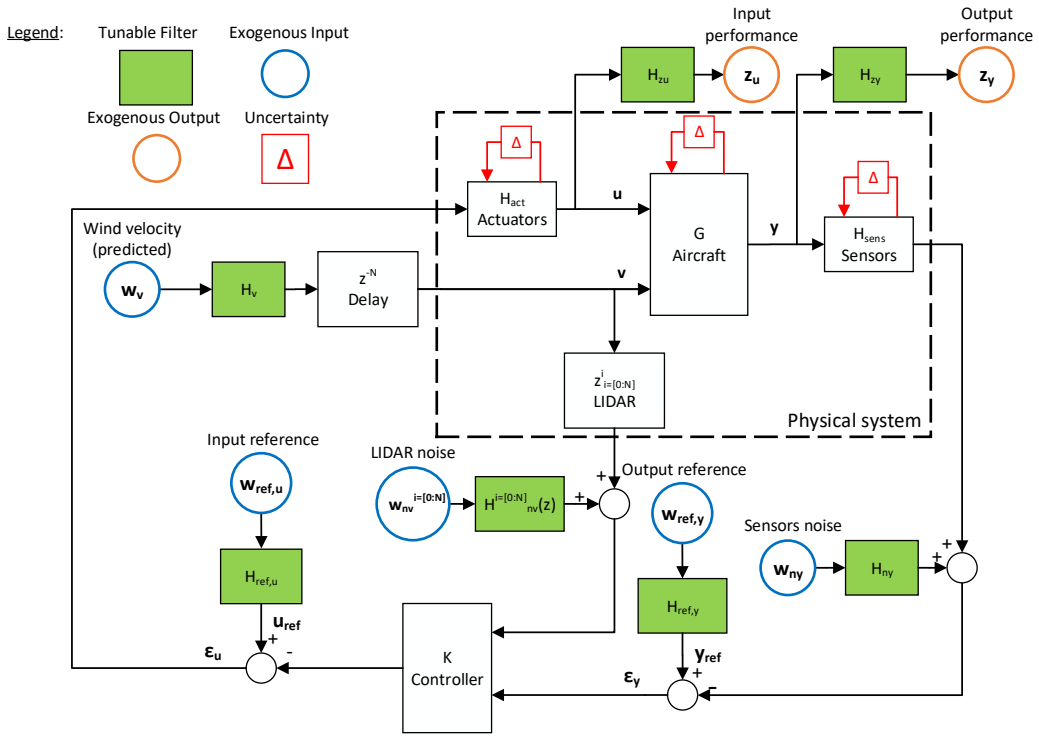

Figure 4.7: Augmented system used for the H_∞ and μ-syntheses

be done in the full knowledge of the interaction between the wind and the aeroelastic dynamics of the aircraft in order to design an effective and secure GLA system. This is an argument for using dynamic model-based control laws such as those obtained with the robust syntheses of sections 4.5 and 4.6.

4.5 Robust GLA using μ-synthesis

4.5.1 H_∞ and μ-syntheses for the flexible aircraft equipped with lidar

The H_∞ and μ-syntheses frameworks described in appendix D are applied to the flexible aircraft equipped with a lidar. The detail of the augmented plant $\boldsymbol{P}$ from Fig. D.4 is shown in Fig. 4.7. By reducing the H_∞ norm of the full system, the influence of each exogenous input to the exogenous output is reduced. The augmented plant $\boldsymbol{P}$ shown in Fig. 4.7 consists of

- the aircraft aeroelastic model G
- the actuators and sensors dynamics
- the lidar sensor noted as pure delay $z^i_{i=[0:N]}$.
- the exogenous input $\boldsymbol{w}$ and output $\boldsymbol{z}$ and their associated tunable filters.

The uncertainties are written in a general form, they can be of different types as explained in section 4.5.1.4. The aircraft model G is normalized in input and output. In addition to improving the numerical convergence of the algorithms, this allows the comparison of the relative values of the entries of the performance output $\boldsymbol{z_y}$. The details of the different components of the augmented plant are shown in Fig. 4.7. The filters and exogenous inputs and outputs are chosen in such a way as to define the GLA problem similarly as in appendix D in terms of a performance criterion and associated constraints. The next sections explain their design in more details.

4.5.1.1 Gust Load Alleviation performance

The main objective of the controller synthesis as explained in section 4.1.2 is the gust load attenuation. It can be summarized as reducing the influence of the wind velocity $\boldsymbol{v}$, taken here as the vertical wind alone, towards the loads. Contrarily to $\boldsymbol{y_{sens}}$ the output $\boldsymbol{y_{loads}}$ is not measured, hence it cannot be used by the controller. However, by including $\boldsymbol{y_{loads}}$ in the exogenous output $\boldsymbol{z_y}$, the controller is designed in such a way as to minimize the loads with the knowledge of the sensors output $\boldsymbol{y_{sens}}$ only. The synthesis of a gust load alleviating controller is then performed as follows. The transfer function H_v of Fig. 4.7 takes the frequency content of the worst case vertical wind. A third order approximation of a von Kármán turbulence with worst case amplitude is considered here. The numerical values can be found in section 4.5.2. With an appropriate output normalization of variable $\boldsymbol{y}$, $\boldsymbol{H_{zy}}$ can be taken as the constant diagonal transfer function, with ones only at the output to minimize. As explained in section 4.2.2, only a few selected loads are to be minimized. With this choice of filters H_v and $\boldsymbol{H_{zy}}$, the minimization of the norm $\left\|\boldsymbol{T}_{\boldsymbol{w_v}\mapsto\boldsymbol{z_y}}\right\|_\infty$ can be achieved by H_∞ synthesis. With the full delay z^{-N}, the exogenous input $\boldsymbol{w_v}$ corresponds, after multiplication by its shaping filter H_v, to the predicted wind.

4.5.1.2 Actuators and Sensors

The actuators must be modeled accurately in order to account for the phase delay and the constraints they create. The transfer function matrix $\boldsymbol{H_{act}}$ of Fig. 4.7 represents the actuators dynamics and are modeled by a second order low-pass filter in the Laplace domain

$$\boldsymbol{H_{act}}(s) = \frac{1}{s^2 + 2\xi\omega_0 s + \omega_0^2}\boldsymbol{I}_{N_u} \tag{4.11}$$

where $\boldsymbol{I}_{N_u}$ is the identity matrix of size N_u, the number of actuators, ω_0 and ξ are the actuators' cutoff frequency and damping ratio respectively. Together with the effect of the aircraft inertia, this limits the capability of the controller to attenuate the high frequency response of the aircraft.

In addition to the actuators dynamics, a saturation function is added in the validation setup used for simulations. The control surfaces cannot exceed a certain deflection angle threshold, and their derivative cannot exceed a certain deflection rate threshold. As it will be seen in the results section, the deflection rate saturation limit is the most constraining in the control synthesis

problem. In the H_∞ framework, the maximum deflection angle and deflection rate are imposed as soft constraints through the filter

$$\boldsymbol{H_{zu}}(s) = \begin{bmatrix} \frac{1}{u_{max}} \boldsymbol{I}_{N_u} \\ \frac{s}{\dot{u}_{max}(\epsilon s+1)} \boldsymbol{I}_{N_u} \end{bmatrix} \tag{4.12}$$

where $\frac{s}{(\epsilon s+1)}$ is a pseudo derivative with $\epsilon \ll 1$, and u_{max} and $\dot{u}_{max}$ are the maximum deflection angle and deflection rate respectively. Note that it has been assumed for simplicity that all the control surfaces have the same saturation limits. With an adequate input normalization, this ensures that when the H_∞ norm of the system is lower than one the saturation constraints are respected. In particular, $\|\boldsymbol{T_{w_v \mapsto z_u}}\|_\infty$ must be lower than one with $\boldsymbol{z_u}$ of dimension $2N_u$. Note that these filters are first written in the Laplace domain, and then converted into the z domain.

The sensors are modeled by $\boldsymbol{H_{sens}}$ as a pure delay, accounting for the sensors measure rate and the on-board computer refresh rate:

$$\boldsymbol{H_{sens}}(s) = e^{-\boldsymbol{\tau_{sens}} s} \tag{4.13}$$

where $\boldsymbol{\tau_{sens}}$ is a diagonal matrix of size N_y with delays associated to each sensor on the diagonal. When written in the z-transform domain, this transfer function becomes rational. The tunable filter $\boldsymbol{H_{ny}}$ (see Fig. 4.7) associated with the measurement noise is taken as the diagonal matrix with expected standard deviation of each sensor's noise on the diagonal.

4.5.1.3 Lidar Sensor and Noise

Two types of lidar are considered in this work: the first type only performs a measurement of the vertical velocity at a fixed distance ahead of the aircraft. The measurement is then delayed several times and buffered as in Fig. 4.7, providing the information of the disturbance at all time steps ahead in time over a certain time horizon. The second type of lidar records also intermediate measurements. In the augmented plant, the intermediate measurements are performed at distances $i\,\delta x$ corresponding to each time step i, where $\delta x = V\,T_s$ is the spatial step between two lidar measurements and T_s is the sampling time. In case of a perfect measure (no noise), this makes no difference. The main difference regards the measurement noise, which is assumed to increase linearly with the distance. This assumption is supported by experiments with different existing lidars [Herbst and Vrancken 2016]. With the first type of lidar (single measurement), the noise standard deviation at the i-th step ahead (time or spatial step equivalently) can be written as

$$\sigma_v^i = k_n L \tag{4.14}$$

where L is the measure distance; k_n is the noise per unit distance, which depends mainly on the lidar accuracy, and to a lesser extent on the the aircraft velocity and the atmosphere turbulence, as explained in section 2.2. Note that the noise does not depend on i. In the second type of lidar

(multiple measurements), the noise standard deviation can be written as

$$\sigma_v^i = i\, k_n \delta x \tag{4.15}$$

In this case, the closest measures give less time to react to the incoming wind, but they are more accurate. The standard deviation is then multiplied by a unit variance white noise. The knowledge of the noise amplitude is included in the H_∞ framework by selecting the lidar noise tunable filters as the constant $H_{nv}^i = \sigma_v^i$. The exogenous input $\boldsymbol{w_{nv}^i}$ of Fig. 4.7 can then be considered as white noises.

With the single-measurement lidar, increasing the length of measurement can become detrimental when the noise becomes too high and starts to overcome the performance benefit obtained by increasing the prediction horizon.

4.5.1.4 Robustness with H_∞ and μ-syntheses

The closed loop should be robust in stability and performance. The former kind of robustness is the capability of the closed loop to remain stable when the controlled system changes, whereas the latter regards the guarantee to maintain performance under system variations, by keeping the H_∞ norm less than one. Ensuring robustness with a state space controller with several input and output is more challenging than with classical controllers consisting of gains and filters as used in aeronautics. The controller must be robust to MIMO uncertainties, which apply simultaneously to the various inputs and outputs. As explained in appendix D, MIMO stability robustness can be imposed by H_∞ synthesis, for example by reducing the maximum H_∞ norm of the input and output sensitivity transfer functions, acting on the modulus margins. Another strategy, adopted in this section, consists in adding uncertainties in the augmented plant, and imposing closed loop robustness to these uncertainties by μ-synthesis, both in stability and performance. In absence of a clear definition of the system's uncertainties, one can define general disk uncertainties (see appendix D) which can lead to MIMO generalizations of gain and phase margins.

Practically, uncertain transfer functions are introduced at the input of the actuators and at the output of the sensors as seen on Fig. 4.8. Each of them is composed of diagonal collections of independent SISO disk uncertainties, defined in appendix D. Each disk uncertainty is an unknown

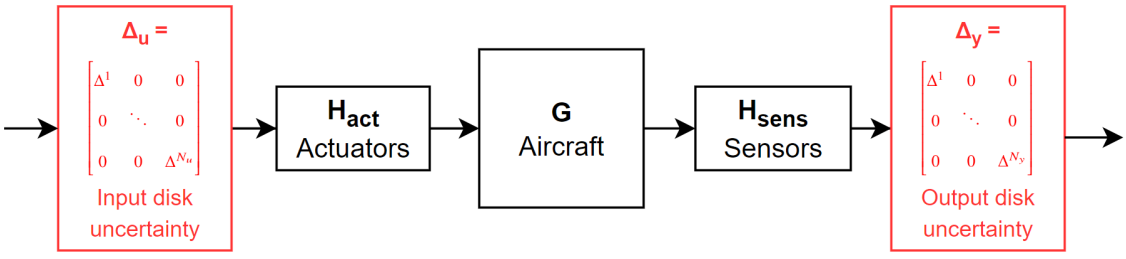

Figure 4.8: Uncertain aeroelastic model with disk uncertainties

complex number with nominal value equal to 1, from which the gain and phase can vary. This framework can be used in different ways for synthesis and analysis. In the most constraining case, independent disk uncertainties are applied simultaneously at each of the input and output ports of the aeroelastic model, with different combinations of gain and phase (the complex number evolves in a disk). This is the case used for synthesis, meaning that the closed loop stability must be imposed and the H_∞ criterion must be minimized in the worst case of simultaneous input and output disk uncertainties. A weaker type of uncertainties is associated to the case in which only gain or phase variations are applied to each disk uncertainty, simultaneously at each input and output port. They lead to the definition of the so-called MIMO gain disk margin, defined by the minimum gain leading to instability when considering combinations of independent gain variations in the various input and output ports. Similarly, MIMO phase disk margins are defined. Multi-input and multi-output phase and gain disk margins are similarly defined, considering only variations in the input ports or in the outputs ports, and are then weaker than their MIMO counterparts. Finally, SISO disk margins are the classical gain and phase margins, considering the variations in a single output or input port of the system.

4.5.2 Simulation setup and studied scenarios

The numerical values used in the simulations are presented in this section and summarized in table 4.1. Some design filters are given in this work by their Laplace transform expression, but they are eventually defined in the z-domain after time discretization of the system with time step T_s equal to 0.02 s. In the control design, the wind is modeled as a 3-rd order approximation of the von Kármán turbulence treated as a transfer function:

$$H_v(s) = \frac{0.02s^3 + 0.3398(L_{turb}/V)^2 s^2 + 2.7478(L_{turb}/V)s + 1}{0.1539(L_{turb}/V)^3 s^3 + 1.9754(L_{turb}/V)^2 s^2 + 2.9958(L_{turb}/V)s + 1} \tag{4.16}$$

The true transfer function associated with the von Kármán PSD (2.8) is of high order and would increase the computational cost of the controller synthesis, so it is only used in simulation. During

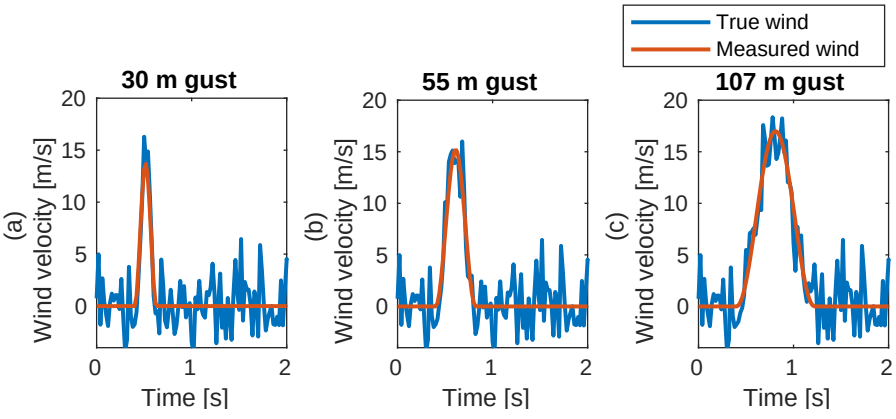

Figure 4.9: Wind velocity with and without lidar measurement noise

Quantity	Symbol	Value
Mach number	M	0.86
Mass configuration	–	Empty aircraft
Altitude	–	9.000 m
Actuators cutoff frequency	ω_0	4 Hz
Actuators damping ratio	ξ	0.85
Maximum deflection angle	u_{max}	30°
Maximum deflection rate	$\dot{u}_{max}$	40°/s
Sensors delays	$\boldsymbol{\tau_{sens}}$	40 ms for each sensor
Lidar measurement distance	L	100 m
Lidar noise coefficient	k_n	0.02 s^{-1}
Discrete gusts gradient	L_{gust}	40 m, 70 m and 107 m
Scale of turbulence	L_{turb}	762 m
Turbulence standard deviation	U_σ	9 m/s
Model order	–	40
Time step	T_s	0.02 s

Table 4.1: Numerical values used in simulations

the controller synthesis, the output of the aircraft system are normalized by the standard deviation of the open loop response to continuous turbulence. When not explicitly specified, the lidar performs one measurement at a time, which is delayed several times to give the wind velocity at intermediary points. This results in a white noise of 2 m/s standard deviation, following the considerations of section 4.5.1.3; the comparison of the wind velocity and the measured wind is shown in Fig. 4.9 for three gusts of different lengths. The measured output of the model are the pitch rate, vertical load factor and angle of attack from sensors. The validation model also includes loads outputs that are not measured by the aircraft, composed of the shear force, bending moment and moment of torsion at 31 locations regularly spaced along the wing span starting at about 10%. Computations have been performed with a 8-core CPU and 32 GB of random access memory, in parallel mode when needed. The design is performed on Matlab thanks to the *musyn* function for unstructured and structured controllers, and the simulations are performed on Simulink. Two important remarks can be formulated.

Remark 6. *The quantities displayed are the increments values, which must be added to the trim quantities of the nonlinear equilibrium described in section 2.3.3 to obtain total values.*

Remark 7. *The open loop case refers to the natural aircraft, in which no control law whatsoever is implemented. In a more complete analysis, the case in which only the flight control law is implemented could be shown too, but this option has been dropped for the sake of conciseness. Compared to the strong GLA strategies studied in this work, the flight control law makes a negligible difference in the aircraft response, as it targets lower frequencies than those involved in the gust and turbulence responses.*

4.5.3 Robust gust loads alleviation with μ-synthesis using a lidar

This section shows time simulations obtained with a robust unstructured controller designed using μ-synthesis. The vertical load factor and the loads (shear force, bending and torsional moments) at the wing root and at the HTP root are all included in the H_∞ criterion to be minimized. By doing so, we can assess the capability of a controller to alleviate different loads at the same time. Disk uncertainties are used to impose stability and performance robustness to MIMO variations: simultaneous gain (up to 1 dB) and phase uncertainties (up to 15°) at different input and output ports simultaneously are used. This is sufficient to obtain large stability margins, as will be explained in the next section. The controller is designed in a way that allows the control surface deflection rates to exceed the theoretical limits of 40°/s when facing the extreme gusts and turbulence. The slight rate saturations implied do not have a significant impact on the performance as studied in section 4.5.7, as long as the closed loop is robust enough. The unstructured controller is of order 171. All the time simulations are performed with the validation models, which includes a saturation and rate limiter.

Fig. 4.10 shows the time response of the aircraft to a 107 m gust (left) and to a continuous turbulence (right). The wind velocity perturbations are shown in (a), with a delay due to the presence of a lidar. The time response of the pitch rate (b), vertical load factor (c) and angle-of-attack (d), the three measurements used by the controller, are also shown. Although the reduction of the pitch rate is not included in the objectives, it is clear that the controller tries to decrease it. A small reduction of the vertical load factor, of about 20 %, can be noted in the gust response. The control surface deflections (e) and deflection rates (f) are shown, with positive angles associated to downward deflections. There is no saturation due to the maximum angle, but the rate limit is reached. The aileron n° 1 is the one closer to the fuselage. The strategy adopted by the controller to reduce different loads simultaneously can be understood from the left of Fig. 4.10. Before the arrival of the gust, the ailerons are deflected downward to create a pitch-down effect, clearly seen on the negative pitch rate. By doing so, the aircraft is preset by orienting it in the direction of the wind, minimizing its effect. The maximum angle-of-attack is reduced to this pitch-down effect, leading to a reduction of the lift created by the wind, as seen on the vertical load factor reduction. When the gusts reaches the aircraft, the ailerons are deflected in the other direction, upward, to provide a local negative lift, which reduces the loads by counteracting the positive force created by the wind.

Fig. 4.11 shows the time response of the loads to the same gust and turbulence. The wing shear and bending moment are first slightly increased: before the gust reaches the aircraft, the downward ailerons deflections create a positive direct lift, in addition to the desired pitch-down moment. The wing root torsional moment is also temporarily decreased during this phase, because of the negative moment induced by this deflection. When the gust reaches the aircraft, the upward ailerons deflections efficiently reduces the wing root shear force and bending moment by direct negative lift, but at the same time creates a positive torsional moment increment. As explained before, the bending and torsional moments cannot be decreased at the same time because of the

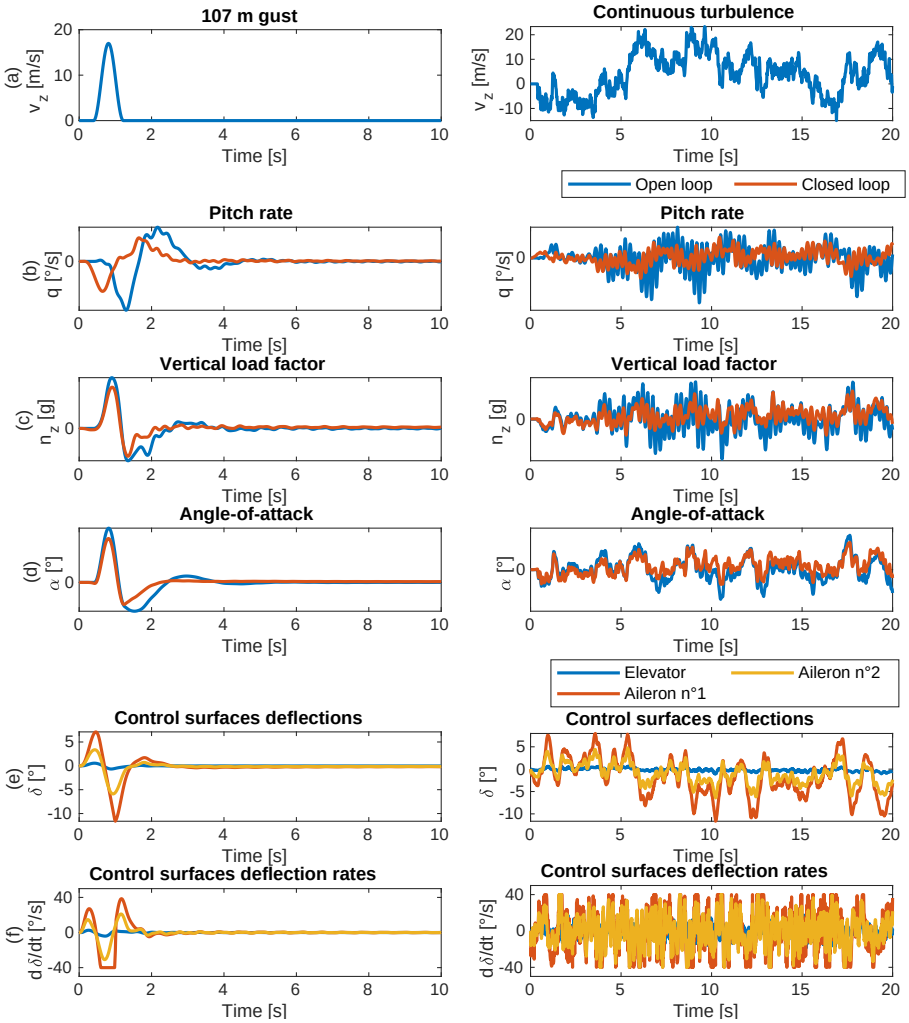

Figure 4.10: Time simulations with full-order μ-synthesis controller with lidar, with vertical load factor, wing root and HTP loads attenuation objective

opposite effect an aileron deflection has on them. The HTP follows approximately the same trend, mainly due to the pitch-down effect as the ailerons do not create direct lift on it. The HTP shear force and bending are strongly alleviated, while the maximum absolute value of torsional moment increases.

An interesting element can be noted on Fig. 4.10 (e): the elevator is almost not used by the controller. This is surprising, as the elevators would be very efficient to tilt the aircraft in the wind direction during the preset phase, before the gust has arrived. A possible explanation would be that the use of the elevator could create loads on the HTP, and since the controller is asked to reduce all the loads simultaneously, including those on the HTP, it decides to use only the ailerons. In order to confirm this explanation, a second controller is designed in the same conditions as the first one, but with only the vertical load factor and the wing root bending moment included in the H_∞ performance objective. Fig. 4.12 shows the time simulations obtained with such a controller.

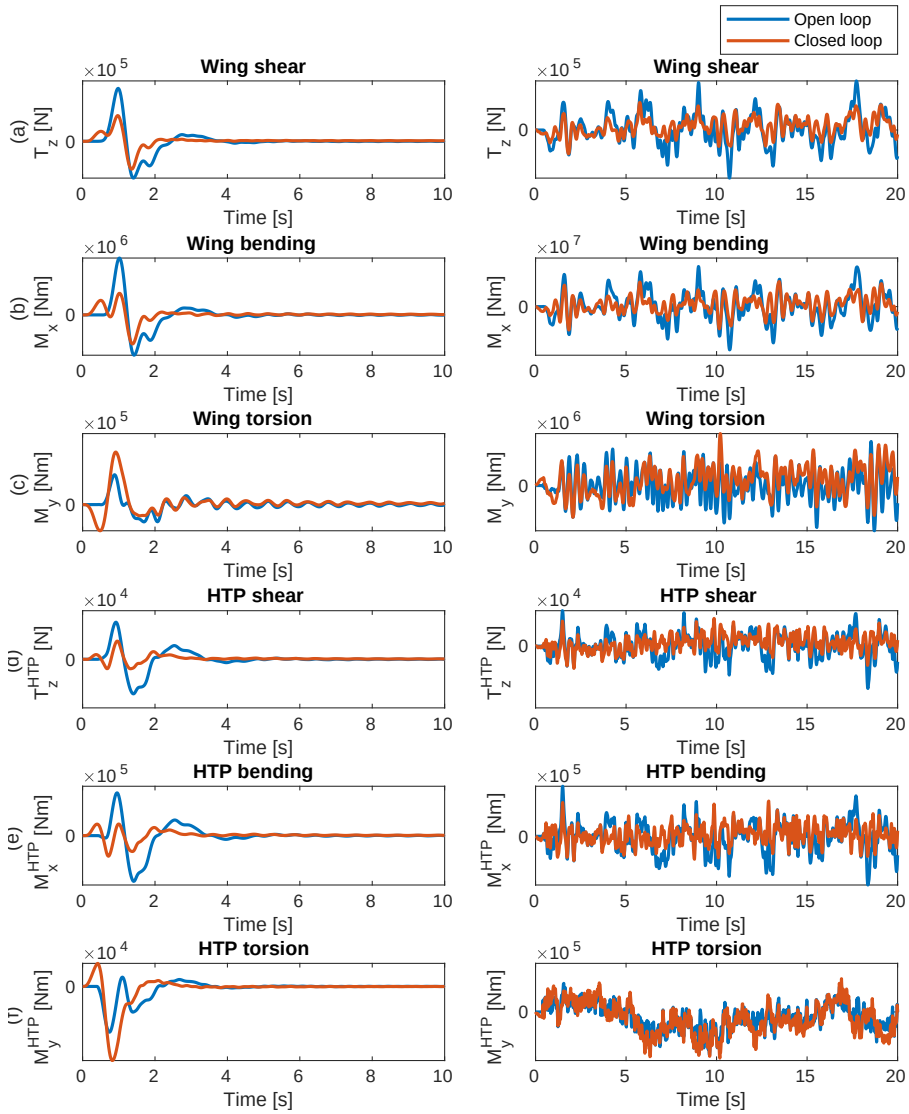

Figure 4.11: Time simulations of loads with full-order μ-synthesis controller with lidar, with vertical load factor, wing root and HTP loads attenuation objective

The global strategy to reduce the loads is the same: first create a negative pitching moment by downward ailerons deflections, and then creating negative direct lift with upward deflections to counteract the loads created by the gust. However, as expected, the elevators are also deflected downward in the first phase to create a pitch-down motion, and are then used in the opposite direction to stabilize the aircraft by counteracting the effects of gust and ailerons. The vertical load factor alleviation is more significant. When looking at the loads on Fig. 4.13, the wing root shear force and bending moment are further decreased compared to the case in which all loads were included in the performance objective. The increase of the wing torsion is also amplified as a side effect. The HTP shear and bending are not reduced anymore, but neither are they increased. This second strategy implies more aircraft motion, using more control surfaces, which results in

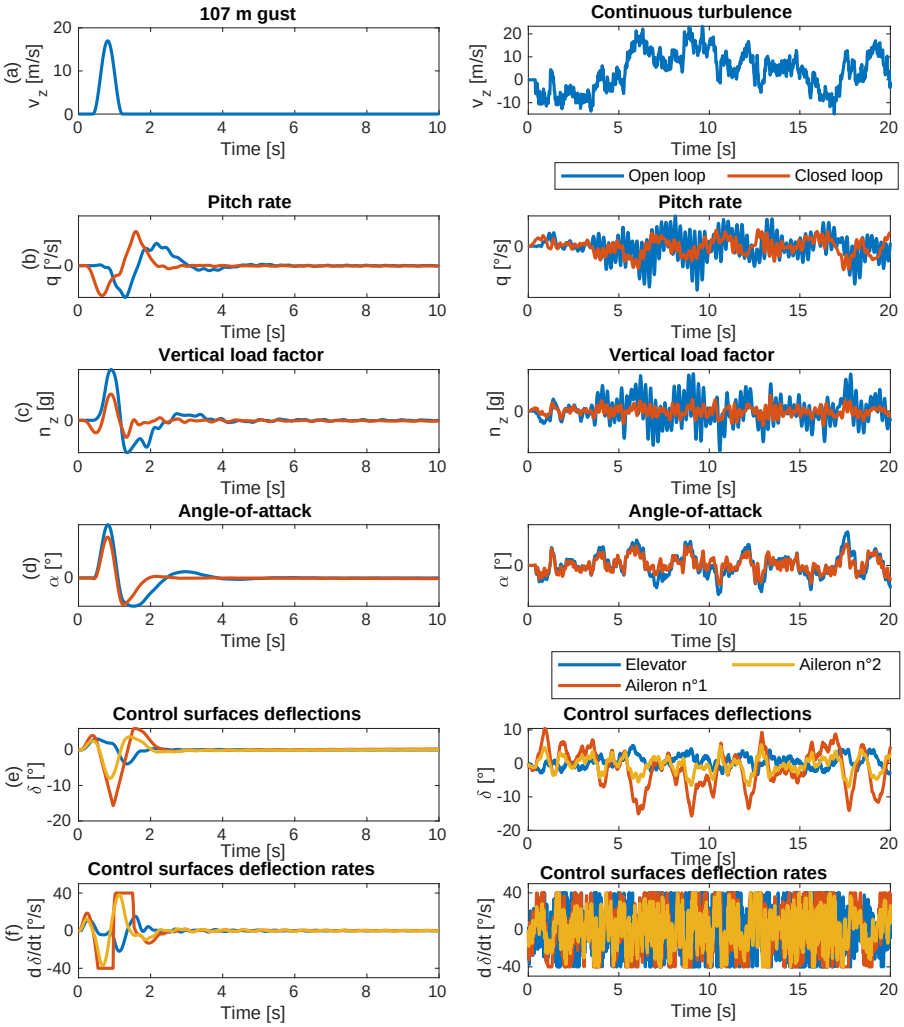

Figure 4.12: Time simulations with full-order μ-synthesis controller with lidar, with only vertical load factor and wing root bending moment attenuation objective

a further alleviation of the targeted loads, but an overall increase in the different loads of the aircraft. Depending on the trade-off decided between the different loads for the aircraft design, either strategy can be possibly adopted.

Finally, a robustness analysis is shown on Fig. 4.14 using the controller minimizing all loads at the same time. In (a), the different control surfaces are considered faulty in turns, with constant zero deflection angle. It can be seen that the system remains stable in case of actuator's fault, and a slight load alleviation remains in the worst case associated to aileron closer to the fuselage. When a sensor is lost (b), the alleviation is almost unaffected and the closed loop remains stable. This is due to the fact that the robust method synthesis used in this section encourages the use of the lidar, as confirmed on (c) where the loss of the lidar sensors leads to a response almost equal to the open loop. The lidar provides a direct measurement of the perturbation, with anticipation, and is then very efficient for GLA. Furthermore, the feedforward part of the controller, associated

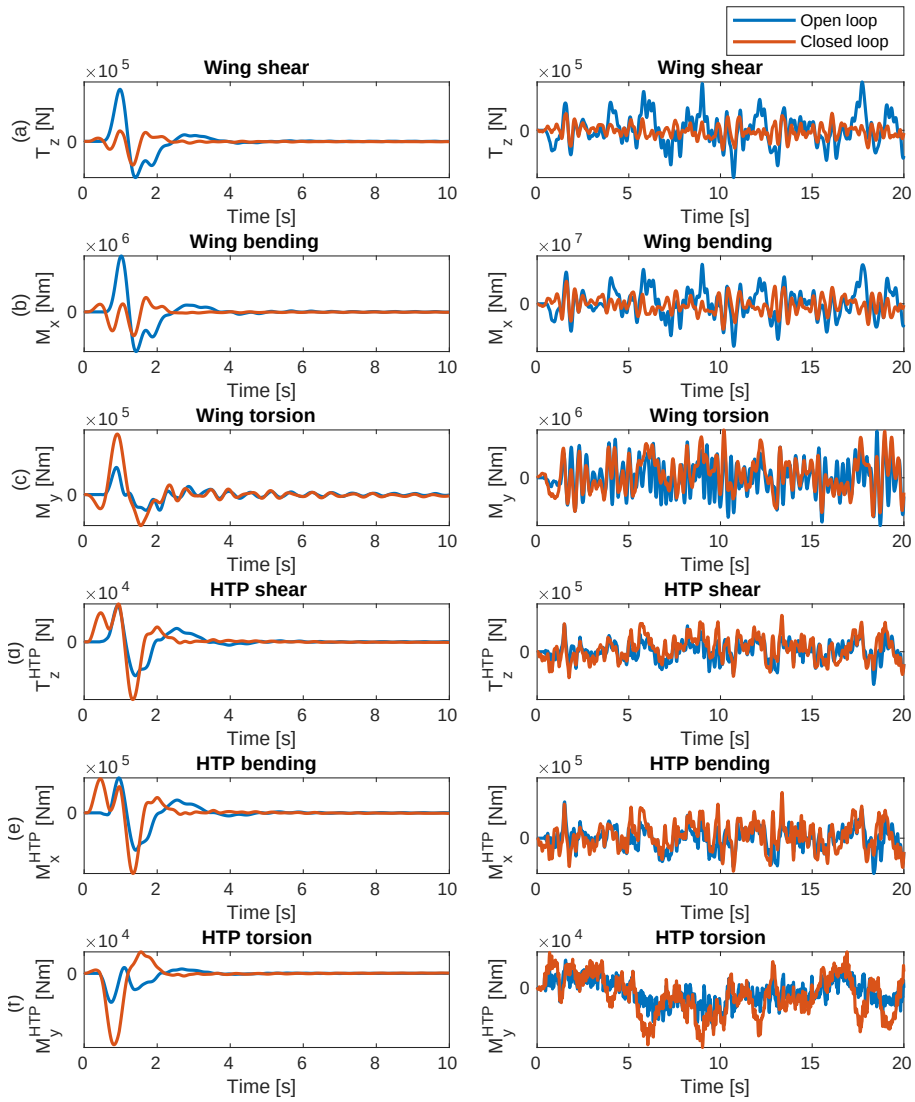

Figure 4.13: Time simulations of loads with full-order μ-synthesis controller with lidar, with only vertical load factor and wing root bending moment attenuation objective

to the lidar measurement, is not included in a closed loop, and in consequence it does not affect the system's stability. It is then easier to ensure stability robustness when using feedforward control than when using its feedback counterpart. The robustness capabilities of the controllers are further studied in the next section.

4.5.4 Multi-load attenuation capability of different robust controllers

This section compares different controllers based on μ-synthesis, through their robustness capabilities, and their ability to reduce several loads at the same time. Two full-order controllers have already been defined using a lidar, trying to reduce the vertical load factor and the wing root

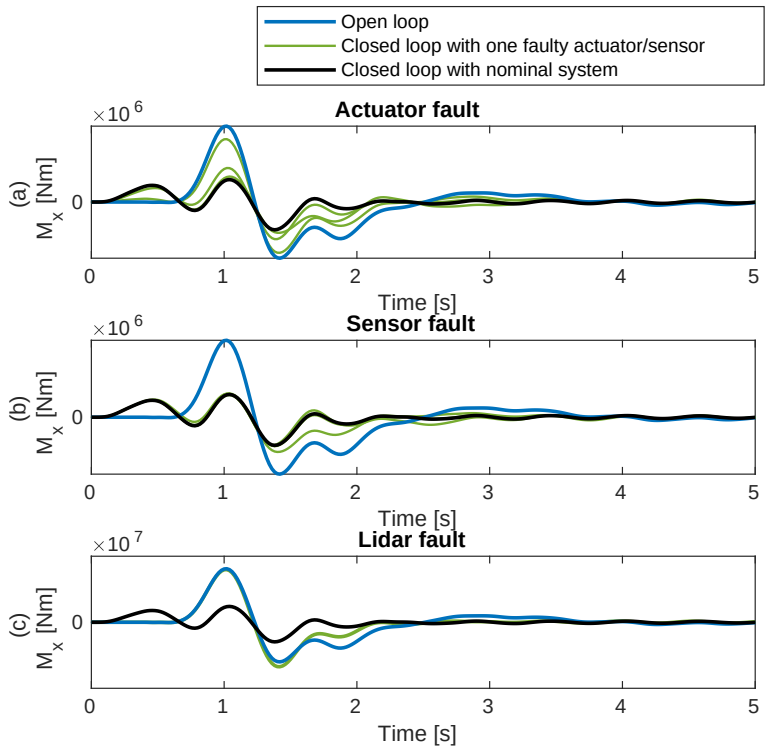

Figure 4.14: Time simulations with faulty actuators and sensors

	MIMO margins		Multi-input margins		SISO margins	
	gain	phase	gain	phase	gain	phase
Full order with lidar	7 dB	40°	15 dB	70°	19 dB	77°
Full order without lidar	3 dB	21°	7 dB	42°	9 dB	50°
2nd order with lidar	5 dB	30°	10 dB	55°	13 dB	65°
Full order with lidar (n_z and M_x)	3 dB	19°	6 dB	37°	10 dB	55°

Table 4.2: Stability margins with different controllers

and HTP loads simultaneously in the first case, or only the vertical load factor and wing root bending moment in the second case. Additionally, a reduced controller of order 2 is designed using structured μ-synthesis, and with all loads included in the H_∞ performance criterion. This allows the study of the capability of obtaining an efficient GLA system with reduced complexity. Furthermore, a fourth controller is designed without lidar (full-order, all loads included), demonstrating the loads alleviation capabilities with the current generation of sensors. Even when a lidar is available, having a GLA controller using classical sensors provides a backup solution, which can be used for reconfiguring the system in case problems occur with the lidar.

Table 4.2 compares the stability margins obtained with the four different controllers. The n_z and M_x controller refers to the case in which only these outputs have been included in the performance criterion. It displays the MIMO margins, considering simultaneous uncertainties in

	c.g.	Wing root			Horizontal tail plane		
	n_z	T_z	M_x	M_y	T_z	M_x	M_y
Full order with lidar	−38%	−42%	−40%	−7%	−31%	−36%	+20%
Full order without lidar	−1%	−4%	−4%	+6%	−3%	−13%	+25%
2nd order with lidar	−35%	−38%	−41%	−11%	−24%	−27%	+15%
Full order with lidar (n_z and M_x)	−64%	−60%	−44%	+1%	+26%	+22 %	+60%

Table 4.3: Loads attenuation capabilities of different controllers for a continuous turbulence. Negative signs mean a reduction of the load (c.g. = center of gravity)

	c.g.	Wing root			Horizontal tail plane		
	n_z	T_z	M_x	M_y	T_z	M_x	M_y
Full order with lidar	−19%	−47%	−49%	+76%	−51%	−55%	+62%
Full order without lidar	−1.4%	−13%	−22%	+32%	−7%	−24%	−9%
2nd order with lidar	−22%	−50%	−56%	+84%	−35%	−58%	+52%
Full order with lidar (n_z and M_x)	−48%	−54%	−57%	+123%	+58%	+62 %	+146%

Table 4.4: Loads attenuation capabilities of different controllers for a 107 m discrete gust. Negative signs mean a reduction of the load (c.g. = center of gravity)

all inputs and output ports of the system, the multi-input margins, with simultaneous uncertainties in the input ports only, and the SISO margins, defined as the lowest gain and phase variation in all input and output ports independently. All controllers are robust, as seen by the high margins. For those using a lidar, it naturally leads to a reduced use of the sensors present in the feedback loop. Considering the controller which does not use a lidar, this robustness might lead to some conservatism, and reduced load alleviation performance. When using μ-synthesis, the robustness is required for both stability and performance, which makes it more difficult to obtain robust controllers without conservatism.

Table 4.3 sums up the load alleviation performance of the controllers for a continuous turbulence. With the full-order controller using a lidar, significant alleviations of the vertical load factor n_z (38 %) and of the wing root bending moment M_x (40 %) are obtained, with actuators saturation and rate limiter included. The wing root torsional moment M_y is not increased by the controller's action, and is even slightly reduced. The HTP bending is also significantly reduced (36 %), while the HTP torsion increases. In absence of lidar, very low attenuations are obtained for a continuous turbulence. Further studies are required to obtain higher load attenuation with lower, yet acceptable robustness. The second-order controller using a lidar leads to load attenuation similar to those obtained in the unstructured case. This encourages the use of structured synthesis, which will be studied in more details in section 4.6. The last controller studied is obtained with structured synthesis, using a lidar, and removing the alleviation objectives on the HTP and on the wing torsion. The attenuation of the vertical load factor is almost doubled, while the loads on the HTP are increased. This confirms the general trend observed in section 4.5.3: when the HTP loads are ignored, the controller uses the elevator in addition to the ailerons to improve the pitch motion, leading to a better control of the vertical load factor, but to an increase of the HTP loads. Table 4.4 shows the load alleviation results for the response to a 107 m gust. In

this case, the vertical load factor is less alleviated, contrarily to the wing root bending moment, which is further reduced. Regarding the wing torsion, it is systematically and strongly increased. Furthermore, the HTP bending alleviation (and shear) is better with respect to the turbulence case, when it is included in the controller design objectives. The alleviation obtained without lidar is, in the discrete gust case, more significant with a 22 % reduction of the wing root bending moment. This analysis tends to show that a lower objective of bending moment reduction can be preferred to avoid excessive increase in the wing torsion, recalling that the consideration of GLA failure imposes a maximum of 33 % alleviation of the total loads in the best case, provided that a low probability of failure can be justified.

Fig. 4.15 shows the time response of the vertical load factor and bending moment to a 107 m discrete gust, comparing the different controllers. The turbulent frequency response is also shown, in a linearized version of the validation model (the saturation and rate limiter effects are not included). The elements of comparison studied before are directly seen: the vertical load factor is not reduced unless the HTP loads alleviation objectives are dropped, and a good bending moment alleviation is obtained. The frequency response shows that the first peak of bending moment, responsible for the maximum loads, is well attenuated. The high frequency (about 4 Hz) peak, which can create oscillations in the aircraft response, is also significantly attenuated.

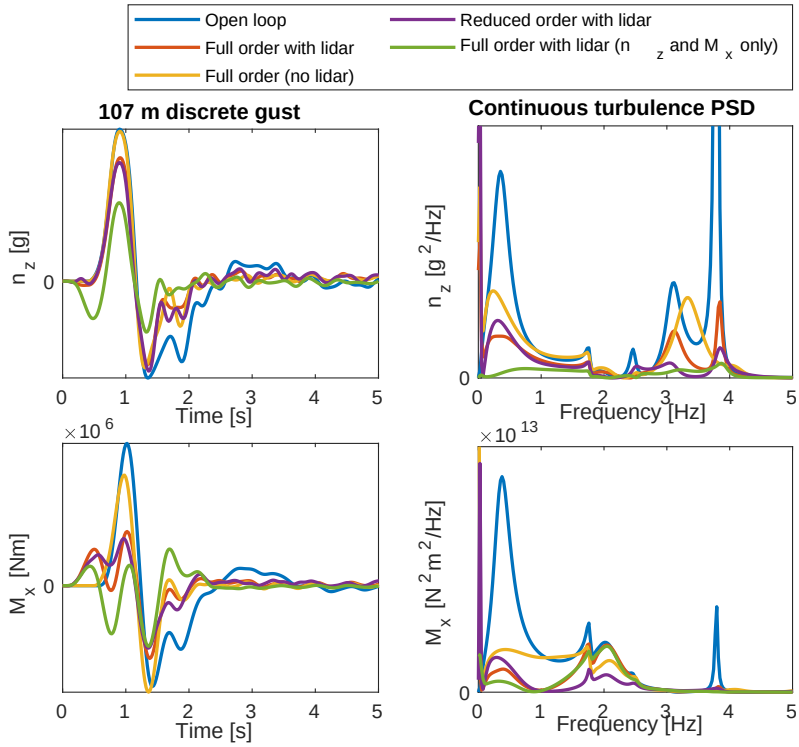

Figure 4.15: Comparison of the vertical load factor and wing root bending moment attenuation of different controllers, with time response to a 107 m discrete gust (left) PSD frequency responses to a continuous turbulence (right)

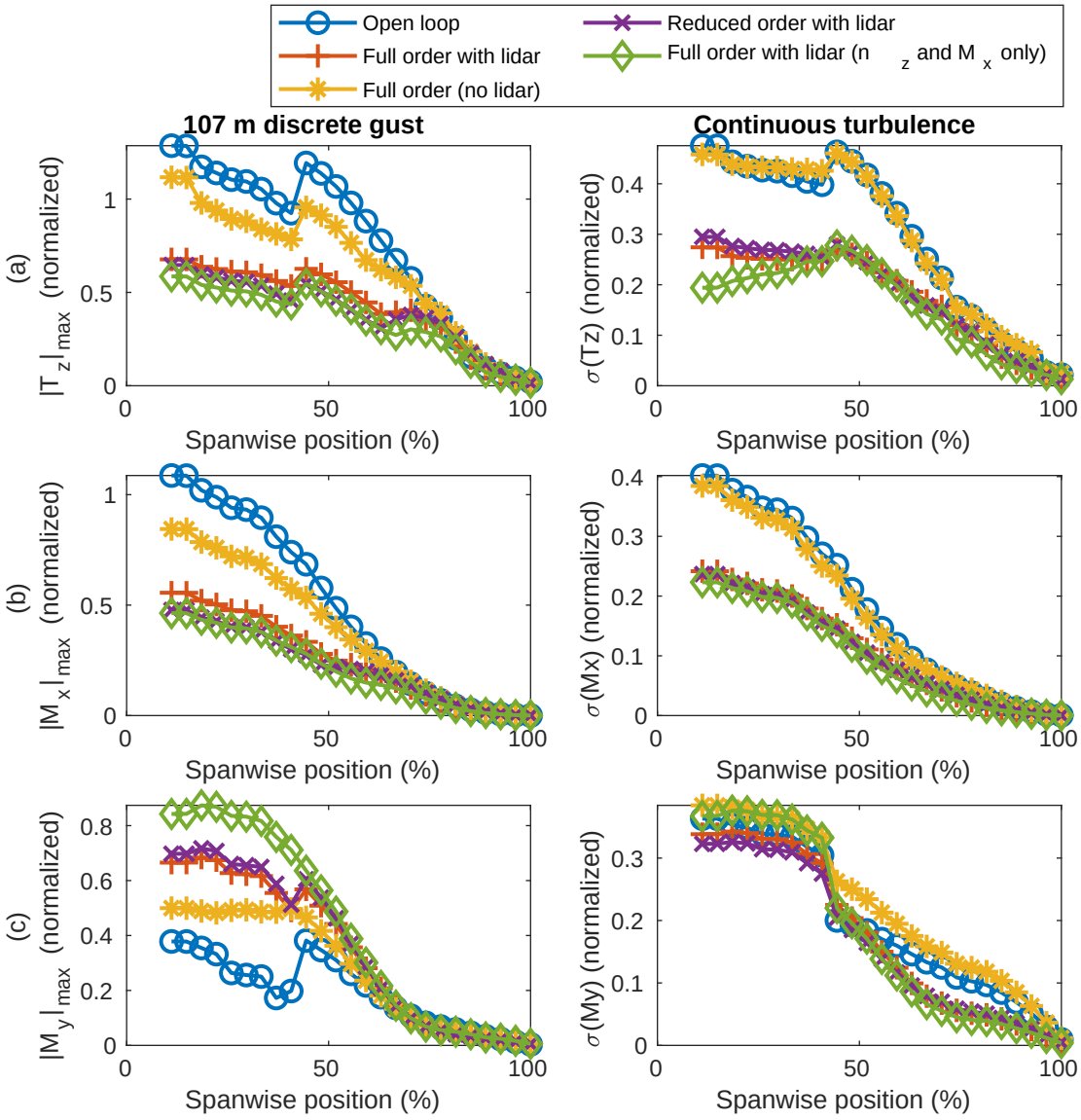

Figure 4.16: Maximum loads at several positions of the wing, with different controllers

Fig. 4.16 concludes this multi-loads attenuation analysis with the loads at different locations along the wing's span. These loads are included in the validation models, but not in the controller synthesis. This first confirms that the reduction of the wing root loads effectively leads to a general reduction of those at other positions, and the highest loads are those at the wing root in open loop and closed loop. This reassures on the fact that the controllers do not create unexpected loads distributions that would not be noticed by looking at the wing root only. An interesting effect can be observed on the torsional moment response to a gust: in the open loop case, it abruptly increases at about 45 % of the wing, starting from the wing root.

4.5.5 Influence of the lidar measurement distance on the loads alleviation capability

This section studies the influence of the distance ahead of the aircraft at which the lidar sensor is able to measure the wind velocity. It has been conducted in [Fournier et al. 2022b] with a framework for synthesis and simulations which differs from the one defined in this work. The aircraft used was the XRF1-v3, another version of the XRF1, with lower aspect ratio than the XRF1-HARW used in the thesis. The main conclusions drawn from this analysis are however applicable here. For each of the 20 different values of the distance at which the lidar can measure the wind velocity, controller has been synthesized and closed loop simulations have been performed. Since the controllers are designed based on different models, the difficulty of this study is to obtain similar control effort in each case a relatively similar robustness, so that the comparison of the

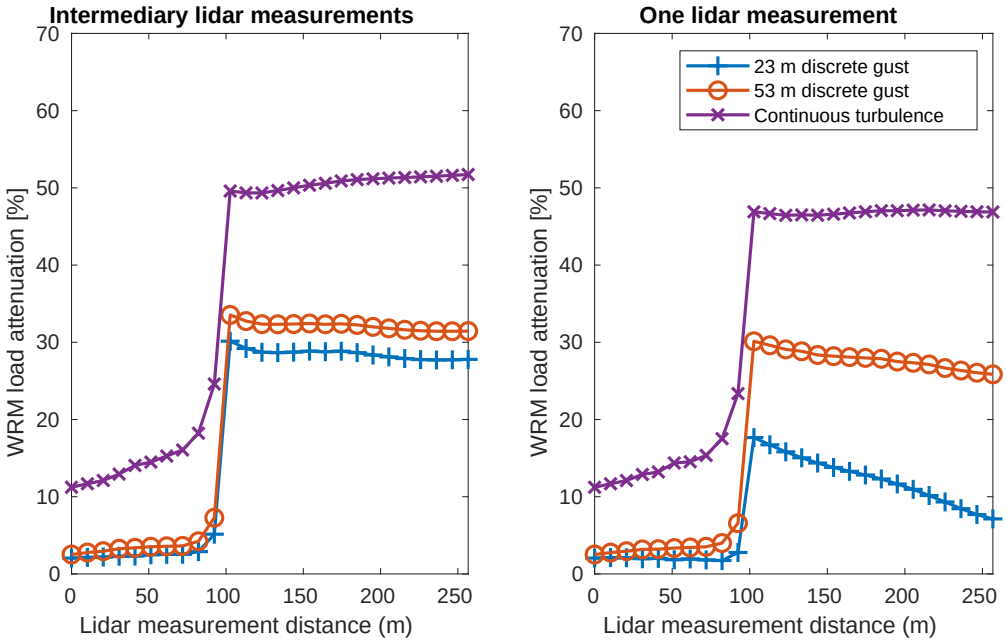

Figure 4.17: Load attenuation of the wing root bending moment with GLA controllers using lidars of varying sensing distance using intermediate measurements (left) or only one measurement (right)

load alleviation performance makes sense. In Fig. 4.17, the bending moment reduction capability of these controllers is shown. The left part shows the case in which intermediary measurements are available, which means, from the assumptions described in section 4.5.1.3, that they have different measurement noise proportional to the distance. Increasing the lidar sensing distance will then add new points at which the wind is measured, with increasing noise, but the closer points keep the same level of noise. It can be seen that the loads alleviation capability increases, first slowly and then abruptly at about 100 m, after which it remains approximately constant. This trend is quite similar for the continuous turbulence and for short gusts of 23 m and 53 m. This distance is the one needed for the aircraft to perform the maneuver described in section 4.5.3, consisting in anticipating the wind by orienting the aircraft in its direction. On the right part of Fig. 4.17, only one measurement is available at the distance shown in x-axis. The wind velocity at intermediary points are still used, obtained by delaying the measurement at maximum distance. In this case, following the assumptions defined in this work, the noise at intermediary points is proportional to the total distance as they all come from the same measurement. A high noise of 4 m/s for each 100 m measurement distance has been used in the simulations to emphasize the effect. It can be seen that for short and intermediary gusts, the load alleviation performance decreases after the optimal distance of about 100 m. The continuous turbulence is less affected by the noise. The longest gust has not been included in this analysis, but should follow approximately the same trend as the continuous turbulence as it is closer in terms of frequency content. This study indicates that the measurement distance of the lidar should be chosen high enough to provide sufficient anticipation capability to the GLA system, but not too high as it could lead to a degraded measurement and alter the GLA performance.

4.5.6 Sensitivity to the lidar measurement noise

The use of a lidar for GLA leads to significant improvements in the loads reduction capability compared to the case in which only classical sensors are used. However, at the time this study is conducted, many uncertainties exist regarding the true accuracy of the lidar sensors. This section studies the influence of white noise and bias on the lidar measurements. Fig. 4.18 shows the bending moment alleviation using a full-order robust controller, with different standard deviation of white noise (left) and different positive or negative measurement biases. In order to isolate the studied effect, no saturation limits are imposed in these results, and the bias and noise are applied separately. An important assumption is made regarding the noise applied at the different lidar measurements, which are assumed uncorrelated in the simulations. The controller has been designed assuming uncorrelated noise too, with a standard deviation of 1 m/s. When no correlation exist between the noises on the different lidar measurement, a regression analysis could theoretically be performed to find the most likely true signal, with better accuracy for measurements close to the aircraft as they benefit from the data measured at higher distances, which supposedly represent the same wind profile. Practically, the controllers designed by μ-synthesis can theoretically filter the lidar signals in a similar way, but are efficient only for the noise PSD given in synthesis. It is then interesting to see how higher noise impacts the controller performance. The left part of

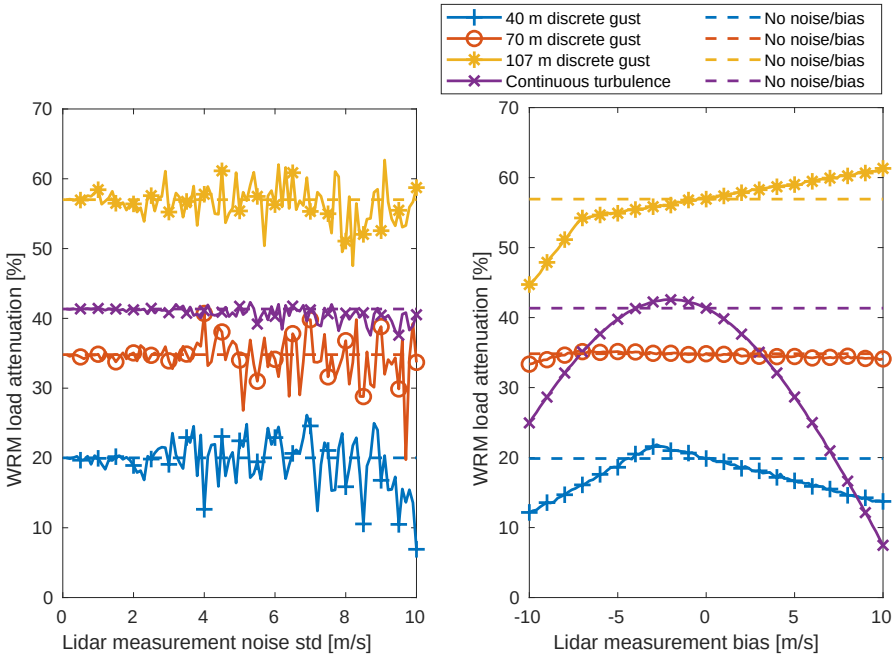

Figure 4.18: Load attenuation of the wing root bending moment with various lidar measurement noise standard deviations (left) and biases (right)

Fig. 4.18 shows that higher noise tends to decrease the bending moment alleviation, but even an extremely high standard deviation of 10 m/s does not lead to significant loss of performance. The bias has a different effect: it creates a drift of the control surface angle. In the discrete gust case, this effect is limited even for high biases, and can create positive or negative loads increments depending on the case. For the continuous turbulence response, the result shown only represents the drift of the bending moment, and is not interpretable as it depends on the simulation duration.

4.5.7 Saturation and rate limitation effects

This section studies the effects of the control surfaces rate limitation on the loads alleviation performance. The robust controllers obtained in this work are obtained within a linear framework, and the effects of control surfaces saturation and rate limitation are nonlinear, and therefore cannot be included in the design phase. The H_∞ and μ-syntheses are performed in a way that prevents the control surfaces' angles and rates to exceed the maximum allowable values in extreme winds, by adjusting the control effort criteria. The rate limitation of 40°/s has been systematically reached before the angle saturation of 30°, hence more attention is given to the former. Slight overshoots of the maximum rate limitation are tolerated when the controller is sufficiently robust, as in the previous sections. The effect of these rate limitations are only studied in post analyses, by verifying that they do not alter significantly the closed loop performance. Some tools exist for analyzing the stability of linear systems with saturation, such as [Hindi and Boyd 1998]. Some techniques have also been developed to synthesize controllers within this framework such as [Hu,

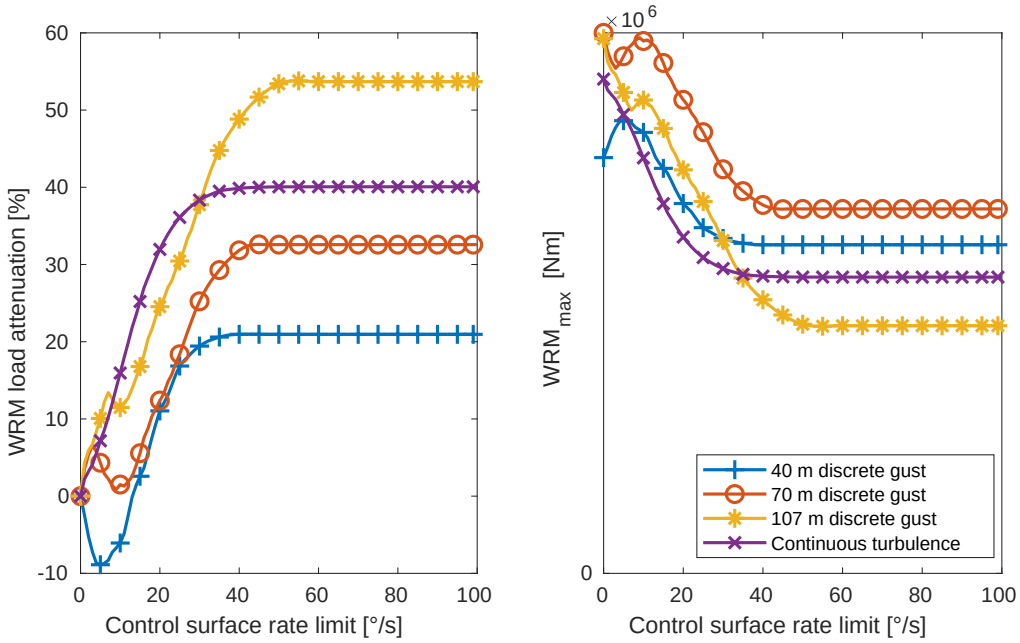

Figure 4.19: Load attenuation (left) and maximum absolute values (right) of the wing root bending moment with various rate limits on the control surfaces

Lin, and Chen 2002] or for the design of so-called anti-windup controllers [Tarbouriech and Turner 2009]. The control surfaces could theoretically be better exploited by taking advantage of their full possible range in terms of angle and rate, leading to higher loads attenuation. This possibility is not studied for at least four reasons:

1. As explained before, high control efforts can lead to side effects, such as the increase of a load which is not included in the controller's objectives. Since alleviating the loads by more than one third does not affect the aircraft design, as explained in section 4.2.6.
2. Aerodynamic nonlinearities can arise when the control surfaces' angles become more important
3. The actuators are less reliable when working at their limits, where high power is needed
4. The linear control framework provides strong tools for robustness and stability based on transfer functions, which cannot be used when saturations are considered.

For these reasons, it is preferred to design linear controllers based on linear models, with relatively low angle deflections. The effects of saturation and rate limitation are studied in post analysis. In order to quantify the loss of load alleviation performance due to the rate limitation, simulations are performed with the full-order controller using a lidar obtained with μ-synthesis. The closed loop response of the aircraft to three discrete gusts of different lengths and to a continuous turbulence are simulated for various rate limitation levels. Fig. 4.19 shows the root bending moment alleviation in each case (left) and the maximum values (right). In the turbulent case, the 2.5σ

values are shown instead. The maximum WRM alleviation is obtained with a rate limit of 50°/s or higher for the longest gust, and 40°/s for the other gusts and the turbulence. The performance decreases fairly linearly with the rate limit for the 107 m gust and for the turbulence. The shorter gusts show a similar trend, with a more complicated behavior at low deflection rates, which can be explained by the harmonics created by the square control signal, interacting with the aircraft dynamics. When looking at the maximum values on the right of Fig. 4.19, it can be noted that the 107 m and the 70 m gusts lead to similar bending moments in open loop, while in closed loop the latter leads to a higher load due to the better controller performance. Indeed, shorter gusts are associated with dynamics of higher frequency, which are more difficult to control due to the actuators dynamics and the aircraft inertia. The critical type of wind in closed loop, for the Mach number and mass configuration used in the simulations, is then the 70 m gust, and since the load alleviation for this gust is optimal at 40°/s, which is the effective limit for the actuators, it shows that the controller has been adequately tuned. Lower control effort would have led to lower effective bending moment alleviation.

4.5.8 Conclusions of the robust GLA study using μ-synthesis

A first GLA study has been conducted in this section. The emphasis has been put on robust control design, based on μ-synthesis, and on the possibility to alleviate several loads simultaneously. Some trends have been highlighted, and conclusions can be drawn from this study. When trying to alleviate at the same time the shear force, bending and torsional moments, at the wing root and on the HTP, some tradeoffs must be conducted. The simultaneous reduction of the bending and torsional moments is generally not possible, as the action of ailerons have opposite effects on them. To reduce the bending moment, an increase of the torsional moment is required. Similarly, alleviating the HTP bending and shear is possible, but leads to lower reductions in the vertical load factor and the wing bending moment. The general strategy of the studied controllers with lidar can be highlighted: before a positive discrete gust reaches the aircraft, the ailerons are deflected downward to create a pitch moment and put the aircraft in the wind direction to reduce this effect. The elevators are used to increase this effect, especially when the HTP loads are not included in the synthesis objectives. If they are, the elevators deflections are lower, to avoid creating loads on the HTP. When the positive gust reaches the aircraft, the ailerons are deflected in the other direction (upward) to create direct negative lift on the wing, opposing to the force created by the wind. This trend is particularly visible with a long discrete gust. For gusts of lower length, the actuators have a shorter time to act on the aircraft dynamics, and the effects of the GLA system are lower. In the continuous turbulence response with 762 m scale, this trend is not visible due to the chaotic nature of turbulence, but the alleviations are similar to those obtained with the longest gust (107 m). The controllers have been designed to demonstrate the potential bending alleviation obtained with GLA using a lidar. Important reductions of the order of 50 % are obtained for the longest gust, and 33 % with a 70 m gust. However, this can lead to significant increases of the torsional moment (up to 80 %). The HTP loads can be reduced by 50 % as long as they are included in the control objectives, otherwise they can be increased by 60 %. Smaller control

effort can be used for future controller design in order to reduce the negative effects of GLA. In absence of lidar, much lower effects on the load have been noted (order of 10 %). This might be due to the high robustness required in this analysis. Indeed, the μ-synthesis imposes both performance and stability robustness, and can therefore lead to conservative design. While the high robustness of controllers with lidar leads to a small use of the sensors present in the control loop (accelerometers, gyroscopes and incidence probe), it does not affect the feedforward part of the controller associated to the lidar. When no lidar is present, there is no feedforward controller and the performance are reduced due to the high robustness. Another conclusion regards the type of wind leading to the highest loads: while the longest discrete gust is the most severe in terms of maximum bending moment in open loop (see section 2.3.11), this is not the case when the GLA controller is present. Indeed, intermediate gusts are more difficult to alleviate due to the higher frequency dynamics involved, resulting in loads closed loop loads. Finally, second-order controllers obtained with structured μ-synthesis have proved almost as efficient as the full-order ones.

Some sensitivity studies have been conducted, showing the effect of rate limitation on the loads alleviation capability of the GLA system. It shows that the actuators constraints must be taken into account when designing a controller. The worst case of wind should be considered in closed loop: while the 107 m and the 70 m gusts lead to similar bending moment in open loop, the latter is less alleviated by the controller and the priority must be given to it. Small overshoot of the rate limit for the 107 m can then be considered acceptable, as it does not affect the worst case of wind. Another sensitivity study highlights an optimal lidar measurement distance of about 100 m. Above this distance, the load alleviation capability does not improve, and can even decrease if it leads to a reduction of the measurement quality. Finally, the influence of lidar noise and bias shows a relatively low sensitivity of the closed loop to inaccuracies in the lidar measurement. This fact is probably due to the existence of several intermediary measurements, providing strong robustness to the system. Further studies are however strongly needed to study these effects, using more refined lidar models (taking into account optical physics) and flight tests.

4.6 Multi-model synthesis and analysis

The conclusions of the last section naturally lead to the study of structure synthesis, and of better robustness constraints. When working with structured synthesis, and accepting the use of nonlinear optimization to design controllers, new possibilities are offered. Multi-model synthesis allows to create controllers based on different models, hence better defining the physical uncertainty of the aircraft models, and stability robustness can be imposed. By doing so, the uncertainty is split between the one known by the user, and the one added for imposing stability margins. The former can be used for both stability and performance robustness, while the latter can be defined for stability only, hence avoiding excessively conservative designs. Furthermore, the use of mixed H_2/H_∞ structured synthesis allows more natural definition of gust load alleviation objectives by H_2 criteria, and using the H_∞ criteria for robustness and control effort limits. Some lessons have

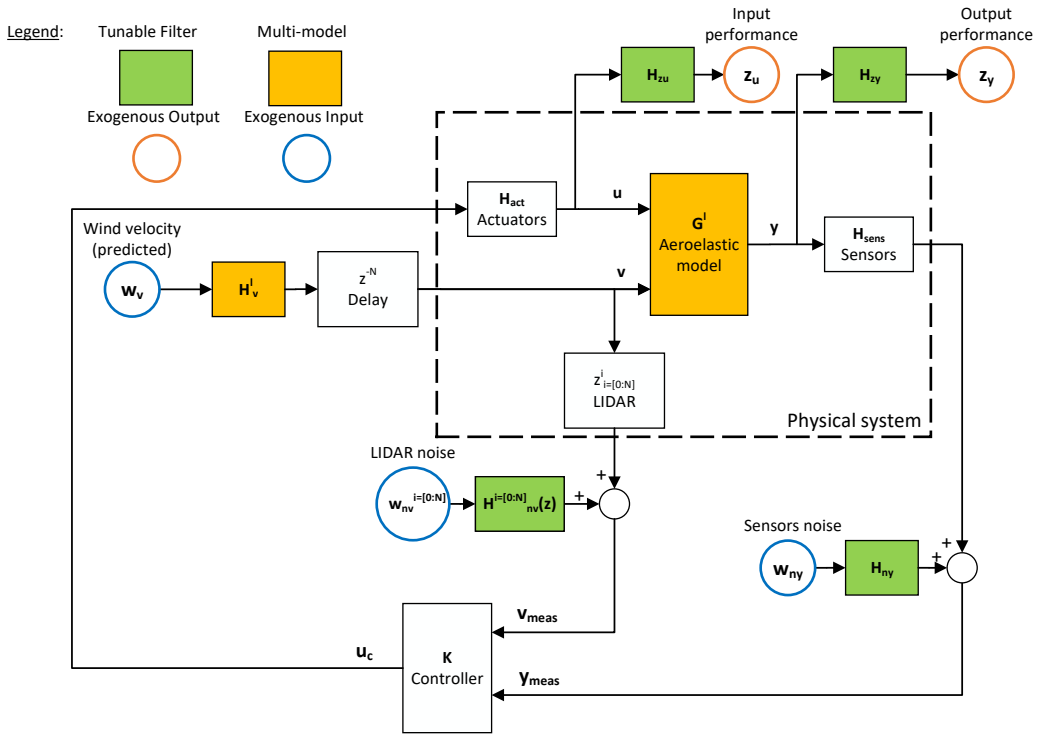

Figure 4.20: Augmented system used for the multi-model H_2/H_∞ synthesis

been learned from the last section, about the possibility to alleviate several loads on the wing and the HTP at the same time, and about the conservative design which can be obtained using μ-synthesis. The controller syntheses in this section focus on a few loads (those at the wing root only) and alleviates the stability robustness constraints imposed in the last section. The controllers are analyzed using multiple models obtained at different Mach number values and mass configurations, in order to identify the maximum loads which can occur in the aircraft life-cycle, following as much as possible the philosophy of aircraft certification.

4.6.1 Multi-model H_2/H_∞ synthesis for the flexible aircraft equipped with lidar

The augmented plant $\boldsymbol{P}$ used in this section is described in Fig. 4.20. Most blocks are the same as in the μ-synthesis framework described in section 4.5.1. Various aeroelastic models $\boldsymbol{G^l}$ are defined in this section, corresponding to different mass configurations and values of the Mach number. The models are indexed by the superscript ^{l}, that goes from 1 to N_l in the numerical applications. Similarly, one turbulence model H_v^l is used for each aeroelastic model, as the variation of velocity and altitude affects the amplitude and PSD of the wind following the considerations of section 2.2 and 2.1.3. It follows that the plant $\boldsymbol{P^l}$ defining the H_2/H_∞ problem is composed of different models. The controller synthesis used in this section is defined by the following optimization

problem:

$$\min_{K} \max_{l=1\dots N_l} \left\| T^l_{\boldsymbol{w_2}\mapsto\boldsymbol{z_2}}(K) \right\|_2 \tag{4.17}$$

$$\text{subject to} \tag{4.18}$$

$$\left\| T^l_{\boldsymbol{w_\infty}\mapsto\boldsymbol{z_\infty}}(K) \right\|_\infty \leq 1 \quad \forall l = 1\dots N_l \tag{4.19}$$

The transfer functions whose H_2 norm must be minimized are the transfer functions from disturbance and measurement noise to the loads output, which are $T_{\boldsymbol{w_v}\mapsto\boldsymbol{z_y}}$, $T_{\boldsymbol{w^i_{nv}}\mapsto\boldsymbol{z_y}}$ and $T_{\boldsymbol{w_{ny}}\mapsto\boldsymbol{z_y}}$. The $\boldsymbol{H_{zy}}$ filter is used to tune the performance H_2 criterion. It includes a high-pass filter, which leads the synthesis not to consider the low-frequency response of the aircraft, which can be handled separately. Furthermore, $\boldsymbol{H_{zy}}$ amplifies the n_z response between 2 Hz and 7 Hz, so that the controllers attenuate more the high-frequency acceleration of the aircraft, which can create motion sickness among the passengers. The H_∞ norm constraint imposes the maximum deflection angle and rate of the control surfaces to stay within the actuators acceptable bounds and is defined with the $T_{\boldsymbol{w_v}\mapsto\boldsymbol{z_u}}$ transfer function. The H_2 criterion is more efficient for optimal performance, as it works on the whole frequency range, while the H_∞ focuses on the one frequency at which the transfer function gain is maximum. An extreme example is the case where there exists a high frequency peak in the system's response, which the controller cannot attenuate due to its limitations. In this case, the closed loop H_∞ norm will be calculated on this peak, and the response at the other frequencies will be ignored, leading to an inefficient controller. Some tuning of the shape filters would be required to ignore the peak in the synthesis, which would increase the system's order and require fine tuning of each model independently. The H_2 criterion is computed on the whole frequency range, and not only on the peak response, hence requires no extra tuning. However, the H_∞ norm provides strong guarantees such as stability, robustness and satisfaction of system's limitations. The mixed H_2/H_∞ synthesis hence provides a good performance while ensuring guarantees in worst case scenarios when required.

The controller $\boldsymbol{K}$ in Eq. (4.17) has a fixed structure, composed of two state-space models: one for the feedforward part that takes the lidar measurement as input, and one for the feedback part that takes the pitch rate, vertical load factor and angle-of-attack as input. In order to reduce the controller's sensitivity to lidar noise or to a failure, one can increase the gain of the $\boldsymbol{H^i_{nv}}$ filter in Fig. 4.20. However, we find it more efficient and straightforward to perform two syntheses: a first synthesis calculates the feedback controller without the feedforward part, then the latter is obtained from a synthesis based on the obtained closed loop. The structured H_2/H_∞ problem with multiple models described above can be directly implemented within Matlab's *systune* function, based on the work described in [Apkarian, Dao, and Noll 2015].

4.6.2 Results using multi-model H_2/H_∞ synthesis GLA

Simulations are performed using the same numerical framework as described in section 4.5.2. The controllers are obtained by multi-model H_2/H_∞ synthesis using 48 different aeroelastic models,

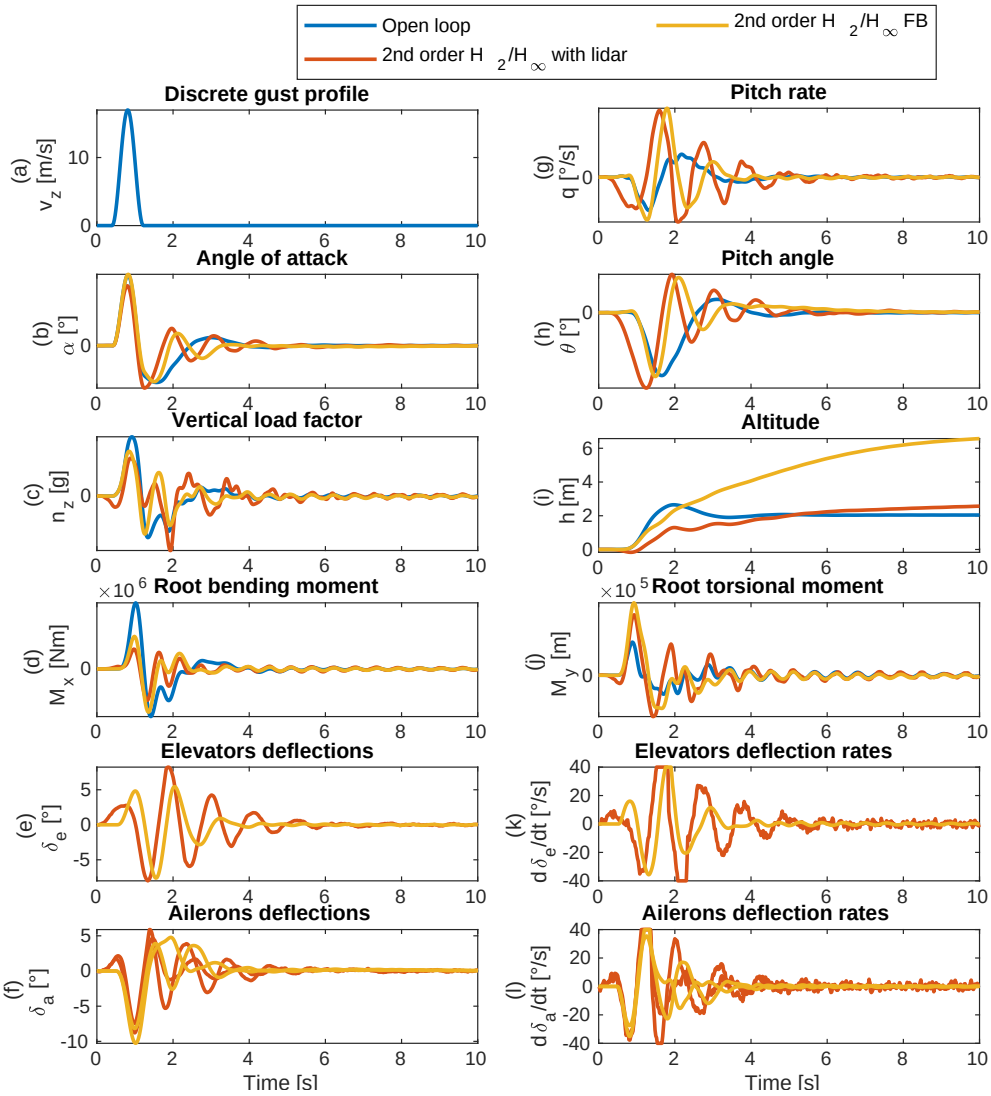

Figure 4.21: Time response to a 107 m discrete gust with GLA controllers obtained by multi-model H_2/H_∞ synthesis

computed at Mach numbers of 0.5, 0.8 and 0.86, and with 16 different mass configurations. 3rd order approximations of the von Kármán wind described in Eq. (4.16) are used as wind model for the controller synthesis, with variations in the different models due to the change of velocity.

Fig. 4.21 shows the time response to a 107 m gust in open loop, and in closed loop with and without lidar, for an empty aircraft flying at Mach 0.86 and CAS= 170 m/s. The vertical load factor (c) and root bending moment (d) are more significantly reduced than with the μ-synthesis methods described in section 4.5, which were studied in the same conditions. The effect is particularly visible in case no lidar is used: while only attenuations of the order of 10 % were obtained with μ-synthesis, they are comparable to the case in which a lidar is used with this implementation of H_2/H_∞ synthesis. The main reason explaining this difference is the fact that

less robustness has been required in the synthesis studied in this section, and the HTP loads attenuation objectives have been dropped. By replacing the general MIMO disk uncertainties used in section 4.5 by a physical uncertainty defined by the multi-models, the closed loop design is less conservative. It is clear that this difference could have been attenuated by lowering the stability margins required when using μ-synthesis, but obtaining a satisfactory trade-off between performance and robustness is more difficult when the uncertainty is not understood. Another reason explaining the good loads alleviation performance visible in Fig. 4.21 is the use of the H_2 criterion in the definition of the loads attenuation criterion. This allows a better action on the whole frequency range of the aircraft dynamics, while the H_∞ criterion focuses on the one frequency leading to the worst gain. The multi-model H_2/H_∞ synthesis leads to a more natural formulation of the problem than the μ-synthesis, which could theoretically lead to similar results at the cost of important efforts of the user to tune the uncertainty and the H_∞ filters, losing at the same time visibility and flexibility of the synthesis process. While the difference of performance is more spectacular in the absence of lidar, it is also visible when the lidar is used. In this case, the controller makes a better use of the feedback part in addition to the feedforward control. It results for these observations that the lidar sensor leads to a lower performance improvement. This conclusion, whose scope will be discussed at the end of this section, must be confirmed by studying the loads obtained at different mass configurations, Mach number values and for several types of wind. Some other observations can be made from Fig. 4.21. The use of the control surfaces in presence of a lidar is globally similar to the one described in section 4.5.3, first orienting the aircraft in the wind direction before the gust reaches it, and then deflecting the ailerons upwards to apply direct negative lift. The elevators are much more solicited, leading to a more complex response of the vertical load factor and pitch rate, with oscillations before converging. When the lidar is not used, the ailerons directly deflect upwards as the gust reaches the aircraft, without going through the preset phase in which a downward deflection creates a pitching moment, possible only with the anticipation provided by a lidar. The elevators are used similarly to the case in which the lidar is present, with a delay. It is interesting to see that in absence of lidar, the first elevators deflection is more important that the one occurring when the lidar is used, creating an important pitch response of the aircraft. This, added to the direct lift created by the ailerons deflection which do not require anticipation, the strategy based only on the feedback loop leads to loads reduction comparable to those obtained with a lidar. This more aggressive control strategy has a cost in terms of robustness, as will be analyzed in section 4.8, and in terms of pitch angle (h), which has a more important transient response than in the open loop case and than with the μ-synthesis controllers.

The correlated loads envelopes introduced in section 2.3.11 are now applied to closed loop with GLA controllers. The loads attenuation results have been obtained by performing simulations on one model only. The ultimate goal, which we try to achieve by the multi-model synthesis, of the GLA system is to reduce the maximum loads (mainly the bending moment and vertical load factor) which can occur in the flight envelope, with the possible aircraft mass configurations and in response to different types of extreme winds. The correlated loads envelopes are the main metric used in this work to compare the loads attenuation performance of the GLA controllers.

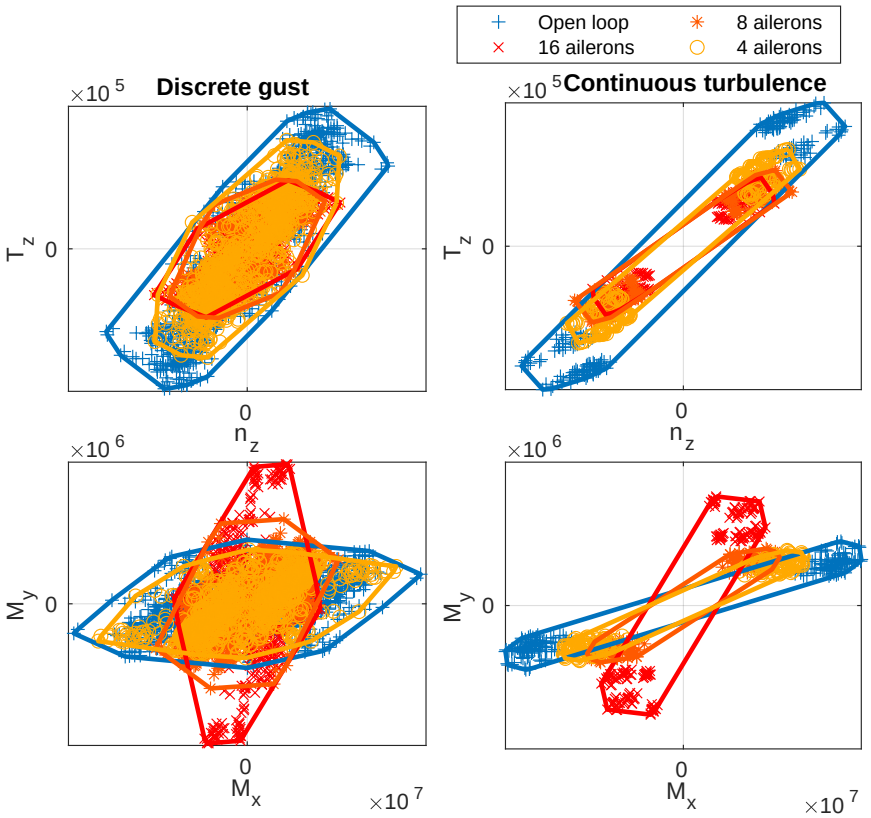

Figure 4.22: n_z/T_z and M_x/M_y correlated loads envelopes with GLA controllers obtained by multi-model H_2/H_∞ synthesis using different numbers of ailerons per wing

In Fig. 4.22 the open loop envelope is compared to the closed loop with controllers obtained by multi-model H_2/H_∞ using a lidar and using different numbers of ailerons per wing. The case with 8 ailerons is the same as the time response of Fig. 4.21. To obtain these envelopes, time simulations have been performed on 48 models, associated to three different Mach number values (0.5, 0.8 and 0.86) and 16 different mass cases representing various loading cases, while the CAS is fixed at a constant value of 170 m/s. 11 cases of wind are considered: five discrete gusts of lengths 40 m, 55 m, 70 m, 85 m and 107 m, positive or negative, and a von Kármán turbulence with 762 m scale. Recall that in the discrete gust case, each point has one coordinate equal to the maximum of one of the two loads defining a pair, while the other coordinate is the value of the other load at the time of this maximum. In the continuous turbulence case, the points are classically obtained by computing the standard deviation of a load and the loads correlations factor (see Eq. (2.53)) using a frequency analysis. However, although techniques exist to account for saturation and rate limits by replacing them by equivalent linear gains, a more direct approach is preferred in this work, by computing the standard deviations with the nonlinear time simulations, and applying the theoretical loads correlations obtained by frequency analysis. This way, it is possible to check that no nonlinear effect affects the closed loop stability and performance. It is important to remind that the quantities studied in this work are increments around a nonlinear trim equilibrium.

Fig. 4.22 shows that the controller obtained by multi-model H_2/H_∞ with 8 ailerons per wing efficiently reduced the worst bending moment due to discrete gusts by about 50 % and the vertical load factor by 45 %. The maximum torsional moment is increased by about 32 %, and the maximum wing root shear force is decreased by 55%. The reduction of maximum shear force, vertical load factor and bending moment is approximately the same for the response to turbulence. The maximum torsional moment, however, is not increased in this case. When only four ailerons are used, the n_z attenuation is still good, but the bending moment reduction is much lower for the gust response, (about 15 %), and lower in the turbulent response but still significant (32 %). When 16 ailerons are used on each wing, the loads are further attenuated, up to 60 % for the bending moment, but the torsional moment is more than doubled. A trade-off in the aircraft design must be conducted when considering the number of ailerons used, keeping in mind the limit of 33 % reduction on the total loads imposed by the consideration of the GLA failure case. Considering that the equilibrium (1 g) loads are of the same of order as the increment due to gust, and accounting for a small safety factor, a maximum of 50 % reduction of the loads increments can be considered, which is in line with the performance obtained. More results regarding the controller obtained by multi-model H_2/H_∞ synthesis will be studied in the overall comparison of section 4.8, and are not shown here to avoid unnecessary repetitions.

4.7 GLA using Model predictive control

The Model Predictive Control (MPC) is another possible strategy for active gust load alleviation, and is compatible with the use of a lidar. The MPC controller contains an internal model of the aircraft dynamics, which is used to predict the states and outputs of the system in given time horizon. Using these predictions, the control surface deflections which minimize a given cost function can be computed by the on-board computer. The loads alleviation objectives are included in the definition of this cost function, and constraints on maximum values of the control surfaces deflections angles and rates can be imposed. In absence of lidar, the future states of the aircraft can only be predicted assuming no external perturbation. In the opposite case, the lidar directly provides the value of the future wind velocity which can be included in the prediction and the on-line optimization. The MPC is then a natural candidate for GLA using or not a lidar, as it allows to include the active loads alleviation objectives and constraints in an optimization problem. The obtained control is nonlinear, and can theoretically lead to higher performance than the linear robust control laws of sections 4.5 and 4.6. The main limitations of MPC-based GLA have already been addressed in the GLA introduction of section 4.1: the need to perform a computationally intensive on-line optimization, no guarantee to converge in finite-time, no available solution to obtain robustness. Furthermore, it has already been noted that decreasing the loads beyond a certain percentage becomes useless for the aircraft design, and the efforts for future GLA systems should be directed towards robustness and implementability rather than pure performance. For these reasons, the MPC technique is only considered as an alternative to the robust techniques developed in this work, and provides a reference of what can be achieved in an optimal nonlinear

framework.

In practice, the MPC controller has an internal state-space model of the form:

$$\boldsymbol{G_{MPC}}: \begin{cases} \boldsymbol{x_m}(k+1) & = \boldsymbol{A_m}\boldsymbol{x_m}(k) + \boldsymbol{B_m}\boldsymbol{u_{com}}(k) + \boldsymbol{E_m}\boldsymbol{v_z}(k) \\ \boldsymbol{y_m}(k) & = \boldsymbol{C_m}\boldsymbol{x_m}(k) \end{cases} \tag{4.20}$$

where $\boldsymbol{A_m}$, $\boldsymbol{B_m}$, $\boldsymbol{E_m}$ and $\boldsymbol{C_m}$ are state-space matrices defining the internal MPC aeroelastic model, $\boldsymbol{x_m}$ are the internal states, $\boldsymbol{y_m}$ are the output of the model, assumed to match with the measured variables $\boldsymbol{y_{meas}}$. A Kalman filter, based on this internal MPC model, is used to predict the future states of the system, assuming additive white noise on the measurements and on the unknown disturbance. At each time step k, the MPC controller aims at finding the present and future values of the control surfaces deflections $\boldsymbol{u_{com}}$ which are solutions of the following optimization problem

$$\min_{\boldsymbol{u_{com}}(k),\dots,\boldsymbol{u_{com}}(k+T_u)} \sum_{k'=k}^{k+T} \boldsymbol{y_m}(k')^T \boldsymbol{Q} \boldsymbol{y_m}(k') + \sum_{k'=k}^{k+T_u} \boldsymbol{u_{com}}(k')^T \boldsymbol{R} \boldsymbol{u_{com}}(k') \tag{4.21}$$

$$\text{s.t.} \begin{cases} \boldsymbol{u_{min}} \leq \boldsymbol{u_{com}}(k') \leq \boldsymbol{u_{max}} & k \leq k' \leq k+T_u \\ \boldsymbol{u_{com}}(k') = \boldsymbol{0} & k+T_u \leq k' \leq k+T \\ \boldsymbol{y_{min}} \leq \boldsymbol{y_m}(k') \leq \boldsymbol{y_{max}} & k \leq k' \leq k+T \end{cases} \tag{4.22}$$

where $\boldsymbol{Q}$ and $\boldsymbol{R}$ are matrices defining the performance objective, T and T_u are respectively the output and input time horizons with $T_u \leq T$. With $\boldsymbol{Q}$, the user can define what output to minimize and the ratio between them. With $\boldsymbol{R}$ the control smoothness can be adjusted: low values can lead to control signals oscillating fast between $\boldsymbol{u_{min}}$ and $\boldsymbol{u_{max}}$, while a high value tends to decrease the control effort. In this work, the constraints on the outputs are only used to impose control rate limitations, defining dummy output variables as derivatives of $\boldsymbol{u_{com}}$. Using a high horizon T allows the controller to target lower frequency dynamics. For the GLA problem studied in this work, a 1 s horizon (50 time steps) is considered sufficient. Using a control horizon T_u lower than T allows to limit the computational cost of the on-line optimization, as it reduces the number of unknown variables. Note that in absence of constraints on the controlled variables and on the outputs, the MPC problem is equivalent to a LQR control synthesis. In this case, the optimal controller is linear, and no on-line optimization is needed.

A time simulation of the response to a 107 m gust is shown in Fig. 4.23, comparing the MPC to the open loop. The aircraft is flying at Mach 0.86, CAS= 170 m/s, in the same conditions as for the internal MPC model. A relatively low $\boldsymbol{R}$ has been selected to emphasize the nonlinear behavior of the controller and the lack of robustness. The vertical load factor and the wing root bending moment are the output to minimize, while the others are also minimized with a weight five times lower (after normalization of the outputs). Maximum rates of 30°/s are imposed to the control surfaces. The output time horizon is equal to $T = 1$ s and the control horizon $T_u = 0.2$ s. The MPC controller is designed using *Simulink*, embedded into the same simulation framework

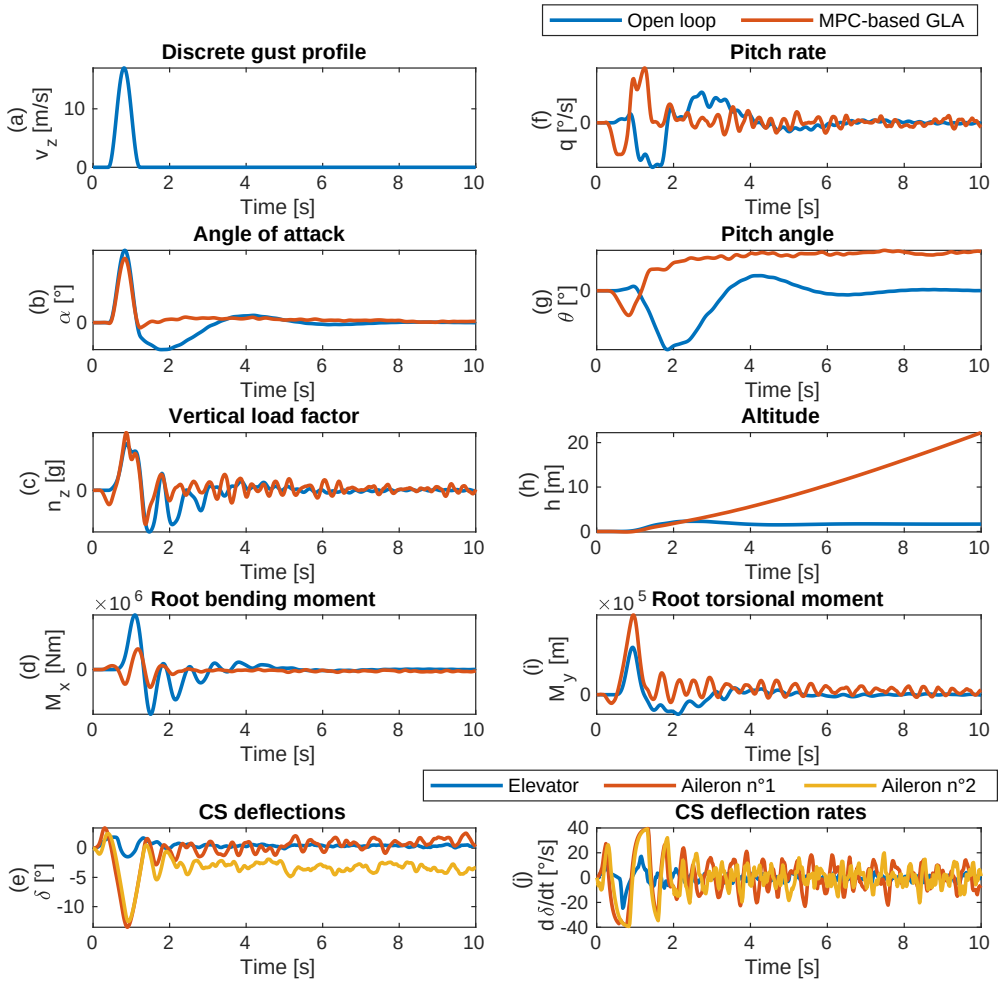

Figure 4.23: Time response to a 107 m discrete gust with MPC-based GLA using a lidar

as for the other studied controllers. It can be seen on Fig. 4.23 that the bending moment is well reduced, but not the vertical load factor. The use of the control surfaces is more erratic than with the robust controllers, with high oscillations in the deflection rates, creating in turn oscillations of the aircraft pitch rate and load factor. Moreover, it can be seen that the two ailerons sometimes have different signs, the two effects approximately canceling each other. This is an unwanted consequence of nonlinear control, which could be attenuated by increasing the $\boldsymbol{R}$ matrix (but also decreasing the loads attenuation performance). When analyzing the deflection angles, it can be noted that the controllers uses the same strategy as described in section 4.5, in which the ailerons and elevators are first deflected downward to align the aircraft with the incoming wind gust, and then deflecting the ailerons upward to counteract the vertical force induced by the wind by direct lift effect. Note that the MPC rate constraints have been imposed to the control order sent to the actuators, and not directly to the control surface rates, explaining the time evolution in figure (j). On Fig. 4.24, the MPC controller is applied to an aeroelastic model with the same Mach number as its internal model, but with a different mass configuration. The high oscillations of the n_z

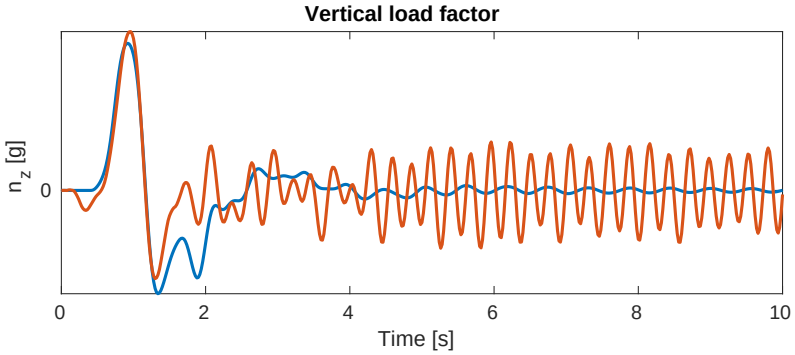

Figure 4.24: Vertical load factor response to a 107 m discrete gust with MPC-based GLA using a lidar on a mass configuration different from the internal MPC model

response show the lack of robustness of the MPC control strategy.

4.8 Comparison of the different GLA strategies

Throughout this chapter, an effort has been done to study different GLA strategies in a unified analysis framework, using similar models for time simulations and in the same wind conditions. Elements of comparison have already been evoked, between the μ-synthesis and the multi-model H_2/H_∞ synthesis with more physical robustness constraints in section 4.6, and between the MPC and the linear robust controllers in section 4.7. This section concludes this comparison by computing the loads envelopes obtained for the different GLA control strategies, and by studying the comfort and motion sickness at different positions of the fuselage. The results of more than 5000 simulations are shown in this section.

Fig. 4.25 shows the loads envelopes obtained with the classical GLA strategy, statically deflecting the ailerons upward to protect the maximum positive bending moment as described in section 4.4. The simulations are performed with a wind starting 10 seconds after the control surfaces have first been deployed, in order to let time for the new equilibrium to be reached. The first observation is that the loads obtained by static ailerons deflection are shifted with respect to the open loop loads, due to the static effect of the control surfaces deflections. Compared to the multi-model robust controller, the reduction of the maximum positive bending moment is lower (31 % compared to the 50 %) in response to discrete gusts. It is interesting to see that, both in open loop and with the static ailerons deflections, two cases situated on the right of the M_x/M_y pair for discrete gusts create a significant increase of the bending moment. The robust controller, designed in a way that minimizes the maximum closed loop loads, avoids this kind of situation and efficiently reduces the loads in each case of wind, Mach number and mass configuration. The shear force is much better alleviated by the robust controller than using static control surfaces deflections. Regarding the vertical load factor, the maximum and minimum values are strongly attenuated by the H_2/H_∞ controller, while it is unaffected by the ailerons deflections. Finally,

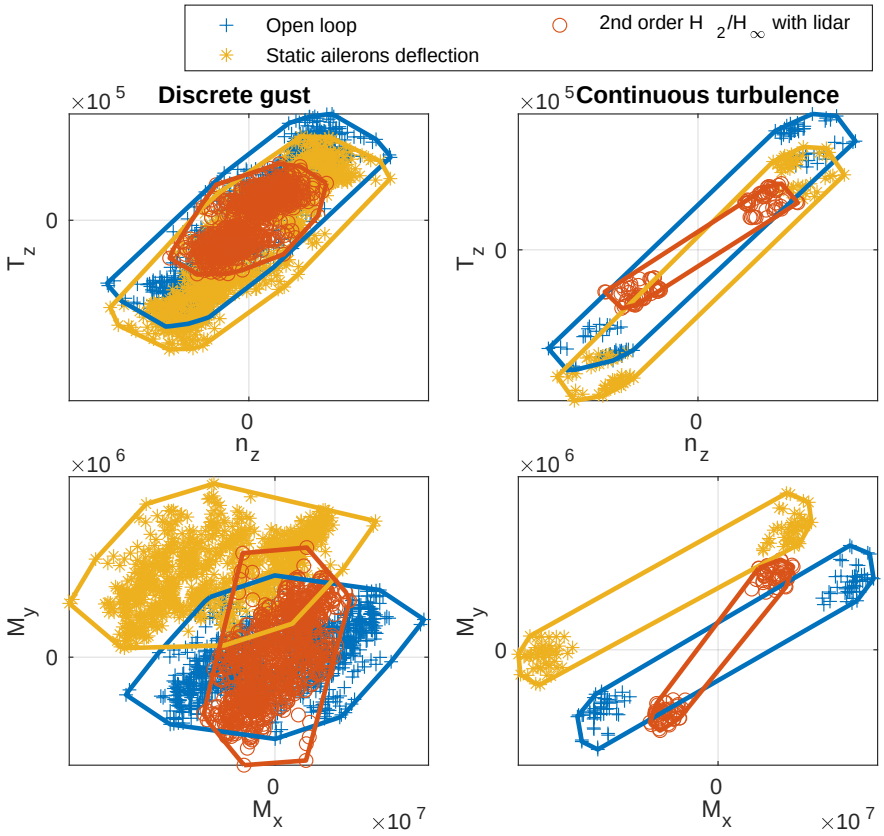

Figure 4.25: n_z/T_z and M_x/M_y correlated loads envelopes: comparison of GLA by static ailerons deflections with a controller obtained by multi-model H_2/H_∞ synthesis

the increase in torsional moment is much higher with the classical GLA technique (+110 % for discrete gusts and +50 % for turbulence) compared to the robust controller (+35% and −15 % respectively). This shows the superiority of dynamical , which have better overall loads attenuation performance with slightly lower ailerons deflection angles (with a maximum of about 10° compared to the 15° static deflections).

Fig. 4.26 shows the loads envelopes obtained with the MPC-based GLA using a lidar described in section 4.7, and compared to a multi-model H_2/H_∞ controller, with a lidar in both cases. The MPC control has been included in the multi-model simulations framework used for robust controllers and static ailerons deflections. Two versions of the MPC controllers have been implemented. The first one (green diamonds on Fig. 4.26) has the same internal model for all simulations, obtained at Mach 0.86 and with an empty aircraft. The second MPC controller (blue squares) has one internal model per Mach number, hence allowing a certain adaptation to the local dynamics. This modification would imply the controller to switch internal model as the aircraft moves on the flight domain. The slow variations of the Mach number and its reliable estimation on-board the aircraft makes this adaptivity possible. If a Mach-dependent LPV aeroelastic model of the aircraft was available, it could be used too in order for the controller to evolve smoothly. An adaptivity to the mass configurations could also be considered, but would require future work

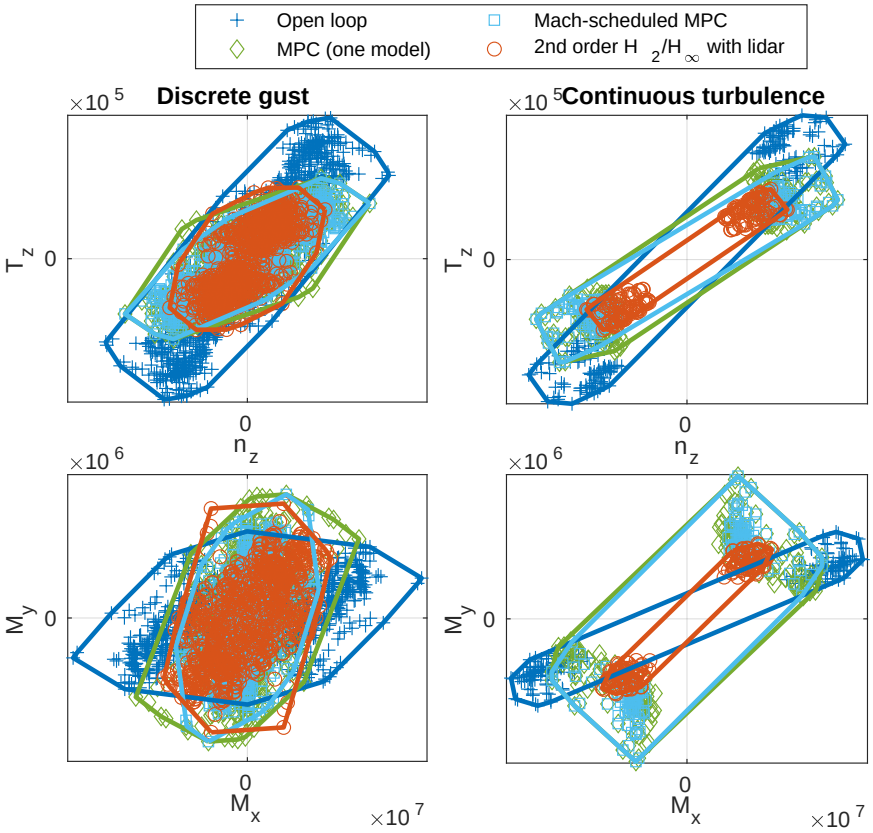

Figure 4.26: n_z/T_z and M_x/M_y correlated loads envelopes: comparison of MPC-based controllers, using a single internal model or with one internal model per Mach number, with a controller obtained by multi-model H_2/H_∞ synthesis

on the system identification of low-order aeroelastic models depending on the mass configuration, and with on-line parametric identification (some elements are discussed in section 3.9.2). When looking at the loads created by the discrete gust, the Mach-adaptive MPC slightly outperforms the robust controller in terms of bending moment alleviation, with a similar increase of the torsional moment. It can be seen that in this case, the adaptivity to the Mach number dynamics leads to a strong improvement in the loads alleviation, with a reduction of the bending moment by 60 % against 35 % when the MPC controller has only one internal model. However, the MPC struggle to reduce the maximum vertical load factor. Furthermore, the alleviation performance is greatly decreased when considering the response to a turbulent wind, and in this case, the robust controller outperforms the MPC on every level. It is not possible to conclude to a superiority of the multi-model H_2/H_∞ controller with respect to the MPC-based GLA, as less efforts have been made in the latter case to study the influence of the hyper-parameters defining the on-line optimization compared to the robust case, which is the main subject of this work. However, these results show that using an off-line trained linear controller can lead to overall loads alleviation performance similar to the one obtained by nonlinear optimization. They also show that robustness is a major concern for MPC, and is one of the main challenges for an practical implementation,

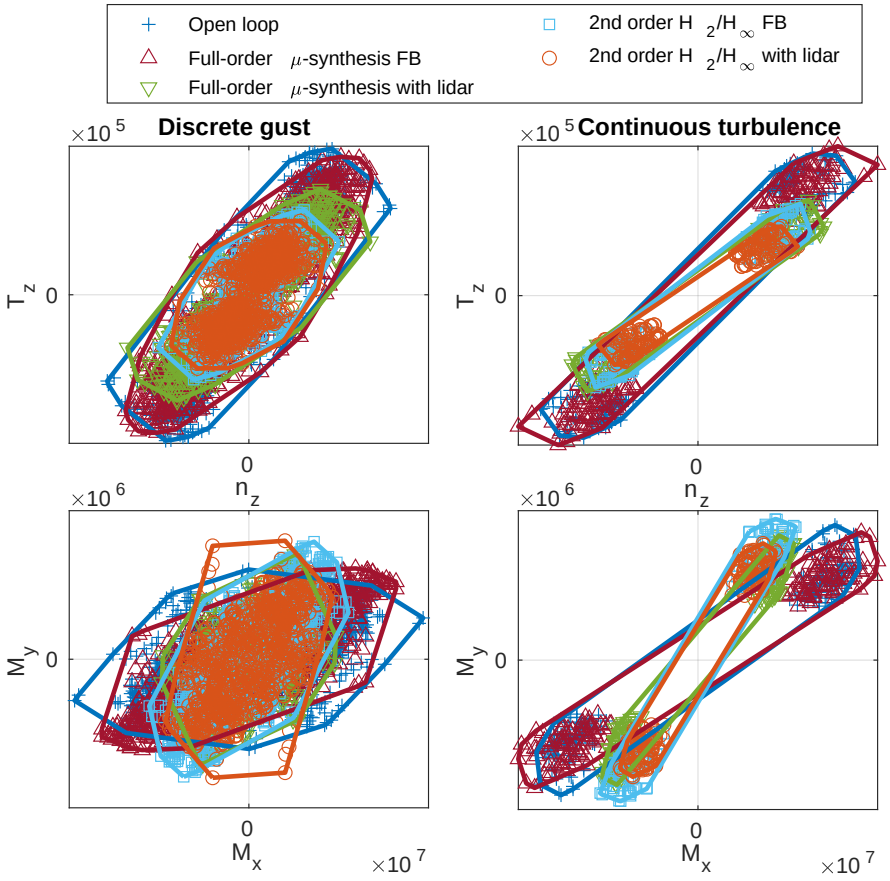

Figure 4.27: n_z/T_z and M_x/M_y correlated loads envelopes with different robust GLA controllers

working efficiently all along the aircraft cycle.

Different types of H_∞ controllers are now compared in similar tests conditions. The GLA controllers obtained by μ-synthesis (full-order) in section 4.5 including multi-loads objectives are compared to the multi-model H_2/H_∞ controllers of section 4.6. The cases in which a lidar is used are compared to the pure feedback controllers. Fig. 4.27 show the loads envelopes obtained with the different robust linear controllers, compared to the open loop case. First, when a lidar is used, the μ-synthesis leads to similar bending moment attenuation as the multi-model synthesis for the gust response, and slightly lower for the turbulence. However, the vertical load factor attenuation is lower with the μ-synthesis. These observations only confirm what had been seen with simulations on a single model. The difference of performance is due in particular to the presence of HTP loads attenuation objectives in the μ-synthesis, as explained in section 4.5.3, and more important robustness constraints. The results mainly show that the GLA controller design method employed in section 4.5, using disk uncertainties and μ-synthesis, leads to a sufficient level of robustness to efficiently reduce the loads not only on the model used for design, but also for a wide range of Mach number values, mass configurations and types of winds. When looking at the results without lidar, the μ-synthesis feedback controller leads to low loads attenuation, as

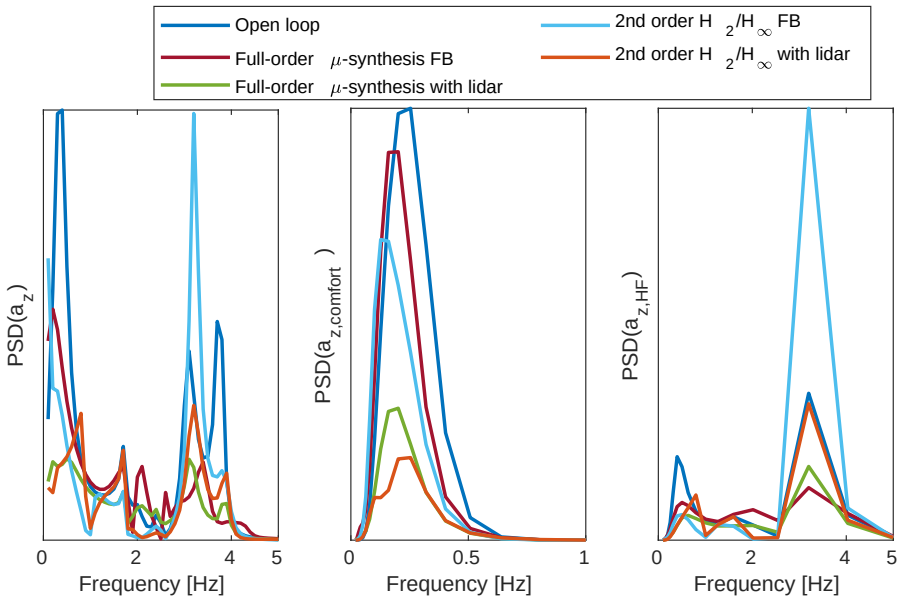

Figure 4.28: PSD of the vertical acceleration at the center of gravity with no weight (left), with comfort weights (middle) and motion sickness weights (right)

was already observed with single-model analyses. The surprising result comes from the feedback GLA controller obtained by multi-model H_2/H_∞: it leads to almost the same loads alleviation capability as the one using a lidar. This effect, which has been discussed in section 4.6.2 based on simulations with a single model, it can be explained by the important use of the elevators, creating at the same time an important pitch response of the aircraft and increasing loads on the HTP (see appendix E.1 for the HTP loads envelopes). If it is deemed acceptable, knowing that the vertical load factor is reduced, then significant attenuation of the loads could be achieved even without a lidar. On the contrary, if for some reason regarding the interaction with the pilot, the control laws, the handling qualities and the HTP loads, much higher constraints on the elevators were imposed, then the lidar would be necessary to reduce the bending moment significantly. These results aim at emphasizing the different extreme strategies available for GLA, and observing the resulting influence on the aircraft loads and attitude. It is clear that these trade-offs can be conducted to find in-between strategies, taking into account the lessons learned from these cases.

Finally, the controllers can be compared in their ability to improve the comfort and the motion sickness in the aircraft. In section 2.3.10, a metric had been defined to quantify these two notions. Under some hypotheses, equivalent accelerations associated to comfort and motion sickness can be computed, by first computing the PSD of the vertical acceleration at a point of the aircraft, and then weighing the PSD and integrating it to compute equivalent standard deviations. Fig. 4.28 shows these PSDs, obtained for a von Kármán turbulence of 762 m and different controllers. On the left, the PSD of the vertical acceleration at center of gravity is shown, and in the middle and on the right, the weighted PSDs for comfort and motion sickness respectively. It can be seen that the comfort criterion is associated to low frequencies, up to 1 Hz, while the motion sickness criterion puts high weights on the high frequencies, between 3 Hz and 5 Hz. A model with a high-frequency

peak in the n_z PSD has been chosen on purpose. It can be seen that the controllers are more efficient at reducing the low-frequency response, resulting in a good reduction improvement of the comfort, while the high-frequency response is either ill damped, or even increased in the case of the multi-model H_2/H_∞ synthesis without lidar. Note that a high-frequency criterion on the n_z attenuation had been added, as explained in section 4.6, to attenuate this phenomenon.

More complete results are shown in Fig. 4.29 for comfort and motion sickness. The weighted PSDs have been computed for different models (same 3 Mach numbers and 16 mass configurations as for the loads envelopes), which accelerations at several positions of the fuselage in output. At each of these positions, the worst cases of equivalent standard deviation for comfort and motion sickness are computed. It must be noted that, due to the frequency analysis required to compute these criteria, the nonlinear effects of saturation and rate limiters are not included here. The point at 0 m is situated a few meters after the nose of the aircraft, and the last point is close to the tail. A first observation is that the worst case of discomfort gets worse as we go from the nose to the tail. This is intuitively explained by considering the fuselage as a beam element, with higher displacements at the tips than at the center of mass. All the controllers are quite efficient at improving the comfort of the aircraft, even the feedback GLA with μ-synthesis, which does not lead to high loads reductions. The multi-model H_2/H_∞ controller is the most efficient, with a 60 % improvement. Regarding the motions sickness, the effect of the GLA controllers is much lower. Those using a lidar manage to improve the worst case of motion sickness, and in particular the one obtained with μ-synthesis. The feedback multi-model H_2/H_∞ controller can increase the motion sickness depending on the fuselage position: this is probably due to a more reactive elevators control as was seen on Fig. 4.21. Poor motion sickness results are obtained with the μ-synthesis feedback controller, and are higher in the y-axis.

In order to also include results coming from simulations with nonlinear saturation and rate-limit effects, and the inclusion of the discrete gust response in the analysis, similar results are obtained by looking only at the unweighted vertical acceleration. Fig. 4.29 shows the worst cases of maximum absolute value of the acceleration due to discrete gusts (left), and the worst cases of standard deviation due to turbulence (right). It can be seen that in general, worst case of vertical load factor is attenuated at each position of the fuselage. It can also be seen that the worst positions on the fuselage, when no frequency weighting is used, are the two extremes (nose and tail).

Finally, a robustness analysis is performed to compare the different linear controllers studied in this work. Fig. 4.31 shows the multi-input frequency-dependent gain and phase disk margins. The disk gain margin is the lower positive scalar for which there exists a combination of simultaneous independent disk uncertainties in the input ports of the aeroelastic plant, all with modulus lower than this gain margin, leading to closed loop instability. Similarly, the phase margin is the lower angle such that there exists a combination on input disk uncertainties with phase lower than this angle, leading to closed loop instability. See section 4.5.1.4 for more details. The frequency at which the instability occurs leads to the frequency-dependent margins of Fig. 4.31. This confirms

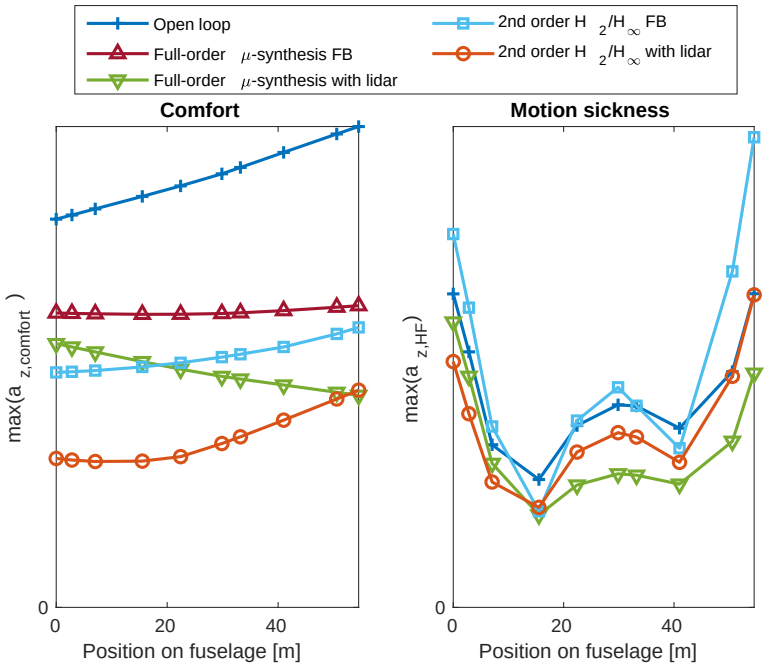

Figure 4.29: Maximum comfort and motion sickness standard deviations in response to a turbulence, at different positions of the fuselage. Each point is the worst case among different Mach number values and mass configurations

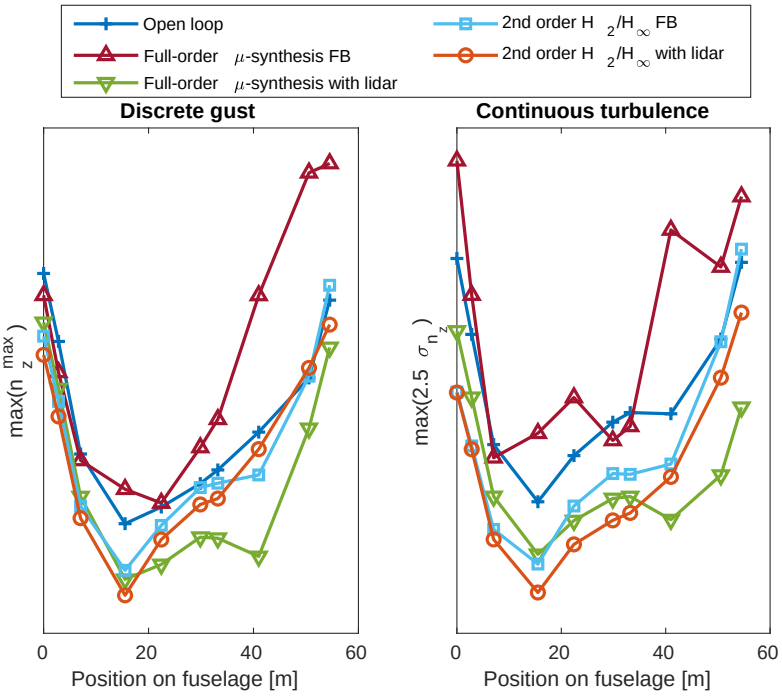

Figure 4.30: Maximum absolute values of the vertical load factor in response to discrete gust of various lengths (right) and maximum standard deviation in response to turbulence (left), at different positions of the fuselage. Each point is the worst case among different Mach number values and mass configurations

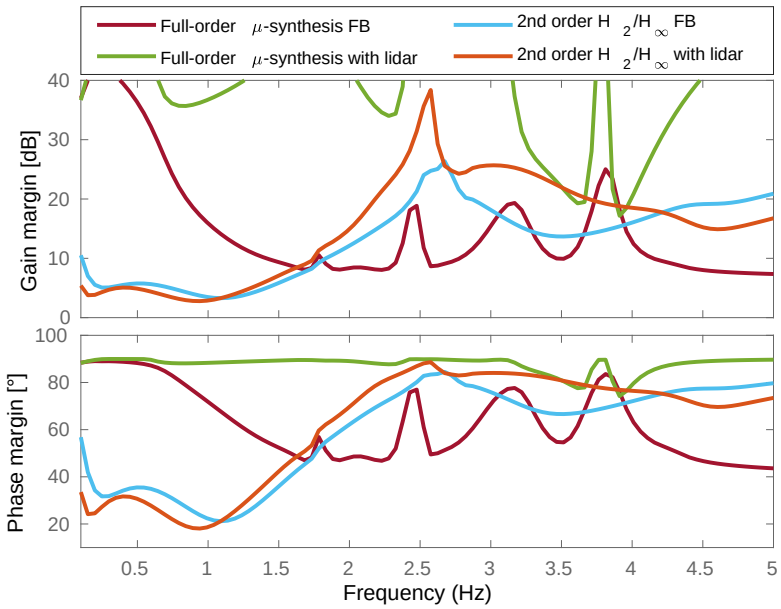

Figure 4.31: Multi-input margins at different frequencies, defined by disk uncertainties

that the controllers obtained by μ-synthesis are more robust than those obtained using multi-model H_2/H_∞ synthesis. It also shows the latter are closer to instability at low-frequency, with gain and phase margins of 4 dB and 20°. Another popular representation of the MIMO stability is the MIMO Nyquist diagram, and is shown in appendix E.2.

4.9 General conclusions about gust load alleviation

Some conclusions were drawn in section 4.5.8 from the study of robust GLA controllers designed by μ-synthesis. General trends on the capability to alleviate different loads on the wing and HTP at the same time were highlighted, and sensitivity analyses were conducted based on simulations on a single aeroelastic model. Three main questions naturally arose from this study: 1) Is it possible to improve the loads alleviation performance using a more aggressive control strategy, yet robust enough to work efficiently on the full range of flight and mass conditions? 2) What are the true loads alleviation capabilities of the robust controllers, in terms of worst case of wind loads (and not only on a single case)? 3) How do the different robust methods compare to each other and to other popular control techniques?

In order to answer these questions, a synthesis method based on different models has been used, in order to better define the physical uncertainty and reduce conservatism in the design. The use of H_2 criterion for loads alleviation objective is a convenient tool when structured synthesis is considered, as it requires less tuning than with H_∞ criteria. The latter are used for actuators and robustness constraints. The controllers hence obtained by multi-model H_2/H_∞ synthesis differ drastically by their use of the elevators, improving significantly the effectiveness of the feedback

part relatively to the feedforward control which uses the lidar as input. The first noteworthy effect is a better control of the vertical load factor, which is more attenuated than with the more robust controllers obtained by μ-synthesis. The second effect is a higher reduction of the worst-case bending moment and shear force, without increasing the torsional moment. This effect is particularly impressive when the lidar is not used, where the overall loads alleviation capability is comparable to the one used with a lidar. Quantitatively, worst-case wing root bending moment, shear force and vertical load factor can be attenuated by approximately 50 % with a lidar. Without lidar, this alleviation approximately goes down to 40 % with the multi-model H_2/H_∞ synthesis. These results correspond to the case in which 8 small ailerons are used on each wing. With only 4 of them, the bending moment reduction is much lower (15 %) and with 16 of them, it goes up to 60 % (but with a 110 % increase of the torsional moment). These loads reduction levels are of the order of magnitude of the maximum attenuation which can have an effect on the aircraft design (see section 4.2.6). Furthermore, when looking at the comfort criteria, the controllers obtained by multi-model H_2/H_∞ synthesis always improve the worst-case maximum equivalent acceleration by about 60 %, at each position of the fuselage. These controllers have been obtained with actuators constraints (the deflection angles are never higher than 15° and a rate limitation of 40°/s is applied). However, the more aggressive control strategy has a cost: first, the use of the elevators leads to important transient response of the pitch rate before converging, with oscillations and an increase of the maximum compared to the open loop case. Furthermore, the acceleration at high frequencies (between 2 Hz and 5 Hz) is generally higher than with robust controllers obtained by μ-synthesis, especially when no lidar is used. This leads to a higher motion sickness for the passengers, as studied with a dedicated criterion. The HTP loads envelopes were not shown for the sake of conciseness, but the multi-model H_2/H_∞ techniques lead to a strong increase of the worst-case bending moment (almost doubled). Finally, the controllers obtained by multi-model H_2/H_∞ synthesis have lower stability robustness margins. With these observations, the interest of using a lidar for GLA is challenged, highly depending on the constraints on the pitch motion an aircraft constructor wants to impose (due to interaction with the control law and the handling qualities), and on the criteria on the HTP loads. High constraints would limit the use of the elevators, strongly reducing the effect of the feedback controller, and high loads alleviation can be obtained only if a lidar is included. If concessions are made on this side, and the priority is given to the bending moment reduction, then the lidar loses importance and significant performance can be obtained with classical sensors.

When compared to other control techniques, the robust controllers lead to a loads alleviation performance similar or better than the MPC-based GLA, which suffer from other issues (robustness, implementability, unwanted nonlinear effects, ...), and better than a classical GLA technique by static ailerons deflection, which leads to a lower decrease of the maximum positive bending moment, no effect on the vertical load factor, and an important increase of the torsional moment. The robust control synthesis then appears as a serious candidate for future GLA implementations, leading to a strong reduction of the worst-case loads while ensuring stability and robustness. Many trade-offs have been highlighted, with many possible designs depending on the priority given to the different wing and HTP loads and to the effects on the pitch motion for instance.

Chapter 5

Active Flutter Suppression

Contents

The last chapter of this thesis is dedicated to a second active control application in aeroelasticity, namely the Active Flutter Suppression (AFS). While GLA was studied in Chapter 4 to reduce the loads aeroelastic models obtained within the flight domain (described in section 2.1.3), the purpose of AFS is precisely to expand it and increase the altitude and velocity bounds imposed by flutter constraints. One of the main requirements for an aircraft certification is that the aeroelastic model should be stable on an envelope defined by the certifications documents such as the European CS-25 [European Aviation Safety Agency (EASA) 2007]. By designing a control law able to improve the aeroelastic stability of the aircraft, hence increasing the velocity and altitude conditions at which the aircraft can safely fly, it could be possible to design more flexible wings with higher aspect ratio and reduced drag. The active flutter suppression is then another technological solution to improve the overall aircraft design by adequately placing the control surfaces and sensors, and using them within a control loop. Contrarily to the GLA case, the certification standards are not directly considered in the AFS study because they are unrealistic for the very unstable XRF1-HARW model used. Rather than looking to stabilize the aircraft on the envelope imposed by certification documents, the philosophy employed in this chapter consists in designing

efficient control laws to systematically expand the stability domain of the aircraft, under realistic actuators and sensors constraints. The modeling techniques studied in Chapter 2 and 3 are a first important step in the design of AFS control laws. Specifically, the definition of aeroelastic models of reduced order allows to use efficient control synthesis techniques, and the possibility to define them with realistic poles and input/output response is critical to study their interaction with the control laws.

5.1 Introduction to Active Flutter Suppression

The interaction of aerodynamics and structural dynamics can result in an instability called flutter. When a fluid flows along a surface, it applies local aerodynamic forces which lead to small deflections of the structure. In turn, this affects the fluid motion by creating a change of its direction called downwash. The fluid dynamics hence has a feedback effect on itself, resulting in the so-called aeroelastic system which accounts for this interaction. Some phenomena occurring on aircraft can only be predicted by aeroelastic analysis, such as nonlinear buffeting and limit cycle oscillations (LCO) [Bisplinghoff, Ashley, and Halfman 1955b]. The flutter instability happens when the increase in aircraft velocity eventually causes certain aeroelastic modes to become unstable, and can be described by linear models.

In order to prevent the flutter phenomenon, or at least increase the velocity at which it occurs, passive solutions can be applied by modifying the aircraft design and adding masses in such a way as to increase the velocity at which flutter occurs. Another approach is to design control laws that use the aircraft sensors to command the control surfaces and stabilize the aeroelastic system. This technique, known as Active Flutter Suppression (AFS), has been studied since the early 1970s [Nissim 1971; Sandford, Abel, and Gray 1975]. It is still an active research topic because of its complexity, requiring the analysis of many modes interactions, which are affected by the flight conditions. AFS also offers many possibilities, ranging from simple structured single-input-single-output (SISO) control laws [Schmidt 2016a] to Linear Parametric Varying (LPV) controllers obtained by modern synthesis methods [Chen, Sun, and Li 2012]. Because of the criticality of AFS systems, simpler techniques may sometimes be preferred for their robustness.

Before reviewing the different strategies that have been considered in the AFS literature, it is worth noting that the development of a control law is strongly dependent on the aeroelastic model used for synthesis, which then becomes an integral part of the control strategy and should be developed with care. This has different impacts on the control design process. First, some synthesis methods rely on certain hypotheses of the aeroelastic model such as linearity, or, as will be seen below, certain assumptions about the dependence of the model upon the aircraft velocity. Hence, a synthesis method must be chosen with full knowledge of the simplifying assumptions it implies on the aeroelastic model. Second, some techniques can be valid for a simple model (such as a 2D beam with few degrees of freedom) and become obsolete when applied to industrial applications involving a higher complexity, which cannot be reduced without losing key information.

The main difficulty in AFS synthesis is to define control strategies that stabilize the aeroelastic system over a range of aircraft velocities, which affect the dynamics in a nonlinear way. Robustness and adaptivity are then key concepts of AFS and can be obtained in different ways. A first solution is to obtain a single controller at a given airspeed with a robustness that ensures stability at other flight points (including the airspeed, Mach number) and mass configurations. Historically, this robust approach has first been employed using simple structured controllers, by using a feedback from a certain set of sensors to actuate the available control surfaces. In [Waszak and Srinathkumar 1991; Waszak and Buttrill 1991], a feedback using a single accelerometer located on the wing tip has been used as input of a third-order filter to control two symmetric pairs of ailerons. The filter is designed by closed loop poles placement, with the objective of stabilizing the flutter modes as much as possible. More recently [Schmidt 2016a; Schmidt 2016b] have used a similar method using two distinct feedback loops: one using the wing tip accelerometer and one using the pitch rate as input, to control the ailerons. In case more sensors are used, the poles placement method becomes tedious and optimization-based synthesis can be used, such as [Ricci et al. 2021] in which a single output feedback (SOF) controller is designed. Another popular technique for using information coming from different sensors is the Linear Quadratic Gaussian (LQG) approach, in which a stabilizing controller that minimizes a certain quadratic cost function is obtained by algebraic Riccati equations. Such a controller uses the system's states as input, and it requires an additional observer to estimate the states from the available measurements. This approach has been implemented in [Tewari 1998; Tewari 1999], where the variable to be minimized is the derivative of the normal acceleration. More recently, the LQG method has been implemented in [Waite et al. 2019] using a reduced order aeroelastic model obtained from accurate unsteady Computational Fluid Dynamics (CFD) calculations. In [Berg et al. 2021] LQG controllers have also been used, with a particular attention on the MIMO robustness of the system, assessed with modern tools such as disk uncertainties. Finally, H_∞ synthesis is an effective method to obtain robust stabilizing controllers, as it allows the minimization of the H_∞ norm which leads more naturally to robustness than quadratic criteria. Furthermore, it leads to dynamic controllers that can have more degrees of freedom than static gains for example. This method has been applied in [Theis, Pfifer, and Seiler 2016; Theis, Pfifer, and Seiler 2020] by carefully selecting the airspeed at which the controller is designed, in such a way as maximizing the flutter velocity. Indeed, designing an AFS law at too high a velocity may lead to low robustness, and the obtained controller can even destabilize the system at airspeed at which is was naturally stable. In [Faïsse et al. 2021], a H_∞ AFS synthesis is embedded into an outer-loop optimization of the aircraft structure. Using μ synthesis is another way to provide robustness in the controller design, and allows to study the effect of parametric and dynamic uncertainties onto the aeroelastic transfer functions and the poles trajectories when the velocity varies, as done in [Patartics et al. 2022].

As opposed to the robust approach, the second main strategy for stabilizing an aeroelastic system over a range of airspeeds is the design of adaptive laws. In this case, the dynamics of the controller can vary as the aircraft approaches flutter, with or without using the airspeed as an input. The most used method consists in designing control laws at different airspeed values, and interpolating them to obtain a control law as a piecewise-affine function of the velocity. This

strategy has been employed in [Marchetti et al. 2020; Ricci et al. 2022] for example, or in [Waitman and Marcos 2020] where H_∞ controllers computed at three different airspeeds are obtained and interpolated. This is made possible by an adequate balanced reduction of the controllers' state-spaces. In this case, the H_∞ norm of the transfer function from the ailerons angles to the modal displacement is the criterion to minimize. Other adaptive approaches consist in directly computing a LPV controller from the model, that must generally also be LPV. In [Chen et al. 2011; Chen, Sun, and Li 2012], a parametric Linear Quadratic Regulator (LQR) formulation is proposed and applied to a velocity-dependent aeroelastic model obtained by interpolation of reduced order models computed using reduced-order Proper Orthogonal Decomposition (POD) method. In [Barker, Balas, and Blue 1999; Barker and Balas 2000], a Linear Fractional Transformation (LFT) formulation is proposed, taking the velocity as uncertain parameters, and allowing the controller to have a rational dependence on it. An H_∞ formulation is proposed in [Moulin 2004] where a LPV controller with a polynomial dependence on the velocity and the air density is obtained, assuming the model follows the same dependence. Another formulation using convex optimization and LMI is proposed in [Alhajjar et al. 2018].

The adaptive methods are attractive as they allow real-time adjustments to the change of the aeroelastic dynamics. However, their practical implementation is not always straightforward. The computational cost for the controller design can become prohibitive when the complexity of the system increases, and some hypotheses on the model used for synthesis can be unrealistic. Some of the most technologically advanced systems for experimentally testing AFS techniques include the F-XDIA project developed by Politecnico di Milano and University of Washington that performed wind tunnels tests with a full model aircraft [Marchetti et al. 2020; Ricci et al. 2021; Berg et al. 2021; Ricci et al. 2022], or the European FlexOp project that recently performed flight test with a demonstrator [Takarics et al. 2020]. A study has been conducted at Airbus in [Fischer, Schröder, and Thormann 2022] with a model close to the one used in the present work, focusing on the practical implementability from an industrial point of view.

A novel strategy is developed in the chapter with the objective of obtaining simple laws, that can be designed and validated with industrial aeroelastic models that include a high number of modes, and that smoothly adapt to the aircraft velocity. This is performed by first developing hybrid system identification methods where a certain number of aeroelastic poles (stable or unstable) are computed and imposed to the model thanks to an adequate pole-residues decomposition and the use of the Loewner method [Mayo and Antoulas 2007; Karachalios, Gosea, and Antoulas 2019]. An H_∞ synthesis is then performed based on multiple models of various airspeed values (lower and higher than the flutter velocity) in a way that imposes the stability at high velocity without making the low-velocity systems unstable. This method then yields a set of LPV controllers, which are subsequently validated with reliable high-order models calculated on a broad range of airspeed values. A systematic procedure is developed to select a reduced number of actuators and sensors based on quantitative criteria. It relies on a genetic algorithm that estimates the configuration leading to the best possible modulus margins achievable by full-order controllers.

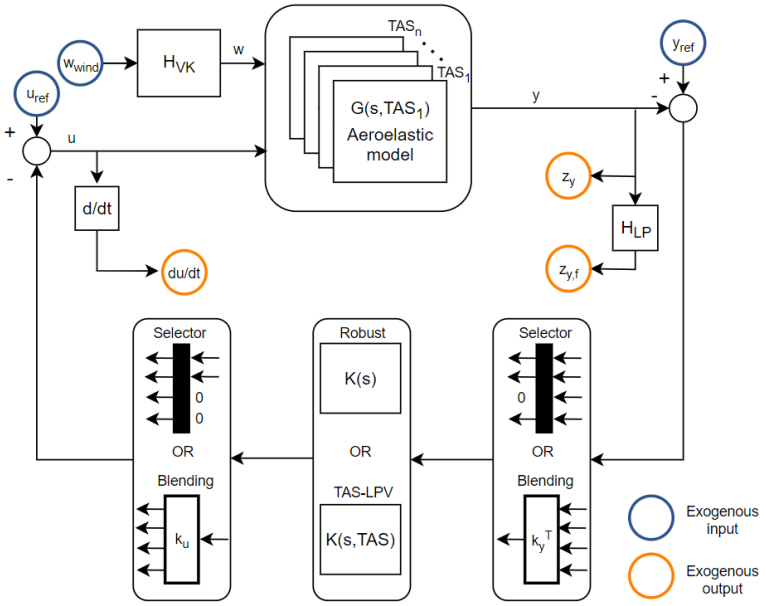

Figure 5.1: General control architecture

The objective of the AFS system developed in this chapter is to increase the flutter velocity in presence of robustness and system's constraints. Translating this objective into a control synthesis problem is not straightforward, and different strategies have been implemented, some of which were presented in the introduction section. This work adopts a robust control approach, with the H_∞ framework. Section 5.2 presents the objectives and methodology of the AFS synthesis developed in this chapter. Section 5.4 describes the H_∞ criterion that the controllers must minimize to achieve AFS with imposed robustness and actuators constraints. Based on this criterion, an optimal actuators and sensors selection is performed in section 5.5 by solving a combinatorial problem, using a genetic algorithm when the number of possible combinations is too high. In the same section, another approach for reducing the number of inputs and outputs is studied, based on the so-called inputs/outputs blending that was proposed in [Pusch, Ossmann, and Luspay 2019]. Finally, section 5.6 describes the multi-model structured H_∞ LPV synthesis used to design AFS controllers.

5.2 AFS objectives and employed methodology

The main objective of the AFS controller is to improve the flutter velocity as much as possible, by stabilizing the aeroelastic system when some poles become unstable. Additionally, the stability robustness of the stabilized closed loop should be maximized, and the control effort required to do so should be minimized. Furthermore, the number of sensors and actuators actually used should be as low as possible, to reduce the cost of the AFS system in view of its practical implementation. Finally, a smooth scheme for the AFS activation is wanted, meaning that the controller's action

should start at a given velocity before flutter arises, and should increase progressively as the open-loop aeroelastic system becomes more unstable.

To achieve these objectives, a LPV controller parameterized by the True AirSpeed (TAS) of the following form is progressively developed:

$$\mathbf{K}: \begin{cases} \dot{\boldsymbol{x}}_{\boldsymbol{K}}(t) & = \boldsymbol{A}_{\boldsymbol{K}}(\mathrm{TAS})\boldsymbol{x}_{\boldsymbol{K}}(t) + \boldsymbol{B}_{\boldsymbol{K}}(\mathrm{TAS})\boldsymbol{y}_{\boldsymbol{meas}}(t) \\ \boldsymbol{u}_{\boldsymbol{com}}(t) & = \boldsymbol{C}_{\boldsymbol{K}}(\mathrm{TAS})\boldsymbol{x}_{\boldsymbol{K}}(t) + \boldsymbol{D}_{\boldsymbol{K}}(\mathrm{TAS})\boldsymbol{y}_{\boldsymbol{meas}}(t) \end{cases} \tag{5.1}$$

where $\boldsymbol{x}_{\boldsymbol{K}}$ are the controller states, $\boldsymbol{y}_{\boldsymbol{meas}}$ and $\boldsymbol{u}_{\boldsymbol{com}}$ are respectively the measured output and control input, and the matrix functions $\boldsymbol{A}_{\boldsymbol{K}}$, $\boldsymbol{B}_{\boldsymbol{K}}$, $\boldsymbol{C}_{\boldsymbol{K}}$ and $\boldsymbol{D}_{\boldsymbol{K}}$ defining the state-space have a polynomial dependence on the TAS. A key driver in the design of the AFS controller is its complexity, that should be as low as possible, keeping in mind its practical implementation and certification on future aircraft. For this reason, controllers of low order are developed, through the structured H_∞ synthesis that take advantage of the multiple sensors and actuators available, and of a dynamical response to ensure good performance. A description of the synthesis methods employed in this chapter can be found in appendix D. Section 5.5 will show how to obtain reduced configurations, in which the number of controller's inputs and outputs is lowered, following the search of a simple controller. The reasoning behind the TAS parameterization is that the aeroelastic dynamics exhibit important variations as the velocity increases. It will be shown in the results section 5.7 that a simple LPV structure, with affine dependence of the state-space matrices on the TAS, leads to significant improvements when a progressive evolution of the system's dynamics is desired as the velocity increases and crosses its open-loop flutter value. Controllers which are robust with respect to the TAS variations will be investigated too. Another cause of aeroelastic dynamics variations is the evolution of the aircraft mass configuration during a flight, or between too flights. This cannot be easily parameterized by a single variable, contrarily to the TAS dependence. Developing an adaptive law for the controllers with respect to this uncertainty is not straightforward, and the robust approach is preferred in this chapter. Designing a LPV controller with robustness to mass variations is a computer-intensive optimization problem, and requires the tuning of different hyper-parameters by the user. For this reason, it is performed in several steps, starting by synthesizing a controller based on a single unstable model, which is used as a starting point for a LPV synthesis, as explained in section 5.6. From a LPV controller designed with models at several TAS values but with the same mass configuration, it must be decided whether the robustness to other mass configurations is ensured, and if it is not, a TAS-LPV synthesis using different mass configurations can be performed. Again, using as a starting point a controller design obtained with a single mass configuration can make the synthesis easier. This controller design strategy implies arbitrarily setting a maximum velocity value at which the closed loop should be stable. The general control architecture is illustrated on Fig. 5.1.

5.3 Aeroelastic models for control synthesis and validation

Two types of models are used in the AFS study. Validations models are obtained by rationalization of the GAF, following the Roger method described in section 3.2. They are of very high order, hence are not fit for controller synthesis, but can be used in simulations and to study the aeroelastic poles in closed and open loops. The controller synthesis is performed using reduced order models obtained by the technique described in section 3.8, which uses aeroelastic poles and residues obtained by the validation models. These so-called synthesis models have a much lower order than those used for validation, and can be used for controller design.

The aeroelastic models are split into longitudinal and lateral dynamics, and controllers are designed separately for each of them. Longitudinal dynamics are associated with symmetrical actuators actions (ailerons and elevators), while the lateral dynamics are associated with rudder deflections and antisymmetric ailerons and elevators deflections. This makes the synthesis computationally easier, and gives visibility to the AFS problem by highlighting its main bottlenecks. It will be identified that the longitudinal dynamics are much more restrictive than the lateral ones. The validation is always performed with the full dynamics, and using both controllers at the same time.

5.4 Synthesis criterion

Different approaches exist to translate the stabilization objectives into quantitative criteria for the controller synthesis. A first important consideration regards the models: using unstable models, such as in [Waitman and Marcos 2020], leads to a stabilization criterion that helps satisfying the design objectives. Requiring stability of several models, such as in [Marchetti et al. 2020; Ricci et al. 2022], leads to a closed loop robustness criterion that, again, goes in the direction of the objectives defined above. Additionally, transfer function attenuation can be required during the synthesis, based on LQG [Tewari 1999] or H_∞ [Waitman and Marcos 2020] criteria. Close to instability, the open-loop transfer function peak associated with the flutter mode increases, and imposing its attenuation in closed loop leads to damping and stability.

In this chapter, we impose the closed loop to be stable at a certain TAS, higher than the open-loop flutter velocity. Different cases of multi-model synthesis will be studied to improve robustness (see section 5.6) and adaptivity. Additionally, four H_∞ criteria are used. The first is the limitation of the control effort, by minimizing the H_∞ norm of the transfer function from the wind velocity to the derivative of the control surfaces angle deflections. Using the wind as an input bringing physical information to the synthesis, by connecting the AFS problem to the main disturbance that an aircraft can face in real applications. An input transfer is applied to the wind exogenous input so that the filter value has a Von Kármán PSD, similarly to the GLA synthesis of [Fournier et al. 2022b]. The derivative of the control surfaces deflections are used as

output instead of the deflection angles because they are far more constraining in the technological development level of current actuators and for the relatively high frequency problem studied here (the flutter modes have a natural frequency around 4 Hz). In addition to this H_∞ constraint, two criteria are defined for MIMO robustness: the H_∞ norm of the transfer function from a reference output to the measured output must be minimized, and similarly for the input. These two transfer functions are the output and input sensitivities, and the inverse of their H_∞ norms are called the modulus margins, as explained in appendix D. These margins can be related to the robustness of multiplicative inverse dynamic MIMO uncertainties. Finally, a fourth criterion is added based on the transfer function from the reference output to the control surfaces deflection angles, with the inverse of a high-pass filter. This criterion helps reducing the high-frequency response of the controller, and is applied to avoid interaction with high-frequency modes.

The final H_∞ cost function to minimize is then the following scalar:

$$F(\boldsymbol{G},\boldsymbol{K}) = \max\left\{a_1 \left\|\boldsymbol{T_{w\mapsto \dot{u}}} H_{VK}\right\|_\infty, a_2 \left\|\boldsymbol{T_{y_{ref}\mapsto y}}\right\|_\infty, a_3 \left\|\boldsymbol{T_{u_{ref}\mapsto u}}\right\|_\infty, a_4 \left\|\boldsymbol{H_{LP}}^{-1}\boldsymbol{T_{y_{ref}\mapsto u}}\right\|_\infty\right\} \tag{5.2}$$

where $\boldsymbol{K}$ is the controller, $\boldsymbol{G}$ is the aeroelastic model, H_{VK} is the Von Kármán equivalent transfer function, $\boldsymbol{H_{LP}}$ is a low-pass filter with flat response at very high frequency so that its inverse is causal, a_1 to a_4 are tuning hyperparameters, and $\boldsymbol{T_{a\mapsto b}}$ designates the transfer function from a generic variable a to another generic variable b. The different signals are depicted on Fig. 5.1. It can be noted that the static gain of the controller $\boldsymbol{K}(0)$ is not minimized here to avoid having too many constraints. Imposing $\boldsymbol{K}(0) \approx \boldsymbol{0}$ leads to reduced interactions with handling qualities and other aeroelastic modes, and can be studied in the future.

5.5 Actuators and sensors selection

The full aircraft model contains many actuators and sensors described in section 2.1. In order to define a realistic configuration, only some control surfaces will be used. The number of sensors used is also limited in an effort to reduce the controller's complexity. The first step to do so is to group the control surfaces: 4 sets of ailerons situated next to each other are defined on each wing, each set having approximately the same total surface. Furthermore, as explained in section 5.2, the model is split into its longitudinal and lateral dynamics, and the inputs and outputs of each model are selected and modified accordingly. Two simplification of the controller are studied based on inputs/outputs selection. The first is an optimal reduction of the sensors and control surface groups used. The second, called inputs/outputs blending, is based on the work of [Pusch, Ossmann, and Luspay 2019]. It consists in selecting a linear combination of the inputs and of the outputs to transforms the MIMO controller synthesis into a SISO problem. The combinations are chosen in a way that maximizes the observability and controllability of a selected mode, in this case the flutter mode (as explained in section 5.2, each of the two dynamics has a problematic flutter mode whose damping continuously increases with velocity).

5.5.1 I/O selection based on closed-loop H_∞ criterion

While several criteria can be used to select the optimal inputs and outputs, such as maximizing the observability or controllability of the system, an effort is made in this chapter to keep the criterion as close as possible to the studied AFS synthesis problem. The objective is then to find the combination of inputs and outputs and the associated controller that minimize the H_∞ cost function defined by Eq. (5.2). As the number of possible combinations can be very high, this problem is computationally very expensive, especially if multi-model structured controller synthesis is performed at each iteration. For this reason, a first simplification is performed with respect to the actual synthesis described in section 5.6 by using unstructured H_∞ synthesis, compatible with the cost function of Eq. (5.2). As the aeroelastic models are of reduced orders, each unstructured synthesis can be performed in a limited time, and an optimal controller is obtained every time as the associated synthesis optimization is convex. The inputs and outputs selection problem hence obtained can then be formulated as:

$$\min_{\substack{u\in\mathcal{I}_u \\ y\in\mathcal{I}_y}} \min_{\boldsymbol{K}} F(\boldsymbol{G_{u,y}}, \boldsymbol{K}) \tag{5.3}$$

under closed loop stability constraint, where $\mathcal{I}_u$ and $\mathcal{I}_y$ are the possible indices for the control inputs and measured outputs respectively, and $\boldsymbol{G_{u,y}}$ is the aeroelastic model with only indices u and y selected in the feedback loop. In case the maximum numbers of inputs and outputs (cardinality of $\mathcal{I}_u$ and $\mathcal{I}_y$) are sufficiently low, an unstructured synthesis can be performed for each possible combination to find the optimum of this problem. However, this is generally not the case and dedicated optimization algorithms for global optimum search of a non-convex problem can be applied. In this chapter, a genetic algorithm [Goldberg 1994] is used, and proves very efficient in reducing the computational cost. It starts with a population of random parameters (here the input and output indices combinations), and computes the cost function (here the maximum modulus margin obtainable by H_∞ synthesis) for each of them. It then applies a set of rules inspired from evolution to select the best candidates and obtain new ones, and repeats the process until a stopping criterion is reached. While not efficient when the parameter space dimension is important and continuous, it is an efficient technique in case only a small discrete number of parameters are possible, which is the case here. When applied with a reduced number of possible combinations, the genetic algorithm has always produced the global optimum after a few minutes, computed separately by trying all possible configurations.

5.5.2 Blending approach

Based on the work of [Pusch, Ossmann, and Luspay 2019], a linear combination of inputs and outputs can easily be found is order to maximize the controllability and observability of a given mode. First, by putting the state-space model of the aeroelastic system in modal form (the matrix $\boldsymbol{A}$ is diagonal), the second-order model $\boldsymbol{G_f}$ associated with the mode of interest (two conjugate

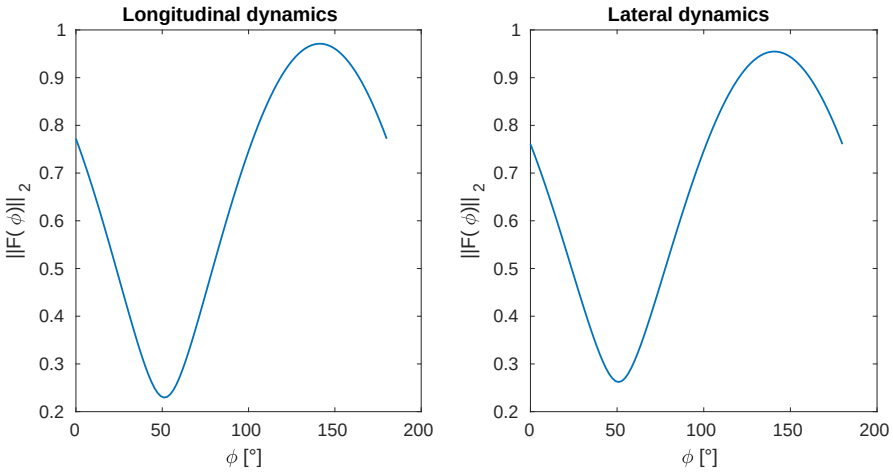

Figure 5.2: Blending cost function

poles) can be isolated from the rest of the dynamics ($\boldsymbol{G_s}$):

$$\boldsymbol{G}(s) = \boldsymbol{G_f}(s) + \boldsymbol{G_s}(s) \tag{5.4}$$

The objective is to find the vertical vectors k_u and k_y that maximize the H_2 norm of the transfer function associated with the mode of interest:

$$\max_{\substack{\|k_u\|_2=1 \\ \|k_y\|_2=1}} \frac{\left\|k_y^T \boldsymbol{G_f} k_u\right\|_2}{\|\boldsymbol{G_f}\|_2} \tag{5.5}$$

where the norms are H_2 when applied to transfer functions and L_2 when applied to vectors. In case $\boldsymbol{G_f}$ is a stable second-order transfer function, [Pusch, Ossmann, and Luspay 2019] shows that the optimization problem (5.5) can be reformulated as follows:

$$\max_{\phi\in[0;\pi]} \|\boldsymbol{F}(\phi)\|_2 \tag{5.6}$$

where the 2-norm of a matrix is defined as its maximum singular value and

$$\boldsymbol{F}(\phi) = \mathcal{R}(\boldsymbol{G_f}(j\omega_n))\cos\phi + \mathcal{I}(\boldsymbol{G_f}(j\omega_n))\sin\phi \tag{5.7}$$

where ω_n is the natural frequency of $\boldsymbol{G_f}$ and $\mathcal{R}$ and $\mathcal{I}$ denote the real and imaginary parts of a complex number respectively. For different values of ϕ ranging from 0 to π, the matrix $\boldsymbol{F}(\phi)$ is easily computed and a SVD is performed each time, leading to its 2-norm. At the value ϕ^* that maximizes the norm, the vectors k_y and k_u respectively correspond to the left and right unitary vectors associated with the highest singular value. As the cost function depends on only one, bounded, parameter, this optimization problem is very simple. Note that the H_2 norm is infinite when the mode of interest is unstable (as in this chapter). In this case, the authors of [Pusch, Ossmann, and Luspay 2019] propose to simply mirror the real part of the unstable poles. The cost function associated with the longitudinal and lateral dynamics of the XRF1-HARW aeroelastic

model can be found in Fig. 5.2.

A method to impose the resulting SISO transfer function to be decoupled from the other poles, by imposing that $\left\|k_y^T \boldsymbol{G_s} k_u\right\|_2 \approx 0$, is also described, but this strongly constrains the optimization (5.5) and leads to an important loss of performance. For this reason, it is not applied in this chapter. Although this so-called blending does not reduce the number of actuators and sensors used, the analysis of the optimal blending vectors k_u and k_y provides information about which inputs and outputs are the most useful based on this modal criterion. By keeping more than one singular value of $\boldsymbol{F}(\phi^*)$, one can increase the number of degrees of freedom of the reduced system. In this case, several blending signals corresponding to different combinations of inputs and outputs can be retained.

5.6 LPV multi-model H_∞ synthesis

Once the sensors and actuators have been selected or blended, the fixed-order controller can be designed in order to minimize a cost function similar to the one defined in Eq. (5.2). In case only one (unstable) model is used for design, the controller can be obtained by the structured H_∞ synthesis that performs the following nonlinear optimization:

$$\min_{\boldsymbol{K}\in\mathcal{K}} F(\boldsymbol{G}, \boldsymbol{K}) \tag{5.8}$$

where $\mathcal{K}$ is the set of controllers $\boldsymbol{K}$ having the structure defined in section 5.5, depending on the choice of inputs and outputs and on the possible multiplication by blending vectors. However, this approach does not ensure that the closed loop at lower TAS values is stable or that its performance according to the selected cost function is acceptable. To do so, a multi-model synthesis must be performed, by imposing stability at different TAS and minimizing the cost function on each of them. In this case, the cost function can depend on the TAS. The optimization associated with this multi-TAS synthesis is:

$$\min_{\boldsymbol{K}\in\mathcal{K}} \max_{i\in\mathcal{T}} F_i(\boldsymbol{G_i}, \boldsymbol{K}) \tag{5.9}$$

where $\mathcal{T}$ is the set of all TAS indices used in the controller design. It can be seen that because of how the multi-model synthesis works, only the maximum of the cost functions computed at the different TAS is minimized. If the cost functions were all minimized at the same time, a TAS-dependent criterion would not necessarily be needed. Since it is not the case, the user must define a cost function profile depending on the TAS. In this chapter, the cost function at a given velocity index i has the same form as the criterion defined before, but is multiplied by a coefficient b_i that makes the constraints stronger at low velocity:

$$F_i(\boldsymbol{G_i}, \boldsymbol{K}) = b_i F(\boldsymbol{G_i}, \boldsymbol{K}) \qquad i \in \mathcal{T} \tag{5.10}$$

A simple procedure is proposed to select these coefficients: a synthesis is performed at each index $i \in \mathcal{T}$ and the b_i are chosen as the optimal value of $F(\boldsymbol{G_i}, \boldsymbol{K_i})$ found independently for each synthesis. This way, if the multi-TAS synthesis based on Eq. (5.9) results in a cost function equal to 1 at each TAS value, it means that the performance is the same as the one obtained with local, independent controllers. The structure of the controller is then of particular importance, as a TAS dependence of a controller of the form of Eq. (5.1) can significantly improve the performance compared to a single robust controller, as explained in the results. Note that with the cost function used in this chapter, the best local controller obtained when the open-loop is stable is $\boldsymbol{K} = \boldsymbol{0}$, which leads to no control effort and sensitivity functions equal to static identity matrix gain. The proposed methodology then encourages to obtain a controller with progressively increasing action as the TAS increases, as defined in the objectives in section 5.2. In order to improve the LPV controller synthesis, the optimization can be initialized using a controller obtained with a single model.

Finally, in order to obtain robustness to mass variations, this problem can be augmented by including several models of different mass configurations at each TAS. The variation of the mass configuration is not parameterized by a single variable, contrarily to the TAS dependence. For this reason, neither the controller nor the cost function depend on it. While this methodology is implemented in this chapter, it does not lead to clear improvement in terms of robustness to mass variations, and the corresponding results will not be shown. Considering the Mach number, similar logics could be applied, either by defining a LPV dependence on the Mach or by imposing robustness to the dynamics variations. It is also possible to switch between different controllers that have been designed separately on a set of different Mach numbers. In this chapter, the Mach number is assumed constant.

5.7 Active flutter suppression results

This section presents the numerical applications of the techniques developed above with the XRF1-HARW aircraft. The numerical values of the parameters are first given in section 5.7.1. Then, the results of the actuators and sensors selection and of the input/output blending are described and analyzed in section 5.7.2. The different controller configurations obtained are compared based on mono-model synthesis in section 5.7.3. The controller structure that leads to the best tradeoff between performance and low complexity is then retained to perform multi-model (LPV and robust logics) at different TAS values in section 5.7.4.

5.7.1 Parameters

The models are computed at a constant Mach number of 0.86 and an altitude of about 8000 m (which varies with the TAS). A minimum flutter velocity of 278 m/s is imposed in closed loop, meaning that the controllers syntheses will always include at least the aeroelastic model at this

velocity. The longitudinal and lateral controllers have a fixed order of 5, resulting in a 10-th order full controller. The open-loop flutter velocity is about 262 m/s. The synthesis models are of 40th order, and the validation model is parameterized by the TAS and its order is about 800. The nominal mass case used in synthesis and analysis corresponds to the empty aircraft. The controllers are validated at the end of the results with four different mass configurations, that cover extreme cases of aircraft weight and center of gravity position along the X-axis (in the direction of the fuselage). In the multi-model synthesis, 7 models are used at different TAS linearly ranging from 254 m/s to 278 m/s. In the H_∞ criterion of Eq. (5.2), the equivalent von Kármán trubulence transfer function is

$$H_{VK}(s) = \frac{0.02s^3 + 0.3398(L_{turb}/\text{TAS})^2 s^2 + 2.7478(L_{turb}/\text{TAS})s + 1}{0.1539(L_{turb}/\text{TAS})^3 s^3 + 1.9754(L_{turb}/\text{TAS})^2 s^2 + 2.9958(L_{turb}/\text{TAS})s + 1} \tag{5.11}$$

where L_{turb} is the turbulence scale, set to 762 m. The low-pass filter is a 3-rd order Butterworth filter with cut-off frequency of 6 Hz. The time simulations are performed with a vertical $1-\cos$ gust of 46 m gradient and 8.5 m/s intensity. The time simulations and root-locus are systematically obtained with the validation model. Note that some numerical values are not given due to confidentiality issues.

5.7.2 Sensors and actuators selection

The two different reduction techniques described in section 5.5 are studied here. In the first, we impose the controller to use 2 groups of actuators and 5 sensors for each of the longitudinal and lateral dynamics. With only one group of actuators used, the performance was strongly deteriorated and very high control effort would have been needed. Recall that the actuators candidates are four groups of ailerons, the elevators and the rudder, while the possible sensors are four accelerometers spaced along each wing's span, five accelerometers along the fuselage, one on each side of the horizontal tail plane, one on the vertical tail plane and one gyroscope at the center of gravity. In total, about 5000 configurations are possible for longitudinal dynamics and 19000 for lateral dynamics. Computing the cost function with all of them would require several hours, hence a genetic algorithm is used instead. After about 15 minutes optimization, the combination found for the longitudinal dynamics is composed of the innermost and the outermost groups of ailerons as actuators, and the accelerometers on the four outermost positions along the wing and at the horizontal tail plane (symmetric actions and measurements are considered for the longitudinal dynamics). Regarding the lateral dynamics, the two outermost groups of ailerons are selected, and the same sensors as for the longitudinal dynamics, but this time with antisymmetric measurements. This confirms the intuition that the actuators on the wing are the most efficient to control flutter, and in particular the outer ailerons, often used in AFS. The fact that the sensors and actuators are almost the same for the longitudinal and lateral dynamics is handy, as it limits the complexity of the full configuration. Considering that the lateral dynamics are much less constraining than the longitudinal dynamics, it is decided to use the configuration found for the former in both cases.

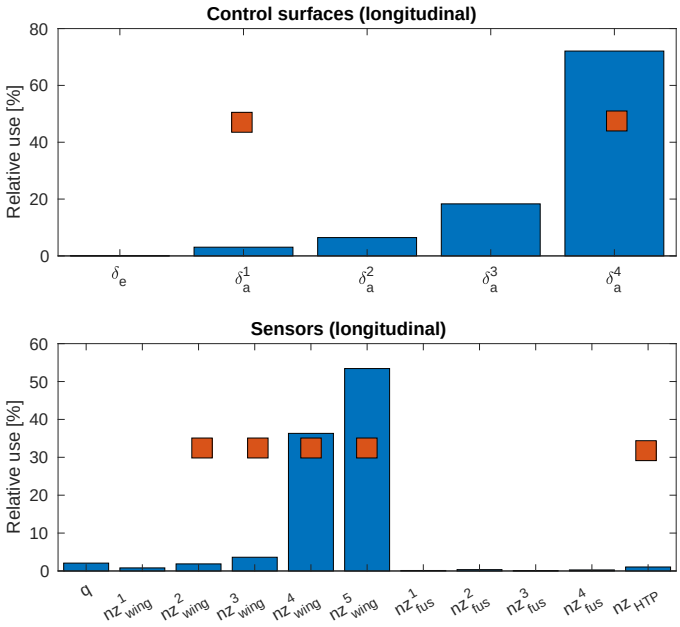

Figure 5.3: Actuators and sensors selection for the longitudinal dynamics by blending vectors (blue) and H_∞-based genetic algorithm (red)

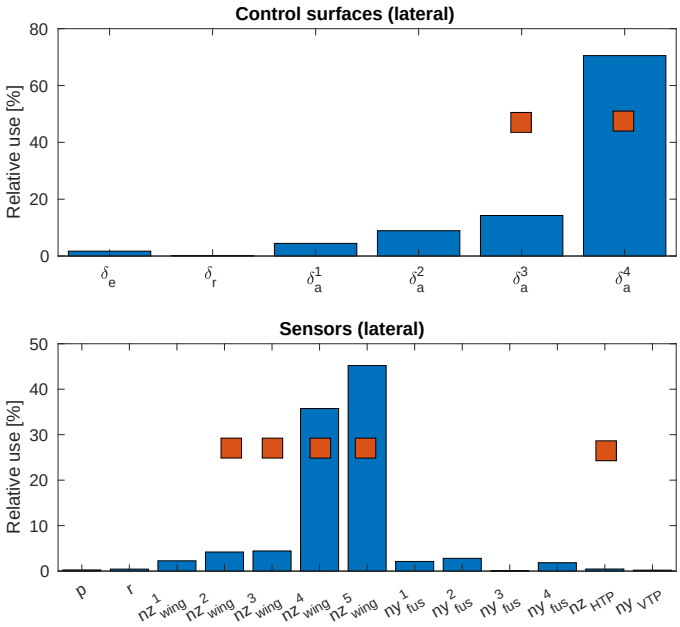

Figure 5.4: Actuators and sensors selection for the lateral dynamics by blending vectors (blue) and H_∞-based genetic algorithm (red)

The second simplification, studied separately, regards the input and output blending method described in section 5.5 and based on the work of [Pusch, Ossmann, and Luspay 2019]. While the idea is different from the actuators and sensors selection analyzed above, the blending method can give hints of which inputs and outputs are the most useful following a criterion based on observability and controllability of the flutter modes. The results are summed up in Fig. 5.3 and 5.4 for the two respective dynamics. The relative use associated with each actuator/sensor obtained by blending is shown, defined as the absolute value of the blending coefficient of a signal divided by the sum of the absolute values for all signals, and the selection by genetic algorithm described above is illustrated by red squares. While the two results agree in general, the use of the innermost aileron for longitudinal dynamics, on the one hand, and of the horizontal tail plane vertical acceleration for both dynamics, on the other hand, differ. It can be explained by the fact that while the modal criterion of the blending method is restricted to the flutter mode, the H_∞ criterion used by the genetic algorithm considers the full aircraft stability. The use of the acceleration at the tail plane might not help the flutter suppression directly but be a useful information for the global stability.

5.7.3 Mono-model synthesis

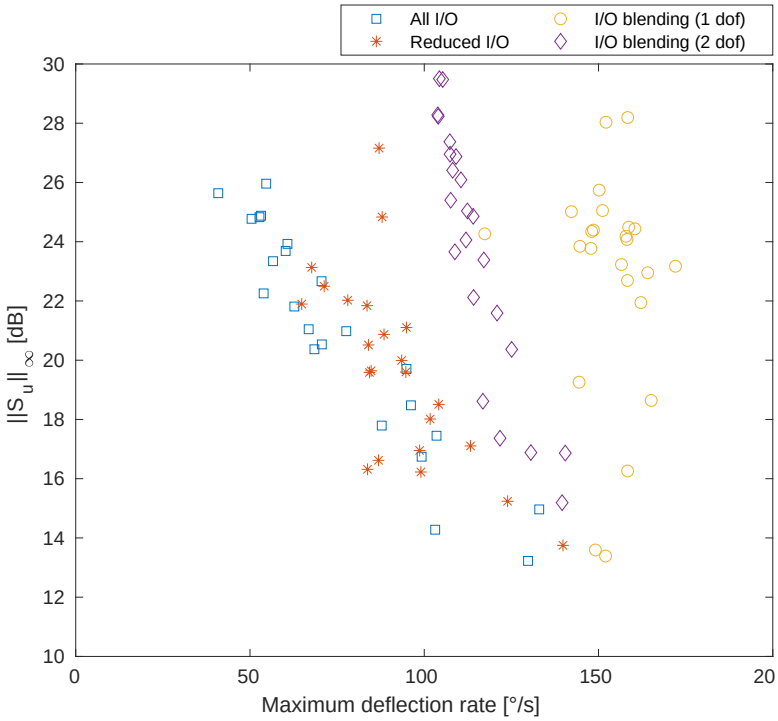

Figure 5.5: Robustness/control effort Pareto front with different tuning parameters and controller structures

Following the control design methodology described in section 5.2, a structured H_∞ synthesis is first performed using a single unstable model, at TAS = 278 m/s. Different combinations

of hyperparameters are studied in order to find an acceptable trade-off between robustness and control effort, and different controller structures are compared. This is done by simply varying the a_1 parameter of the cost function defined in Eq. (5.2), that regulates the control effort limitation. A controller is synthesized for 25 different linearly spaced values of a_1, and a Pareto front based on the analysis of each resulting closed loop is shown in Fig. 5.5. The y-axis displays the H_∞ norm of the input sensitivity function, which is the inverse of the input modulus margin. A point situated in the upper part of the figure is then less robust than a point in the lower part. For each closed loop, a time-simulation is performed with a vertical wind gust whose parameters are described in section 5.7.1, and the maximum control surface deflection rate is shown in the x-axis of Fig. 5.5. The case in which all of sensors and actuators are used is compared to the reduced configuration retained from the optimal selection and to the inputs/outputs blending of section 5.7.2, with one and two degrees of freedom. The two degrees of freedom case means that two input and two output blending vectors are used, leading to a 2×2 controller. It can be seen that, in general, the variation of the parameter a_1 leads to a trade-off between robustness and control effort. With all sensors and actuators included, maximum deflection rates as low as 50 °/s are obtained as response to a gust, which is achievable by the ailerons typically implemented on current generations of industrial aircraft. The configuration with two groups of control surfaces and five sensors (red asterisks on Fig. 5.5) leads to results that are very close to the full configuration. Note that, although not shown for the sake of conciseness, the performance obtained with only one group of actuators has proved significantly worse than with the full configuration. Finally, the results with inputs/outputs blending are also shown. When one degree of freedom is used, that is, the configuration where one input and one output blending vectors are used, leading to a SISO controller, the performance is significantly deteriorated compared to the full configuration of the optimal selection. When using instead two inputs and outputs vectors, which result in a reduced flutter transfer function with the same H_2 norm as the initial one (see section 5.5 for details), the performance is better but still worse than with the full or reduced configurations. This shows that in the case studied in this chapter, the criterion of expressing the unstable modes is not fully representative of the overall AFS design problem. In the end, the reduced configuration is retained for the good trade-off between controller simplicity and performance it leads to, and is used in the rest of the results. A value of a_1 leading to an input sensitivity norm of 18 dB and a maximum deflection rate of 120 °/s is selected, in order to have an acceptable robustness. While this deflection rate is typically too high to be implemented with current industrial technologies, future dedicated actuators could be able to overcome this limit. Furthermore, increasing the surface of the wing-tip ailerons that have been selected would reduce the required deflection rate.

Using the validation model, the root locus of the open loop and closed loop at different TAS values are displayed in Fig. 5.6. The two flutter modes with continuously decreasing damping ratio are clearly identified by they real part that becomes positive at high velocity. The third flutter mode is also seen, with a real part becoming positive and then negative again at increasing speeds. The stabilizing action of the controller leads to all modes becoming stable at velocity under 278 m/s. Note that the closed loop is globally robust to the difference between the synthesis and validation models. Furthermore, the closed loop poles location have a smooth dependence on

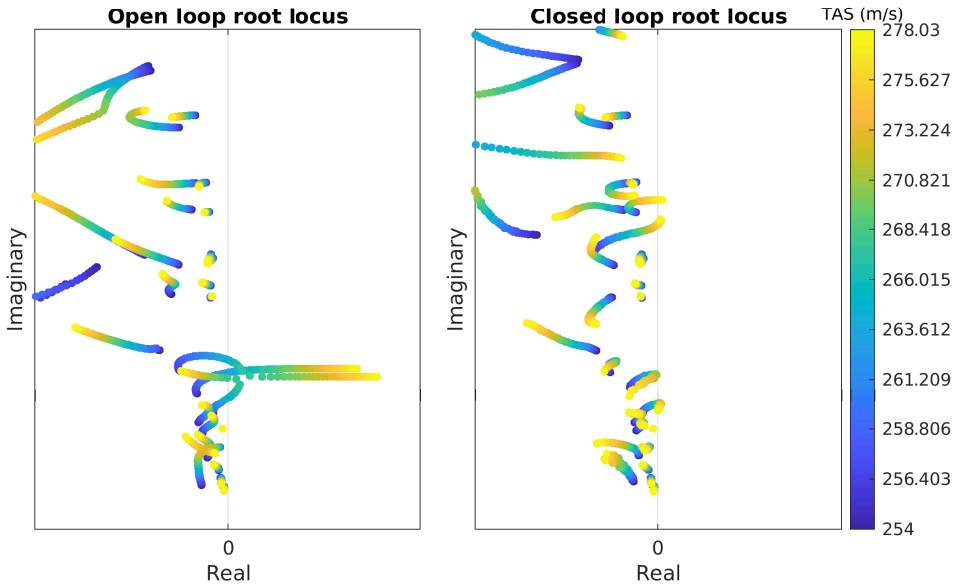

Figure 5.6: Root locus at various TAS obtained with the validation model and a controller synthesized with a single model

the velocity thanks to the limitation of high-frequency controller action. However, two cases of slightly negative damping occur: one at high velocity, that means that the controller is slightly less efficient with the validation model than with the synthesis model, slightly lowering the closed loop flutter velocity. The second type of closed loop instability occurs at intermediate velocities, which is more problematic as it has a bigger impact on the flutter velocity. It means that performing the controller synthesis at one TAS is not enough. Either a more specific definition of the uncertainties the closed loop should be robust to or a better adaptivity to the change of dynamics due to the TAS variations are required. This motivates the multi-model synthesis described in section 5.6, with or without TAS dependence of the controller.

5.7.4 Multi-TAS synthesis

In order to obtain better stability and lower control effort at intermediary values of the TAS, multi-model structured H_∞ syntheses is implemented based on the method described in section 5.6. The objective function computed separately on each synthesis model is shown in Fig. 5.7. Starting from the controller obtained with a single model in the previous section 5.7.3 (called mono-model in Fig. 5.7), it can be seen that the performance at TAS values lower than the one used for design are bad, which explains the stability issue that was noted on the root locus (Fig. 5.6). There is no guarantee that the intermediary models are stable, hence the use of a dotted line. The first step in including intermediary models in the synthesis is done by designing a controller for each of the seven TAS values, with the same cost function. The results are given in Fig. 5.7 with the blue curve with asterisk markers. As expected, the cost function obtained with local controllers is better at each TAS. It is equal to 1 for models that are stable in open loop,

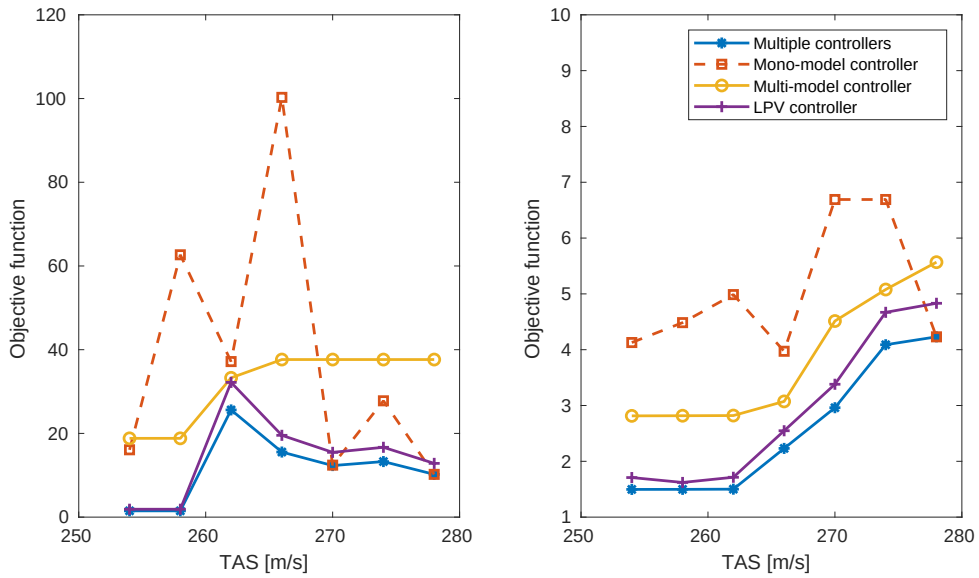

Figure 5.7: Cost function (defined in Eq. (5.2)) obtained with different multi-TAS control designs for the longitudinal (left) and the lateral (right) dynamics. Multiple controllers = one controller defined for each velocity. Mono-model controller = one controller defined at maximum velocity. Multi-model controller = one controller defined using multiple models computed at various velocities. LPV controller = one controller with affine dependence of the velocity

corresponding to controller transfer functions equal to zero at all frequencies. The values of the cost function obtained for individually synthesized controllers are used as an objective profile for the synthesis of multi-model controllers, as explained in section 5.6: in the best case, it will end with a multi-model cost function defined by Eq. (5.9) equal to one, corresponding to the same local performance as the one obtained with individual designs. The first multi-model synthesis is performed with a single robust controller, which does not depend on the TAS.

In Fig. 5.8, the cost functions obtained with a robust controller and using four different objective function profiles are shown. The first profile (blue solid line) is the one directly obtained from individual syntheses, and leads to bad performances at high velocity. For this reason the objective function profile can be smoothed, leading to smoother performances along the TAS profile. The other profiles are obtained by progressively diminishing the weighting difference between low and high TAS, the purple dotted line corresponding to the same weights at each TAS. Fig. 5.8 clearly shows the trade-off that must be made between the control performances at high and low velocities, according the criterion used in this chapter. The yellow curve has been selected, for the robust multi-model synthesis, and is compared to the other designs in Fig. 5.7. A significant deterioration of the overall control efficiency is noted when comparing the robust controller to the individual designs, demonstrating the need of an adaptation law to better follow the aeroelastic dynamics as the TAS varies. To this end, a LPV controller with affine dependence on the TAS is designed using the objective profile obtained from individual syntheses. This directly leads to good overall performances as seen on Fig. 5.7 with the purple line and "+" markers, that is very close to the best possible profile. In this case, a first-order polynomial dependence is enough to create the

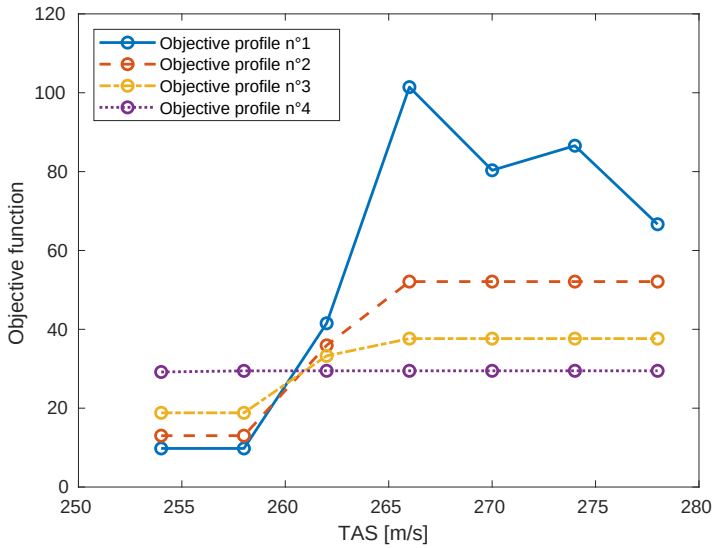

Figure 5.8: Cost function obtained with robust multi-model synthesis, for different objective profiles, defined by the set of weight given to each velocity in the TAS-dependent cost function

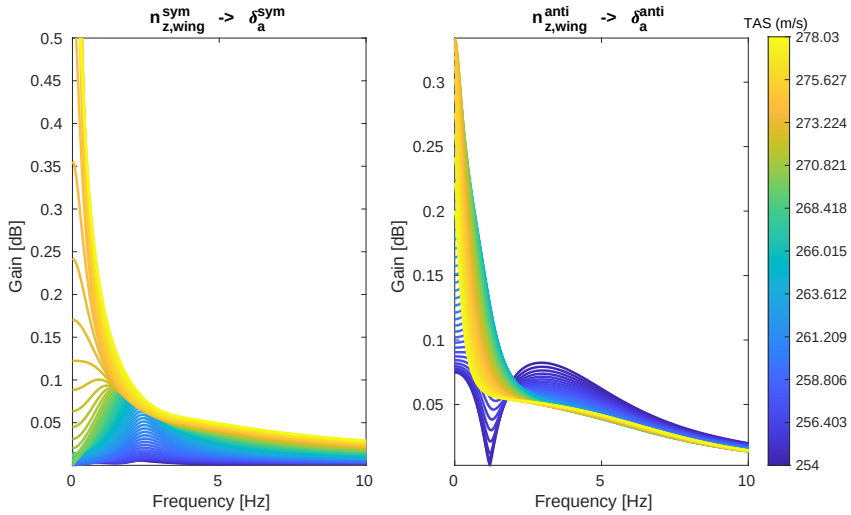

Figure 5.9: LPV controller bode diagram for one longitudinal (left) and one lateral (right) transfer functions

desired closed loop behavior at different velocities.

The Bode diagrams of two input/output combinations of the LPV controller transfer function are shown in Fig. 5.9. The first combination is from the wing-tip load factor to the wing-tip symmetrical ailerons deflection, representative of the longitudinal dynamics. It can be seen that the controller amplitude starts from almost zero at the TAS which triggers the AFS system, and increases at higher velocity. The second combination regards the lateral dynamics with the same actuators and sensors but with antisymmetric action and measurement. The evolution with increasing velocity is less clear in this case, which can be explained by the fact that the

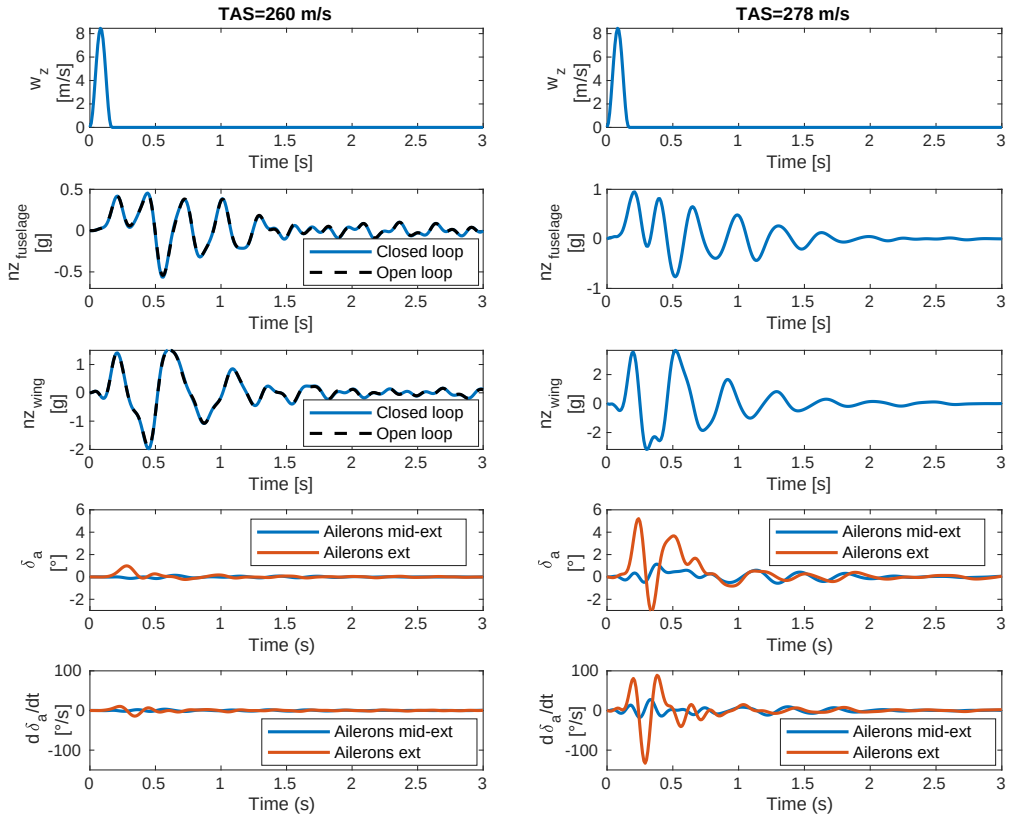

Figure 5.10: Time simulations of the closed loop response to a vertical gust, using a controller with reduced number of actuators and sensors

lateral dynamics are less constraining than the longitudinal ones, and lower control amplitudes are required at high velocity.

The time simulations obtained using the validation model at two values of the TAS and using the LPV controller selected from the previous considerations are shown in Fig. 5.10. The wind velocity w_z is displayed, followed by the vertical load factors response on the fuselage and at a location situated at the middle of the wing. At 260 m/s, the open loop is stable and can be compared to the closed loop: the objective of not disturbing the aeroelastic response at stable velocities is reached. However, the figure also shows the limit of the criterion used in this chapter: as no attenuation of the peak associated with the flutter modes has been required, the oscillations are not damped. The control action is low at low velocity, and reaches 120°/s at 278 m/s. The deflection angles are always lower than 10°, which is below the typical actuators constraints of the order of 30°. This also mean that no aerodynamic nonlinearity should be created from the controller's action. It can also be noted that the outer ailerons are more solicited than those that are closer to the middle of the wing. For this aircraft model, increasing the surface of the outer ailerons could then increase the AFS performances. The closed loop load factors at 278 m/s cannot be compared to the open loop case as it is unstable. It can however be seen that the fuselage load factor remains below 1 g.

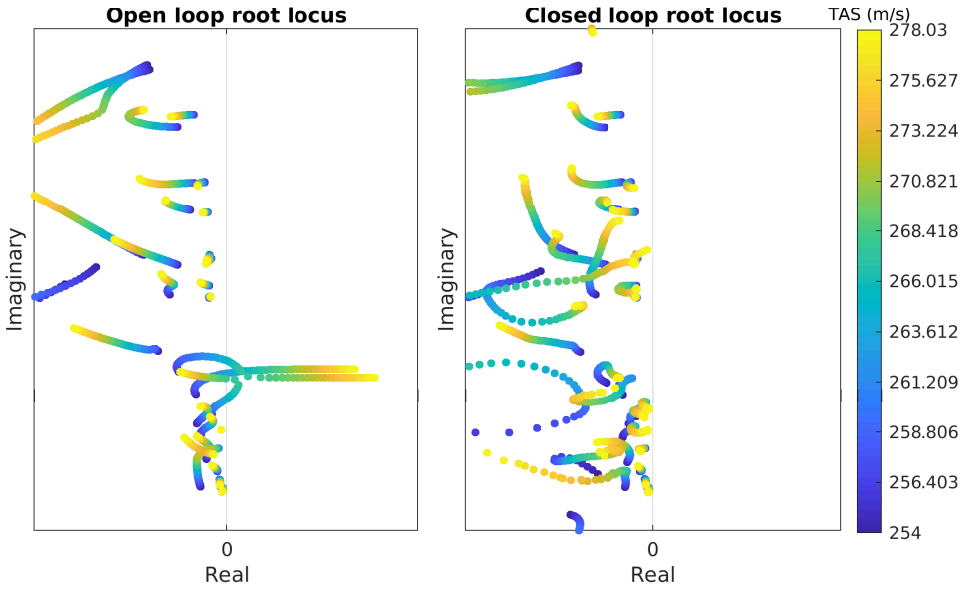

Figure 5.11: Root locus at various TAS obtained with the validation model and a LPV controller

Similarly to the controller that had been designed with a single model, the root loci of the closed loop obtained with the validation model and the LPV controller are plotted at different velocities in Fig. 5.11. This time, the real part of all modes are negative for all velocities. This confirms the interest of using a multi-model synthesis for AFS, with good multi-TAS closed-loop performances thanks to the LPV law.

Finally, an analysis of the LPV controller is performed using validation models corresponding to four mass configurations, and the results are shown in Fig. 5.12. As explained in section 5.7.1, they have been selected to cover extreme cases of aircraft mass and center of gravity position. The first mass configuration is the same as the one used for synthesis. The global evolution of the poles shows a certain robustness to the uncertainties associated with the mass variations. While the modes are generally all stable, one of them becomes unstable in the two last mass configurations. A first solution to solve this problem could be to include in the controller design several aeroelastic models corresponding to different mass configurations. While this synthesis problem can look numerically expensive at first glance, the fact that low-order models are used with split longitudinal and lateral dynamics, and the use of initial conditions in the optimization from the LPV problem with one mass case, a controller can be obtained in a few minutes. However, no improvement has been found with respect to the results shown in Fig. 5.12. This shows the difficulty of the AFS problem studied in this chapter. Not only the controller should stabilize the aeroelastic system at different velocities under important actuators constraints, but the flutter modes and their shape are susceptible to differ depending on the mass configuration. Additional research is needed to decide whether robustness to the mass configuration is possible or not, in which case adaptive laws could be required.

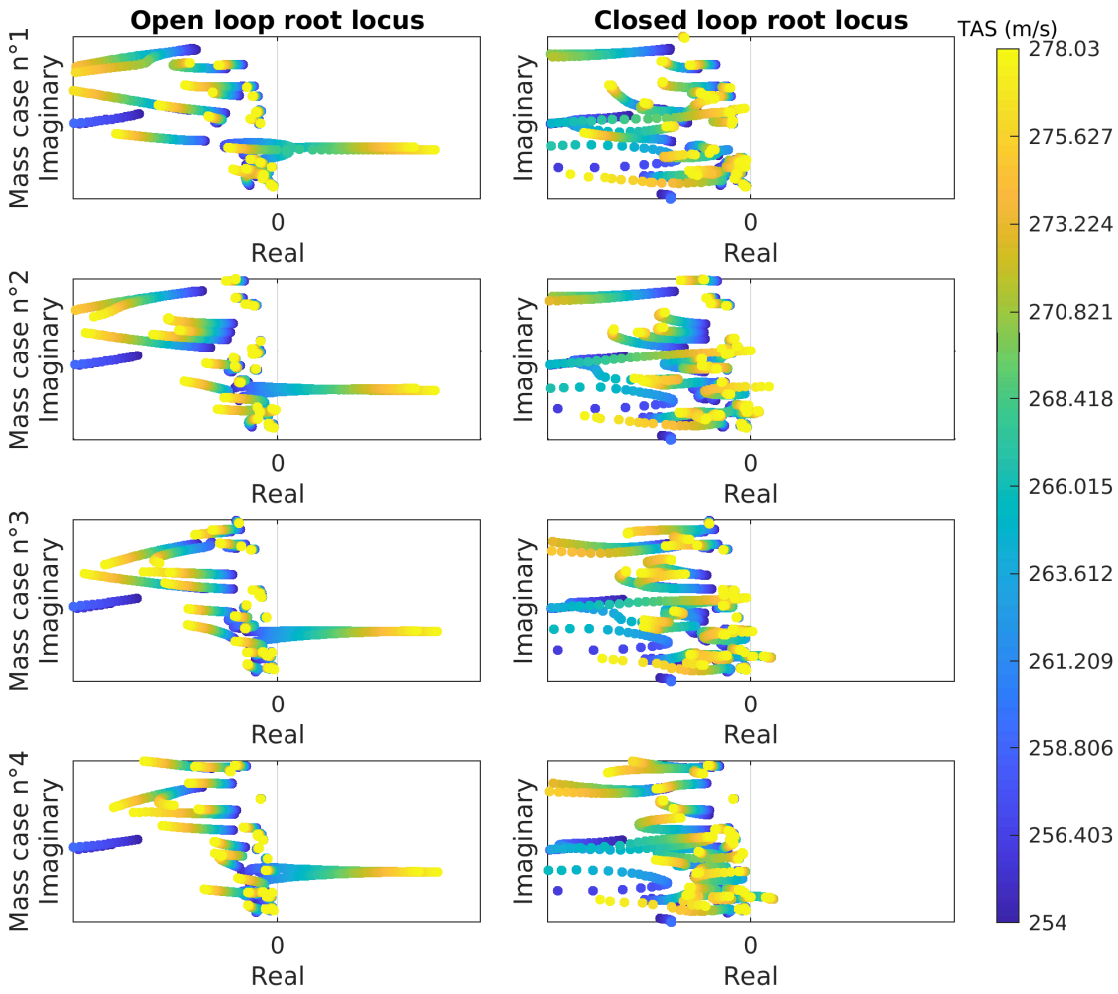

Figure 5.12

5.8 Conclusion about active flutter suppression

This chapter has proposed a complete control strategy for Active Flutter Suppression, starting from a hybrid reduced-order modeling of the aeroelastic system that uses frequency response data and aeroelastic modes knowledge. Based on a common objective function, an optimal sensors and actuators selection with reduced numerical complexity is proposed and different steps of controller strategy are described, form multiple mono-model syntheses at different velocities to LPV design with possible extension to multiple mass configurations. The simplicity of the controller is sought throughout this process, in the view of future industrial implementation.

The ailerons and accelerometers situated at the wing tips have been found to be the most useful for this AFS problem, using two criteria based on closed loop and observability/controllability of the flutter modes respectively. However, it has been found that additional sensors and actuators are needed, probably to maintain the overall stability of the aircraft and not only the one associated with the flutter modes. The synthesis based on a single unstable model has shown its limits when

validated at different velocities, and although the multi-TAS robust controller synthesis shows some improvements with respect to the former, it still leads to loss of performances compared to what can be possibly achieved with controllers designed independently at different velocities. The TAS-dependent LPV law has proved, on the contrary, very efficient, even with a simple affine dependence of the state-space matrices that constitute them on the velocity.

While these results are promising, some issues remain unsolved, such as the design of a controller valid at different mass cases and different values of the Mach number. Because of the important dependence of the aeroelastic dynamics on these parameters, a robust approach might not be sufficient and some adaptive strategy might be needed.

Chapter 6

Conclusion

Contents

6.1 Summary of the work accomplished

This thesis has investigated different subjects related to the aeroelastic dynamics of an aircraft, and to its active control. The starting point was the study of active Gust Loads Alleviation of a flexible aircraft using a lidar. By appropriately using the available control surfaces and sensors of an aircraft, gust load alleviation aims at reducing the maximum loads susceptible to be created in the structure due to important turbulences or wind gusts. Including a gust load alleviation system in the design of an aircraft could lead to significant mass savings, hence improving its overall performance, by reducing the size of the parts responsible for ensuring the structural integrity of the aircraft (such as the wing spar). The investigation of techniques dedicated to the design of gust load alleviation control has quickly highlighted the need to study the aeroelastic modeling in depth, by developing reduction and identification techniques which allow to design controllers in adequate conditions. Indeed, the state-space models of the linearized aeroelastic equations obtained by the classical techniques used in the industry tend to be of very high order, leading to unnecessarily long control synthesis with many numerical issues. Instead, an approach leading to reduced-order models has been developed, focusing only on the characteristics that are truly useful for gust load alleviation, namely the input/output response accuracy on a limited range of frequencies with preserved stability (when working only at flight points at which the aircraft is stable, the reduced-order model should be stable too). To this effect, the reduced-order modeling process becomes an integral part of the control synthesis, selecting the model's features for their effect on the controller synthesized based on it, hence not for approximation purposes alone. A second application, active flutter suppression, has been studied as a secondary objective of the thesis. It consists in stabilizing the aircraft at flight points in which the interaction between aerodynamics

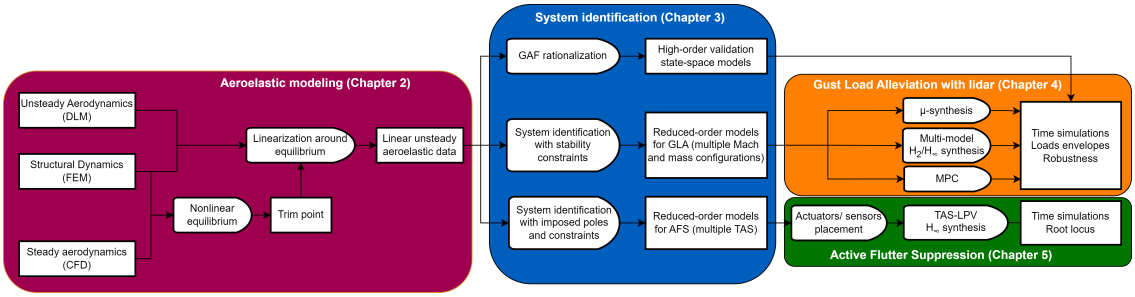

Figure 6.1: Overview of the process followed in the thesis

and structural dynamics would create an aeroelastic instability called flutter. A dedicated active controller is designed to this aim, hence increasing the velocity at which flutter occurs. Such a technique could allow the design of aircraft with more aerodynamically efficient wings of high aspect ratio and low weight, but more subject to flutter and other aeroelastic phenomena. The reduced-order models used for gust load alleviation are not totally appropriate for active flutter suppression, as this problem also requires an accurate representation of the aeroelastic modes. In order to include this objective in the reduced-order aeroelastic modeling process, dedicated system identification techniques have been required for active flutter suppression. An overview of the general process followed during the thesis is illustrated in Fig. 6.1.

This thesis has put strong emphasis on defining objectives as close as possible to the industrial needs, and translating them into control and system identification criteria which can be met using modern techniques. The challenges and constraints of active aeorelasticity such as gust load alleviation and active flutter suppression have evolved throughout this work, to go in the direction of a real-life implementation on flight demonstrators and future generations of commercial aircraft. This was made possible thanks to the collaboration with the Loads and Aeroelastic department of Airbus, which helped defining not only the typical constraints of the systems and methods used in aeronautics, but also the philosophy adopted for the design and the certification of an aircraft. This collaboration has allowed to work on complex models obtained by industrial tools, to define the system's limitations and the certification methodology based on feedback from engineers working on commercial airplanes design, and to study the problem from different angles, taking into account the interaction between several subsystems.

More specifically, the contributions to the research in aeronautics and control theory can be listed as follows:

- **Reduced-order aeroelastic modeling methodology**. It consists of generating frequency response of the system with inputs and outputs of interest, and then applying system frequency-based identification techniques
- **Application of the subspace and Loewner identification methods to aeroelastic data**. They are compared on different frequency ranges with multiple inputs and outputs used for active control.

- **Procedure to impose poles location constraints in the system identification process**. Already existing for subspace methods, it was extended to the Loewner framework.
- **Novel mathematical techniques to impose some poles in system identification**. State-space models are identified based on frequency data, with a set of pre-computed poles imposed to the identified model, with the possibility to add constraints on the free poles' location.
- **A novel technique to identify multiple state-space models with common C matrix using the Loewner framework**. This leads to the definition of a polytopic model with possible applications to robust and adaptive controls.
- **A framework for designing robust gust load alleviation controllers based on multi-input multi-output disk uncertainties and μ-synthesis**. It has a structure compatible with flight control laws implemented on current generations of commercial aircraft.
- **The study of the capability of a gust load alleviation controller to reduce simultaneously different loads on the wing and the horizontal tail plane**. It highlights the different possible strategies which can be adopted, depending on the priority given to certain loads.
- **A multi-model H_2/H_∞ synthesis process**. It is developed in order to reduce the control design conservatism, by defining physical uncertainties in line with the aircraft certification process for gust loads.
- **Analysis tools based on correlated loads envelopes**. They quantify the loads attenuation performance of gust load alleviation systems, using validation models at multiple Mach number values and mass configurations, with different extreme winds, including saturation and rate limiter nonlinearities.
- **An overall comparison of different control strategies for gust load alleviation**. It includes constrained model-predictive control and a simple logic of static ailerons deflection.
- **Sensitivity analysis**. They are conducted to better understand the influence on the loads alleviation performance of the lidar measurement distance, the lidar measurement noise, the effects of control surface saturation and rate limitation, and the number of ailerons used.
- **A complete active flutter suppression design methodology**.
  - definition of a common H_∞ criterion promoting robustness and reduced control effort
  - selection of the optimal sensors and actuators location for longitudinal and lateral dynamics, based on closed-loop criteria. A genetic-based optimization with unstructured H_∞ synthesis at each function evaluation has been defined to accelerate the process
  - synthesis of a reduced-order controller using an unstable model, at the maximum considered velocity

– linear-parameter varying controller synthesis with velocity dependence, using the previous step to initialize the optimization.

6.2 Other research directions and perspectives

This thesis has focused on one methodology for reduced-order aeroelastic modeling, and on the use of linear robust control for gust load alleviation and active flutter suppression. Other directions are worth mentioning here, either because they have been tried and deemed less promising than those adopted in this work, or because they could be of interest for the future of research in control and aeroservoelasticity theories.

6.2.1 Aeroelastic modeling and system identification methods

Further studies in the field of system identification could benefit to the synthesis of gust load alleviation and active flutter suppression controllers, but also to aircraft simulations for the loads computations. The Loewner method has proved very efficient to obtain directly accurate state-space models from frequency data, with few intermediary steps. While the mathematical methods described in this document to impose constraints on the poles locations have mainly used the subspace method, other attempts to do so with the Loewner method have been unsuccessful. Section 3.4.2 has illustrated a procedure to impose stability with this method, it is applied after the identification process, in post-analysis. Working directly on the Loewner matrices to shape the identified state-space model is an interesting direction, which could serve not only the field of aeroelastic modeling, but also the system identification theory itself. Another critical direction for aeroelastic modeling and control regards the definition of parameterized models. The multi-model philosophy developed for gust load alleviation and active flutter suppression has some drawbacks, typically due to the fact that the different models are obtained using distinct identification processes. Continuity between these models, and in some cases consistency, are not ensured using this multi-model approach. A single model with parametric dependence on the flight conditions and on some parameters defining the mass configuration, would be ideal for analysis and possibly for control synthesis (granted that the numerical complexity does not become too high). Some elements have been proposed in section 3.9, with the use of the Loewner method for polytopic and linear-parametric varying identifications. Models with linear fractional transformation parametric dependence are not studied, but can be of great interest for their compatibility with μ-synthesis. This approach can be a promising direction for aeroservoelasticity and flight control, leading the way to unified formulations of controllers smoothly adapting to the conditions, with the benefits of a model-based approach. Finally, the identification methods studied in this work often rely on semi-definite programming, as it is often the case in system identification and control theories. The recent and promising study of so-called "sparse" problems proposes to go beyond the classical semi-definite programming framework, considering optimization problems which can be convex

but not differentiable (ex: the Lasso problem, which includes a non-differentiable 1-norm within the optimization objective) or even non-convex, solved for example by finding solutions of the "closest" convex problem. Examples of this approach to system identification can be found in [Yılmaz et al. 2018] and [Miller, Singh, and Sznaier 2020], using fast algorithms based on Frank-Wolfe algorithm (see [Vinyes and Obozinski 2017] for example) or alternating direction method of multipliers (ADMM) described in [Boyd et al. 2011]. By getting rid of the semi-definite framework, more general problems can be considered and with the potential to handle higher quantities of data and more variables, although generally providing less certainties of convergence.

6.2.2 Active control methods

Concerning active control methods, an important step would be, in accordance to what has been said above for parametric models, to define adaptive controllers with strong a-priori knowledge of the dynamics. While this does not seem to be a critical direction for gust load alleviation, as it has been shown in this work that a robust approach leads to almost optimal results, it can be of significant importance for active flutter suppression. Due to the higher-frequency dynamics included, the controller must target accurately certain modes, which can vary when the flight condition and mass configuration change. While the robustness is difficult to obtain in the active flutter suppression problem, as demonstrated in this work, adaptivity could be a promising approach if high confidence in the modeling process can be demonstrated. Concerning gust load alleviation, the main research direction to continue the work undertaken in this thesis would be a more practical integration in the aircraft. This would require taking into account many interactions with other subsystems and with industrial constraints. One major aspect would regard the compatibility with the existing flight control laws, which has been considered in this work but using a simplified framework. The definition of a robust logic for the activation of the gust load alleviation system is critical to prevent it from being excessively intrusive in most flight conditions. While this work has mainly adopted the "loads" point of view, a better understanding of the overall control system and laws would then be needed to take the gust load alleviation to the next step. With the lessons learned from this thesis, the current understanding of the challenges and issues related to gust load alleviation has already reached a level of maturity which could allow an implementation on a flight demonstrator. This would be crucial to better understand the difference between aeroelastic models and reality, and how this would affect the ability to efficiently reduce the aircraft loads. Furthermore, one of the main unknown in this thesis concerns the lidar sensor, whose limitations are not yet well understood. Different lidar have been flight-tested, but due to the variety of technologies and applications, the understanding of how reliable the remote wind velocity measurement can be still has much room for improvement. Testing these technologies on true systems, and potentially looking at the influence on other promising techniques for gust load alleviation such as the folding wingtips, will be a cornerstone in preparing them for the implementation in the design of future generations of commercial aircraft.

Appendix A

Minimal state realization of MIMO transfer functions

This appendix describes a procedure developed in this work to obtain a minimal state realization of a MIMO transfer function expressed in pole-residue form. Only the case in which poles have a simple multiplicity is studied here. The reader can refer to [Kailath 1980] for more details of the general case.

Poles with simple multiplicity

We consider the pole-residue decomposition of a MIMO transfer function $\boldsymbol{H}$ whose poles have a simple multiplicity:

$$\boldsymbol{H}(s) = \boldsymbol{R_0} + \sum_{i=1}^{n} \frac{\boldsymbol{R_i}}{s - \lambda_i} \tag{A.1}$$

where $\lambda_i \in \mathbb{C}$ are the poles, $\boldsymbol{R_i} \in \mathbb{C}^{N_y \times N_u}$ are the residues with $\text{rank}(\boldsymbol{R_i}) = r_i$. For each residue $\boldsymbol{R_i}$, a rank-revealing decomposition can be performed, using for example SVD. The transfer function can then be rewritten as

$$\boldsymbol{H}(s) = \boldsymbol{R_0} + \sum_{i=1}^{n} \frac{\boldsymbol{C_i B_i}}{s - \lambda_i} \tag{A.2}$$

where $\boldsymbol{C_i} \in \mathbb{C}^{N_y \times r_i}$ and $\boldsymbol{B_i} \in \mathbb{C}^{r_i \times N_u}$ are full-rank matrices. Writing

$$\frac{\boldsymbol{C_i B_i}}{s - \lambda_i} = \boldsymbol{C_i}(s\boldsymbol{I_{r_i}} - \boldsymbol{A_i})^{-1}\boldsymbol{B_i} \tag{A.3}$$

with $\boldsymbol{A_i} = \lambda_i \boldsymbol{I_{r_i}}$, the transfer function can be expressed in the following form:

$$\boldsymbol{H}(s) = \boldsymbol{R_0} + \sum_{i=1}^{n} \boldsymbol{C_i}(s\boldsymbol{I_{r_i}} - \boldsymbol{A_i})^{-1}\boldsymbol{B_i} \tag{A.4}$$

Each state realization $(\boldsymbol{A_i}, \boldsymbol{B_i}, \boldsymbol{C_i}, \boldsymbol{0})$ is clearly minimal as $\boldsymbol{B_i}$ is full row-rank and $\boldsymbol{C_i}$ is full column-rank. Now assembling the state matrices as:

$$\boldsymbol{A} = \begin{bmatrix} \boldsymbol{A_1} & & \boldsymbol{0} \\ & \ddots & \\ \boldsymbol{0} & & \boldsymbol{A_n} \end{bmatrix}; \qquad \boldsymbol{B} = \begin{bmatrix} \boldsymbol{B_1} \\ \vdots \\ \boldsymbol{B_n} \end{bmatrix}; \qquad \boldsymbol{C} = \begin{bmatrix} \boldsymbol{C_1} & \dots & \boldsymbol{C_n} \end{bmatrix}; \qquad \boldsymbol{D} = \boldsymbol{R_0} \tag{A.5}$$

leads to a realization $(\boldsymbol{A}, \boldsymbol{B}, \boldsymbol{C}, \boldsymbol{D})$ of the transfer function $\boldsymbol{H}$ of order $N = \sum_{i=1}^{n} r_i$. When the residues $\boldsymbol{R_i}$ are full-rank for $i \geq 1$, the minimal state realization is of order $n \min(N_u, N_y)$. It must now be demonstrated that this realization is minimal. Due to the structure of the matrices $\boldsymbol{A}$ and $\boldsymbol{C}$, the observability matrix of this realization is expressed as:

$$\mathcal{O} = \begin{bmatrix} \boldsymbol{C_1} & \boldsymbol{C_2} & \dots & \boldsymbol{C_n} \\ \boldsymbol{C_1 A_1} & \boldsymbol{C_2 A_2} & \dots & \boldsymbol{C_n A_n} \\ \vdots & \vdots & \ddots & \vdots \\ \boldsymbol{C_1 A_1}^{N-1} & \boldsymbol{C_2 A_2}^{N-1} & \dots & \boldsymbol{C_n A_n}^{N-1} \end{bmatrix} = \begin{bmatrix} \boldsymbol{C_1} & \boldsymbol{C_2} & \dots & \boldsymbol{C_n} \\ \boldsymbol{C_1}\lambda_1 & \boldsymbol{C_2}\lambda_2 & \dots & \boldsymbol{C_n}\lambda_n \\ \vdots & \vdots & \ddots & \vdots \\ \boldsymbol{C_1}\lambda_1^{N-1} & \boldsymbol{C_2}\lambda_2^{N-1} & \dots & \boldsymbol{C_n}\lambda_n^{N-1} \end{bmatrix} \in \mathbb{C}^{N_y N \times N} \tag{A.6}$$

To demonstrate the observability of the system, i.e. that $\mathcal{O}$ is full column-rank, we propose a "reductio ad absurdum" proof. Let assume that the columns of $\mathcal{O}$ are linearly dependent:

$$\begin{aligned} &\exists\, (\boldsymbol{\mu_i})_{i=1\dots n} \text{ such that } (\boldsymbol{\mu_1}, \dots, \boldsymbol{\mu_n}) \neq \boldsymbol{0} \text{ and} \\ &\sum_{i=1}^{n} \boldsymbol{C_i \mu_i} \lambda_i^k = \boldsymbol{0} \quad \text{for } k = 0 \dots N-1 \end{aligned} \tag{A.7}$$

These equations for $k = 1 \dots n$ can be written in the following matrix form:

$$\begin{bmatrix} \boldsymbol{C_1 \mu_1} & \dots & \boldsymbol{C_n \mu_n} \end{bmatrix} \begin{bmatrix} 1 & \lambda_1 & \dots & \lambda_1^{n-1} \\ 1 & \lambda_2 & \dots & \lambda_2^{n-1} \\ \vdots & \vdots & \ddots & \vdots \\ 1 & \lambda_n & \dots & \lambda_n^{n-1} \end{bmatrix} = \boldsymbol{0} \tag{A.8}$$

The right matrix in the product is known as the Vandermonde matrix of the vector composed of the poles λ_i. It is known to be invertible when the λ_i are distinct from each other, which is the case here. It follows that the left matrix must be equal to zero, and

$$\boldsymbol{C_i \mu_i} = \boldsymbol{0} \quad i = 1 \dots n \tag{A.9}$$

Since the matrices $\boldsymbol{C_i}$ are full column-rank, the $\boldsymbol{\mu_i}$ are all equal to zero, which contradicts the initial assumption of Eq. (A.7), hence demonstrating that the observability matrix is full column-rank. The same reasoning can be done with controllability, proving that the realization is observable and controllable, hence minimal.

General case

In the general case, poles can have a multiplicity higher than one, and the pole-residue form of the transfer function is

$$\boldsymbol{H}(s) = \boldsymbol{R_0} + \sum_{i=1}^{n} \sum_{j=1}^{m_i} \frac{\boldsymbol{R_i}}{(s-\lambda_i)^j} \tag{A.10}$$

where m_i is the multiplicity of pole λ_i. In this case, the procedure described above does not apply. Indeed, it is possible to derive a state-space realization of each term of the double sum based on the technique used when poles are simple, but when they cannot be simply concatenated to form a minimal realization. The general case is studied in [Kailath 1980], using the so-called Smith-McMillan form of a MIMO transfer function.

Appendix B

Recovering the D matrix from a descriptor model

As explained in section 3.3.2, the Loewner method leads to a continuous-time descriptor model described in Eq. (3.42). In case the system is causal, the descriptor model can be transformed into a classical continuous-time state-space model composed of matrices $\boldsymbol{A}$, $\boldsymbol{B}$, $\boldsymbol{C}$ and $\boldsymbol{D}$. We propose a procedure to recover this state-space formulation in the case the system is causal and does not include integrators. This can be justified by the fact that in case an integrator is present, the low-frequency response will tend to infinity for some input/output pairs, leading to ill-conditioned Loewner matrices. If the data does not include low frequencies, then the response will not be infinite, and the integrator can be approximated by a low-frequency pole. Then, the proposed procedure is valid even in presence of an integrator, as long as frequency data are not too low.

We start by finding the generalized eigenvalues of the matrices $\boldsymbol{E} \in \mathbb{R}^{n\times n}$ and $\boldsymbol{A} \in \mathbb{R}^{n\times n}$ obtained from the Loewner method:

$$\boldsymbol{EP} = \boldsymbol{AP\Lambda} \tag{B.1}$$

where $\boldsymbol{P} \in \mathbb{C}^{n\times n}$ is a real invertible matrix and $\boldsymbol{\Lambda} \in \mathbb{C}^{n\times n}$ is diagonal with generalized eigenvalues of $(\boldsymbol{E}, \boldsymbol{A})$. Note that $\boldsymbol{P}$ can easily be converted to a real matrix, and $\boldsymbol{\Lambda}$ to a real block-diagonal matrix of the form of Eq. (3.64) to obtain the modal form. The generalized eigenvalues correspond to the inverse of the poles of the descriptor system. The reason for not working directly with the poles of the system is that the $\boldsymbol{D}$ term is associated to poles of the system with infinite modulus, hence the inverse have zero values.

We apply a variable substitution in Eq. (3.42) by writing $\boldsymbol{x} = \boldsymbol{P\xi}$, which leads to:

$$\begin{cases} \boldsymbol{EP\dot{\xi}} = \boldsymbol{AP\Lambda\dot{\xi}} = \boldsymbol{AP\xi} + \boldsymbol{Bu} \\ \boldsymbol{y} = \boldsymbol{CP\xi} \end{cases} \tag{B.2}$$

which is the modal form of the system. We then split the poles between those with nonzero values and those with zero values:

$$\boldsymbol{\Lambda} = \begin{bmatrix} \boldsymbol{\Lambda_1} & 0 \\ 0 & 0 \end{bmatrix}, \qquad \boldsymbol{\xi} = \begin{bmatrix} \boldsymbol{\xi_1} \\ \boldsymbol{\xi_2} \end{bmatrix}, \qquad \boldsymbol{P} = \begin{bmatrix} \boldsymbol{P_1} & \boldsymbol{P_2} \end{bmatrix}, \qquad \boldsymbol{P}^{-1} = \begin{bmatrix} \boldsymbol{P_1^{inv}} \\ \boldsymbol{P_2^{inv}} \end{bmatrix} \tag{B.3}$$

Since by assumption the system does not include integrators, the matrix $\boldsymbol{A}$ is invertible and so is $\boldsymbol{AP}$ since $\boldsymbol{P}$ is full rank. We can then rewrite the first equation of (B.2) as

$$\boldsymbol{\Lambda}\dot{\boldsymbol{\xi}} = \boldsymbol{\xi} + (\boldsymbol{AP})^{-1}\boldsymbol{Bu} \tag{B.4}$$

By taking the first rows of Eq. (B.4), associated to the non-zero generalized eigenvalues, we obtain the state equation:

$$\dot{\boldsymbol{\xi}}_{\mathbf{1}} = {\boldsymbol{\Lambda}_{\mathbf{1}}}^{-1}\boldsymbol{\xi}_{\mathbf{1}} + {\boldsymbol{\Lambda}_{\mathbf{1}}}^{-1}\boldsymbol{P}_{\mathbf{1}}^{\boldsymbol{inv}}\boldsymbol{A}^{-1}\boldsymbol{Bu} \tag{B.5}$$

where $\boldsymbol{\Lambda}_{\mathbf{1}}$ is invertible since it contains only the nonzero values of $\boldsymbol{\Lambda}$. By taking the last rows of Eq. (B.4), we obtain a second equation that connects $\boldsymbol{\xi}_{\mathbf{2}}$ to $\boldsymbol{u}$:

$$\mathbf{0} = \boldsymbol{\xi}_{\mathbf{2}} + \boldsymbol{P}_{\mathbf{2}}^{\boldsymbol{inv}}\boldsymbol{A}^{-1}\boldsymbol{Bu} \tag{B.6}$$

By injecting into the output equation of Eq. (B.2), we obtain:

$$\boldsymbol{y} = \boldsymbol{CP}_{\mathbf{1}}\boldsymbol{\xi}_{\mathbf{1}} + \boldsymbol{CP}_{\mathbf{2}}\boldsymbol{\xi}_{\mathbf{2}} = \boldsymbol{CP}_{\mathbf{1}}\boldsymbol{\xi}_{\mathbf{1}} - \boldsymbol{CP}_{\mathbf{2}}\boldsymbol{P}_{\mathbf{2}}^{\boldsymbol{inv}}\boldsymbol{A}^{-1}\boldsymbol{Bu} \tag{B.7}$$

This concludes the definition of a state-space model $(\boldsymbol{A'}, \boldsymbol{B'}, \boldsymbol{C'}, \boldsymbol{D'})$ with matrices:

$$\boldsymbol{A'} = {\boldsymbol{\Lambda}_{\mathbf{1}}}^{-1}, \qquad \boldsymbol{B'} = {\boldsymbol{\Lambda}_{\mathbf{1}}}^{-1}\boldsymbol{P}_{\mathbf{1}}^{\boldsymbol{inv}}\boldsymbol{A}^{-1}\boldsymbol{B}, \qquad \boldsymbol{C'} = \boldsymbol{CP}_{\mathbf{1}}, \qquad \boldsymbol{D'} = -\boldsymbol{CP}_{\mathbf{2}}\boldsymbol{P}_{\mathbf{2}}^{\boldsymbol{inv}}\boldsymbol{A}^{-1}\boldsymbol{B} \tag{B.8}$$

Appendix C

MIMO identification with imposed poles: other methods

Section 3.5 investigates techniques to identify MIMO state-space models based on frequency data $(\boldsymbol{H}(\omega_i), \omega_i)_{i=1\dots N}$, in which a set of previously computed poles is imposed. Two other techniques are presented in this appendix, that achieve the same objective. They have been found less efficient than the one described in the development, but can be of interest for the reader.

C.1 SIMO identification with common basis

The first method consists in first identifying single-input multi-output (SIMO) models for each data column, and then finding state-transformation matrices to write them in the same basis. The SIMO identification can be done based on the transfer function form of the models, and then be transformed in state-space without increasing the order (recall that a transfer function of order n can easily be expressed as a state-space of order $\min(N_u, N_y)$, which is equal to 1 if the system is SIMO). The idea behind this method is that the matrices $\boldsymbol{A}$ and $\boldsymbol{C}$ are common for all columns of a state-space model's response.

Assuming a discrete-time framework, the transfer function of the identified model associated to the i_u-th input assumes the following form:

$$\hat{\boldsymbol{H}}^{\boldsymbol{i_u}}_{\boldsymbol{SIMO}}(z) = \frac{\sum_{i=0}^{n} \boldsymbol{a_i^{i_u}} z^i}{\left(\sum_{i=0}^{\bar{n}} b_i z^i\right)\left(\sum_{i=0}^{n-\bar{n}} d_i z^i\right)} \quad \forall i_u = 1 \dots N_u \tag{C.1}$$

Where the $\sum_{i=0}^{\bar{n}} b_i z^i = \prod_{i=1}^{\bar{n}} (z - \bar{\lambda}_i)$ is imposed by known poles $\bar{\lambda}_i$, the d_i and $\boldsymbol{a_i^{i_u}} \in \mathbb{R}^{N_y \times 1}$ are coefficient to be estimated. The polynomial with coefficients d_i corresponds to the $n - \bar{n}$ poles to be estimated by the process. Without loss of generality the coefficient $d_{n-\bar{n}}$ can be fixed to 1 as the $\boldsymbol{a_n^{i_u}}$ coefficients control the value of $\hat{\boldsymbol{H}}^{\boldsymbol{i_u}}_{\boldsymbol{SIMO}}(z = 0)$. The coefficients d_i and $\boldsymbol{a_i^{i_u}}$ are then

obtained by the following minimization problem:

$$\min_{\substack{(d_i,\boldsymbol{a_l^{i_u}})\\ i=1\dots n-\bar{n};\, l=0\dots n;\, i_u=1\dots N_u}} \sum_{i_u=1}^{N_u}\sum_{k=1}^{N} \left\| \hat{\boldsymbol{H}}^{\boldsymbol{i_u}}_{\boldsymbol{SIMO}}(e^{j\omega_k}) - \boldsymbol{H^{i_u}}(\omega_k) \right\|_2 \tag{C.2}$$

where H^{i_u} is the i_u-th column data. This linear least-square problem admits the following closed form:

$$\begin{Bmatrix} \boldsymbol{d} \\ \boldsymbol{a^1} \\ \vdots \\ \boldsymbol{a^{N_u}} \end{Bmatrix} = \begin{bmatrix} \boldsymbol{M_d^1} & \boldsymbol{M_a} & & 0 \\ \vdots & & \ddots & \\ \boldsymbol{M_d^{N_u}} & 0 & & \boldsymbol{M_a} \end{bmatrix}^{\dagger} \begin{Bmatrix} \boldsymbol{Z^1} \\ \vdots \\ \boldsymbol{Z^{N_u}} \end{Bmatrix} \tag{C.3}$$

with

$$\boldsymbol{M_d^{i_u}} = \begin{bmatrix} \tilde{\boldsymbol{H}}^{\boldsymbol{i_u}}(\omega_1) & e^{j\omega_1}\tilde{\boldsymbol{H}}^{\boldsymbol{i_u}}(\omega_1) & \dots & e^{(n-\bar{n}-1)j\omega_1}\tilde{\boldsymbol{H}}^{\boldsymbol{i_u}}(\omega_1) \\ \vdots & \vdots & & \vdots \\ \tilde{\boldsymbol{H}}^{\boldsymbol{i_u}}(\omega_N) & e^{j\omega_N}\tilde{\boldsymbol{H}}^{\boldsymbol{i_u}}(\omega_N) & \dots & e^{(n-\bar{n}-1)j\omega_N}\tilde{\boldsymbol{H}}^{\boldsymbol{i_u}}(\omega_N) \end{bmatrix} \in \mathbb{C}^{N_y N\times(n-\bar{n})} \tag{C.4}$$

$$\boldsymbol{M_a} = \begin{bmatrix} -1 & -e^{j\omega_1} & \dots & -e^{nj\omega_1} \\ \vdots & \vdots & & \vdots \\ -1 & -e^{j\omega_N} & \dots & -e^{nj\omega_N} \end{bmatrix} \in \mathbb{C}^{N\times(n+1)} \tag{C.5}$$

$$\boldsymbol{Z^{i_u}} = \begin{Bmatrix} -e^{(n-\bar{n})j\omega_1}\tilde{\boldsymbol{H}}^{\boldsymbol{i_u}}(\omega_1) \\ \vdots \\ -e^{(n-\bar{n})j\omega_N}\tilde{\boldsymbol{H}}^{\boldsymbol{i_u}}(\omega_N) \end{Bmatrix} \in \mathbb{C}^{N_y N\times 1} \tag{C.6}$$

and $\tilde{\boldsymbol{H}}^{\boldsymbol{i_u}}$ is defined as

$$\tilde{\boldsymbol{H}}^{\boldsymbol{i_u}}(\omega) = \left(\sum_{i=0}^{N} b_i e^{i(j\omega)}\right)\boldsymbol{H^{i_u}}(\omega) \tag{C.7}$$

The vectors $\boldsymbol{d}$ and $\boldsymbol{a^{i_u}}$ contain the identified coefficients organized as $\boldsymbol{d} = \begin{Bmatrix} d_1 & \dots & d_{n-\bar{n}} \end{Bmatrix}^T$ and $\boldsymbol{a^{i_u}} = \begin{Bmatrix} \boldsymbol{a_0^{i_u}}^T & \dots & \boldsymbol{a_n^{i_u}}^T \end{Bmatrix}^T$. Once they are computed, the SIMO transfer functions $\hat{\boldsymbol{H}}^{\boldsymbol{i_u}}_{\boldsymbol{SIMO}}$ are fully known, and can be transformed into SIMO state-space models of order n. By calling $(\boldsymbol{A_i}, \boldsymbol{B_i}, \boldsymbol{C_i}, \boldsymbol{D_i})_{i=1\dots N_u}$ the set of matrices defining each SIMO state-space model, we are looking at N_u state transformation matrices $\boldsymbol{T_i} \in \mathbb{R}^{n\times n}$ which are invertible and verify:

$$\begin{cases} \boldsymbol{T_i}^{-1}\boldsymbol{A_i}\boldsymbol{T_i} = \boldsymbol{A} \\ \boldsymbol{C_i}\boldsymbol{T_i} = \boldsymbol{C} \end{cases} \qquad \forall i = 1\dots N_u \tag{C.8}$$

In this equation, the $\boldsymbol{T_i}$ are unknown and so are the $\boldsymbol{A}$ and $\boldsymbol{C}$. Note that the $\boldsymbol{A_i}$ have the same eigenvalues, which are conserved by the state transformations $\boldsymbol{T_i}$. This equation has a nonlinear dependence on the different variables $\boldsymbol{T_i}$, $\boldsymbol{A}$ and $\boldsymbol{C}$, but by fixing A to an arbitrary matrix with the same eigenvalues as the $\boldsymbol{A_i}$, and multiplying the first line of Eq. (C.8) by $\boldsymbol{T_i}$, the problem

becomes linear in the unknown $\boldsymbol{T_i}$ and $\boldsymbol{C}$:

$$\begin{cases} \boldsymbol{A_i T_i} = \boldsymbol{T_i A} \\ \boldsymbol{C_i T_i} = \boldsymbol{C} \end{cases} \quad \forall i = 1 \dots N_u \tag{C.9}$$

However, this feasibility formulation does not lead to invertible matrices $\boldsymbol{T_i}$, and there is no simple way to impose them to be invertible without over-constraining the problem.

A solution is proposed in this work by using observability matrices instead of $\boldsymbol{A}$ and $\boldsymbol{C}$. This has the inconvenient of increasing the dimensions of the matrices, but allows for a more compact formulation. Instead of the problem described in Eq. (C.8), we formulate the problem as follows: from observabilty matrices $\boldsymbol{\mathcal{O}_i}$ defined as

$$\boldsymbol{\mathcal{O}_i} = \begin{bmatrix} \boldsymbol{C_i} \\ \boldsymbol{C_i A_i} \\ \vdots \\ \boldsymbol{C_i {A_i}^{n-1}} \end{bmatrix} \tag{C.10}$$

find a transformed observability matrix $\boldsymbol{\mathcal{O}} \in \mathbb{R}^{(nN_y)\times n}$and invertible transformation matrices $\boldsymbol{T_i} \in \mathbb{R}^{n\times n}$ such as

$$\boldsymbol{\mathcal{O}_i T_i} = \boldsymbol{\mathcal{O}} \quad \forall i = 1 \dots N_u \tag{C.11}$$

which can be written as

$$\boldsymbol{\Gamma} \begin{bmatrix} \boldsymbol{T_1} \\ \vdots \\ \boldsymbol{T_{N_u}} \\ \boldsymbol{\mathcal{O}} \end{bmatrix} = \boldsymbol{0_{(nN_u N_y)\times n}} \tag{C.12}$$

with

$$\boldsymbol{\Gamma} = \begin{bmatrix} \boldsymbol{\mathcal{O}_1} & & 0 & -\boldsymbol{I_{nN_y}} \\ & \ddots & & \vdots \\ 0 & & \boldsymbol{\mathcal{O}_{N_u}} & -\boldsymbol{I_{nN_y}} \end{bmatrix} \in \mathbb{C}^{nN_u N_y \times n(N_u+N_y)} \tag{C.13}$$

where the left matrix factor is known and the right matrix factor contains all the unknowns. This problem hence comes down to finding n column vectors $\boldsymbol{X_k} \in ker(\boldsymbol{\Gamma})$ such that all $\boldsymbol{T_i}$ formed with the $\boldsymbol{X_k}$ are full rank, $ker(\boldsymbol{\Gamma})$ denoting the null space of matrix $\boldsymbol{\Gamma}$. In order to meet such a condition, we propose to compute the singular values decomposition (SVD) of the matrix $\boldsymbol{\Gamma}$:

$$\boldsymbol{\Gamma} = \boldsymbol{U S V^*} \tag{C.14}$$

Where $\boldsymbol{U}$ and $\boldsymbol{V}$ are unitary matrices ($\boldsymbol{U^*U} = \boldsymbol{UU^*} = \boldsymbol{I}$, same for $\boldsymbol{V}$), $\boldsymbol{S}$ contains the singular values of $\boldsymbol{\Gamma}$ in descending order on its diagonal, and zeros elsewhere. Rows of the matrix $\boldsymbol{V}$ corresponding to singular values of $\boldsymbol{\Gamma}$ equal to zero verify $\boldsymbol{\Gamma V_i} = 0$. If they correspond to singular values almost equal to zero, the equality becomes an approximate equality. By taking only rows of

$\boldsymbol{V_i}$ that make the rank of each $\boldsymbol{T_i}$ increase, starting from the last line of $\boldsymbol{V}$, we can build matrices $\boldsymbol{T_i}$ which are invertible. The corresponding observability matrix $\boldsymbol{\mathcal{O}}$ is obtained simultaneously. This way, the optimization process finds a common basis in which the observability matrices of all column systems are expressed as the matrix $\boldsymbol{\mathcal{O}}$. Once $\boldsymbol{\mathcal{O}}$ has been obtained, new approximations of the $\boldsymbol{T_i}$ can be obtained as $\boldsymbol{T_i'} = \boldsymbol{\mathcal{O}_i}^{\dagger}\boldsymbol{\mathcal{O}}$, which improves the identification accuracy. The issue with this method is that by repeatedly rejecting rows of $\boldsymbol{V}$ that do not make the rank of each $\boldsymbol{T_i}$ increase, we can end up using vectors associated to nonzero singular values of $\boldsymbol{\Gamma}$.

When $\boldsymbol{\mathcal{O}}$ is obtained, we can retrieve $\boldsymbol{A}$ and $\boldsymbol{C}$ in a similar way as with the subspace method presented in section 3.3.1, by taking $\boldsymbol{C}$ as the first N_y rows of $\boldsymbol{\mathcal{O}}$ and $\boldsymbol{A}$ as the matrix that minimizes the mean square error with the observability matrix. Otherwise, $\boldsymbol{A}$ and $\boldsymbol{C}$ can be obtained by transformation of certain $\boldsymbol{A_i}$ and $\boldsymbol{C_i}$ by multiplication with matrices $\boldsymbol{T_i}$. If the vectors selected from the rows of $\boldsymbol{V}$ are all associated to zero singular values, the two ways of retrieving $\boldsymbol{A}$ and $\boldsymbol{C}$ are theoretically equivalent, but practically this is not the case due to numerical issues. The matrices $\boldsymbol{B}$ and $\boldsymbol{D}$ can then be obtained in a similar way as with the subspace method described in 3.3.1. This technique implies matrices of higher dimensions than the one described in section 3.5, and there is no guarantee that we can find invertible state transformation matrices $\boldsymbol{T_i}$, hence it is not used in the main development.

C.2 Markov parameters estimation method

Another method can be obtained using markov parameters, in order to identify a state-space system with constraints. This method uses a framework described in [Bako, Mercère, and Lecoeuche 2009]. It is assumed that all poles of the model are known. It starts with the following lemma:

Lemma 1
Let $(\boldsymbol{A}, \boldsymbol{B}, \boldsymbol{C}) \in \mathbb{R}^{n\times n} \times \mathbb{R}^{n\times N_u} \times \mathbb{R}^{N_y\times n}$ *and define*

$$\boldsymbol{v_k}(x) = \begin{bmatrix} 1 & x & \dots & x^{k-1} \end{bmatrix}^T \tag{C.15}$$

$$\boldsymbol{\Delta_k}(\boldsymbol{A}, \boldsymbol{B}) = \begin{bmatrix} \boldsymbol{A}^{k-1}\boldsymbol{B} & \dots & \boldsymbol{AB} & \boldsymbol{B} \end{bmatrix} \tag{C.16}$$

for any $k \geq 1$. *Denote with* $m_A(x) = d_0 + d_1 x + \cdots + d_{n-1}x^{n-1} + x^n$ *the minimal polynomial of* $\boldsymbol{A}$ *and introduce the notation*

$$\boldsymbol{R_A} = \begin{bmatrix} 1 & 0 & \dots & 0 \\ d_{n-1} & 1 & & \vdots \\ \vdots & \ddots & \ddots & 0 \\ d_1 & \dots & d_{n-1} & 1 \end{bmatrix} \tag{C.17}$$

Then for a given frequency ω

$$\boldsymbol{C}\left[e^{j\omega}\boldsymbol{I_n}-\boldsymbol{A}\right]^{-1}\boldsymbol{B}=\frac{1}{m_A(e^{j\omega})}\boldsymbol{C\Delta_n}(\boldsymbol{A},\boldsymbol{B})\left[(\boldsymbol{R_A v_n}(e^{j\omega}))\otimes\boldsymbol{I_{N_u}}\right] \tag{C.18}$$

where $\otimes$ denotes the Kronecker product.

The proof can be obtained by using similar arguments as in [Bako, Mercère, and Lecoeuche 2009]. If the poles of the system are known, then the minimal polynomial m_A of $\boldsymbol{A}$ is known, and by noting $\hat{\boldsymbol{H}}(e^{j\omega})=\boldsymbol{C}\left[e^{j\omega}\boldsymbol{I_n}-\boldsymbol{A}\right]^{-1}\boldsymbol{B}+\boldsymbol{D}$ the transfer function associated to the identified state-space model, we obtain

$$m_A(e^{j\omega})\hat{\boldsymbol{H}}(e^{j\omega})=\begin{bmatrix}\boldsymbol{CA}^{n-1}\boldsymbol{B} & \dots & \boldsymbol{CAB} & \boldsymbol{CB} & \boldsymbol{D}\end{bmatrix}\begin{bmatrix}(\boldsymbol{R_A v_n}(e^{j\omega}))\otimes\boldsymbol{I_{N_u}}\\ m_A(e^{j\omega})\boldsymbol{I_{N_u}}\end{bmatrix} \tag{C.19}$$

The first Markov parameters $\boldsymbol{h_0}=\boldsymbol{D}$, $\boldsymbol{h_1}=\boldsymbol{CB}$ up to $\boldsymbol{h_n}=\boldsymbol{CA}^{n-1}\boldsymbol{B}$ can be obtained by the following minimization problem

$$\min_{\substack{\boldsymbol{h_i}\\ i=0\dots N}}\sum_{i=1}^{N}\left\|m_A(e^{j\omega_i})[\hat{\boldsymbol{H}}(e^{j\omega_i})-\boldsymbol{H}(\omega_i)]\right\|_F \tag{C.20}$$

which comes down to a linear least-mean square problem. Markov parameters of higher orders can subsequently be obtained by noting that $m_A(\boldsymbol{A})=\boldsymbol{0}$, which implies that:

$$\boldsymbol{h_{n+1}}=-a_0\boldsymbol{CB}-a_1\boldsymbol{CAB}-\dots-a_{n-1}\boldsymbol{CA}^{n-1}\boldsymbol{B} \tag{C.21}$$

and then recursively to any order. This allows to compute the Hankel associated to the Markov parameters:

$$\mathcal{H}=\begin{bmatrix}\boldsymbol{h_1} & \boldsymbol{h_2} & \dots & \boldsymbol{h_n}\\ \boldsymbol{h_2} & \boldsymbol{h_3} & \dots & \boldsymbol{h_{n+1}}\\ \vdots & \vdots & \ddots & \vdots\\ \boldsymbol{h_n} & \boldsymbol{h_{n+1}} & \dots & \boldsymbol{h_{2n-1}}\end{bmatrix} \tag{C.22}$$

A rank factorization of this Hankel matrix writes

$$\mathcal{H}=\begin{bmatrix}\boldsymbol{C}\\ \boldsymbol{CA}\\ \vdots\\ \boldsymbol{CA}^{n-1}\end{bmatrix}\begin{bmatrix}\boldsymbol{B} & \boldsymbol{AB} & \dots & \boldsymbol{A}^{n-1}\boldsymbol{B}\end{bmatrix} \tag{C.23}$$

which gives an estimation of the observability matrix and controllability matrix of the system, in a common basis. Matrices $\boldsymbol{A}$, $\boldsymbol{B}$ and $\boldsymbol{C}$ can then be obtained in a similar way as described in section 3.3.1, and $\boldsymbol{D}$ has already been computed as $\boldsymbol{h_0}$. Note that it has been assumed that all poles are known in advance. If the poles are partially known, the method can be modified to identify at the same time the Markov parameters and the unknown part of the polynomial m_A, in

a similar way as done in C.1, still leading to a linear least-mean square problem. The full method is not described for the sake of conciseness.

Appendix D

H_∞, H_2/H_∞ and μ syntheses

This appendix describes the H_∞ framework, and the different variations used in this work. It includes a quick presentation of the some optimization methods used to synthesize controllers within this framework.

D.1 Unstructured H_∞ and μ syntheses

D.1.1 H_∞-synthesis and modulus margins

The H_∞-synthesis works with closed-loop systems of the form of Fig. D.1, where $\boldsymbol{P}$ is the augmented plant and $\boldsymbol{K}$ the controller. Both of them are state-space models, expressed in continuous-time (the discrete case is not described here). The objective of the H_∞ synthesis is to find a controller $\boldsymbol{K}$ that minimizes H_∞ norm of the closed loop transfer function from $\boldsymbol{w_\infty}$ to $\boldsymbol{z_\infty}$ under closed-loop stability constraint. By decomposing the augmented plant as

$$\boldsymbol{P} = \begin{bmatrix} \boldsymbol{P_{zw}} & \boldsymbol{P_{zu}} \\ \boldsymbol{P_{yw}} & \boldsymbol{P_{yu}} \end{bmatrix} \tag{D.1}$$

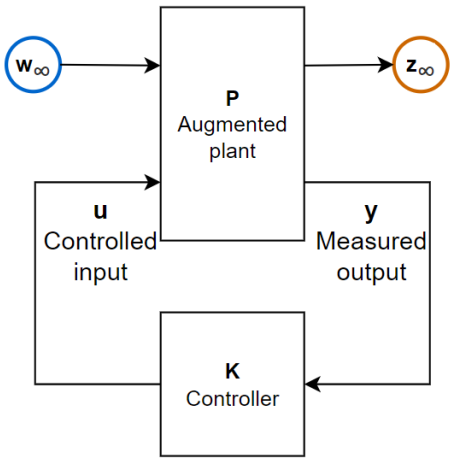

Figure D.1: H_∞ framework

this comes down to ensuring that

$$\|\boldsymbol{T}_{\boldsymbol{w_\infty}\mapsto\boldsymbol{z_\infty}}\|_\infty \leq \gamma \tag{D.2}$$

where $\boldsymbol{T}_{\boldsymbol{w_\infty}\mapsto\boldsymbol{z_\infty}}$ is obtained as the linear fractional transform (LFT) defined as:

$$\boldsymbol{T}_{\boldsymbol{w_\infty}\mapsto\boldsymbol{z_\infty}} = \mathrm{LFT}(\boldsymbol{P},\boldsymbol{K}) = \boldsymbol{P_{zw}} + \boldsymbol{P_{zu}}\boldsymbol{K}(\boldsymbol{I}-\boldsymbol{P_{yu}}\boldsymbol{K})^{-1}\boldsymbol{P_{yw}} \tag{D.3}$$

recalling that the H_∞ norm of a MIMO transfer function $\boldsymbol{G}$ is defined as:

$$\|\boldsymbol{G}\|_\infty = \max_{\omega\in\mathbb{R}^+} \bar{\sigma}(\boldsymbol{G}(j\omega)) \tag{D.4}$$

where $\bar{\sigma}$ gives the highest singular value of a matrix. The exogenous input and output $\boldsymbol{w_\infty}$ and $\boldsymbol{z_\infty}$ can then be defined in such a way that the constraints of Eq. (D.2) impose the desired closed-loop behavior of the system. Many classical control constraints can be translated into the H_∞ framework. Examples can be found in chapters 5 and 4 where closed loop specifications for AFS and GLA problems are respectively defined as H_∞ constraints.

While some closed-loop specifications translate in a straightforward way into H_∞ constraints, it is not the case of robustness, which can have several definitions. It is worth noting that, although H_∞-synthesis is generally included in the so-called robust control techniques, robustness is not enforced unless specific criteria are included in the synthesis problem. Robustness is a general concept, which denotes the ability of the system to behave adequately in presence of non-nominal conditions. In the case studied in this appendix, two types of closed-loop robustness can be defined, in terms of stability and of performance. The first one describes the extent to which the nominal system can be modified without making the closed-loop unstable. This leads to the definition of the classical stability margins for SISO systems. The former is the maximum gain that can multiply the nominal system without destabilizing it, and the latter is associated to the maximum phase shift applied to the complex transfer function. Similarly, the performance robustness can be defined as the maximum uncertainty applied to the nominal system for which the H_∞ criterion of (D.2) is still respected.

The gain and phase margins make only sense for SISO systems, and in the MIMO case different types of modifications of the nominal system must be defined to account for the possible uncertainties. Contrarily to the SISO case, the MIMO uncertainties can be applied simultaneously on different input and output ports of the nominal system. In this work, a class of MIMO uncertainties called inverse multiplicative uncertainties are used. They are illustrated on Fig. D.2. In the input case, the uncertain system is written as

$$\boldsymbol{G_{unc}}(s) = \boldsymbol{G_{nom}}(s)(\boldsymbol{I}-\boldsymbol{\Delta_u})^{-1} \tag{D.5}$$

where $\boldsymbol{G_{nom}}$ is the nominal system, and $\boldsymbol{\Delta_u}$ is called dynamic uncertainty, which can be any transfer function with bounded H_∞ norm. The input modulus margin β_u is then defined as the maximum H_∞ norm of $\boldsymbol{\Delta_u}$ which leaves the uncertain system stable. Similarly, when considering

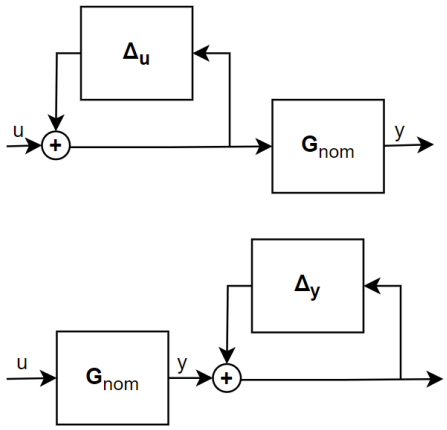

Figure D.2: Input (top) and output (bottom) inverse multiplicative uncertainties

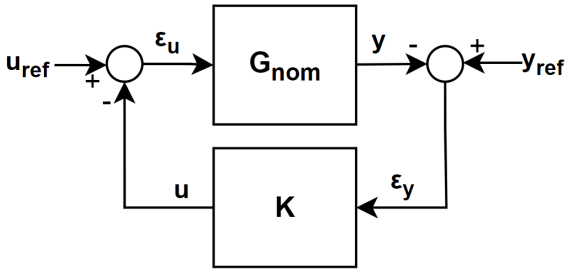

Figure D.3: Reference input and output signals

output inverse multiplicative uncertainties, the uncertain system is defined as

$$\boldsymbol{G_{unc}}(s) = (\boldsymbol{I} - \boldsymbol{\Delta_y})^{-1}\boldsymbol{G_{nom}}(s) \tag{D.6}$$

and the output modulus margin β_y is the maximum H_∞ norm of the dynamic uncertainty $\boldsymbol{\Delta_y}$ that leaves the system stable. These uncertainties have the advantage of being compatible with the H_∞ framework. Practically when considering closed-loop margins, if the controlled input of the nominal system is written as $\boldsymbol{\epsilon_u} = \boldsymbol{u_{ref}} - \boldsymbol{u}$ and the measured output as $\boldsymbol{\epsilon_y} = \boldsymbol{y_{ref}} - \boldsymbol{y}$ as depicted on Fig. D.3, then it can be shown using the small gain theorem that the input and output modulus margins are the inverses of H_∞ norms of the input and output sensitivities S_u and S_y respectively:

$$\beta_u = \frac{1}{\|\boldsymbol{S_u}\|_\infty} = \frac{1}{\left\|\boldsymbol{T}_{\boldsymbol{u_{ref}} \mapsto \boldsymbol{\epsilon_u}}\right\|_\infty} \tag{D.7}$$

and

$$\beta_y = \frac{1}{\|\boldsymbol{S_y}\|_\infty} = \frac{1}{\left\|\boldsymbol{T}_{\boldsymbol{y_{ref}} \mapsto \boldsymbol{\epsilon_y}}\right\|_\infty} \tag{D.8}$$

Even when the references signals u_{ref} and y_{ref} are not part of the control problem, they can be artificially added to the augmented plant used for control design as exogenous inputs in order to add MIMO robustness criteria to the H_∞ synthesis. This class of uncertainties has the advantage of being compatible with the H_∞ framework through simple signals definitions. However, they

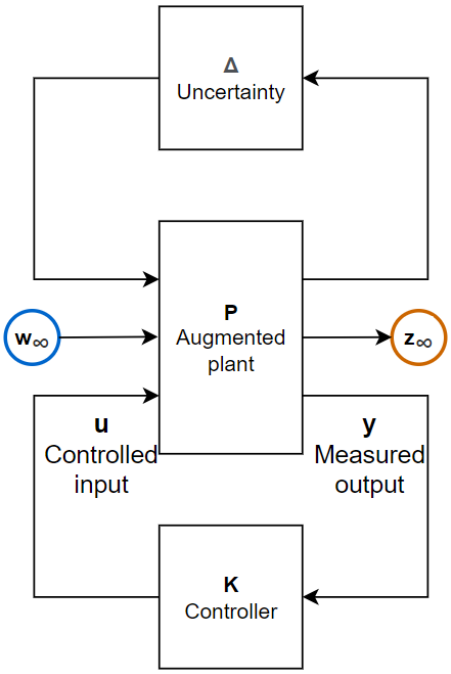

Figure D.4: H_∞ framework with uncertainties, for μ-synthesis

are very strong constraints as the dynamic uncertainties $\boldsymbol{\Delta_u}$ and $\boldsymbol{\Delta_y}$ can represent any transfer function. It can be noted that, when several exogenous inputs and outputs are included to define H_∞ closed-loop criteria, from $\boldsymbol{w_1}$ and $\boldsymbol{w_2}$ to $\boldsymbol{z_1}$ and $\boldsymbol{z_2}$ for instance, also the criteria associated to crossed transfer function are included, in this case $\boldsymbol{w_1}$ to $\boldsymbol{z_2}$ and $\boldsymbol{w_2}$ to $\boldsymbol{z_1}$. If only the criteria defined by $\boldsymbol{w_1}$ to $\boldsymbol{z_1}$ and $\boldsymbol{w_2}$ to $\boldsymbol{z_2}$ was initially wanted, this creates some conservatism in the controller design. Also note that robustness to the input and output uncertainties are considered separately in this framework.

The H_∞ synthesis has become popular in the 90's, with the progress in computational sciences. This is due to the fact that the solutions to an H_∞ problem can be fully defined, and that a particular solution can be obtained by efficient computations such as relying on Riccati equations [Doyle et al. 1988] or linear matrix inequalities (LMI) problems [Gahinet and Apkarian 1994]. With these efficient methods, the controller is referred to as unstructured, in the sense that no constraint on its form are imposed during the synthesis. This leads to state-space controllers of the same order as the augmented plant $\boldsymbol{P}$, which is an important drawback of the unstructured synthesis, as low-order controllers are generally preferred for practical applications.

D.1.2 μ-synthesis and disk uncertainties

Stability robustness to inverse multiplicative uncertainties can be expressed as a H_∞ criterion, as described above in section D.1.1. The μ-synthesis considers a broader framework for handling uncertainties. It works with the closed loop shown in Fig. D.4, defined by two LFTs of the

augmented plant $\boldsymbol{P}$, the lower one with the controller feedback and the upper one with the uncertainty $\boldsymbol{\Delta}$. The latter is a diagonal collection of dynamic uncertainties. The objective of μ-synthesis is to find a controller $\boldsymbol{K}$ that minimizes γ such that

$$\|\boldsymbol{T}_{\boldsymbol{w}_\infty \mapsto \boldsymbol{z}_\infty}\|_\infty \leq \gamma \tag{D.9}$$

in which the closed loop, obtained for a scaled uncertainty $\boldsymbol{\Delta}/\gamma$, must be stable. A low gamma then implies closed-loop stability and a good H_∞ criterion under high uncertainties. A major implication is that μ-synthesis tries to maximize not only the stability robustness, but also the performance robustness, to the uncertainty defined by $\boldsymbol{\Delta}$.

Is some cases, the definition of the uncertainties arise naturally from the robust control problem studied. In others, one can define artificial uncertainties as a way to provide MIMO robustness to the system. This is the case of this work, where a conservative design based on disk margins [Blight, Daily, and Gangsaas 1994; Seiler, Packard, and Gahinet 2020] is presented. Disk uncertainties are a practical way to define variations of the nominal plant at different input and output ports simultaneously. Output symmetric disk uncertainties are multiplied by the nominal plant from the left. They are defined as

$$\boldsymbol{\Delta_y}^{disk} = \begin{bmatrix} \Delta^1 & 0 & 0 \\ 0 & \ddots & 0 \\ 0 & 0 & \Delta^{N_y} \end{bmatrix} \tag{D.10}$$

with

$$\Delta^i = \frac{1+\eta\delta_i}{1-\eta\delta_i} \qquad i = 1 \dots N_y \tag{D.11}$$

where δ_i are uncertain complex parameters lying inside the unit disk, N_y is the number of outputs and η is a positive parameter defining the uncertainty level. Similar input uncertainties $\boldsymbol{\Delta_u}^{disk}$ are also defined, multiplying from the right and with dimension N_u. Note that for $\eta = 0$, the multiplicative uncertainty is equal to identity, meaning that the system is nominal. The minimum value of η that leads to unstable closed-loop will define the disk margin. These uncertainties are less restrictive than the general dynamic uncertainties defined in Eq. (D.5) and (D.6), and they can apply simultaneously on the various input and outputs. With μ-synthesis, a controller that ensures robustness to simultaneous MIMO uncertainties of this type, both in stability and performance, can be found. An advantage of this formulation is the fact that the disk margins can be used to compute guaranteed gain and phase margins, as explained in [Seiler, Packard, and Gahinet 2020]. Disk uncertainties provide a more comprehensive assessment of robust stability as they account for simultaneous gain and phase uncertain variations, at different inputs and outputs at the same time.

Contrarily to unstructured H_∞-synthesis, unstructured μ-synthesis cannot be performed based on a LMI formulation or by solving Riccati equations. It can be solved by the iterative D-K process [Vidyasagar and Kimura 1986], which alternates K steps where H_∞ synthesis is performed, and D steps where the closed-loop robustness is assessed and the H_∞ norm to be reduced by the next

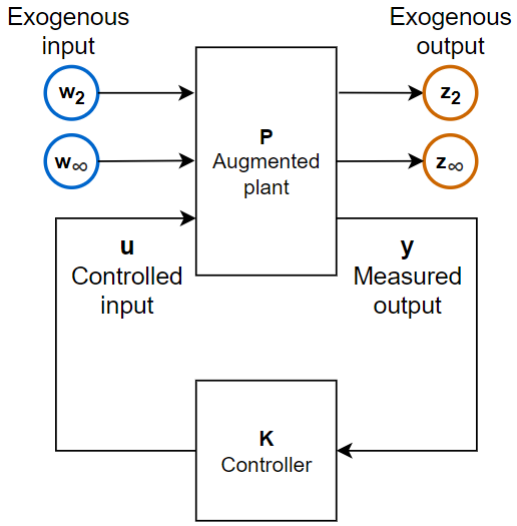

Figure D.5: H_2/H_∞ framework

K step is scaled according to the robustness performance. Although convergence is not ensured, this algorithm is numerically efficient.

D.2 Structured multi-model H_2/H_∞

Controllers of fixed structure can also be obtained using the same H_∞ framework. For instance, a controller can be defined as a PID or a fixed-order state-space model. A nonlinear optimization is then required, with no guarantee of finding a gobal minimum. With structured synthesis, there is more freedom in the definition of the control problem, but with a higher computational cost and sometimes requiring several attempts with different initializations of the optimization process. Note that the use of parallel computation can significantly reduce the time needed to find an acceptable controller. Two particular variations of the H_∞ synthesis are studied in this work.

First, instead of minimizing the H_∞ norm of a closed loop transfer function, one can consider also minimizing its H_2 norm. Recall that the H_2 norm of a transfer function G is defined as:

$$\|\boldsymbol{G}\|_2 = \sqrt{\frac{1}{2\pi}\int_{-\infty}^{\infty} \|\boldsymbol{G}(j\omega)\|_F \, d\omega} \tag{D.12}$$

Considering the closed loop defined in Fig. D.5, and ignoring here the possibility of including uncertainties, the H_2/H_∞ synthesis problem is to find a controller $\boldsymbol{K}$ which stabilizes the closed-

loop and minimizes γ such that

$$\|\boldsymbol{T}_{\boldsymbol{w_\infty}\mapsto\boldsymbol{z_\infty}}\|_\infty \leq \gamma \tag{D.13}$$

$$\|\boldsymbol{T}_{\boldsymbol{w_2}\mapsto\boldsymbol{z_2}}\|_2 \leq \gamma \tag{D.14}$$

$$\tag{D.15}$$

Adding a H_2 criterion allows more flexibility in the definition of the control objectives. For example in GLA, we are not only interested in minimizing the peak response of a load, but also its standard deviation in order to attenuate the oscillations associated to modes with different natural frequencies.

A second variation to the classical H_∞ framework, of particular importance for aeroservoelasticity, is the use of different models in the controller design. If a set of augmented plants $\boldsymbol{P_i}$ has been computed for $i = 1 \dots m$, it is possible to perform a multi-model H_2/H_∞ synthesis, which seeks at minimizing γ such that each closed-loop associated to the plants $\boldsymbol{P_i}$ is stable, and that

$$\|\boldsymbol{T}_{\boldsymbol{w_\infty}\mapsto\boldsymbol{z_\infty}}\|_\infty = \|\mathrm{LFT}(\boldsymbol{P_i}, \boldsymbol{K})\|_\infty \leq \gamma \quad \forall i = 1 \dots m \tag{D.16}$$

$$\|\boldsymbol{T}_{\boldsymbol{w_2}\mapsto\boldsymbol{z_2}}\|_\infty = \|\mathrm{LFT}(\boldsymbol{P_i}, \boldsymbol{K})\|_2 \leq \gamma \quad \forall i = 1 \dots m \tag{D.17}$$

Different multi-model structures of the controller are possible. Using a robust logic, a unique controller can be obtained for each model. In this case, the multi-model approach allows to define uncertainties that correspond to true variations of the operating point. This is particularly useful when considering aeroelastic systems at different Mach number, velocity, and with different mass configurations. Alternatively, if the different models used for the controller design correspond to the variations of a parameter $\boldsymbol{p}$, it is possible to define a controller structure with dependence upon it, like LPV models of the form:

$$\boldsymbol{K} : \begin{cases} \dot{\boldsymbol{x}} & = \boldsymbol{A}(\boldsymbol{p})\boldsymbol{x} + \boldsymbol{B}(\boldsymbol{p})\boldsymbol{y_{meas}} \\ \boldsymbol{u_{com}} & = \boldsymbol{C}(\boldsymbol{p})\boldsymbol{x} + \boldsymbol{D}(\boldsymbol{p})\boldsymbol{y_{meas}} \end{cases} \tag{D.18}$$

In this case, the multi-model approach allows the controller to adapt in real-time to the changes in the system dynamics. A combination of robust and LPV logic is also possible, defining multi-dimensional sets of models, with controller dependence upon a parameter for a dimension of this set and robustness with respect to another dimension. All the structured synthesis approaches described in this section are implemented in matlab's *systune* function.

Appendix E

Additional GLA results

E.1 HTP loads envelopes

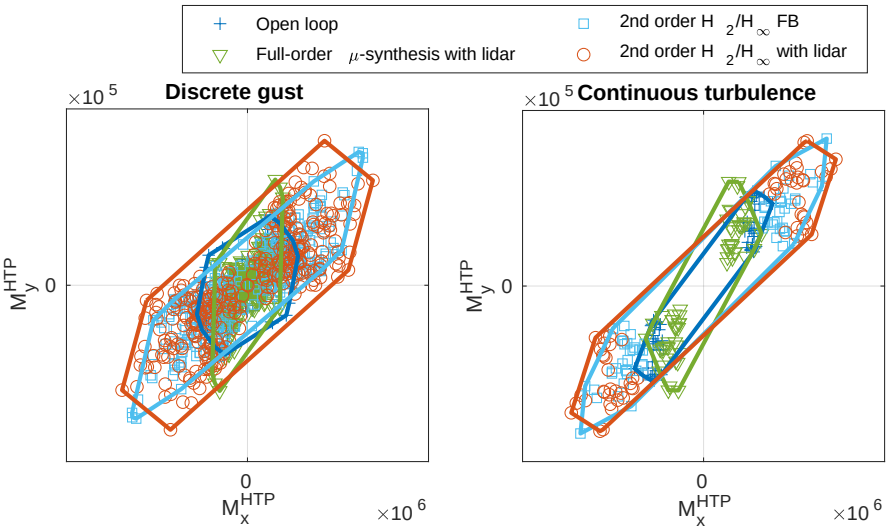

Figure E.1: M_x/M_y correlated loads envelopes on the HTP with different robust GLA controllers

The M_x/M_y loads envelopes on the HTP are shown on Fig. E.1 for different robust controllers. The controller obtained by μ-synthesis with a lidar was designed with an HTP loads reduction objective. It successfully reduces the HTP bending moment, but the torsion is increased. The controllers designed by H_2/H_∞, without HTP loads reduction objectives, strongly increase the HTP bending and torsional moment compared to the open loop case.

E.2 MIMO nyquist diagram

Another popular representation of the MIMO stability is the Nyquist diagram, shown in Fig. E.2 for different robust linear controllers. The eigenvalues of the response of the MIMO open-loop (cut at the aeroelastic plant input) are plotted at different frequencies. The associated stability criterion (generalized Nyquist criterion, see [MacFarlane and Postlethwaite 1977] for more details) states that whenever this open-loop is stable, the closed loop remains stable as long as the eigenvalues

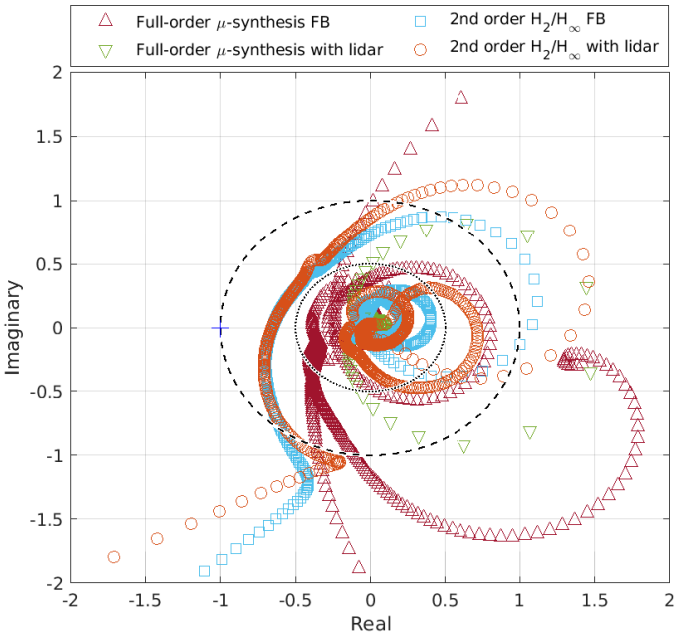

Figure E.2: MIMO nyquist diagrams of different robust GLA controllers

loci of the open-loop do not encircle the -1 point. For flight control systems, the root eigenvalues loci should then remain as far as possible to the -1 point to avoid instability. This representation does not bring additional information with respect to the frequency-dependent disk margins of Fig. 4.31, and is less straightforward.

E.3 Loads envelopes results

This section presents two results from [Fournier et al. 2022b] using loads envelopes. The simulation framework is different from the one used in this work, but the conclusions remain valid. In Fig. E.3, the correlated M_x/M_y envelopes are shown in open loop and using a multi-model H_2/H_∞ GLA controller. In addition, the conditions (Mach, mass configuration) leading to the convex hull of the closed-loop envelope have been selected to design local controllers based on each of them. For each of these conditions, a different controller is designed, using mono-model H_2/H_∞ synthesis, and the simulations are performed on aeroelastic models computed at these conditions. This allows to see the gain in terms of performance we could get from using controllers which perfectly adapt to the local dynamics. It can be observed that there is no clear gain in using adaptive controller, even in the perfect case of adaptation.

Another result, shown if Fig. E.4 compares envelopes obtained with multi-model H_2/H_∞ GLA controllers of different orders. While the order 2 leads to significant loads reduction compared to a static gain controller, going higher does not seem to improve the performance, and it even degrades it for off-design simulations (discrete gust, while the controller is designed for turbulence).

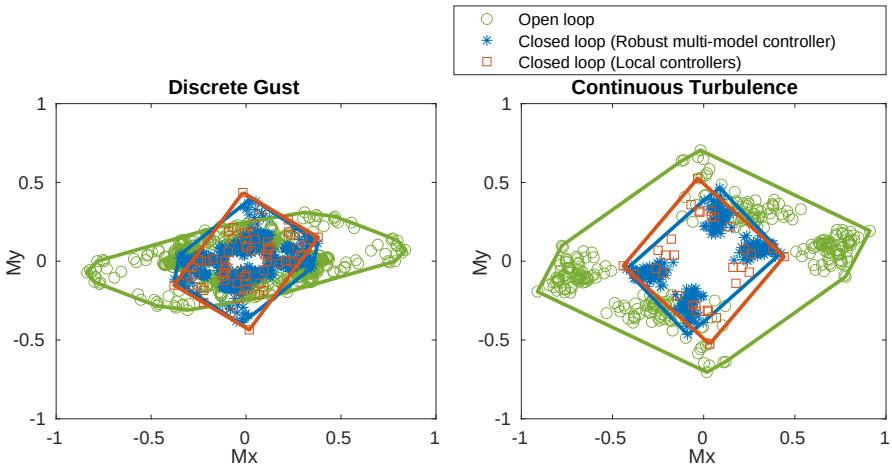

Figure E.3: M_x/M_y correlated loads envelopes. Comparison of a robust controller designed with multiple models, and local controllers designed for each model

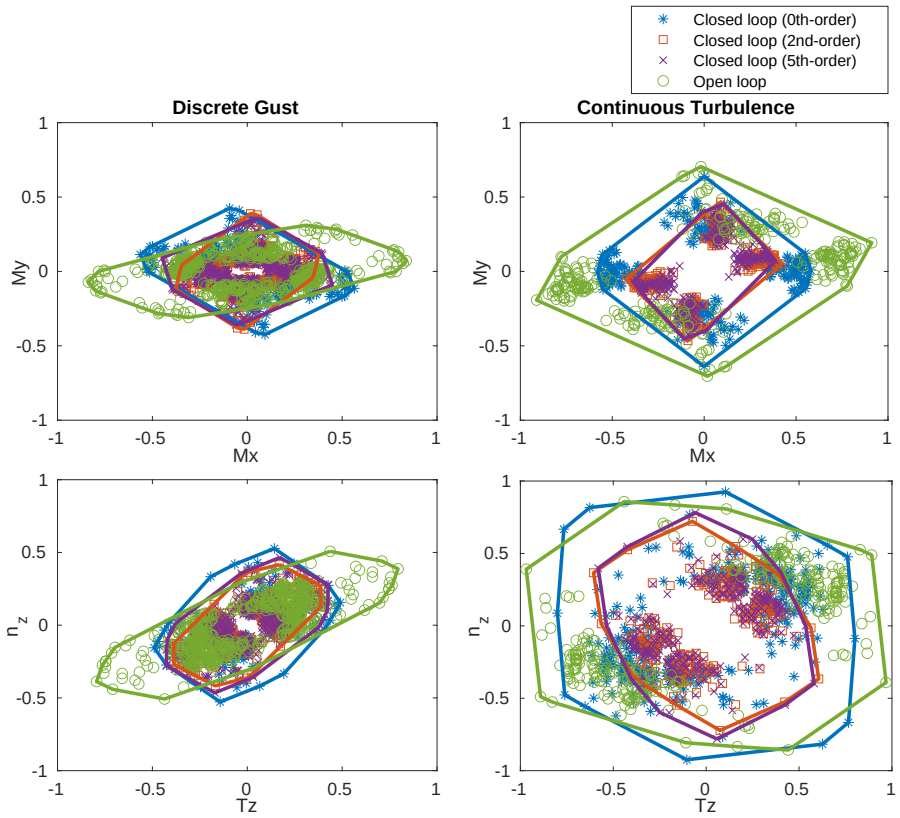

Figure E.4: M_x/M_y and T_z/n_z correlated loads envelopes, for different controller's order

Appendix F

Résumé de la thèse en Français

F.1 Introduction

L'objectif général de ce travail est de développer des solutions pour réduire les charges dues au vent appliquées à la cellule, en vue d'améliorer les performances globales de l'avion, et le confort des passagers. Ceci doit être réalisé dans un environnement industriel d'avion, et les interactions avec les autres sous-systèmes composant l'avion doivent être prises en compte, ainsi que les principales contraintes imposées par les documents de certification. Ce travail ne vise pas à interagir directement avec la conception globale de l'avion, comme le fait l'optimisation multidisciplinaire (MDO). Au contraire, en étudiant certains des nouveaux défis en termes de charges, de stabilité aéroélastique et de modélisation qu'impliquent les prochaines générations d'avions à haute efficacité, l'accent est mis sur le développement de nouvelles techniques qui peuvent être incluses dans les conceptions futures.

L'objectif principal de ce travail est l'allègement des charges dues au vent (Gust Load Alleviation en anglais, GLA), qui vise à réduire les charges dues au vent de vent. Des objectifs intermédiaires sont nécessaires pour y parvenir : la modélisation de l'avion et la stabilisation aéroélastique. Le premier vise à trouver des modèles mathématiques utilisés pour les simulations, la conception et l'analyse des commandes. Idéalement, ils devraient être simples, précis et représenter tous les effets physiques d'intérêt. Bien sûr, un tel modèle n'existe pas, et de nouvelles techniques doivent être développées et des compromis doivent être faits en fonction de l'application. La suppression active de flottement (Active Flutter Suppression en anglais, AFS), quant à elle, consiste à s'assurer que l'instabilité de flottement ne se produit pas pendant les opérations nominales, avec des marges de sécurité. En raison de leur complexité et de l'influence qu'ils exercent sur d'autres sujets connexes, ces objectifs intermédiaires sont primordiaux en soi.

Outre la logique générale suivie par ce travail, l'analyse robuste multi-modèle est un fil rouge reliant les différents sujets. Inspirée par la logique de certification consistant à placer l'avion dans toutes les conditions extrêmes possibles, une approche multirobuste est utilisée pour la synthèse et l'analyse des commandes, ce qui nécessite des techniques de modélisation dédiées. Alors que de nombreuses études se concentrent sur des avions évoluant dans une condition fixe, ce travail étudie un modèle aéroélastique plus général sous la forme de plusieurs instantanés linéaires dans différentes conditions de vol et de masse. Cette logique multi-modèle est liée aux concepts de

robustesse et d'adaptabilité, qui sont au cœur du défi actuel de l'aéro-servoélasticité.

F.2 Définition de la dynamique des aéronefs

F.2.1 Le concept de l'avion XRF1-HARW

Les modèles présentés dans cette thèse sont basés sur le XRF1, un concept d'avion développé par Airbus à des fins de recherche. Si sa configuration générale est similaire à celle d'un avion commercial à long rayon d'action, les ailes sont plus souples et plus effilées. Cette configuration est très efficace du point de vue de la conception globale, car elle permet de réduire la traînée par rapport aux modèles commerciaux actuels. Cependant, la flexibilité accrue des ailes crée de nouveaux défis en termes de modélisation et de certification. L'interaction entre l'aérodynamique et la structure de l'aile crée des phénomènes dits aéroélastiques. Avec une aile très flexible, les modes structurels interagissent plus directement avec la dynamique du vol et créent des charges dynamiques plus élevées. En outre, les vibrations introduites peuvent être légèrement amorties et même devenir instables (phénomène de flottement). Le concept XRF1 permet d'étudier ces nouveaux défis et les solutions possibles telles que GLA et AFS, dans un environnement réaliste de grand avion commercial. Plusieurs versions du XRF1 ont été publiées. Dans la plupart des résultats et sauf indication contraire, la version XRF1-HARW (High Aspect Ratio Wing) est utilisée dans ce travail. Elle a été développée dans le cadre d'un partenariat entre Airbus et l'Université du Michigan (Ann Arbor). Comme son nom l'indique, elle présente un rapport d'aspect (RA) particulièrement élevé de 13, contre une valeur typique de 8 dans les générations actuelles d'avions commerciaux à long rayon d'action. La rigidité en torsion des ailes a également été fixée à une faible valeur afin d'amplifier sa flexibilité et son instabilité.

F.2.2 Modélisation aéroélastique

La modélisation aéroélastique utilisée dans ce travail vise à définir les équations de mouvement de l'avion qui prennent en compte l'interaction entre la structure et l'aérodynamique avec une grande précision. En même temps, la modélisation aéroélastique doit être adaptée à la conception des commandes, pour laquelle les modèles linéaires sont souvent préférés en raison de la disponibilité d'outils d'analyse et de synthèse basés sur ces modèles. En outre, les modèles aéroélastiques doivent être aussi simples que possible, avec la plus petite dimension d'état possible, afin de permettre des techniques de conception de contrôle exigeantes en termes de calcul.

F.2.2.1 Etat de l'art

La modélisation aéroélastique des aéronefs remonte au milieu du vingtième siècle, lorsque les équations de la dynamique du vol ont commencé à inclure des corrections dues à l'interaction quasi-stationnaire entre le mouvement rigide et l'aérodynamique (voir [Bisplinghoff, Ashley, and Halfman 1955b] et [Etkin 1959]). Avec le développement des capacités informatiques, des techniques plus avancées basées sur les méthodes de la dynamique des fluides numérique (CFD) ont permis de modéliser l'aérodynamique avec une plus grande précision, en tenant compte de la géométrie complète de l'avion et en utilisant une théorie non linéaire et instable qui peut capturer les effets transsoniques. Toutefois, la réalisation de simulations aéroélastiques aussi précises est une tâche coûteuse en termes de calcul. De nombreuses applications, notamment les calculs de charges dynamiques, les simulations de dynamique de vol, la synthèse de contrôleurs et l'analyse de stabilité, nécessitent un modèle aéroélastique réduit dont l'évaluation prend moins de temps. Une approche populaire consiste à générer des données temporelles des forces aérodynamiques généralisées (GAF) obtenues par des calculs CFD et à dériver un modèle non linéaire qui peut être couplé à la dynamique structurelle pour obtenir un modèle aéroélastique réduit [Lucia, Beran, and Silva 2004]. Plusieurs techniques existent, notamment la théorie de Volterra [Stalford et al. 1987; Jenkins 1989], la décomposition orthogonale appropriée (POD) [Hall, Thomas, and Dowell 2000; Romanowski and Dowell 1995; Kim 1998], la méthode de l'équilibre harmonique (HB) [Thomas, Dowell, and Hall 2002] ou, plus récemment, les modèles basés sur des réseaux neuronaux [Huang, Hu, and Zhao 2014]. Des techniques spécifiques doivent être développées pour réduire le nombre de calculs CFD de haute fidélité qui doivent être effectués pour générer les données temporelles [Lee-Rausch and Batina 1996; Hall, Thomas, and Dowell 2000]. L'utilisation de modèles non linéaires et de calculs aérodynamiques précis tels que la CFD est bien adaptée à la simulation et à l'analyse. Lorsque l'on considère la dynamique de vol d'un aéronef flexible, les équations de Lagrange sont généralement utilisées et peuvent être simplifiées par un choix précis de l'axe de référence. La littérature [Waszak and Schmidt 1988; Schmidt and Raney 2001; Reschke 2005] a également souvent utilisé des axes moyens, par rapport auxquels les moments linéaires et angulaires associés aux vibrations structurelles sont nuls. Les travaux de [Guimarães Neto et al. 2016] ont proposé à la place une formulation avec un choix arbitraire d'axes corporels.

Dans leur formulation originale, les méthodes citées ci-dessus conduisent à des modèles non linéaires qui peuvent être utilisés pour les simulations d'une grande catégorie d'aéronefs, y compris les aéronefs très flexibles avec de grandes déflexions aéroélastiques [Patil and Hodges 2006; Su and Cesnik 2010]. Pour la conception de contrôleurs, un modèle linéaire est souvent préféré en raison de la disponibilité d'outils de synthèse et d'analyse basés sur l'analyse de fréquence. L'atténuation des charges dues au vent [Fournier et al. 2022b; Fournier et al. 2022a] et la suppression active du flottement [Livne 2018] sont des sujets de recherche actifs typiques qui sont souvent basés sur des modèles linéaires. Si un équilibre d'assiette de l'avion a été calculé à l'aide de techniques non linéaires, on peut faire l'hypothèse de petits déplacements et déflexions autour de ce point, comme cela a été fait dans [Ustinov, Sidoruck, and Goman 2005; Luspay et al. 2019], ce qui permet de définir une dynamique structurelle linéaire des déplacements incrémentaux. En supposant en outre

que l'aérodynamique est linéaire (en supposant par exemple un faible angle d'attaque et de faibles déviations des gouvernes), les GAF qui sont proportionnels aux déplacements modaux peuvent être calculés à l'aide de la CFD, ou des techniques plus rapides (mais moins précises) telles que la méthode du doublet de treillis (DLM) [Albano and Rodden 1969; Kalman, Rodden, and Giesling 1971], qui fonctionne dans le domaine des fréquences, ou son équivalent dans le domaine temporel Unsteady Lattice Vortex Method (UVLM) [Konstadinopoulos et al. 1985] utilisé par exemple dans [Hesse and Palacios 2014; Hesse and Palacios 2016]. La DLM et l'UVLM sont toutes deux basées sur la théorie du potentiel instable qui conduit à un GAF proportionnel aux déplacements modaux, et peuvent donc être facilement couplées à un modèle structurel obtenu par la méthode intégrée des éléments finis (FEM), par exemple. L'utilisation de la DLM permet de calculer le GAF à différentes valeurs de fréquence, sur la base desquelles des modèles LTI peuvent être identifiés.

F.2.3 Équations aéroélastiques linéarisées

Les équations aéroélastiques sont obtenues à l'aide de la procédure suivante : tout d'abord, les équations non linéaires des mouvements sont obtenues à l'aide d'une formulation lagrangienne. Les déplacements structurels sont inclus et supposés faibles par rapport aux dimensions de l'avion. Une méthode d'éléments finis est utilisée pour modéliser l'inertie de l'avion et les matrices élastiques. L'aérodynamique est modélisée à l'aide de la CFD. En alternant les analyses structurelles et aérodynamiques, et en itérant jusqu'à convergence, un équilibre aéroélastique non linéaire peut être trouvé. Ensuite, sur la base de ce point d'équilibre, le modèle aéroélastique final est obtenu en linéarisant les équations de mouvement autour de l'équilibre. Il résulte de l'interaction entre la dynamique structurelle, décrite par le même modèle FEM que dans le calcul de l'assiette, et l'aérodynamique linéaire instable, obtenue par DLM. Cette dernière offre la possibilité de modéliser la dynamique de l'avion sur la gamme de fréquences d'intérêt pour GLA et AFS, avec un coût de calcul inférieur à celui de la CFD instationnaire linéarisée (mais avec une précision moindre). Cette interaction conduit à des équations aéroélastiques instables sur un ensemble physique de coordonnées, appelé l'ensemble g. Afin de réduire le nombre de degrés de liberté, une analyse modale est effectuée, en définissant les coordonnées généralisées (modales) avec l'indice h. Chaque coordonnée généralisée est associée à un mode aéroélastique de l'avion. Les équations aéroélastiques finales dans le domaine des fréquences sont les suivantes

$$\left[-\omega^2 \boldsymbol{M_{hh}} + j\omega \boldsymbol{B_{hh}} + \boldsymbol{K_{hh}} - \bar{q}\boldsymbol{Q_{hh}}(M,\kappa)\right] \boldsymbol{X_h}(j\omega) = \bar{q}\boldsymbol{Q_{h\delta}}(M,\kappa)\boldsymbol{\Delta}(j\omega) + \bar{q}\boldsymbol{Q_{hv}}(M,\kappa)\frac{\boldsymbol{V}(j\omega)}{\mathrm{TAS}} \quad \text{(F.1)}$$

où $\boldsymbol{M_{hh}}$, $\boldsymbol{B_{hh}}$ et $\boldsymbol{K_{hh}}$ sont les matrices d'inertie, d'amortissement et d'élasticité dans les coordonnées généralisées, $\boldsymbol{X_h}$ est le vecteur des déplacements modaux dans le domaine fréquentiel, $\bar{q}$ est la pression dynamique, $\boldsymbol{Q_{hh}}$, $\boldsymbol{Q_{h\delta}}$ et $\boldsymbol{Q_{hv}}$ sont les contributions linéaires des déplacements modaux, des déflexions des gouvernes et de la vitesse du vent aux forces aérodynamiques. Ces forces dépendent du nombre de Mach et de la fréquence réduite $\kappa = \frac{\omega b}{\mathrm{TAS}}$ où b est l'envergure de

l'aile, TAS est la vitesse vraie et ω est la fréquence.

A la fin de ce chapitre, une question importante reste ouverte : comment approximer les équations aéroélastiques à l'aide de modèles LTI ? En effet, la linéarité mentionnée précédemment est liée à la relation entrée/sortie : la propriété de superposition s'applique, permettant l'expression d'une sortie comme la somme des contributions à différentes entrées. Cependant, comme la dépendance en fréquence des forces aérodynamiques n'est pas formalisée sous la forme d'une fonction rationnelle, aucune représentation dans le domaine temporel n'est disponible. Le chapitre suivant 3 est consacré à cette question, en examinant les approximations des équations aéroélastiques dans les modèles d'espace d'état.

F.3 Identification de système

F.3.1 Introduction

F.3.1.1 Contexte de la modélisation aéroélastique d'ordre réduit

Les modèles aéroélastiques définis au chapitre 2 sont linéaires, en ce sens que si y_1 et y_2 sont les réponses du modèle à u_1 et u_2 respectivement, alors une combinaison linéaire d'entrées $a_1u_1+a_2u_2$ conduit à une combinaison linéaire de sorties de la même forme $a_1y_1 + a_2y_2$. Cependant, la méthode DLM conduit à des valeurs de GAF à différentes fréquences réduites, qui ne peuvent pas être directement utilisées par les techniques de conception de contrôle ou pour l'analyse de la stabilité et de la robustesse. Des modèles d'espace d'état invariants dans le temps (LTI) peuvent être obtenus sur la base de ces valeurs, à l'aide de techniques d'identification du système, puis utilisés pour la simulation, l'analyse et la synthèse des commandes. L'approche classique consiste à utiliser les approximations de Roger [Roger 1977] ou de Karpel [Karpel 1982] qui ajustent une fonction de transfert composée d'un polynôme du second ordre et de termes de retard à partir des données GAF, comme dans [Waite et al. 2018]. Une autre méthode populaire est l'algorithme de réalisation des systèmes propres (ERA) [Juang and Pappa 1985] qui identifie un modèle d'espace d'état basé sur des données temporelles, utilisé par plusieurs études sur la suppression active du flottement [Silva and Raveh 2001; Silva 2018; Waite et al. 2018; Waite et al. 2019]. Avec les hypothèses de petits déplacements autour d'un équilibre de compensation et d'une aérodynamique linéaire, des modèles aéroélastiques linéaires peuvent être obtenus avec cette procédure.

Les modèles aéroélastiques obtenus par rationalisation GAF conservent l'interprétation physique des états, qui peuvent être assimilés aux déplacements modaux et aux retards aérodynamiques par exemple. Cependant, en l'absence de méthodes dédiées pour réduire leur ordre, ces modèles peuvent être prohibitifs pour les techniques de synthèse de contrôle numériquement intensives. D'après l'expérience de l'auteur, les techniques de réduction classiques, telles que la troncature équilibrée, [Green 1988], conduisent à une mauvaise approximation du modèle initial lorsque ce dernier est

d'ordre très élevé et numériquement mal conditionné. Le présent travail étudie une stratégie différente, en travaillant directement sur l'identification de la fonction de transfert aéroélastique complète, au lieu de la GAF. La réponse en fréquence de la fonction de transfert aéroélastique est d'abord évaluée à différentes fréquences, et des algorithmes d'identification à entrées et sorties multiples (MIMO) basés sur ces données sont utilisés pour obtenir directement des modèles d'espace d'état d'ordre réduit. L'aérodynamique est modélisée par DLM pour obtenir directement le GAF dans le domaine des fréquences, et un modèle FEM intégré est utilisé pour la dynamique structurelle. En se concentrant sur la réponse correspondant aux entrées et sorties d'intérêt, seules les caractéristiques principales sont modélisées, ce qui conduit à des ordres beaucoup plus faibles qu'avec l'approche classique. Cependant, la dépendance vis-à-vis des paramètres de vol (tels que Mach et l'altitude) est perdue, et un modèle doit être obtenu pour chaque condition séparément. L'identification des sous-espaces est un ensemble de techniques de pointe pour l'estimation d'un modèle d'espace d'état MIMO à partir de données temporelles ou fréquentielles, dont on trouvera un aperçu dans [Qin 2006]. La méthode Loewner [Mayo and Antoulas 2007; Karachalios, Gosea, and Antoulas 2019] est une autre approche prometteuse, basée sur la théorie de l'interpolation rationnelle. En l'absence de contraintes de stabilité, il n'est pas garanti que ces méthodes produisent des modèles qui reflètent la stabilité du véritable système, en particulier lorsque son ordre n'est pas connu à l'avance. Cette difficulté, reconnue dans [Kergus et al. 2018] par exemple, est un défaut typique de l'approche boîte noire, qui perd l'interprétabilité physique du système aéroélastique dont les pôles ne sont pas exactement modélisés. La première étape pour faire face à ce problème est d'imposer la stabilité du modèle identifié. Ceci est fait dans ce travail en utilisant les résultats de [Miller and De Callafon 2013] basés sur [Chilali and Gahinet 1996; Lacy and Bernstein 2003], dans lequel une identification basée sur le sous-espace est proposée avec un ensemble général de contraintes imposées aux pôles, qui inclut la contrainte de stabilité. La deuxième étape pour améliorer l'interprétabilité physique des modèles consiste à imposer un ensemble de pôles aéroélastiques connus qui ont été estimés au préalable par la méthode p-k [Hassig 1971] par exemple, tandis que d'autres pôles sont laissés comme paramètres libres pour améliorer la précision de l'approximation. Avec cette méthode hybride, l'objectif est d'assurer la stabilité des pôles mathématiques qui aident à approximer la vraie fonction de transfert, tout en imposant que certains pôles d'intérêt soient correctement modélisés, avec des applications directes dans les synthèses GLA et AFS, mais aussi dans des simulations aéroélastiques efficaces. Des techniques spécifiques sont développées sur la base de l'identification des sous-espaces et inspirées par [Tang, Wu, and Shi 2017], pour imposer des pôles avec et sans contraintes sur les pôles additionnels.

F.3.1.2 Identification du modèle de l'espace d'état

L'objectif de ce chapitre est d'identifier des modèles d'espace d'état qui se rapprochent des systèmes aéroélastiques définis par la dynamique des déplacements modaux (2.41) et par l'expression des sorties d'intérêt définies par l'équation (2.42), (2.46) et (2.47). Le modèle d'état peut être défini

sous forme de temps discret :

$$\begin{cases} \boldsymbol{x}_{k+1} = \boldsymbol{A}\boldsymbol{x}_k + \boldsymbol{B}\boldsymbol{u}_k \\ \boldsymbol{y}_k = \boldsymbol{C}\boldsymbol{x}_k + \boldsymbol{D}\boldsymbol{u}_k \end{cases} \tag{F.2}$$

où k est le temps discret, ou alternativement sous forme de temps continu :

$$\begin{cases} \dot{\boldsymbol{x}}(t) = \boldsymbol{A}\boldsymbol{x}(t) + \boldsymbol{B}\boldsymbol{u}(t) \\ \boldsymbol{y}(t) = \boldsymbol{C}\boldsymbol{x}(t) + \boldsymbol{D}\boldsymbol{u}(t) \end{cases} \tag{F.3}$$

où t est le temps continu. $\boldsymbol{x}$ est le vecteur d'état, $\boldsymbol{u}$ et $\boldsymbol{y}$ sont respectivement les vecteurs d'entrée et de sortie, et les matrices $\boldsymbol{A} \in \mathbb{R}^{n\times n}$, $\boldsymbol{B} \in \mathbb{R}^{n\times N_u}$, $\boldsymbol{C} \in \mathbb{R}^{N_y\times n}$ et $\boldsymbol{D} \in \mathbb{R}^{N_y\times N_u}$ sont des matrices définissant le modèle.

F.3.2 Identification d'un modèle d'espace d'état MIMO à partir de données fréquentielles

F.3.2.1 Méthodes d'identification des sous-espaces

L'idée des méthodes des sous-espaces est de trouver une réalisation de certaines données, c'est-à-dire de définir une famille d'états qui décrit mathématiquement les données, sans nécessairement avoir une interprétation physique. Le terme "sous-espace" vient du fait qu'un nombre réduit d'états est recherché, ce qui conduit à la recherche des sous-espaces de faible dimension dans lesquels les états évoluent. Les méthodes des sous-espaces sont des techniques efficaces qui permettent l'identification de modèles d'espace d'état MIMO à partir de séries temporelles composées des sorties mesurées et des entrées connues d'un système donné. Il existe plusieurs variantes, dont les plus célèbres sont l'analyse canonique des variables (CVA) proposée par [Larimore 1990], la N4SID proposée par [Van Overschee and De Moor 1994], la MOESP proposée par [Verhaegen and Dewilde 1992] et la méthode du filtre observateur-Kalman (OKID) proposée par [Phan et al. 1992]. Bien que ces méthodes aient été développées à l'aide de stratégies différentes, elles reposent sur des procédures similaires qui se résument toutes à la décomposition de la valeur singulière d'une certaine matrice avec différentes pondérations possibles, comme l'a démontré [Van Overschee and De Moor 1995] et résumé [Qin 2006]. Les méthodes des sous-espaces estiment soit la séquence d'états du modèle identifié, soit sa matrice d'observabilité (ou de contrôlabilité), ce qui conduit dans les deux cas à une réalisation de l'espace d'état. Dans ce dernier cas, après avoir organisé les données en matrices de Hankel, l'influence des entrées connues peut être supprimée par une projection sur l'espace orthogonal de la matrice de Hankel d'entrée, ce qui ne laisse qu'un terme d'observabilité et un terme de bruit. Ce dernier peut être supprimé sous certaines hypothèses (bruit non corrélé et nombre suffisant de mesures). La possibilité de traiter des données bruitées est un point fort des techniques des sous-espaces et une amélioration par rapport à la méthode ERA qui, dans sa formulation initiale, n'inclut pas l'annulation du bruit. En outre, la méthode ERA exige que les entrées connues soient impulsives, alors que les méthodes des sous-espaces

s'appliquent à toute séquence d'entrées suffisamment excitante. Suivant le point de vue OKID [Phan et al. 1992] et sous l'hypothèse de l'observabilité, un filtre de Kalman virtuel avec un gain arbitrairement élevé peut être inclus dans la procédure d'identification pour estimer la séquence d'états et limiter les effets du bruit, tout en maintenant les pôles dans une région qui préserve les problèmes numériques de se produire. Des analogues de ces méthodes peuvent être définis lorsque l'on utilise des données fréquentielles comme dans le présent travail. De plus, lorsque les données proviennent de simulations et non de mesures, l'absence de bruit peut conduire à une identification très précise. La technique proposée par McKelvey et Ljung dans [McKelvey, Akcay, and Ljung 1996], une variante de MOESP, est utilisée dans ce travail pour identifier des modèles d'espace d'état MIMO d'ordre fixe basés sur des données fréquentielles, et servira de base pour le développement de nouvelles techniques. Il convient de noter que lorsqu'elles sont appliquées à l'identification en boucle fermée, les méthodes des sous-espaces peuvent être confrontées à des problèmes supplémentaires, comme le souligne [Qin 2006]. Cependant, le présent travail se concentre uniquement sur l'identification en boucle ouverte.

F.3.3 Méthode de Loewner

Une autre approche d'identification pour les systèmes MIMO, la méthode Loewner [Mayo and Antoulas 2007; Karachalios, Gosea, and Antoulas 2019], identifie un modèle d'espace d'état à temps continu basé sur des données fréquentielles. Cette méthode provient du domaine de l'interpolation rationnelle, et elle recherche un espace d'état qui correspond parfaitement aux données fréquentielles, dans un premier temps. Une réduction basée sur la décomposition en valeurs singulières est ensuite effectuée, conduisant à un modèle d'ordre réduit qui approxime les données. La méthode de Loewner est bien adaptée aux données sans bruit.

F.4 Identification MIMO avec contraintes d'emplacement des pôles

F.4.0.1 Identification des sous-espaces avec contraintes de localisation des pôles

L'algorithme d'identification des sous-espaces ou la méthode de Loewner ne garantissent pas la stabilité du modèle d'état identifié. Même si le système réel est stable, un modèle d'espace d'état d'ordre réduit peut contenir des pôles instables. Cela conduit à des simulations temporelles divergentes et peut poser des problèmes lorsqu'il est utilisé pour la conception d'un contrôleur, par exemple. Pour cette raison, il est courant de simplement supprimer les pôles instables du modèle identifié, comme étudié dans [Köhler 2014]. Cette post-analyse peut conduire à une mauvaise capacité d'approximation lorsque le modèle identifié comprend un grand nombre de modes instables. Cette limitation motive le développement de techniques dédiées, dans lesquelles la contrainte de stabilité fait partie du processus d'identification, et n'est pas imposée a posteriori.

[Lacy and Bernstein 2003] présente un algorithme d'identification basé sur des méthodes des sous-espaces pour imposer la stabilité au modèle d'espace d'état, en utilisant l'optimisation convexe. Les travaux de [Miller and De Callafon 2013] ont proposé un algorithme d'identification de l'espace d'état basé sur l'optimisation convexe dans lequel l'emplacement des pôles est contraint de manière similaire à ce qui a été fait dans [Chilali and Gahinet 1996] pour la synthèse de H_∞. L'ensemble $\mathcal{D}^{\boldsymbol{\alpha},\boldsymbol{\beta}}$ définit les contraintes que nous voulons mettre sur les pôles, paramétrées par les matrices $\boldsymbol{\alpha}$ et $\boldsymbol{\beta}$. La stabilité en temps continu ou en temps discret est un cas particulier de ces contraintes. Dans cette section, cette technique est présentée comme une introduction aux méthodes développées dans ce travail.

F.4.0.2 Méthode de Loewner avec contraintes de localisation des pôles

la connaissance de l'auteur, il n'existe aucun exemple dans la littérature de méthodes imposant la stabilité avec l'identification du système de Loewner. Au lieu de cela, les instables sont généralement simplement supprimés après le processus d'identification, ou une procédure telle que celle décrite dans [Köhler 2014] peut être appliquée pour trouver le système d'espace d'état stable le plus proche dans le sens RH_2 ou RH_∞. Dans tous les cas, la stabilité est appliquée en post-analyse, ce qui peut conduire à une perte de précision de la modélisation par rapport à un processus d'identification qui inclut des contraintes de stabilité.

Une procédure peut être appliquée pour identifier un espace d'état stable à l'aide de la méthode de Loewner, de manière similaire à ce qui est fait avec les méthodes des sous-espaces dans [Miller and De Callafon 2013]. Tout d'abord, les matrices $\boldsymbol{A_0}$, $\boldsymbol{B_0}$, $\boldsymbol{C_0}$ et $\boldsymbol{D_0}$ sont obtenues avec la méthode de Loewner sans contrainte de localisation des pôles. Ensuite, une matrice $\boldsymbol{A}$ est trouvée en résolvant un problème d'optimisation similaire à celui de [Miller and De Callafon 2013].

F.4.1 Identification MIMO avec pôles imposés

Cette section présente une nouvelle approche pour l'identification hybride d'un modèle d'état, où certains pôles sont imposés et les pôles restants sont des paramètres libres. Une méthode permettant d'obtenir un modèle d'état dont les pôles sont tous connus au préalable est décrite [Tang, Wu, and Shi 2017]. Nous généralisons cette procédure au cas où certains pôles sont inconnus, afin de donner des degrés de liberté supplémentaires à l'identification, et une meilleure adéquation aux données fréquentielles. De plus, dans la plupart des applications réelles, une petite partie des vrais pôles du système est connue, comme dans les équations aéroélastiques. Une alternative à cette méthode est obtenue en travaillant sur les paramètres définissant la fonction de transfert MIMO. Cette méthode présente deux inconvénients principaux : premièrement, elle implique des opérations sur des polynômes, qui posent des problèmes numériques lorsque l'ordre augmente. Deuxièmement, en fixant l'ordre de la fonction de transfert à n, le modèle d'état associé sera d'ordre $\min(nN_y, nN_u)$ avec n pôles distincts (sous certaines hypothèses). Pour cette raison,

l'approche de la fonction de transfert ne sera pas appliquée dans la section des résultats.

La technique de [Tang, Wu, and Shi 2017] nécessite la connaissance a-priori de tous les pôles du système identifié. Une technique appelée System Identification with Orthogonal eigenvectors (SIDORT) est développée dans ce travail, pour identifier un modèle dont seuls certains pôles sont connus. Pour ce faire, de nouveaux pôles doivent être identifiés avec leurs vecteurs propres associés. Une difficulté vient du fait que ces vecteurs propres doivent être linéairement indépendants, formant une matrice inversible. Une procédure est proposée, basée sur l'hypothèse que les vecteurs propres libres sont orthogonaux entre eux et avec ceux imposés au modèle. Pour ce faire, nous commençons par trouver une famille orthogonale de vecteurs de l'espace orthogonal à l'espace généré par les vecteurs propres imposés (ceci est réalisé à l'aide d'une seule SVD). Ensuite, nous montrons que la recherche des pôles libres et des vecteurs propres associés est un problème classique de valeurs propres.

F.4.2 Identification MIMO avec pôles imposés et contraintes de localisation

F.4.2.1 Identification des sous-espaces par le problème des pseudo-valeurs propres (SIDPEV)

Si l'hypothèse d'orthogonalité des vecteurs propres inconnus est abandonnée, la matrice $\boldsymbol{P}$ du problème généralisé des valeurs propres (3.57) peut être obtenue par une optimisation non convexe. Nous commençons par obtenir les vecteurs propres $\bar{\boldsymbol{P}}$ associés aux pôles imposés de la même manière que dans la section 3.5. La matrice $\boldsymbol{P}$ associée aux vecteurs propres inconnus peut alors être obtenue de manière itérative, en résolvant successivement un problème d'optimisation pour chaque vecteur propre inconnu. Ce problème d'optimisation peut être approximé par un problème d'inégalité matricielle bilinéaire en relaxant les contraintes de rang en contraintes de positivité matricielle. Sinon, le problème peut être résolu par une méthode d'optimisation non linéaire avec contrainte, telle que la méthode du point intérieur [Byrd, Hribar, and Nocedal 1999; Waltz et al. 2006], avec la contrainte de rang non linéaire exprimée comme une borne inférieure positive sur la valeur singulière minimale de la matrice, par exemple. Cette dernière option est préférée pour sa robustesse. On peut constater que le gradient de la fonction objective par rapport aux variables est facile à calculer. En outre, chaque paire valeur propre/vecteur propre est calculée indépendamment, de sorte que chaque problème d'optimisation a un faible nombre de variables, ce qui fait que la méthode n'est pas trop gourmande en ressources informatiques.

F.4.2.2 Optimisation non linéaire directe avec contraintes (DNOC)

Les méthodes exposées précédemment visent à décomposer le problème général de l'identification de modèles dans l'espace d'état avec des pôles imposés et des contraintes sur les pôles incon-

nus d'une manière qui limite le coût de calcul. Ce faisant, les erreurs dues à des hypothèses trop contraignantes ou à des solutions sous-optimales peuvent s'accumuler et augmenter l'erreur d'approximation. Une autre stratégie consiste à résoudre les différentes étapes simultanément par une seule optimisation.

Une identification directe d'un modèle d'espace d'état avec des pôles imposés et des contraintes sur les pôles inconnus peut être obtenue en recherchant le modèle identifié dans sa forme canonique modale et en résolvant un problème d'optimisation non convexe avec contrainte. Les matrices $\boldsymbol{A}$, $\boldsymbol{B}$, $\boldsymbol{C}$ et $\boldsymbol{D}$ sont obtenues simultanément, par un algorithme de point intérieur [Byrd, Hribar, and Nocedal 1999; Waltz et al. 2006] par exemple. Le coût de calcul devrait être plus élevé qu'avec les autres méthodes décrites ci-dessus, en raison du nombre élevé de variables et de la non-convexité de l'optimisation. En raison de la nature non convexe du problème, les solveurs tels que la méthode du point intérieur ne garantissent pas la convergence vers un minimum global.

F.4.3 Identification par décomposition pôle-résidu

Cette section présente une stratégie différente, qui tire parti de la capacité d'estimation d'ordre réduit des méthodes d'identification en boîte noire telles que la méthode de Loewner, tout en imposant avec précision les pôles aéroélastiques. Elle commence par l'identification d'un modèle d'espace d'état fiable, potentiellement d'ordre élevé, à l'aide de la méthode GAF RFA par exemple. L'idée est de conserver la partie du modèle associée aux pôles d'intérêt et de réduire le reste. Pour ce faire, on procède à une décomposition pôle-résidus de la fonction de transfert du modèle d'espace d'état aéroélastique d'ordre complet en supposant que chaque pôle est simple :

$$\boldsymbol{H}(s) = \sum_{i=1}^{n} \frac{\boldsymbol{R_i}}{s - \lambda_i} \tag{F.4}$$

où les $\boldsymbol{R_i} \in \mathbb{C}^{N_y \times N_u}$ sont des matrices appelées résidus associées aux pôles λ_i. En plaçant le système d'espace d'état aéroélastique dans la base dans laquelle la matrice $\boldsymbol{A}$ est diagonale (ce qui est possible car les pôles sont supposés être de multiplicité 1), les $\boldsymbol{R_i}$ seraient le produit d'une colonne de $\boldsymbol{C}$ et d'une ligne de $\boldsymbol{B}$, ce qui montre que leur rang est égal à 1. Cependant, comme la matrice $\boldsymbol{A}$ est d'ordre très élevé, sa diagonalisation n'est pas numériquement efficace. Une solution efficace pour calculer les résidus consiste à évaluer la fonction de transfert $(s - \lambda_i)\boldsymbol{H}(s)$ à $s = \lambda_i$, ce qui donne directement la valeur de $\boldsymbol{R_i}$. Pour ce faire, il faut disposer de moyens efficaces pour calculer la réponse en fréquence d'une fonction de transfert d'ordre élevé, comme par exemple la fonction *freqresp* de Matlab.

Seuls les pôles aéroélastiques d'intérêt sont calculés avec la procédure d'identification proposée dans cette section. En particulier, seuls les pôles dans la gamme de fréquences d'intérêt peuvent être calculés pour réduire l'ordre du système final. En utilisant le fait que la fonction de transfert

a des coefficients réels, elle peut être écrite comme suit :

$$\boldsymbol{H}(s) = \sum_{k=1}^{\bar{n}} \left(\frac{\boldsymbol{R_k}}{s - \lambda_k} + \frac{\overline{\boldsymbol{R_k}}}{s - \overline{\lambda_k}} \right) + \boldsymbol{H_{diff}}(s) \tag{F.5}$$

où $\boldsymbol{H_{diff}}(s)$ est la différence entre la fonction de transfert complète et la partie que nous souhaitons imposer. L'idée de cette méthodologie est d'effectuer une réduction du modèle de $\boldsymbol{H_{diff}}$, en l'approximant avec un modèle d'espace d'état d'ordre réduit. Cela se fait ici en évaluant sa réponse en fréquence et en l'utilisant pour identifier un modèle réduit par la méthode de Loewner. Notez que ce nouveau modèle doit être stable, en supposant que nous avons inclus tous les modes instables dans l'ensemble sélectionné. Le modèle final d'espace d'état d'ordre réduit avec des pôles imposés a alors la fonction de transfert suivante

$$\boldsymbol{H^{ROM}}(s) = \sum_{k=1}^{\bar{n}} \left(\frac{\boldsymbol{R_k}}{s - \lambda_k} + \frac{\overline{\boldsymbol{R_k}}}{s - \overline{\lambda_k}} \right) + \boldsymbol{H_{diff}^{ROM}}(s) \tag{F.6}$$

où $\boldsymbol{H_{diff}^{ROM}}$ a été identifié par la méthode de Loewner avec stabilité imposée. Chaque sous-système associé à un pôle aéroélastique choisi λ_k peut être mis sous une forme d'espace d'état d'ordre 2, et l'espace d'état complet du modèle d'ordre réduit (ROM) avec des pôles imposés peut être obtenu avec la matrice bloc-diagonale $\boldsymbol{A}$ composée des matrices d'état de chaque sous-système, et les matrices associées $\boldsymbol{B}$ et $\boldsymbol{C}$ sont obtenues par concaténation. Cette méthode présente l'avantage de découpler linéairement la partie du système associée aux pôles imposés de la partie réduite. En outre, elle permet non seulement de s'assurer que les pôles sélectionnés sont représentés avec précision dans le modèle, mais aussi qu'ils affectent la fonction de transfert de la même manière que dans le modèle fiable défini à la première étape de la procédure.

F.4.4 Comparaison des techniques d'identification

Dans ce travail, des techniques de modélisation d'ordre réduit destinées aux systèmes aéroélastiques sont présentées et testées. La fonction de transfert aéroélastique complète correspondant à certaines entrées et sorties d'intérêt est identifiée sur la base de sa réponse en fréquence. La méthode de Loewner a été appliquée et comparée à un algorithme des sous-espaces, dans lequel la possibilité d'appliquer des contraintes sur les pôles a été étudiée. En outre, afin d'améliorer l'interprétabilité physique des modèles identifiés, des techniques dédiées ont été développées spécifiquement pour ce travail afin d'imposer un ensemble de pôles connus a-priori qui peuvent être stables ou instables. Ces méthodes ont été comparées à travers différents scénarios, en commençant par des modèles stables et instables de différents ordres, pour finalement être appliquées à des données aéroélastiques dans lesquelles les pôles imposés ont été calculés par la méthode p-k au préalable.

Il ressort de ce travail que les différentes méthodes décrites sont valables sur la gamme des ordres réduits étudiés (jusqu'à 80). La réponse de la fonction de transfert est systématiquement

approchée avec une erreur qui reste inférieure d'au moins un ordre de grandeur à la valeur réelle, à condition que l'ordre réduit soit suffisamment élevé. Les différentes contraintes (localisation des pôles, pôles imposés) sont appliquées avec succès par les méthodes concernées.

Une première comparaison peut être effectuée entre l'algorithme des sous-espaces de McKelvey et la méthode d'interpolation de Loewner, lorsqu'aucune contrainte n'est appliquée aux modèles identifiés. La méthode de Loewner est légèrement plus lente que l'algorithme des sous-espaces, mais elle est plus efficace pour l'approximation d'un système d'ordre réduit. Ceci a été vérifié en utilisant des données générées avec un modèle d'espace d'état aléatoire d'ordre fixe et avec un modèle aéroélastique. Un autre avantage de la méthode de Loewner est qu'elle conduit à un modèle à temps continu, qui peut plus facilement être transformé en un espace d'état à temps discret de n'importe quel temps d'échantillonnage si nécessaire. Bien que cela ne soit pas montré dans ce travail par souci de concision, des conclusions similaires peuvent être tirées avec différents nombres d'entrées et de sorties. En outre, l'algorithme des sous-espaces stable basé sur [Miller and De Callafon 2013] est capable d'approximer une fonction de transfert avec une erreur comparable à l'algorithme des sous-espaces de McKelvey et avec un temps de calcul similaire dans la gamme d'ordre réduite considérée dans ce travail, tout en garantissant la stabilité. Elle peut donc être appliquée pour obtenir des modèles utilisés dans les simulations et la synthèse de contrôle sans les problèmes d'instabilité classiques obtenus avec les méthodes de Loewner et des sous-espaces.

Une deuxième comparaison concerne les différentes techniques définies pour imposer certains pôles du système, avec et sans contraintes sur les pôles restants. La méthode SIDORT ajoute très peu de complexité à l'algorithme de McKelvey, étant donné que l'étape supplémentaire concerne principalement les problèmes de valeurs propres et la décomposition SVD pour les matrices de petite taille. Cependant, elle souffre de deux limitations principales : la première est l'hypothèse d'orthogonalité entre les vecteurs propres associés aux pôles imposés et ceux associés aux pôles libres respectivement. La seconde est le fait qu'elle n'impose pas la stabilité des pôles restants. Elle approxime les données avec une bonne précision, mais inférieure à celle des autres techniques présentées dans le présent travail. Lorsqu'elle est appliquée aux données aéroélastiques, l'erreur ne semble pas diminuer systématiquement à mesure que l'ordre réduit augmente. On peut également noter qu'il n'est pas possible d'obtenir une approximation parfaite des données lorsque l'ordre réduit est le même que l'ordre du modèle générant les données, en raison de la contrainte d'orthogonalité conservatrice. En comparaison, la méthode SIDPEV conduit à des erreurs d'approximation plus faibles à la fois avec les données d'essai et les données aéroélastiques, et bien qu'elle repose sur une optimisation non linéaire avec des contraintes qui nécessite de multiples exécutions avec différentes conditions initiales, son temps de calcul reste faible à des ordres inférieurs ou égaux à 40. De plus, avec une initialisation appropriée, elle semble toujours converger vers une solution satisfaisante. Enfin, la méthode DNOC repose sur une optimisation directe pour trouver les matrices de l'espace d'état du modèle d'ordre réduit avec des contraintes sur les pôles. En raison du nombre élevé de variables, cette méthode nécessite des temps de calcul importants, mais finit par converger vers des solutions avec une bonne précision d'approximation. On peut noter que lorsque la complexité du système augmente (ordre supérieur ou, dans le cas

des données aéroélastiques, gamme de fréquences plus large), le nombre d'itérations nécessaires pour converger augmente. Pour une utilisation pratique, lorsque des pôles doivent être imposés au modèle identifié, la méthode SIDPEV semble la plus appropriée.

Quelques remarques sur les limites de cette étude peuvent être formulées pour préparer les travaux futurs. Concernant le choix de travailler avec la réponse en fréquence de la fonction de transfert aéroélastique complète, il faut noter qu'une identification différente doit être effectuée pour chaque configuration de masse et aérodynamique (nombre de Mach, altitude), sans possibilité d'utiliser une structure commune. Une deuxième remarque concerne la complexité des algorithmes. Dans ce travail, seuls des modèles de taille limitée évalués sur des quantités de données relativement faibles ont été pris en compte, et des problèmes numériques tels que des limitations de mémoire pourraient survenir avec des systèmes plus importants. Enfin, bien que des efforts aient été faits pour améliorer la convergence de l'algorithme DNOC, différents schémas d'optimisation pourraient être étudiés afin de favoriser la convergence vers de meilleures solutions dans des délais plus courts.

En outre, les résultats obtenus avec la technique de décomposition pôle-résidu montrent que la précision de l'approximation est meilleure avec les méthodes de résidus qu'avec l'algorithme DNOC, pour des données allant jusqu'à 5 Hz, et similaire pour des données allant jusqu'à 10 Hz avec des ordres élevés. Le coût de calcul est bien inférieur à celui du DNOC, car la tâche la plus longue est l'identification d'un modèle d'ordre élevé par GAFs RFA, qui prend environ deux minutes, quel que soit l'ordre du modèle réduit final. L'identification de la partie différentielle $\boldsymbol{H}_{\boldsymbol{diff}}^{\boldsymbol{ROM}}$ prend quelques dixièmes de secondes au maximum, selon que les contraintes de stabilité sont incluses ou non (voir la Fig. 3.5 pour plus de détails). Lorsqu'une bonne précision est requise, avec des pôles imposés et d'éventuelles contraintes de stabilité, la méthode avec décomposition pôle-résidu décrite dans cette section est alors plus performante que les autres. Le fait que la précision soit plus faible aux ordres inférieurs peut s'expliquer par le nombre plus faible de degrés de liberté avec cette technique, par rapport aux autres. En effet, à 20-ième ordre par exemple, puisque 16 pôles sont déjà imposés, seul un modèle de 4-ième ordre peut être calculé pour s'ajuster aux données. Les résidus associés aux pôles imposés sont fixes pour la méthode des résidus, alors qu'ils sont libres avec les autres méthodes. Enfin, on peut noter que la présence de contraintes de stabilité a une faible influence sur la précision de l'approximation. En conclusion, la méthode d'identification basée sur la décomposition pôle-résidu est la plus précise et la plus rapide lorsqu'une grande précision est requise, mais elle nécessite l'identification préalable d'un modèle rationnel fiable et sa décomposition pôle-résidu, ce qui conduit à une procédure globale plus lourde.

F.5 Allègement de charges dues au vent

F.5.1 Introduction à l'allégement de charges dues au vent

L'allègement actif des charges dues au vent gagnera probablement en importance dans les futures générations d'aéronefs. L'autonomie du système de commande de vol électrique (EFCS) de l'aéronef, au détriment de la liberté de manœuvre du pilote en vol, permettra des lois de commande d'atténuation de la charge plus efficaces en réduisant le risque d'une intervention préjudiciable du pilote et en coordonnant les systèmes de commande de vol et d'atténuation des charges dues au vent. En outre, de nombreux nouveaux concepts d'aéronefs choisissent d'augmenter le rapport d'aspect de l'aile et de réduire son poids structurel afin d'améliorer l'efficacité énergétique de l'aéronef. Cela augmente la flexibilité de la cellule, ce qui conduit à des fréquences de modes aéroélastiques qui s'approchent des fréquences de la dynamique de vol, créant des interactions dynamique de vol-aéroélastique (voir [Chang, Hodges, and Patil 2008] et [Silvestre and Paglione 2008] par exemple). Le développement récent de capteurs lidar [Herbst and Vrancken 2016; Rabadan et al. 2010] capables de mesurer le vent vertical et latéral à plusieurs centaines de mètres en amont de l'avion ouvre de nouvelles perspectives pour l'atténuation des charges dues au vent, en anticipant la réponse de l'avion à la perturbation du vent entrant. Avec la disponibilité des capacités de calcul, cela motive le développement de techniques d'atténuation des charges dues au vent plus complexes, basées sur une automatisation complète de l'avion et tirant parti de sa dynamique aéroélastique complète. Alors que les lois actives d'atténuation des charges dues au vent mises en œuvre sur la génération actuelle d'aéronefs ne permettent de réduire les charges que de manière statique, des techniques de contrôle plus complexes pourraient atténuer la réponse dynamique complète de l'aéronef lorsqu'il est confronté à une rafale de vent ou à une turbulence, améliorant ainsi le confort des passagers et réduisant les charges dans une gamme de fréquences plus large.

La méthode la plus simple pour atténuer les charges dues au vent d'un aéronef flexible est le contrôle par rétroaction (feedback control), également largement utilisé dans les commandes de vol (flight control). Elle est basée sur les données de sortie mesurées de l'aéronef, généralement la vitesse de tangage, la vitesse de lacet et le facteur de charge verticale obtenus à partir de gyroscopes et d'accéléromètres. Le contrôle par rétroaction permet une conception directe des pôles de la boucle fermée, assurant la stabilité et la robustesse aux incertitudes du système, sans dépendre de la connaissance exacte du système de l'avion. Afin d'améliorer la réduction des charges, un contrôleur de type feedforward qui utilise directement la mesure de la perturbation du vent peut être utilisé en plus du contrôle par rétroaction [Alam, Hromcik, and Hanis 2015; Wildschek et al. 2010; Magar et al. 2017] ou il peut être utilisé seul [Zhao, Yue, and Hu 2016; Li, Wang, and Ronch 2016; Wildschek et al. 2006]. En théorie, il est possible d'obtenir un contrôleur feedforward parfait par inversion directe de la dynamique du système, mais cela est généralement impossible en raison des limitations de l'actionneur, et le contrôleur résultant serait très sensible aux incertitudes du système. [Caverly et al. 2017] a utilisé une telle technique en plus d'un contrôleur linéaire et d'un observateur de perturbations pour l'atténuation des charges

dues au vent d'un avion flexible. [Wang et al. 2019] a développé une méthode basée sur l'inversion de la dynamique avec l'estimation de l'état tout en assurant la robustesse aux incertitudes du système. Ces deux méthodes fonctionnent avec un modèle non linéaire de l'avion. Une alternative prometteuse est l'utilisation de la commande adaptative, dans laquelle la dynamique du système est constamment estimée et la commande est adaptée en conséquence. Elle s'appuie généralement sur un modèle de réponse impulsionnelle finie (FIR) du contrôleur [Zeng et al. 2010; Wildschek et al. 2006; Wildschek et al. 2007; Zhao, Yue, and Hu 2016; Li, Wang, and Ronch 2016; Wang, Li, and Ronch 2015].

Les développements des dernières décennies, tels que le programme AWIATOR d'Airbus [Schmitt et al. 2007] ou le programme DELICAT du DLR [Vrancken et al. 2016], grâce auxquels les capteurs lidar aéroportés émettent un laser et mesurent la lumière diffusée par les molécules d'air, ouvrent de nouvelles perspectives en matière d'atténuation de la charge dues au vent, non seulement en diminuant les effets du vent, mais aussi en les prévenant. Alors que des structures de contrôle simples sont couramment utilisées pour le contrôle par rétroaction, il n'est pas simple de trouver une structure de contrôle qui prenne en compte les prévisions de vent. Les méthodes de contrôle prédictif de modèle (MPC) qui effectuent une optimisation en ligne peuvent être utilisées, elles ont été appliquées à l'atténuation des charges dues au vent [Haghighat, Liu, and Martins 2012; Giesseler et al. 2012] et à l'allègement de la charge des manœuvres [Freitas Virgilio Pereira et al. 2019; Gaulocher, Roos, and Cumer 2007]. Des stratégies plus complexes basées sur la décomposition en ondelettes du signal lidar ont été utilisées afin d'affecter le signal aux différents actionneurs en fonction de la fréquence et de l'amplitude de la rafale [Fezans and Joos 2017; Fezans, Schwithal, and Fischenberg 2017]. En l'absence de mesure lidar, les états futurs du système ne peuvent pas être prédits, et [Vuillemin, Martin, and Poussot-Vassal 2021] ont développé une technique MPC dans laquelle les valeurs de contrôle optimales sont calculées en supposant que la vitesse future du vent appartient à un ensemble discret. L'optimisation vise à minimiser le pire des cas parmi ces profils de vent possibles, qui peuvent être considérés comme différentes rafales de $1 - \cos$ par exemple, offrant ainsi une certaine robustesse par rapport à la vitesse du vent. Les techniques MPC peuvent être très efficaces grâce à l'optimisation en ligne, qui calcule les valeurs idéales des variables contrôlées en fonction d'un modèle et d'un critère à minimiser sur un horizon temporel futur. Cependant, elles présentent deux inconvénients majeurs. Le premier est qu'elles nécessitent que l'ordinateur de bord de l'avion effectue des calculs lourds, ce qui n'est pas conforme à l'évolution technologique et aux réglementations actuelles. Le second inconvénient est l'absence de robustesse dans la formulation MPC classique. Certaines techniques ont été développées pour assurer la robustesse dans le cadre du MPC, et [Morari and Lee 1999] passe en revue certaines d'entre elles. En utilisant un modèle polytopique, on peut effectuer une optimisation en ligne basée sur des inégalités matricielles linéaires (LMI) pour calculer la valeur des variables de contrôle, comme dans [Kothare, Balakrishnan, and Morari 1996] ou [Zhang, Wang, and Wang 2014]. L'une des limites de ces techniques est l'importance des calculs nécessaires pour résoudre les LMI basées sur des modèles multiples. En outre, elles conduisent à des signaux contrôlés qui sont proportionnels aux états à un moment donné, perdant ainsi l'aspect non linéaire de la méthode MPC classique.

Les synthèses H_∞ et μ [Doyle, A, and Tannenbaum 2009; Skogestad 1996; Vidyasagar and Kimura 1986] fournissent un cadre dans lequel on peut effectuer une optimisation multi-objectifs basée sur les mesures de plusieurs capteurs, y compris le lidar, tout en assurant la conformité avec les contraintes de robustesse et les limites du système. Contrairement à la MPC, la stabilité et la robustesse de la boucle fermée peuvent être imposées avec ces méthodes, et le coût de calcul en ligne est beaucoup plus faible parce que les contrôleurs sont obtenus hors ligne. Déjà utilisée pour la GLA robuste avec des capteurs classiques [Zeng, Kukreja, and Moulin 2012; Cook, Palacios, and Goulart 2013; Ferrier et al. 2018], l'application de H_∞ à la GLA basée sur un lidar a été proposée dans [Khalil and Fezans 2019] où la réduction des charges supplémentaires obtenue avec un lidar sans bruit a été évaluée sur un modèle d'aéronef simple comprenant deux modes élastiques, sans contraintes de robustesse.

F.5.2 Présentation de l'étude GLA

L'objectif principal de la GLA active, comme son nom l'indique, est de réduire les charges dues au vent à l'aide des mesures des capteurs disponibles en utilisant les surfaces de contrôle de l'avion. Cet objectif peut être décomposé en différents sous-objectifs : le premier est la réduction de la valeur absolue maximale des charges structurelles (force de cisaillement, moment de flexion, moment de torsion) à différents endroits de la structure de l'avion (ailes, fuselage, HTP et VTP) dans les scénarios les plus défavorables. Les lois GLA mises en œuvre sur les générations actuelles d'aéronefs se concentrent sur cet objectif, en réduisant la valeur positive maximale du moment de flexion. Un deuxième sous-objectif consiste à atténuer la réponse dynamique de l'avion à différentes fréquences, en réduisant les vibrations structurelles, en stabilisant l'avion et en améliorant le confort des passagers. La capacité du pilote à lire correctement les données de vol et à commander l'avion est également affectée par les vibrations du cockpit, et le remplacement des commandes analogiques traditionnelles par des écrans tactiles numériques dans les futures générations d'avions amplifie la nécessité d'atténuer les effets à haute fréquence des turbulences. Le facteur de charge dynamique (accélération) joue un rôle important dans le confort et le mal des transports, et est fortement corrélé aux charges (ex : facteur de charge verticale et moment de flexion de l'aile). Ces objectifs se résument donc grosso modo à réduire la DSP des charges et des facteurs de charge en réponse à des vents extrêmes, dans les conditions de vol les plus défavorables. Une diminution du pic le plus élevé des PSD conduit à une diminution des charges maximales, et l'atténuation des pics à haute fréquence supprime les vibrations structurelles. Les principales contraintes pour atteindre ces objectifs sont les limites des surfaces de contrôle et des capteurs. Les modèles mathématiques utilisés pour définir ces limitations sont simples et décrits dans les différentes applications étudiées dans ce travail.

Sur la base des techniques de conception de contrôle utilisées dans la littérature pour la GLA active avec ou sans lidar, la principale direction retenue est le contrôle robuste. Le cadre de H_∞ présente plusieurs avantages, tels que la robustesse en boucle fermée, la possibilité d'obtenir des contrôleurs simples, la facilité d'implémentation du lidar dans ce cadre, et la flexibilité dans la

définition des objectifs de contrôle. Le MPC est également étudié en raison des performances optimales qu'il peut théoriquement fournir.

F.6 GLA robuste avec μ-synthèse

F.6.1 H_∞ et μ-synthèses pour l'avion flexible équipé de lidar

Les synthèses H_∞ et μ sont appliquées à l'avion flexible équipé d'un lidar. En réduisant la norme H_∞ du système complet, l'influence de chaque entrée exogène sur la sortie exogène est réduite. L'installation augmentée $\boldsymbol{P}$ représentée sur la Fig. 4.7 se compose de

- le modèle aéroélastique de l'avion G
- la dynamique des actionneurs et des capteurs
- le capteur lidar noté comme retard pur $z^i_{i=[0:N]}$.
- les entrées exogènes $\boldsymbol{w}$ et les sorties $\boldsymbol{z}$ et leurs filtres accordables associés.

Les incertitudes sont écrites sous une forme générale, elles peuvent être de différents types. Le modèle d'aéronef G est normalisé en entrée et en sortie. Outre l'amélioration de la convergence numérique des algorithmes, cela permet de comparer les valeurs relatives des entrées de la sortie de performance $\boldsymbol{z_y}$. Les détails des différents composants de l'installation augmentée sont présentés à la figure 4.7. Les filtres et les entrées et sorties exogènes sont choisis de manière à définir le problème GLA en termes de critère de performance et de contraintes associées.

F.6.1.1 Robustesse avec H_∞ et μ-synthèses

La boucle fermée doit être robuste en termes de stabilité et de performance. Le premier type de robustesse est la capacité de la boucle fermée à rester stable lorsque le système contrôlé change, tandis que le second concerne la garantie de maintenir les performances en cas de variations du système, en maintenant la norme H_∞ inférieure à un. Assurer la robustesse d'un contrôleur à espace d'état avec plusieurs entrées et sorties est plus difficile qu'avec les contrôleurs classiques composés de gains et de filtres tels qu'utilisés en aéronautique. Le contrôleur doit être robuste aux incertitudes MIMO, qui s'appliquent simultanément aux différentes entrées et sorties. La robustesse de la stabilité MIMO peut être imposée par la synthèse H_∞, par exemple en réduisant la norme maximale H_∞ des fonctions de transfert de sensibilité d'entrée et de sortie, en agissant sur les marges de module. Une autre stratégie, adoptée dans cette section, consiste à ajouter des incertitudes dans le système augmentée et à imposer une robustesse en boucle fermée à ces incertitudes par μ-synthèse, à la fois en termes de stabilité et de performance. En l'absence d'une

définition claire des incertitudes du système, on peut définir des incertitudes générales de disque qui peuvent conduire à des généralisations MIMO des marges de gain et de phase.

En pratique, des fonctions de transfert incertaines sont introduites à l'entrée des actionneurs et à la sortie des capteurs. Chacune d'entre elles est composée de collections diagonales d'incertitudes de disque SISO indépendantes. Chaque incertitude de disque est un nombre complexe inconnu dont la valeur nominale est égale à 1, à partir duquel le gain et la phase peuvent varier. Ce cadre peut être utilisé de différentes manières pour la synthèse et l'analyse. Dans le cas le plus contraignant, des incertitudes de disque indépendantes sont appliquées simultanément à chacun des ports d'entrée et de sortie du modèle aéroélastique, avec différentes combinaisons de gain et de phase (le nombre complexe évolue dans un disque). C'est le cas utilisé pour la synthèse, ce qui signifie que la stabilité en boucle fermée doit être imposée et que le critère H_∞ doit être minimisé dans le pire des cas d'incertitudes simultanées sur disque à l'entrée et à la sortie. Un type d'incertitudes plus faible est associé au cas où seules des variations de gain ou de phase sont appliquées à chaque incertitude de disque, simultanément à chaque port d'entrée et de sortie. Elles conduisent à la définition de ce que l'on appelle la marge de disque de gain MIMO, définie par le gain minimum conduisant à l'instabilité lorsque l'on considère des combinaisons de variations de gain indépendantes dans les différents ports d'entrée et de sortie. De même, les marges de disque de phase MIMO sont définies. Les marges de disque de gain et de phase multi-entrées et multi-sorties sont définies de manière similaire, en considérant uniquement les variations dans les ports d'entrée ou dans les ports de sortie, et sont alors plus faibles que leurs homologues MIMO. Enfin, les marges de disque SISO sont les marges de gain et de phase classiques, qui prennent en compte les variations d'un seul port d'entrée ou de sortie du système.

F.6.1.2 Conclusions de l'étude GLA robuste utilisant μ-synthèse

Une première étude GLA a été menée en utilisant la μ-synthèse. L'accent a été mis sur la conception d'un contrôle robuste, basé sur la μ-synthèse, et sur la possibilité d'alléger plusieurs charges simultanément. Certaines tendances ont été mises en évidence et des conclusions peuvent être tirées de cette étude. Lorsque l'on essaie de réduire simultanément la force de cisaillement, les moments de flexion et de torsion à l'emplanture de l'aile et sur la PTH, il faut faire des compromis. La réduction simultanée des moments de flexion et de torsion n'est généralement pas possible, car l'action des ailerons a des effets opposés sur ces moments. Pour réduire le moment de flexion, il faut augmenter le moment de torsion. De même, il est possible d'atténuer la flexion et le cisaillement de la HTP, mais cela entraîne des réductions moindres du facteur de charge verticale et du moment de flexion de l'aile. La stratégie générale des contrôleurs étudiés avec lidar peut être mise en évidence : avant qu'une rafale discrète positive n'atteigne l'avion, les ailerons sont déviés vers le bas pour créer un moment de tangage et placer l'avion dans la direction du vent afin de réduire cet effet. Les gouvernes de profondeur sont utilisées pour augmenter cet effet, en particulier lorsque les charges HTP ne sont pas incluses dans les objectifs de synthèse. Si c'est le cas, les déflexions des gouvernes de profondeur sont plus faibles, afin d'éviter de créer des charges

sur la HTP. Lorsque la rafale positive atteint l'avion, les ailerons sont braqués dans l'autre sens (vers le haut) pour créer une portance négative directe sur l'aile, opposée à la force créée par le vent. Cette tendance est particulièrement visible avec une longue rafale discrète. Pour les rafales de moindre longueur, les actionneurs ont moins de temps pour agir sur la dynamique de l'avion, et les effets du système GLA sont moindres. Dans la réponse à la turbulence continue avec une échelle de 762 m, cette tendance n'est pas visible en raison de la nature chaotique de la turbulence, mais les allégements sont similaires à ceux obtenus avec la rafale la plus longue (107 m). Les contrôleurs ont été conçus pour démontrer l'atténuation potentielle de la flexion obtenue avec le GLA à l'aide d'un lidar. Des réductions importantes de l'ordre de 50 % sont obtenues pour la rafale la plus longue, et 33 % avec une rafale de 70 m. Cependant, cela peut conduire à des augmentations significatives du moment de torsion (jusqu'à 80 %). Les charges HTP peuvent être réduites de 50 % tant qu'elles sont incluses dans les objectifs de contrôle, sinon elles peuvent être augmentées de 60 %. Un effort de contrôle plus faible peut être utilisé pour la conception future du contrôleur afin de réduire les effets négatifs de la GLA. En l'absence de lidar, des effets beaucoup plus faibles sur la charge ont été observés (de l'ordre de 10 %). Cela pourrait être dû à la grande robustesse requise dans cette analyse. En effet, la synthèse μ impose à la fois la robustesse des performances et de la stabilité, et peut donc conduire à une conception conservatrice. Si la grande robustesse des contrôleurs avec lidar conduit à une faible utilisation des capteurs présents dans la boucle de contrôle (accéléromètres, gyroscopes et sonde d'incidence), elle n'affecte pas la partie feedforward du contrôleur associé au lidar. Lorsqu'il n'y a pas de lidar, il n'y a pas de contrôleur en amont et les performances sont réduites en raison de la grande robustesse. Une autre conclusion concerne le type de vent conduisant aux charges les plus élevées : alors que la rafale discrète la plus longue est la plus sévère en termes de moment de flexion maximal en boucle ouverte, ce n'est pas le cas lorsque le contrôleur GLA est présent. En effet, les rafales intermédiaires sont plus difficiles à atténuer en raison de la dynamique de fréquence plus élevée qu'elles impliquent, ce qui entraîne des charges en boucle fermée. Enfin, les contrôleurs de second ordre obtenus avec la μ-synthèse structurée se sont avérés presque aussi efficaces que les contrôleurs de plein ordre.

Certaines études de sensibilité ont été menées, montrant l'effet de la limitation du taux sur la capacité de réduction des charges du système GLA. Elles montrent que les contraintes des actionneurs doivent être prises en compte lors de la conception d'un contrôleur. Le cas de vent le plus défavorable doit être considéré en boucle fermée : alors que les rafales de 107 m et de 70 m conduisent à un moment de flexion similaire en boucle ouverte, ce dernier est moins atténué par le contrôleur et la priorité doit lui être donnée. Un léger dépassement de la limite de vitesse pour la rafale de 107 m peut alors être considéré comme acceptable, car il n'affecte pas le cas de vent le plus défavorable. Une autre étude de sensibilité met en évidence une distance de mesure optimale du lidar d'environ 100 m. Au-delà de cette distance, la capacité d'allègement de la charge ne s'améliore pas, et peut même diminuer si elle conduit à une réduction de la qualité de la mesure. Enfin, l'influence du bruit et du biais du lidar montre une sensibilité relativement faible de la boucle fermée aux imprécisions de la mesure lidar. Ce fait est probablement dû à l'existence de plusieurs mesures intermédiaires, qui confèrent une grande robustesse au système. D'autres études sont cependant nécessaires pour étudier ces effets, en utilisant des modèles de lidar plus raffinés

(prenant en compte la physique optique) et des essais en vol.

F.6.2 Synthèse multimodèle H_2/H_∞ pour l'avion flexible équipé d'un lidar

Le système augmenté $\boldsymbol{P}$ utilisée dans ce travail est décrite dans la figure 4.20. La plupart des blocs sont identiques à ceux du cadre de synthèse μ décrit dans la section 4.5.1. Divers modèles aéroélastiques $\boldsymbol{G^l}$ sont définis dans cette section, correspondant à différentes configurations de masse et valeurs du nombre de Mach. Les modèles sont indexés par l'exposant ^{l}, qui va de 1 à N_l dans les applications numériques. De même, un modèle de turbulence H_v^l est utilisé pour chaque modèle aéroélastique, car la variation de la vitesse et de l'altitude affecte l'amplitude et la DSP du vent. Il s'ensuit que le système $\boldsymbol{P^l}$ définissant le problème H_2/H_∞ est composée de différents modèles. La synthèse du contrôleur utilisée dans ce travail est définie par le problème d'optimisation suivant :

$$\min_K \max_{l=1\dots N_l} \left\| T^l_{\boldsymbol{w_2}\mapsto\boldsymbol{z_2}}(K) \right\|_2 \tag{F.7}$$

$$\text{subject to} \tag{F.8}$$

$$\left\| T^l_{\boldsymbol{w_\infty}\mapsto\boldsymbol{z_\infty}}(K) \right\|_\infty \leq 1 \quad \forall l = 1\dots N_l \tag{F.9}$$

Les fonctions de transfert dont la norme H_2 doit être minimisée sont les fonctions de transfert des perturbations et du bruit de mesure vers la sortie des charges, qui sont $T_{\boldsymbol{w_v}\mapsto\boldsymbol{z_y}}$, $T_{\boldsymbol{w^i_{nv}}\mapsto\boldsymbol{z_y}}$ et $T_{\boldsymbol{w_{ny}}\mapsto\boldsymbol{z_y}}$. Le filtre $\boldsymbol{H_{zy}}$ est utilisé pour ajuster le critère de performance H_2. Il comprend un filtre passe-haut, ce qui conduit la synthèse à ne pas prendre en compte la réponse à basse fréquence de l'avion, qui peut être traitée séparément. En outre, $\boldsymbol{H_{zy}}$ amplifie la réponse n_z entre 2 Hz et 7 Hz, de sorte que les contrôleurs atténuent davantage l'accélération à haute fréquence de l'avion, qui peut provoquer le mal des transports chez les passagers. La contrainte normative H_∞ impose l'angle et le taux de déviation maximum des surfaces de contrôle pour rester dans les limites acceptables des actionneurs et est définie avec la fonction de transfert $T_{\boldsymbol{w_v}\mapsto\boldsymbol{z_u}}$. Le critère H_2 est plus efficace pour obtenir des performances optimales, car il fonctionne sur toute la gamme de fréquences, alors que le critère H_∞ se concentre sur la seule fréquence à laquelle le gain de la fonction de transfert est maximal. Un exemple extrême est le cas où il existe un pic de haute fréquence dans la réponse du système, que le contrôleur ne peut pas atténuer en raison de ses limitations. Dans ce cas, la norme H_∞ de la boucle fermée sera calculée sur ce pic, et la réponse aux autres fréquences sera ignorée, ce qui conduira à un contrôleur inefficace. Un réglage des filtres de forme serait nécessaire pour ignorer le pic dans la synthèse, ce qui augmenterait l'ordre du système et nécessiterait un réglage fin de chaque modèle indépendamment. Le critère H_2 est calculé sur l'ensemble de la gamme de fréquences, et pas seulement sur la réponse maximale, et ne nécessite donc pas de réglage supplémentaire. Cependant, la norme H_∞ fournit des garanties solides telles que la stabilité, la robustesse et la satisfaction des limites du système. La synthèse mixte H_2/H_∞ fournit donc une bonne performance tout en assurant des garanties dans les scénarios les plus

défavorables lorsque cela est nécessaire.

Le contrôleur $\boldsymbol{K}$ de l'équation (4.17) a une structure fixe, composée de deux modèles d'espace d'état : un pour la partie de réaction qui prend la mesure lidar comme entrée, et un pour la partie de rétroaction qui prend le taux de tangage, le facteur de charge verticale et l'angle d'attaque comme entrée. Afin de réduire la sensibilité du contrôleur au bruit du lidar ou à une défaillance, il est possible d'augmenter le gain du filtre $\boldsymbol{H_{nv}^{i}}$ de la figure 4.20. Cependant, nous trouvons plus efficace et plus simple d'effectuer deux synthèses : une première synthèse calcule le contrôleur de rétroaction sans la partie de rétroaction, puis cette dernière est obtenue à partir d'une synthèse basée sur la boucle fermée obtenue. Le problème structuré H_2/H_∞ avec plusieurs modèles décrit ci-dessus peut être directement implémenté dans la fonction *systune* de Matlab, sur la base des travaux décrits dans [Apkarian, Dao, and Noll 2015].

F.6.3 Conclusions générales sur l'allègement des charges dues au vent

Les tendances générales relatives à la capacité d'atténuer simultanément différentes charges sur l'aile et la HTP ont été mises en évidence, et des analyses de sensibilité ont été réalisées sur la base de simulations effectuées à l'aide d'un modèle aéroélastique unique. Trois questions principales ont naturellement émergé de cette étude : 1) Est-il possible d'améliorer les performances d'allègement des charges en utilisant une stratégie de contrôle plus agressive, mais suffisamment robuste pour fonctionner efficacement sur toute la gamme des conditions de vol et de masse ? 2) Quelles sont les capacités réelles d'allègement des charges des contrôleurs robustes, en termes de charges de vent dans le pire des cas (et pas seulement dans un seul cas) ? 3) Comment les différentes méthodes robustes se comparent-elles entre elles et avec d'autres techniques de contrôle courantes ?

Afin de répondre à ces questions, une méthode de synthèse basée sur différents modèles a été utilisée, afin de mieux définir l'incertitude physique et de réduire le conservatisme dans la conception. L'utilisation du critère H_2 pour l'objectif d'allègement des charges est un outil pratique lorsqu'une synthèse structurée est envisagée, car il nécessite moins de réglages qu'avec les critères H_∞. Ces derniers sont utilisés pour les actionneurs et les contraintes de robustesse. Les contrôleurs obtenus par la synthèse multi-modèle H_2/H_∞ diffèrent radicalement par leur utilisation des ascenseurs, améliorant de manière significative l'efficacité de la partie feedback par rapport au contrôle feedforward qui utilise le lidar comme entrée. Le premier effet notable est un meilleur contrôle du facteur de charge verticale, qui est plus atténué qu'avec les contrôleurs plus robustes obtenus par μ-synthèse. Le deuxième effet est une réduction plus importante du moment de flexion et de la force de cisaillement dans le cas le plus défavorable, sans augmentation du moment de torsion. Cet effet est particulièrement impressionnant lorsque le lidar n'est pas utilisé, où la capacité globale d'allègement des charges est comparable à celle utilisée avec un lidar. Quantitativement, le moment de flexion à l'emplanture de l'aile, la force de cisaillement et le facteur de charge verticale les plus défavorables peuvent être atténués d'environ 50 % avec un lidar. Sans lidar, cette atténuation descend approximativement à 40 % avec la synthèse multi-modèle H_2/H_∞.

Ces résultats correspondent au cas où 8 petits ailerons sont utilisés sur chaque aile. Avec seulement 4 d'ailerons, la réduction du moment de flexion est beaucoup plus faible (15) et avec 16 d'ailerons, elle passe à 60 (mais avec une augmentation de 110 du moment de torsion). Ces niveaux de réduction des charges sont de l'ordre de grandeur de l'atténuation maximale qui peut avoir un effet sur la conception de l'avion. En outre, si l'on considère les critères de confort, les contrôleurs obtenus par synthèse multimodèle H_2/H_∞ améliorent toujours l'accélération équivalente maximale dans le pire des cas d'environ 60 %, à chaque position du fuselage. Ces contrôleurs ont été obtenus avec des contraintes sur les actionneurs (les angles de déviation ne sont jamais supérieurs à 15° et une limitation de vitesse de 40°/s est appliquée). Cependant, la stratégie de contrôle plus agressive a un coût : tout d'abord, l'utilisation des gouvernes de profondeur entraîne une réponse transitoire importante de la vitesse de tangage avant de converger, avec des oscillations et une augmentation du maximum par rapport au cas de la boucle ouverte. En outre, l'accélération à haute fréquence (entre 2 Hz et 5 Hz) est généralement plus élevée qu'avec les contrôleurs robustes obtenus par μ-synthèse, en particulier lorsqu'aucun lidar n'est utilisé. Cela conduit à un mal des transports plus important pour les passagers, comme cela a été étudié avec un critère spécifique. Les enveloppes de charges HTP n'ont pas été montrées par souci de concision, mais les techniques multi-modèles H_2/H_∞ conduisent à une forte augmentation du moment de flexion dans le cas le plus défavorable (presque doublé). Enfin, les contrôleurs obtenus par synthèse multimodèle H_2/H_∞ ont des marges de stabilité et de robustesse plus faibles. Avec ces observations, l'intérêt d'utiliser un lidar pour la GLA est remis en question, dépendant fortement des contraintes sur le mouvement de tangage qu'un constructeur d'avion veut imposer (en raison de l'interaction avec la loi de contrôle et les qualités de maniabilité), et des critères sur les charges HTP. Des contraintes élevées limiteraient l'utilisation des gouvernes de profondeur, réduisant fortement l'effet du régulateur à rétroaction, et l'allégement des charges élevées ne peut être obtenu que si un lidar est inclus. Si des concessions sont faites de ce côté et que la priorité est donnée à la réduction du moment de flexion, le lidar perd de son importance et des performances significatives peuvent être obtenues avec des capteurs classiques.

Comparés à d'autres techniques de contrôle, les contrôleurs robustes conduisent à une performance d'allègement des charges similaire ou meilleure que la GLA basée sur MPC, qui souffre d'autres problèmes (robustesse, implémentabilité, effets non linéaires indésirables, ...), et meilleure qu'une technique GLA classique par déflexion statique des ailerons, qui conduit à une diminution plus faible du moment de flexion positif maximum, sans effet sur le facteur de charge vertical, et à une augmentation importante du moment de torsion. La synthèse de contrôle robuste apparaît alors comme un candidat sérieux pour les futures mises en œuvre de la GLA, conduisant à une forte réduction des charges les plus défavorables tout en garantissant la stabilité et la robustesse. De nombreux compromis ont été mis en évidence, avec de nombreuses conceptions possibles en fonction de la priorité accordée aux différentes charges de l'aile et de la HTP et aux effets sur le mouvement de tangage, par exemple.

F.7 Suppression active du flottement

F.7.1 Introduction à la suppression active du flottement

L'interaction entre l'aérodynamique et la dynamique structurelle peut entraîner une instabilité appelée flottement. Lorsqu'un fluide s'écoule le long d'une surface, il applique des forces aérodynamiques locales qui entraînent de petites déformations de la structure. Cela affecte à son tour le mouvement du fluide en créant un changement de direction appelé "downwash". La dynamique des fluides a donc un effet de rétroaction sur elle-même, ce qui donne lieu à ce que l'on appelle le système aéroélastique, qui tient compte de cette interaction. Certains phénomènes qui se produisent sur les avions ne peuvent être prédits que par l'analyse aéroélastique, tels que le buffeting non linéaire et les oscillations de cycle limite (LCO) [Bisplinghoff, Ashley, and Halfman 1955b]. L'instabilité du flottement se produit lorsque l'augmentation de la vitesse de l'avion finit par rendre instables certains modes aéroélastiques, et peut être décrite par des modèles linéaires.

La principale difficulté dans la synthèse AFS est de définir des stratégies de contrôle qui stabilisent le système aéroélastique sur une gamme de vitesses de l'avion, qui affectent la dynamique de manière non linéaire. La robustesse et l'adaptabilité sont donc des concepts clés de l'AFS et peuvent être obtenus de différentes manières. Une première solution consiste à obtenir un contrôleur unique à une vitesse donnée avec une robustesse qui garantit la stabilité à d'autres points de vol (y compris la vitesse, le nombre de Mach) et les configurations de masse. Historiquement, cette approche robuste a d'abord été employée à l'aide de contrôleurs structurés simples, en utilisant un retour d'information provenant d'un certain ensemble de capteurs pour actionner les surfaces de contrôle disponibles. Dans [Waszak and Srinathkumar 1991; Waszak and Buttrill 1991], un retour d'information provenant d'un seul accéléromètre situé sur l'extrémité de l'aile a été utilisé comme entrée d'un filtre du troisième ordre pour contrôler deux paires symétriques d'ailerons. Le filtre est conçu en plaçant des pôles en boucle fermée, dans le but de stabiliser autant que possible les modes de flottement. Plus récemment, [Schmidt 2016a; Schmidt 2016b] ont utilisé une méthode similaire en utilisant deux boucles de rétroaction distinctes : l'une utilisant l'accéléromètre de bout d'aile et l'autre utilisant le taux de tangage comme entrée, pour contrôler les ailerons. Dans le cas où plusieurs capteurs sont utilisés, la méthode de placement des pôles devient fastidieuse et une synthèse basée sur l'optimisation peut être utilisée, comme [Ricci et al. 2021] dans laquelle un contrôleur de rétroaction à sortie unique (SOF) est conçu. Une autre technique populaire pour utiliser les informations provenant de différents capteurs est l'approche linéaire quadratique gaussienne (LQG), dans laquelle un contrôleur stabilisateur qui minimise une certaine fonction de coût quadratique est obtenu par des équations algébriques de Riccati. Un tel contrôleur utilise les états du système comme entrée et nécessite un observateur supplémentaire pour estimer les états à partir des mesures disponibles. Cette approche a été mise en œuvre dans [Tewari 1998; Tewari 1999], où la variable à minimiser est la dérivée de l'accélération normale. Plus récemment, la méthode LQG a été mise en œuvre dans [Waite et al. 2019] à l'aide d'un modèle aéroélastique d'ordre réduit obtenu à partir de calculs de dynamique des fluides numériques (CFD) instation-

naires précis. Dans [Berg et al. 2021] des contrôleurs LQG ont également été utilisés, avec une attention particulière sur la robustesse MIMO du système, évaluée avec des outils modernes tels que les incertitudes de disque. Enfin, la synthèse H_∞ est une méthode efficace pour obtenir des contrôleurs stabilisateurs robustes, car elle permet de minimiser la norme H_∞ qui conduit plus naturellement à la robustesse que les critères quadratiques. De plus, elle conduit à des contrôleurs dynamiques qui peuvent avoir plus de degrés de liberté que les gains statiques par exemple. Cette méthode a été appliquée dans [Theis, Pfifer, and Seiler 2016; Theis, Pfifer, and Seiler 2020] en choisissant soigneusement la vitesse à laquelle le contrôleur est conçu, de manière à maximiser la vitesse de flottement. En effet, la conception d'une loi AFS à une vitesse trop élevée peut conduire à une faible robustesse, et le contrôleur obtenu peut même déstabiliser le système à une vitesse à laquelle il était naturellement stable. Dans [Faïsse et al. 2021], une synthèse AFS H_∞ est intégrée dans une optimisation en boucle externe de la structure de l'avion. L'utilisation de la synthèse μ est une autre façon d'assurer la robustesse dans la conception du contrôleur, et permet d'étudier l'effet des incertitudes paramétriques et dynamiques sur les fonctions de transfert aéroélastiques et les trajectoires des pôles lorsque la vitesse varie, comme cela est fait dans [Patartics et al. 2022].

Contrairement à l'approche robuste, la deuxième stratégie principale pour stabiliser un système aéroélastique sur une gamme de vitesses est la conception de lois adaptatives. Dans ce cas, la dynamique du contrôleur peut varier au fur et à mesure que l'avion s'approche du flottement, avec ou sans utilisation de la vitesse comme donnée d'entrée. La méthode la plus utilisée consiste à concevoir des lois de contrôle à différentes valeurs de vitesse et à les interpoler pour obtenir une loi de contrôle sous la forme d'une fonction affine par morceaux de la vitesse. Cette stratégie a été employée dans [Marchetti et al. 2020; Ricci et al. 2022] par exemple, ou dans [Waitman and Marcos 2020] où des contrôleurs H_∞ calculés à trois vitesses différentes sont obtenus et interpolés. Cela est possible grâce à une réduction équilibrée adéquate des espaces d'état des contrôleurs. Dans ce cas, la norme H_∞ de la fonction de transfert des angles des ailerons au déplacement modal est le critère à minimiser. D'autres approches adaptatives consistent à calculer directement un contrôleur LPV à partir du modèle, qui doit généralement être LPV. Dans [Chen et al. 2011; Chen, Sun, and Li 2012], une formulation paramétrique de régulateur quadratique linéaire (LQR) est proposée et appliquée à un modèle aéroélastique dépendant de la vitesse, obtenu par interpolation de modèles d'ordre réduit calculés à l'aide de la méthode de décomposition orthogonale appropriée (POD) d'ordre réduit. Dans [Barker, Balas, and Blue 1999; Barker and Balas 2000], une formulation de transformation fractionnaire linéaire (LFT) est proposée, prenant la vitesse comme paramètre incertain, et permettant au contrôleur d'avoir une dépendance rationnelle sur elle. Une formulation H_∞ est proposée dans [Moulin 2004] où un contrôleur LPV avec une dépendance polynomiale sur la vitesse et la densité de l'air est obtenu, en supposant que le modèle suit la même dépendance. Une autre formulation utilisant l'optimisation convexe et LMI est proposée dans [Alhajjar et al. 2018].

Les méthodes adaptatives sont attrayantes car elles permettent des ajustements en temps réel au changement de la dynamique aéroélastique. Cependant, leur mise en œuvre pratique n'est pas toujours simple. Le coût de calcul pour la conception du contrôleur peut devenir prohibitif

lorsque la complexité du système augmente, et certaines hypothèses sur le modèle utilisé pour la synthèse peuvent être irréalistes. Parmi les systèmes les plus avancés sur le plan technologique pour tester expérimentalement les techniques AFS, on peut citer le projet F-XDIA développé par le Politecnico di Milano et l'Université de Washington qui a réalisé des essais en soufflerie avec un modèle complet d'avion [Marchetti et al. 2020; Ricci et al. 2021; Berg et al. 2021; Ricci et al. 2022], ou le projet européen FlexOp qui a récemment réalisé des essais en vol avec un démonstrateur [Takarics et al. 2020]. Une étude a été menée chez Airbus à [Fischer, Schröder, and Thormann 2022] avec un modèle proche de celui utilisé dans le présent travail, en se concentrant sur la mise en œuvre pratique d'un point de vue industriel.

Une nouvelle stratégie est développée dans le but d'obtenir des lois simples, qui peuvent être conçues et validées avec des modèles aéroélastiques industriels comprenant un grand nombre de modes, et qui s'adaptent en douceur à la vitesse de l'avion. Pour ce faire, on développe d'abord des méthodes d'identification de systèmes hybrides dans lesquelles un certain nombre de pôles aéroélastiques (stables ou instables) sont calculés et imposés au modèle grâce à une décomposition adéquate des résidus de pôles et à l'utilisation de la méthode de Loewner [Mayo and Antoulas 2007; Karachalios, Gosea, and Antoulas 2019]. Une synthèse H_∞ est ensuite réalisée sur la base de plusieurs modèles de différentes valeurs de vitesse (inférieures et supérieures à la vitesse de flottement) de manière à imposer la stabilité à haute vitesse sans rendre instables les systèmes à faible vitesse. Cette méthode permet d'obtenir un ensemble de contrôleurs LPV, qui sont ensuite validés par des modèles fiables d'ordre élevé calculés sur une large gamme de valeurs de vitesse. Une procédure systématique est mise au point pour sélectionner un nombre réduit d'actionneurs et de capteurs sur la base de critères quantitatifs. Elle s'appuie sur un algorithme génétique qui estime la configuration conduisant aux meilleures marges de module possibles réalisables par des contrôleurs d'ordre complet.

F.7.2 Objectifs de l'AFS et méthodologie employée

L'objectif principal du contrôleur AFS est d'améliorer autant que possible la vitesse de flottement en stabilisant le système aéroélastique lorsque certains pôles deviennent instables. En outre, la robustesse de la stabilité de la boucle fermée stabilisée doit être maximisée et l'effort de contrôle nécessaire pour y parvenir doit être minimisé. En outre, le nombre de capteurs et d'actionneurs effectivement utilisés doit être aussi faible que possible, afin de réduire le coût du système AFS en vue de sa mise en œuvre pratique. Enfin, un schéma souple pour l'activation de l'AFS est souhaité, ce qui signifie que l'action du contrôleur doit commencer à une vitesse donnée avant l'apparition du flottement et doit augmenter progressivement au fur et à mesure que le système aéroélastique en boucle ouverte devient de plus en plus instable.

Pour atteindre ces objectifs, un contrôleur LPV paramétré par la vitesse air vraie (TAS) de la

forme suivante est progressivement développé :

$$\mathbf{K} : \begin{cases} \dot{\boldsymbol{x}}_{\boldsymbol{K}}(t) & = \boldsymbol{A}_{\boldsymbol{K}}(\mathrm{TAS})\boldsymbol{x}_{\boldsymbol{K}}(t) + \boldsymbol{B}_{\boldsymbol{K}}(\mathrm{TAS})\boldsymbol{y}_{\boldsymbol{meas}}(t) \\ \boldsymbol{u}_{\boldsymbol{com}}(t) & = \boldsymbol{C}_{\boldsymbol{K}}(\mathrm{TAS})\boldsymbol{x}_{\boldsymbol{K}}(t) + \boldsymbol{D}_{\boldsymbol{K}}(\mathrm{TAS})\boldsymbol{y}_{\boldsymbol{meas}}(t) \end{cases} \tag{F.10}$$

où $\boldsymbol{x}_{\boldsymbol{K}}$ sont les états du contrôleur, $\boldsymbol{y}_{\boldsymbol{meas}}$ et $\boldsymbol{u}_{\boldsymbol{com}}$ sont respectivement la sortie mesurée et l'entrée de contrôle, et les fonctions matricielles $\boldsymbol{A}_{\boldsymbol{K}}$, $\boldsymbol{B}_{\boldsymbol{K}}$, $\boldsymbol{C}_{\boldsymbol{K}}$ et $\boldsymbol{D}_{\boldsymbol{K}}$ définissant l'espace d'état ont une dépendance polynomiale sur le TAS. Un facteur clé dans la conception du contrôleur AFS est sa complexité, qui doit être aussi faible que possible, en gardant à l'esprit sa mise en œuvre pratique et sa certification sur les futurs aéronefs. Pour cette raison, des contrôleurs d'ordre faible sont développés, à travers la synthèse structurée H_∞ qui tire parti des multiples capteurs et actionneurs disponibles, et d'une réponse dynamique pour assurer de bonnes performances. La section 5.5 montre comment obtenir des configurations réduites, dans lesquelles le nombre d'entrées et de sorties du contrôleur est réduit, suite à la recherche d'un contrôleur simple. Le raisonnement qui sous-tend le paramétrage TAS est que la dynamique aéroélastique présente des variations importantes à mesure que la vitesse augmente. Il est démontré dans la section des résultats 5.7 qu'une structure LPV simple, avec une dépendance affine des matrices de l'espace d'état sur le TAS, conduit à des améliorations significatives lorsqu'une évolution progressive de la dynamique du système est souhaitée au fur et à mesure que la vitesse augmente et franchit sa valeur de flottement en boucle ouverte. Les contrôleurs qui sont robustes par rapport aux variations du TAS seront également étudiés. Une autre cause de variation de la dynamique aéroélastique est l'évolution de la configuration de la masse de l'avion au cours d'un vol ou entre deux vols. Cette évolution ne peut pas être facilement paramétrée par une seule variable, contrairement à la dépendance du TAS. Le développement d'une loi adaptative pour les contrôleurs en fonction de cette incertitude n'est pas simple, et l'approche robuste est privilégiée dans ce chapitre. La conception d'un contrôleur LPV robuste aux variations de masse est un problème d'optimisation à forte intensité informatique et nécessite le réglage de différents hyperparamètres par l'utilisateur. Pour cette raison, elle est réalisée en plusieurs étapes, en commençant par la synthèse d'un contrôleur basé sur un modèle instable unique, qui est utilisé comme point de départ pour une synthèse LPV. À partir d'un contrôleur LPV conçu avec des modèles à plusieurs valeurs TAS mais avec la même configuration de masse, il faut décider si la robustesse à d'autres configurations de masse est assurée et, si ce n'est pas le cas, une synthèse TAS-LPV utilisant différentes configurations de masse peut être réalisée. Là encore, l'utilisation comme point de départ d'une conception de contrôleur obtenue avec une seule configuration de masse peut faciliter la synthèse. Cette stratégie de conception du contrôleur implique la fixation arbitraire d'une valeur de vitesse maximale à laquelle la boucle fermée doit être stable. L'architecture générale de la commande est illustrée sur la Fig. 5.1.

F.7.3 Conclusion sur la suppression active du flottement

Ce chapitre a proposé une stratégie de contrôle complète pour la suppression active du flottement, à partir d'une modélisation hybride d'ordre réduit du système aéroélastique qui utilise les

données de réponse en fréquence et la connaissance des modes aéroélastiques. Sur la base d'une fonction objective commune, une sélection optimale de capteurs et d'actionneurs avec une complexité numérique réduite est proposée et différentes étapes de la stratégie de contrôle sont décrites, depuis de multiples synthèses mono-modèle à différentes vitesses jusqu'à la conception LPV avec une extension possible à des configurations de masses multiples. La simplicité du contrôleur est recherchée tout au long de ce processus, en vue d'une future mise en œuvre industrielle.

Les ailerons et les accéléromètres situés aux extrémités de l'aile se sont avérés les plus utiles pour ce problème AFS, en utilisant deux critères basés respectivement sur la boucle fermée et l'observabilité/contrôle des modes de flottement. Cependant, il s'est avéré que des capteurs et des actionneurs supplémentaires sont nécessaires, probablement pour maintenir la stabilité globale de l'avion et pas seulement celle associée aux modes de flottement. La synthèse basée sur un modèle instable unique a montré ses limites lorsqu'elle a été validée à différentes vitesses, et bien que la synthèse de contrôleur robuste multi-TAS montre certaines améliorations par rapport à la première, elle conduit toujours à une perte de performances par rapport à ce qui peut être obtenu avec des contrôleurs conçus indépendamment à différentes vitesses. La loi LPV dépendante des TAS s'est avérée, au contraire, très efficace, même avec une simple dépendance affine des matrices de l'espace d'état qui les constituent par rapport à la vitesse.

Bien que ces résultats soient prometteurs, certaines questions restent en suspens, comme la conception d'un contrôleur valable pour différents cas de masse et différentes valeurs du nombre de Mach. En raison de la dépendance importante de la dynamique aéroélastique par rapport à ces paramètres, une approche robuste pourrait ne pas suffire et une stratégie adaptative pourrait être nécessaire.

F.8 Perspectives

Cette thèse s'est concentrée sur une méthodologie de modélisation aéroélastique d'ordre réduit, et sur l'utilisation de la commande robuste linéaire pour l'atténuation des charges dues au vent et la suppression active du flottement. D'autres directions méritent d'être mentionnées ici, soit parce qu'elles ont été essayées et jugées moins prometteuses que celles adoptées dans ce travail, soit parce qu'elles pourraient être intéressantes pour l'avenir de la recherche dans les théories de la commande et de l'aéroservoélasticité.

F.8.1 Modélisation aéroélastique et méthodes d'identification des systèmes

Des études plus poussées dans le domaine de l'identification des systèmes pourraient être utiles pour la synthèse des contrôleurs d'atténuation des charges dues au vent et de suppression active du flottement, mais aussi pour les simulations d'aéronefs en ce qui concerne les calculs des charges.

La méthode de Loewner s'est avérée très efficace pour obtenir directement des modèles d'espace d'état précis à partir de données fréquentielles, avec peu d'étapes intermédiaires. Si les méthodes mathématiques décrites dans le présent document pour imposer des contraintes sur l'emplacement des pôles ont principalement utilisé la méthode des sous-espaces, d'autres tentatives pour le faire avec la méthode de Loewner ont été infructueuses. La section 3.4.2 a illustré une procédure pour imposer la stabilité avec cette méthode, elle est appliquée après le processus d'identification, en post-analyse. Travailler directement sur les matrices de Loewner pour façonner le modèle d'état identifié est une orientation intéressante, qui pourrait servir non seulement le domaine de la modélisation aéroélastique, mais aussi la théorie de l'identification des systèmes elle-même. Une autre direction critique pour la modélisation et le contrôle aéroélastiques concerne la définition de modèles paramétrés. La philosophie multi-modèle développée pour l'atténuation des charges dues au vent et la suppression active du flottement présente certains inconvénients, généralement dus au fait que les différents modèles sont obtenus à l'aide de processus d'identification distincts. La continuité entre ces modèles, et dans certains cas la cohérence, ne sont pas assurées par cette approche multi-modèle. Un modèle unique dépendant paramétriquement des conditions de vol et de certains paramètres définissant la configuration de la masse serait idéal pour l'analyse et éventuellement pour la synthèse des commandes (à condition que la complexité numérique ne devienne pas trop élevée). Certains éléments ont été proposés dans la section 3.9, avec l'utilisation de la méthode de Loewner pour les identifications variables polytopiques et linéaires-paramétriques. Les modèles avec une dépendance paramétrique de transformation fractionnaire linéaire ne sont pas étudiés, mais peuvent être d'un grand intérêt pour leur compatibilité avec la μ-synthèse. Cette approche peut être une direction prometteuse pour l'aéroservoélasticité et le contrôle du vol, ouvrant la voie à des formulations unifiées de contrôleurs s'adaptant en douceur aux conditions, avec les avantages d'une approche basée sur le modèle. Enfin, les méthodes d'identification étudiées dans ce travail reposent souvent sur la programmation semi-définie, comme c'est souvent le cas dans les théories d'identification et de contrôle des systèmes. L'étude récente et prometteuse des problèmes dits "sparse" propose d'aller au-delà du cadre classique de la programmation semi-définie, en considérant des problèmes d'optimisation qui peuvent être convexes mais non différentiables (ex : le problème Lasso, qui inclut une norme 1 non différentiable dans l'objectif d'optimisation) ou même non convexes, résolus par exemple en trouvant les solutions du problème convexe "le plus proche". On trouvera des exemples de cette approche de l'identification des systèmes dans [Yılmaz et al. 2018] et [Miller, Singh, and Sznaier 2020], à l'aide d'algorithmes rapides basés sur l'algorithme de Frank-Wolfe (voir [Vinyes and Obozinski 2017] par exemple) ou la méthode des multiplicateurs à direction alternée (ADMM) décrite dans [Boyd et al. 2011]. En s'affranchissant du cadre semi-défini, il est possible d'envisager des problèmes plus généraux et de traiter des quantités plus importantes de données et un plus grand nombre de variables, même si les certitudes de convergence sont généralement moindres.

F.8.2 Méthodes de contrôle actif

Pour ce qui est des méthodes de contrôle actif, une étape importante consisterait, conformément à ce qui a été dit plus haut pour les modèles paramétriques, à définir des contrôleurs adaptatifs avec une forte connaissance a-priori de la dynamique. Bien que cela ne semble pas être une orientation critique pour l'atténuation des charges dues au vent, puisqu'il a été montré dans ce travail qu'une approche robuste conduit à des résultats presque optimaux, cela peut être d'une importance significative pour la suppression active du flottement. En raison de la dynamique à haute fréquence incluse, le contrôleur doit cibler avec précision certains modes, qui peuvent varier lorsque les conditions de vol et la configuration de la masse changent. Bien que la robustesse soit difficile à obtenir dans le problème de la suppression active du flottement, comme démontré dans ce travail, l'adaptativité pourrait être une approche prometteuse si une grande confiance dans le processus de modélisation peut être démontrée. En ce qui concerne l'atténuation des charges dues au vent, la principale direction de recherche pour poursuivre le travail entrepris dans cette thèse serait une intégration plus pratique dans l'avion. Cela nécessiterait de prendre en compte de nombreuses interactions avec d'autres sous-systèmes et des contraintes industrielles. Un aspect majeur serait la compatibilité avec les lois de contrôle de vol existantes, qui a été prise en compte dans ce travail mais en utilisant un cadre simplifié. La définition d'une logique robuste pour l'activation du système d'atténuation des charges dues au vent est essentielle pour éviter qu'il ne soit excessivement intrusif dans la plupart des conditions de vol. Bien que ce travail ait principalement adopté le point de vue des "charges", une meilleure compréhension du système de contrôle global et des lois serait alors nécessaire pour faire passer l'atténuation des charges dues au vent à l'étape suivante. Grâce aux enseignements tirés de cette thèse, la compréhension actuelle des défis et des problèmes liés à l'atténuation des charges dues au vent a déjà atteint un niveau de maturité qui pourrait permettre une mise en œuvre sur un démonstrateur de vol. Cela serait crucial pour mieux comprendre la différence entre les modèles aéroélastiques et la réalité, et comment cela affecterait la capacité à réduire efficacement les charges de l'avion. En outre, l'une des principales inconnues de cette thèse concerne le capteur lidar, dont les limites ne sont pas encore bien comprises. Différents lidars ont été testés en vol, mais en raison de la diversité des technologies et des applications, la compréhension de la fiabilité de la mesure de la vitesse du vent à distance peut encore être améliorée. L'essai de ces technologies sur des systèmes réels, et l'étude éventuelle de leur influence sur d'autres techniques prometteuses d'atténuation des charges dues au vent, telles que les extrémités d'ailes repliables, constitueront la pierre angulaire de leur préparation à la mise en œuvre dans la conception des futures générations d'aéronefs commerciaux.

Bibliography

Alam, Mushfiqul, Martin Hromcik, and Tomas Hanis (2015). "Active gust load alleviation system for flexible aircraft: Mixed feedforward/feedback approach." In: *Aerospace Science and Technology* 41, pp. 122–133. DOI: 10.1016/j.ast.2014.12.020 (cit. on pp. 95, 217).

Albano, Edward and William P. Rodden (1969). "A doublet-lattice method for calculating lift distributions on oscillating surfaces in subsonic flows." In: *AIAA Journal* 7.2, pp. 279–285. DOI: 10.2514/3.5086 (cit. on pp. 27, 35, 206).

Alhajjar, Ali M. et al. (2018). "LPV Modeling and Control for Active Flutter Suppression of a Smart Airfoil." In: *2018 AIAA Guidance, Navigation, and Control Conference*. DOI: 10.2514/6.2018-1342 (cit. on pp. 152, 227).

Antoulas, A.C., A.C. Ionita, and S. Lefteriu (2012). "On two-variable rational interpolation." In: *Linear Algebra and its Applications* 436.8. Special Issue dedicated to Danny Sorensen's 65th birthday, pp. 2889–2915. ISSN: 0024-3795. DOI: https://doi.org/10.1016/j.laa.2011.07.017 (cit. on p. 88).

Antoulas, Athanasios C., Sanda Lefteriu, and A. Cosmin Ionita (2017). "Chapter 8: A Tutorial Introduction to the Loewner Framework for Model Reduction." In: *Model Reduction and Approximation*, pp. 335–376. DOI: 10.1137/1.9781611974829.ch8 (cit. on pp. 67, 68).

Apkarian, Pierre, Minh Ngoc Dao, and Dominikus Noll (2015). "Parametric Robust Structured Control Design." In: *IEEE Transactions on Automatic Control* 60.7, pp. 1857–1869. DOI: 10.1109/TAC.2015.2396644 (cit. on pp. 132, 224).

Bako, L., G. Mercère, and S. Lecoeuche (2009). "Identification of Multivariable Canonical State-Space Representations." In: *IFAC Proceedings Volumes* 42.10. 15th IFAC Symposium on System Identification, pp. 1638–1643. ISSN: 1474-6670. DOI: https://doi.org/10.3182/20090706-3-FR-2004.00272 (cit. on pp. 188, 189).

Banakh, Viktor and Igor Smalikho (2013). *Coherent Doppler wind lidars in a turbulent atmosphere*. Artech House (cit. on p. 8).

Banakh, Viktor A, Igor N Smalikho, and Christian Werner (2000). "Effect of aerosol particle microstructure on cw Doppler lidar signal statistics." In: *Applied Optics* 39.30, pp. 5393–5402 (cit. on p. 8).

Barker, Jeffrey M. and Gary J. Balas (2000). "Comparing Linear Parameter-Varying Gain-Scheduled Control Techniques for Active Flutter Suppression." In: *Journal of Guidance, Control, and Dynamics* 23.5, pp. 948–955. DOI: 10.2514/2.4637 (cit. on pp. 152, 227).

Barker, Jeffrey M., Gary J. Balas, and Paul A. Blue (1999). "Gain-Scheduled Linear Fractional Control for Active Flutter Suppression." In: *Journal of Guidance, Control, and Dynamics* 22.4, pp. 507–512. DOI: 10.2514/2.4418 (cit. on pp. 152, 227).

Berg, John et al. (2021). "Analytical and Experimental Evaluation of Multivariable Stability Margins in Active Flutter Suppression Wind Tunnel Tests." In: *AIAA Scitech 2021 Forum*. DOI: 10.2514/6.2021-1261 (cit. on pp. 151, 152, 227, 228).

Bisplinghoff, R.L., H. Ashley, and R.L. Halfman (1955a). *Aeroelasticity*. Addison-Wesley Publishing Company. ISBN: 9780201005950 (cit. on p. 3).

Bisplinghoff, R.L., H. Ashley, and R.L. Halfman (1955b). "Aeroelasticity." In: Addison-Wesley Publishing Company, pp. 632–641. ISBN: 9780201005950 (cit. on pp. 27, 150, 205, 226).

Blight, James D., R. Lane Daily, and Dagfinn Gangsaas (1994). "Practical control law design for aircraft using multivariable techniques." In: 59.1, pp. 93–137. DOI: 10.1080/00207179408923071 (cit. on p. 195).

Botez, RM et al. (2018). "Numerical and experimental transition results evaluation for a morphing wing and aileron system." In: *The Aeronautical Journal* 122.1251, pp. 747–784 (cit. on p. 7).

Boyd, Stephen et al. (2011). "Distributed optimization and statistical learning via the alternating direction method of multipliers." In: *Foundations and Trends® in Machine learning* 3.1, pp. 1–122 (cit. on pp. 177, 231).

Byrd, Richard H., Mary E. Hribar, and Jorge Nocedal (1999). "An Interior Point Algorithm for Large-Scale Nonlinear Programming." In: *SIAM Journal on Optimization* 9.4, pp. 877–900. DOI: 10.1137/S1052623497325107 (cit. on pp. 74, 77, 212, 213).

Carpenter, Trenton J. and Roberto Albertani (2015). "Aerodynamic Load Estimation from Virtual Strain Sensors for a Pliant Membrane Wing." In: *AIAA Journal* 53.8, pp. 2069–2079. DOI: 10.2514/1.J053291 (cit. on p. 8).

Caverly, Ryan et al. (2017). "Gust-Load Alleviation of a Flexible Aircraft using a Disturbance Observer." In: *AIAA Guidance, Navigation, and Control Conference*. American Institute of Aeronautics and Astronautics. DOI: 10.2514/6.2017-1718 (cit. on pp. 95, 217).

Chang, Chong-Seok, Dewey H Hodges, and Mayuresh J Patil (2008). "Flight dynamics of highly flexible aircraft." In: *Journal of Aircraft* 45.2, pp. 538–545 (cit. on pp. 95, 217).

Che, Jiaxing, Irene Gregory, and Chengyu Cao (2012). "Integrated Flight/Structural Mode Control for Very Flexible Aircraft Using L1 Adaptive Output Feedback Controller." In: *AIAA Guidance, Navigation, and Control Conference*. American Institute of Aeronautics and Astronautics. DOI: 10.2514/6.2012-4439 (cit. on p. 95).

Chen, Gang, Jian Sun, and Yue-ming Li (2012). "Adaptive Reduced-Order-Model-Based Control-Law Design for Active Flutter Suppression." In: *Journal of Aircraft* 49.4, pp. 973–980. DOI: 10.2514/1.C031236 (cit. on pp. 150, 152, 227).

Chen, Gang et al. (2011). "Linear Parameter Varying Control for Active Flutter Suppression Based on Adaptive Reduced Order Model." In: *52nd AIAA/ASME/ASCE/AHS/ASC Structures, Structural Dynamics and Materials Conference*. DOI: 10.2514/6.2011-1773 (cit. on pp. 152, 227).

Chilali, Mahmoud and Pascal Gahinet (Mar. 1996). "H-infinity Design with Pole Placement Constraints: an LMI Approach." In: *Automatic Control, IEEE Transactions on* 41, pp. 358 –367. DOI: 10.1109/9.486637 (cit. on pp. 59, 69, 70, 208, 211).

Cook, Michael V (2012). "Flight dynamics principles: a linear systems approach to aircraft stability and control." In: Butterworth-Heinemann, pp. 138–209. ISBN: 008098276X (cit. on pp. 43, 44).

Cook, Robert G., Rafael Palacios, and Paul Goulart (2013). "Robust Gust Alleviation and Stabilization of Very Flexible Aircraft." In: *AIAA Journal* 51.2, pp. 330–340. DOI: 10.2514/1.J051697 (cit. on pp. 96, 219).

Derrien, Jean-Claude (2012). "Electromechanical actuator (EMA) advanced technologies for flight controls." In: *International congress of the aeronautical sciences*, pp. 1–10 (cit. on p. 7).

Diederich, F.W. and J.A. Drischler (1957). *Effect of Spanwise Variations in Gust Intensity on the Lift Due to Atmospheric Turbulence*. Technical note. National Advisory Committee for Aeronautics (cit. on p. 25).

Doyle, John, Francis A, and Allen Tannenbaum (Jan. 2009). "Feedback Control Theory." In: Macmillan Publishing Co., pp. 45–59. DOI: 10.1007/978-0-387-85460-1_1 (cit. on pp. 96, 219).

Doyle, John et al. (1988). "State-space solutions to standard H2 and H control problems." In: *1988 American Control Conference*, pp. 1691–1696. DOI: 10.23919/ACC.1988.4789992 (cit. on p. 194).

Es, G.W.H. Van (2007). *Analysis of aircraft weight and balance related safety occurrences*. National Aerospace Laboratory NLR (cit. on p. 21).

Etkin, B. (1959). "Dynamics of Flight – Stability and Control." In: Wiley, New York, pp. 120–126. ISBN: 9780471089360 (cit. on pp. 27, 205).

European Aviation Safety Agency (EASA) (Sept. 2007). *Certification Specifications for Large Aeroplanes, Amendment 3* (cit. on pp. 3, 23–25, 101, 102, 149).

Faïsse, Emmeline et al. (2021). "Adding Control in Multidisciplinary Design Optimization of a Wing for Active Flutter Suppression." In: *AIAA Scitech 2021 Forum*. DOI: 10.2514/6.2021-0892 (cit. on pp. 151, 227).

Ferrier, Yvonne et al. (2018). "Active Gust Load Alleviation of High-Aspect Ratio Flexible Wing Aircraft." In: *2018 AIAA Guidance, Navigation, and Control Conference*. American Institute of Aeronautics and Astronautics. DOI: 10.2514/6.2018-0620 (cit. on pp. 96, 219).

Fezans, N., J. Schwithal, and D. Fischenberg (2017). "In-flight remote sensing and identification of gusts, turbulence, and wake vortices using a Doppler LIDAR." In: *CEAS Aeronautical Journal* 8.2, pp. 313–333. DOI: 10.1007/s13272-017-0240-9 (cit. on pp. 96, 218).

Fezans, Nicolas and Hans-Dieter Joos (2017). "Combined Feedback and LIDAR-Based Feedforward Active Load Alleviation." In: *AIAA Atmospheric Flight Mechanics Conference*. American Institute of Aeronautics and Astronautics. DOI: 10.2514/6.2017-3548 (cit. on pp. 96, 218).

Fischer, Annette, Frank Schröder, and Reik Thormann (2022). "Active Flutter Suppression From an Industrial Perspective." In: *International Forum on Aeroelasticity and Structural Dynamics (IFASD)* (cit. on pp. 152, 228).

Fonte, Federico, Sergio Ricci, and Paolo Mantegazza (2015). "Gust Load Alleviation for a Regional Aircraft Through a Static Output Feedback." In: *Journal of Aircraft* 52.5, pp. 1559–1574. DOI: 10.2514/1.c032995 (cit. on p. 95).

Fournier, Hugo et al. (2022a). "Robust Gust Load Alleviation at Different Flight Points and Mass configurations." In: *AIAA SCITECH 2022 Forum*. DOI: 10.2514/6.2022-0285 (cit. on pp. 11, 27, 205).

Fournier, Hugo et al. (2022b). "Robust Gust Load Alleviation of Flexible Aircraft Equipped with Lidar." In: *Journal of Guidance, Control, and Dynamics* 45.1, pp. 58–72. DOI: 10.2514/1.G006084 (cit. on pp. 11, 27, 125, 155, 200, 205).

Fournier, Hugo et al. (2023a). "Active Flutter Suppression H Synthesis using Multiple Models with Imposed Aeroelastic Poles." In: *AIAA SCITECH 2023 Forum*, p. 0686 (cit. on p. 11).

Fournier, Hugo et al. (2023b). "Reduced-Order Identification of Aeroelastic Systems with Constrained and Imposed Poles." In: *Journal of Guidance, Control, and Dynamics* 46.6, pp. 1038–1051. DOI: 10.2514/1.G007099 (cit. on p. 11).

Freitas Virgilio Pereira, Mateus de et al. (2019). "Model Predictive Control Architectures for Maneuver Load Alleviation in Very Flexible Aircraft." In: *AIAA Scitech 2019 Forum*. American Institute of Aeronautics and Astronautics. DOI: 10.2514/6.2019-1591 (cit. on pp. 96, 218).

Gahinet, Pascal and Pierre Apkarian (1994). "A linear matrix inequality approach to H control." In: *International Journal of Robust and Nonlinear Control* 4.4, pp. 421–448. DOI: https://doi.org/10.1002/rnc.4590040403 (cit. on p. 194).

Gaulocher, Sebastian L., Clément Roos, and Christelle Cumer (2007). "Aircraft Load Alleviation During Maneuvers Using Optimal Control Surface Combinations." In: *Journal of Guidance, Control, and Dynamics* 30.2, pp. 591–600. DOI: 10.2514/1.25577 (cit. on pp. 96, 218).

Giesing, Joseph P. and Terez P. Kalman (1971). "Subsonic unsteady aerodynamics for general configurations." In: *10th Aerospace Sciences Meeting*, p. 26 (cit. on pp. 35, 36).

Giesseler, H.-G. et al. (2012). "Model Predictive Control for Gust Load Alleviation." In: *IFAC Proceedings Volumes* 45.17, pp. 27–32. DOI: 10.3182/20120823-5-nl-3013.00049 (cit. on pp. 96, 218).

Goldberg, David E (1994). "Genetic and evolutionary algorithms come of age." In: *Communications of the ACM* 37.3, pp. 113–120. DOI: 10.1145/175247.175259 (cit. on p. 157).

Green, M. (1988). "A relative error bound for balanced stochastic truncation." In: *IEEE Transactions on Automatic Control* 33.10, pp. 961–965. DOI: 10.1109/9.7255 (cit. on pp. 58, 207).

Guimarães Neto, Antônio B. et al. (2016). "Formulation of the Flight Dynamics of Flexible Aircraft Using General Body Axes." In: *AIAA Journal* 54.11, pp. 3516–3534. DOI: 10.2514/1.J054752 (cit. on pp. 27, 28, 205).

Haghighat, Sohrab, Hugh H. T. Liu, and Joaquim R. R. A. Martins (2012). "Model-Predictive Gust Load Alleviation Controller for a Highly Flexible Aircraft." In: *Journal of Guidance, Control, and Dynamics* 35.6, pp. 1751–1766. DOI: 10.2514/1.57013 (cit. on pp. 96, 218).

Hall, Kenneth C., Jeffrey P. Thomas, and Earl H. Dowell (2000). "Proper Orthogonal Decomposition Technique for Transonic Unsteady Aerodynamic Flows." In: *AIAA Journal* 38.10, pp. 1853–1862. DOI: 10.2514/2.867 (cit. on pp. 27, 205).

Harder, Robert L and Robert N Desmarais (1972). "Interpolation using surface splines." In: *Journal of aircraft* 9.2, pp. 189–191 (cit. on p. 37).

Hassig, H.J. (1971). "An approximate true damping solution of the flutter equation by determinant iteration." In: *Journal of Aircraft* 8.11, pp. 885–889. DOI: 10.2514/3.44311 (cit. on pp. 43, 59, 208).

Herbst, Jonas and Patrick Vrancken (2016). "Design of a monolithic Michelson interferometer for fringe imaging in a near-field, UV, direct-detection Doppler wind lidar." In: *Applied Optics* 55.25, p. 6910. DOI: 10.1364/ao.55.006910 (cit. on pp. 8, 95, 112, 217).

Hesse, Henrik and Rafael Palacios (2014). "Reduced-Order Aeroelastic Models for Dynamics of Maneuvering Flexible Aircraft." In: *AIAA Journal* 52.8, pp. 1717–1732. DOI: 10.2514/1.J052684 (cit. on pp. 28, 206).

Hesse, Henrik and Rafael Palacios (2016). "Dynamic Load Alleviation in Wake Vortex Encounters." In: *Journal of Guidance, Control, and Dynamics* 39.4, pp. 801–813. DOI: 10.2514/1.G000715 (cit. on pp. 28, 206).

Hindi, Haitham and Stephen Boyd (1998). "Analysis of linear systems with saturation using convex optimization." In: *Proceedings of the 37th IEEE conference on decision and control (Cat. No. 98CH36171)*. Vol. 1. IEEE, pp. 903–908 (cit. on p. 127).

Hoblit, Frederic M (1988). *Gust loads on aircraft: concepts and applications*. American Institute of Aeronautics and Astronautics, Inc. ISBN: 1600860605 (cit. on p. 2).

Holloway, Richard B., Paul M. Burris, and Robert P. Johannes (1970). "Aircraft performance benefits from modern control systems technology." In: *Journal of Aircraft* 7.6, pp. 550–553. DOI: 10.2514/3.44211 (cit. on p. 5).

Hu, Tingshu, Zongli Lin, and Ben M Chen (2002). "An analysis and design method for linear systems subject to actuator saturation and disturbance." In: *Automatica* 38.2, pp. 351–359 (cit. on p. 127).

Huang, Rui, Haiyan Hu, and Yonghui Zhao (2014). "Nonlinear Reduced-Order Modeling for Multiple-Input/Multiple-Output Aerodynamic Systems." In: *AIAA Journal* 52.6, pp. 1219–1231. DOI: 10.2514/1.J052323 (cit. on pp. 27, 205).

Jenkins, Jerry E. (1989). "Relationships among nonlinear aerodynamic indicial response models, oscillatory motion data, and stability derivatives." In: *16th Atmospheric Flight Mechanics Conference*. DOI: 10.2514/6.1989-3351 (cit. on pp. 27, 205).

Juang, Jer-Nan and Richard S. Pappa (1985). "An eigensystem realization algorithm for modal parameter identification and model reduction." In: *Journal of Guidance, Control, and Dynamics* 8.5, pp. 620–627. DOI: 10.2514/3.20031 (cit. on pp. 58, 207).

Kailath, Thomas (1980). "Linear systems." In: vol. 156. Prentice-Hall Englewood Cliffs, NJ, pp. 439–455 (cit. on pp. 179, 181).

Kalman, T. P., W. P. Rodden, and J. P. Giesling (1971). "Application of the Doublet-Lattice Method to Nonplanar Configurations in Subsonic Flow." In: *Journal of Aircraft* 8.6, pp. 406–413. DOI: 10.2514/3.59117 (cit. on pp. 27, 206).

Karachalios, Dimitrios, Ion Gosea, and A.C. Antoulas (Aug. 2019). "The Loewner framework for system identification and reduction." In: De Gruyter. DOI: 10.1515/9783110498967-006 (cit. on pp. 58, 66, 152, 208, 210, 228).

Karpel, Mordechay (1982). "Design for Active Flutter Suppression and Gust Alleviation Using State-Space Aeroelastic Modeling." In: *Journal of Aircraft* 19.3, pp. 221–227. DOI: 10.2514/3.57379 (cit. on pp. 58, 62, 207).

Kergus, Pauline, Fabrice Demourant, and Charles Poussot-Vassal (2020). "Identification of parametric models in the frequency-domain through the subspace framework under LMI constraints." In: *International Journal of Control* 93.8, pp. 1879–1890. DOI: 10.1080/00207179.2018.1535717 (cit. on p. 88).

Kergus, Pauline et al. (2018). "Data-driven control design in the Loewner framework: Dealing with stability and noise." In: *2018 European Control Conference (ECC)*, pp. 1704–1709. DOI: 10.23919/ECC.2018.8550216 (cit. on pp. 58, 208).

Khalil, Ahmed and Nicolas Fezans (2019). "Performance Enhancement of Gust Load Alleviation Systems for Flexible Aircraft using H∞ Optimal Control with Preview." In: *AIAA Scitech 2019 Forum*. American Institute of Aeronautics and Astronautics. DOI: 10.2514/6.2019-0822 (cit. on pp. 96, 219).

Kim, Taehyoun (1998). "Frequency-Domain Karhunen-Loeve Method and Its Application to Linear Dynamic Systems." In: *AIAA Journal* 36.11, pp. 2117–2123. DOI: 10.2514/2.315 (cit. on pp. 27, 205).

Konstadinopoulos, P. et al. (1985). "A vortex-lattice method for general, unsteady aerodynamics." In: *Journal of Aircraft* 22.1, pp. 43–49. DOI: 10.2514/3.45078 (cit. on pp. 28, 35, 206).

Kothare, Mayuresh V, Venkataramanan Balakrishnan, and Manfred Morari (1996). "Robust constrained model predictive control using linear matrix inequalities." In: *Automatica* 32.10, pp. 1361–1379 (cit. on pp. 89, 96, 218).

Köhler, M. (2014). "On the closest stable descriptor system in the respective spaces RH2 and RH-infinity." In: *Linear Algebra and its Applications* 443, pp. 34–49. ISSN: 0024-3795. DOI: https://doi.org/10.1016/j.laa.2013.11.012 (cit. on pp. 69, 70, 210, 211).

Lacy, S.L. and D.S. Bernstein (2003). "Subspace identification with guaranteed stability using constrained optimization." In: *IEEE Transactions on Automatic Control* 48.7, pp. 1259–1263. DOI: 10.1109/TAC.2003.814273 (cit. on pp. 59, 69, 208, 211).

Larimore, W.E. (1990). "Canonical variate analysis in identification, filtering, and adaptive control." In: *29th IEEE Conference on Decision and Control*, 596–604 vol.2. DOI: 10.1109/CDC.1990.203665 (cit. on pp. 63, 209).

Lee, Lawton H. and Kameshwar Poolla (Mar. 1999). "Identification of Linear Parameter-Varying Systems Using Nonlinear Programming." In: *Journal of Dynamic Systems, Measurement, and Control* 121.1, pp. 71–78. ISSN: 0022-0434. DOI: 10.1115/1.2802444 (cit. on p. 88).

Lee-Rausch, Elizabeth M. and John T. Batina (1996). "Wing flutter computations using an aerodynamic model based on the Navier-Stokes equations." In: *Journal of Aircraft* 33.6, pp. 1139–1147. DOI: 10.2514/3.47068 (cit. on pp. 27, 205).

Li, Feng, Yongzhi Wang, and Andrea Da Ronch (2016). "Flight Testing an Adaptive Feedforward Controller for Gust Loads Alleviation on a Flexible Aircraft." In: *AIAA Atmospheric Flight Mechanics Conference*. American Institute of Aeronautics and Astronautics. DOI: 10.2514/6.2016-3100 (cit. on pp. 95, 217, 218).

Livne, Eli (2018). "Aircraft Active Flutter Suppression: State of the Art and Technology Maturation Needs." In: *Journal of Aircraft* 55.1, pp. 410–452. DOI: 10.2514/1.c034442 (cit. on pp. 27, 205).

Lovera, Marco and Guillaume Mercere (2007). "Identification for gain-scheduling: a balanced subspace approach." In: *2007 American Control Conference*, pp. 858–863. DOI: 10.1109/ACC.2007.4282899 (cit. on p. 88).

Lucia, David J., Philip S. Beran, and Walter A. Silva (2004). "Reduced-order modeling: new approaches for computational physics." In: *Progress in Aerospace Sciences* 40.1, pp. 51–117. ISSN: 0376-0421. DOI: https://doi.org/10.1016/j.paerosci.2003.12.001 (cit. on pp. 27, 205).

Luspay, Tamás et al. (2019). "Flight control design for a highly flexible flutter demonstrator." In: *AIAA Scitech 2019 Forum*. American Institute of Aeronautics and Astronautics. DOI: 10.2514/6.2019-1817 (cit. on pp. 27, 95, 205).

MacFarlane, A. G. J. and I. Postlethwaite (1977). "The generalized Nyquist stability criterion and multivariable root loci." In: *International Journal of Control* 25.1, pp. 81–127. DOI: 10.1080/00207177708922217 (cit. on p. 199).

Magar, Kaman S. Thapa et al. (2017). "Active Gust Alleviation using Artificial Hair Sensors and Feedforward Control." In: *AIAA Guidance, Navigation, and Control Conference*. American Institute of Aeronautics and Astronautics. DOI: 10.2514/6.2017-1485 (cit. on pp. 95, 217).

Marchetti, Luca et al. (2020). "Active Flutter Suppression Analysis and Wind Tunnel Studies of a Commercial Transport Configuration." In: *AIAA Scitech 2020 Forum*. DOI: 10.2514/6.2020-1677 (cit. on pp. 152, 155, 227, 228).

Mayo, A.J. and A.C. Antoulas (2007). "A framework for the solution of the generalized realization problem." In: *Linear Algebra and its Applications* 425.2-3, pp. 634–662. DOI: 10.1016/j.laa.2007.03.008 (cit. on pp. 58, 66, 68, 152, 208, 210, 228).

McKelvey, T., H. Akcay, and L. Ljung (1996). "Subspace-based multivariable system identification from frequency response data." In: *IEEE Transactions on Automatic Control* 41.7, pp. 960–979. DOI: 10.1109/9.508900 (cit. on pp. 63, 210).

Mechanical vibration and shock — Evaluation of human exposure to whole-body vibration — Part 1: General requirements (May 1997). Standard. Geneva, CH: International Organization for Standardization (cit. on p. 52).

Miller, Daniel N. and Raymond A. De Callafon (2013). "Subspace Identification with Eigenvalue Constraints." In: *Automatica* 49.8, 2468–2473. ISSN: 0005-1098. DOI: 10.1016/j.automatica.2013.04.028 (cit. on pp. 59, 69, 84, 208, 211, 215).

Miller, Jared, Rajiv Singh, and Mario Sznaier (2020). "MIMO System Identification by Randomized Active-Set Methods." In: *2020 59th IEEE Conference on Decision and Control (CDC)*, pp. 2246–2251. DOI: 10.1109/CDC42340.2020.9304402 (cit. on pp. 177, 231).

Mokrani, Bilal et al. (2019). "Multiple-Input Multiple-Output Experimental Aeroelastic Control Using a Receptance-Based Method." In: *AIAA Journal* 57.7, pp. 3066–3077. DOI: 10.2514/1.J057855 (cit. on p. 95).

Morari, Manfred and Jay H Lee (1999). "Model predictive control: past, present and future." In: *Computers & Chemical Engineering* 23.4-5, pp. 667–682 (cit. on pp. 96, 218).

Moulin, B. and M. Karpel (2007). "Gust Loads Alleviation Using Special Control Surfaces." In: *Journal of Aircraft* 44.1, pp. 17–25. DOI: 10.2514/1.19876 (cit. on p. 94).

Moulin, Boris (2004). "Robust Controller Design for Active Flutter Suppression." In: *AIAA Guidance, Navigation, and Control Conference and Exhibit 2004*. DOI: 10.2514/6.2004-5115 (cit. on pp. 152, 227).

MSC.Software Corporation (2004). "MSC.Nastran Version 68, Aeroelastic Analysis User's Guide." In: pp. 26–126 (cit. on pp. 32, 33, 37).

Nissim, E (Mar. 1971). "Flutter Suppression Using Active Controls Based on the Concept of Aerodynamic Energy." In: NASA TN D-6199 (cit. on pp. 5, 150).

Office, U.S. Government Printing (1962). *U.S. Standard Atmosphere* (cit. on p. 19).

Oliver, John E (2008). *Encyclopedia of world climatology*. Springer Science & Business Media, p. 449 (cit. on p. 23).

P, William P. Rodden, Jean A. McGrew, and Terez P. Kalman (1972). "Comment on'interpolation using surface splines.'" In: *Journal of aircraft* 9.12, pp. 869–871 (cit. on p. 37).

Pankonien, Alexander M and Daniel J Inman (2015). "Spanwise morphing trailing edge on a finite wing." In: *Active and Passive Smart Structures and Integrated Systems 2015*. Vol. 9431. SPIE, pp. 248–262 (cit. on p. 7).

Patartics, Bálint et al. (2022). "Application of Structured Robust Synthesis for Flexible Aircraft Flutter Suppression." In: *IEEE Transactions on Control Systems Technology* 30.1, pp. 311–325. DOI: 10.1109/TCST.2021.3066096 (cit. on pp. 151, 227).

Patil, Mayuresh J. and Dewey H. Hodges (2006). "Flight Dynamics of Highly Flexible Flying Wings." In: *Journal of Aircraft* 43.6, pp. 1790–1799. DOI: 10.2514/1.17640 (cit. on pp. 27, 205).

Phan, Minh et al. (1992). "Improvement of observer/Kalman filter identification (OKID) by residual whitening." In: *Guidance, Navigation and Control Conference*. DOI: 10.2514/6.1992-4385 (cit. on pp. 63, 209, 210).

Previtali, Francesco, Andres F. Arrieta, and Paolo Ermanni (2014). "Performance of a Three-Dimensional Morphing Wing and Comparison with a Conventional Wing." In: *AIAA Journal* 52.10, pp. 2101–2113. DOI: 10.2514/1.J052764 (cit. on pp. 7, 8).

Pusch, Manuel, Daniel Ossmann, and Tamás Luspay (2019). "Structured Control Design for a Highly Flexible Flutter Demonstrator." In: *Aerospace* 6.3. ISSN: 2226-4310 (cit. on pp. 153, 156–158, 163).

Qin, S. Joe (2006). "An overview of subspace identification." In: *Computers and Chemical Engineering* 30.10. Papers form Chemical Process Control VII, pp. 1502–1513. ISSN: 0098-1354. DOI: https://doi.org/10.1016/j.compchemeng.2006.05.045 (cit. on pp. 58, 63, 208–210).

Rabadan, Guillermo Jenaro et al. (2010). "Airborne Lidar for Automatic Feedforward Control of Turbulent In-Flight Phenomena." In: *Journal of Aircraft* 47.2, pp. 392–403. DOI: 10.2514/1.44950 (cit. on pp. 95, 217).

Regan, Christopher D. and Christine V. Jutte (2012). "Survey of Applications of Active Control Technology for Gust Alleviation and New Challenges for Lighter-weight Aircraft." In: NASA TM-2012-216008 (cit. on p. 94).

Reschke, Christian (2005). "Flight loads analysis with inertially coupled equations of motion." In: *AIAA Atmospheric Flight Mechanics Conference and Exhibit*. DOI: 10.2514/6.2005-6026 (cit. on pp. 27, 28, 30, 205).

Ricci, Sergio et al. (2021). "An Active Flutter Suppression (AFS) Project: Overview, Results and Lessons Learned." In: *AIAA Scitech 2021 Forum*. DOI: 10.2514/6.2021-0908 (cit. on pp. 151, 152, 226, 228).

Ricci, Sergio et al. (2022). "Wind Tunnel System for Active Flutter Suppression Research: Overview and Insights." In: *AIAA Journal (not published yet)*. DOI: 10.2514/1.J061985 (cit. on pp. 152, 155, 227, 228).

Rodden, William P., Paul F. Taylor, and Terez P. Kalman (1972). "Refinement of the nonplanar aspects of the subsonic doublet-lattice lifting surface method." In: *Journal of Aircraft* 9.1, pp. 69–73. DOI: 10.2514/3.44322 (cit. on p. 35).

Rodden, William P., Paul F. Taylor, and Samuel C. McIntosh (1998). "Further Refinement of the Subsonic Doublet-Lattice Method." In: *Journal of Aircraft* 35.5, pp. 720–727. DOI: 10.2514/2.2382 (cit. on p. 35).

Roger, K.L. (1977). "Airplane Math Modeling Methods for Active Control Design." English. In: *AGARD-CP-228*, pp. 1–11 (cit. on pp. 58, 61, 207).

Romanowski, Michael and Earl Dowell (1995). "Aeroelastic analysis of an airfoil using eigenmode based reduced order unsteady aerodynamics." In: *36th Structures, Structural Dynamics and Materials Conference*. DOI: 10.2514/6.1995-1380 (cit. on pp. 27, 205).

Rosero, JA et al. (2007). "Moving towards a more electric aircraft." In: *IEEE Aerospace and Electronic Systems Magazine* 22.3, pp. 3–9 (cit. on p. 7).

Sandford, Maynard C., Irving Abel, and David L. Gray (1975). "Transonic Study of Active Flutter Suppression Based on an Energy Concept." In: *Journal of Aircraft* 12.2, pp. 72–77. DOI: 10.2514/3.59804 (cit. on pp. 5, 150).

Schmidt, David K. (2016a). "Stability Augmentation and Active Flutter Suppression of a Flexible Flying-Wing Drone." In: *AIAA Guidance, Navigation, and Control Conference*. DOI: 10.2514/6.2016-2099 (cit. on pp. 150, 151, 226).

Schmidt, David K. (2016b). "Stability Augmentation and Active Flutter Suppression of a Flexible Flying-Wing Drone." In: *Journal of Guidance, Control, and Dynamics* 39.3, pp. 409–422. DOI: 10.2514/1.G001484 (cit. on pp. 151, 226).

Schmidt, David K. and David L. Raney (2001). "Modeling and Simulation of Flexible Flight Vehicles." In: *Journal of Guidance, Control, and Dynamics* 24.3, pp. 539–546. DOI: 10.2514/2.4744 (cit. on pp. 27, 205).

Schmitt, Nikolaus Peter et al. (2007). "The AWIATOR airborne LIDAR turbulence sensor." In: *Aerospace Science and Technology* 11.7-8, pp. 546–552. DOI: 10.1016/j.ast.2007.03.006 (cit. on pp. 8, 95, 218).

Seiler, P., A. Packard, and P. Gahinet (2020). "An Introduction to Disk Margins [Lecture Notes]." In: *IEEE Control Systems Magazine* 40.5, pp. 78–95. DOI: 10.1109/MCS.2020.3005277 (cit. on p. 195).

Silva, Walter and Daniella Raveh (Feb. 2001). "Development of Unsteady Aerodynamic State-Space Models from CFD-Based Pulse Responses." In: *19th AIAA Applied Aerodynamics Conference*. DOI: 10.2514/6.2001-1213 (cit. on pp. 58, 207).

Silva, Walter A. (2018). "AEROM: NASA's Unsteady Aerodynamic and Aeroelastic Reduced-Order Modeling Software." In: *Aerospace* 5.2. ISSN: 2226-4310. DOI: 10.3390/aerospace5020041 (cit. on pp. 58, 207).

Silva Campos, Víctor Costa da, Anh-Tu Nguyen, and Reinaldo Martinez Palhares (2016). "LMI-based adaptive control for uncertain polytopic systems." In: *2016 IEEE 55th Conference on Decision and Control (CDC)*, pp. 3222–3227. DOI: 10.1109/CDC.2016.7798753 (cit. on p. 89).

Silvestre, Flávio and Pedro Paglione (2008). "Dynamics and control of a flexible aircraft." In: *AIAA atmospheric flight mechanics conference and exhibit*, p. 6876 (cit. on pp. 95, 217).

Skogestad, Sigurd (1996). "Multivariable feedback control : analysis and design." In: Chichester New York: Wiley, pp. 40–62. ISBN: 9780471942771 (cit. on pp. 96, 219).

Stalford, Harold et al. (1987). "Accurate Modeling of Nonlinear Systems using Volterra Series Submodels." In: *1987 American Control Conference*, pp. 886–891. DOI: 10.23919/ACC.1987.4789437 (cit. on pp. 27, 205).

Stanford, Bret (2019). "Gradient-Based Aeroservoelastic Optimization with Static Output Feedback." In: *AIAA Scitech 2019 Forum*. American Institute of Aeronautics and Astronautics. DOI: 10.2514/6.2019-0216 (cit. on p. 95).

Su, Weihua and Carlos E. S. Cesnik (2010). "Nonlinear Aeroelasticity of a Very Flexible Blended-Wing-Body Aircraft." In: *Journal of Aircraft* 47.5, pp. 1539–1553. DOI: 10.2514/1.47317 (cit. on pp. 27, 205).

Takarics, Béla et al. (2020). "Active Flutter Mitigation Testing on the FLEXOP Demonstrator Aircraft." In: *AIAA Scitech 2020 Forum*. DOI: 10.2514/6.2020-1970 (cit. on pp. 152, 228).

Tang, Wei, Jian Wu, and Zhongke Shi (2017). "Identification of reduced-order model for an aeroelastic system from flutter test data." In: *Chinese Journal of Aeronautics* 30.1, pp. 337–347. ISSN: 1000-9361. DOI: https://doi.org/10.1016/j.cja.2016.12.024 (cit. on pp. 59, 71, 72, 208, 211, 212).

Tarbouriech, Sophie and Matthew Turner (2009). "Anti-windup design: an overview of some recent advances and open problems." In: *IET control theory & applications* 3.1, pp. 1–19 (cit. on p. 128).

Tewari, Ashish (1998). "Robust optimal controllers for active flutter suppression." In: *Guidance, Navigation, and Control Conference and Exhibit*. DOI: 10.2514/6.1998-4142 (cit. on pp. 151, 226).

Tewari, Ashish (1999). "Output rate weighted active flutter suppression." In: *Guidance, Navigation, and Control Conference and Exhibit*. DOI: 10.2514/6.1999-4312 (cit. on pp. 151, 155, 226).

Theis, Julian, Harald Pfifer, and Peter Seiler (2020). "Robust Modal Damping Control for Active Flutter Suppression." In: *Journal of Guidance, Control, and Dynamics* 43.6, pp. 1056–1068. DOI: 10.2514/1.G004846 (cit. on pp. 151, 227).

Theis, Julian, Harald Pfifer, and Peter J. Seiler (2016). "Robust Control Design for Active Flutter Suppression." In: *AIAA Atmospheric Flight Mechanics Conference*. DOI: 10.2514/6.2016-1751 (cit. on pp. 151, 227).

Thomas, Jeffrey P., Earl H. Dowell, and Kenneth C. Hall (2002). "Nonlinear Inviscid Aerodynamic Effects on Transonic Divergence, Flutter, and Limit-Cycle Oscillations." In: *AIAA Journal* 40.4, pp. 638–646. DOI: 10.2514/2.1720 (cit. on pp. 27, 205).

Ustinov, Alexander, Maria Sidoruck, and Mikhail Goman (Aug. 2005). "Control Law Design for Flexible Aircraft: Comparison of the H-Infinity-based and Classical Methods." In: *AIAA Guidance, Navigation, and Control Conference and Exhibit*. American Institute of Aeronautics and Astronautics. DOI: 10.2514/6.2005-6265 (cit. on pp. 27, 95, 205).

Van Overschee, Peter and Bart De Moor (1994). "N4SID: Subspace algorithms for the identification of combined deterministic-stochastic systems." In: *Automatica* 30.1. Special issue on statistical signal processing and control, pp. 75–93. ISSN: 0005-1098. DOI: https://doi.org/10.1016/0005-1098(94)90230-5 (cit. on pp. 63, 209).

Van Overschee, Peter and Bart De Moor (1995). "A unifying theorem for three subspace system identification algorithms." In: *Automatica* 31.12. Trends in System Identification, pp. 1853–1864. ISSN: 0005-1098. DOI: https://doi.org/10.1016/0005-1098(95)00072-0 (cit. on pp. 63, 209).

Verdult, Vincent and Michel Verhaegen (2002). "Subspace identification of multivariable linear parameter-varying systems." In: *Automatica* 38.5, pp. 805–814. ISSN: 0005-1098. DOI: https://doi.org/10.1016/S0005-1098(01)00268-0 (cit. on p. 88).

Verhaegen, Michel and Patrick Dewilde (1992). "Subspace model identification Part 1. The output-error state-space model identification class of algorithms." In: *International Journal of Control* 56.5, pp. 1187–1210. DOI: 10.1080/00207179208934363 (cit. on pp. 63, 209).

Vidyasagar, M. and H. Kimura (1986). "Robust controllers for uncertain linear multivariable systems." In: *Automatica* 22.1, pp. 85 –94. ISSN: 0005-1098. DOI: https://doi.org/10.1016/0005-1098(86)90107-X (cit. on pp. 96, 195, 219).

Vinyes, Marina and Guillaume Obozinski (2017). "Fast column generation for atomic norm regularization." In: *Artificial Intelligence and Statistics*. PMLR, pp. 547–556 (cit. on pp. 177, 231).

Vrancken, Patrick et al. (Nov. 2016). "Airborne forward-pointing UV Rayleigh lidar for remote clear air turbulence detection: system design and performance." In: *Applied Optics* 55.32, p. 9314. DOI: 10.1364/ao.55.009314 (cit. on pp. 8, 95, 218).

Vuillemin, Pierre, David Quero Martin, and Charles Poussot-Vassal (2021). "Performance evaluation of gust load alleviation systems for flexible aircraft via optimal control." In: *arXiv preprint arXiv:2107.00266* (cit. on pp. 96, 218).

Waite, Josiah et al. (2018). "Active Flutter Suppression Controllers Derived from Linear and Nonlinear Aerodynamics: Application to a Transport Aircraft Model." In: *Applied Aerodynamics Conference*. DOI: 10.2514/6.2018-2836 (cit. on pp. 58, 207).

Waite, Josiah et al. (2019). "Active Flutter Suppression Using Reduced Order Modeling for Transonic Aeroservoelastic Control Law Development." In: *AIAA Aviation 2019 Forum*. DOI: 10.2514/6.2019-3025 (cit. on pp. 58, 151, 207, 226).

Waitman, Sérgio and Andrés Marcos (2020). "H-infinity Control Design for Active Flutter Suppression of Flexible-Wing Unmanned Aerial Vehicle Demonstrator." In: *Journal of Guidance, Control, and Dynamics* 43.4, pp. 656–672. DOI: 10.2514/1.G004618 (cit. on pp. 152, 155, 227).

Waltz, Richard et al. (July 2006). "An interior algorithm for nonlinear optimization that combines line search and trust region steps." In: *Math. Program.* 107, pp. 391–408. DOI: 10.1007/s10107-004-0560-5 (cit. on pp. 74, 77, 212, 213).

Wang, X. et al. (2019). "Flexible Aircraft Gust Load Alleviation with Incremental Nonlinear Dynamic Inversion." In: *Journal of Guidance, Control, and Dynamics* 42.7, pp. 1519–1536. DOI: 10.2514/1.g003980 (cit. on pp. 95, 218).

Wang, Yongzhi, Feng Li, and Andrea Da Ronch (2015). "Adaptive Feedforward Control Design for Gust Loads Alleviation of Highly Flexible Aircraft." In: *AIAA Atmospheric Flight Mechanics Conference*. American Institute of Aeronautics and Astronautics. DOI: 10.2514/6.2015-2243 (cit. on pp. 95, 218).

Waszak, Martin and Carey Buttrill (1991). "Design of an active flutter suppression system for the Active Flexible Wing." In: *Aircraft Design and Operations Meeting*. DOI: 10.2514/6.1991-3111 (cit. on pp. 151, 226).

Waszak, Martin and S. Srinathkumar (1991). "Active flutter suppression - Control system design and experimental validation." In: *Navigation and Control Conference*. DOI: 10.2514/6.1991-2629 (cit. on pp. 151, 226).

Waszak, Martin R. and David K. Schmidt (1988). "Flight dynamics of aeroelastic vehicles." In: *Journal of Aircraft* 25.6, pp. 563–571. DOI: 10.2514/3.45623 (cit. on pp. 27, 28, 30, 205).

Wildschek, Andreas et al. (2006). "Active Wing Load Alleviation with an Adaptive Feed-forward Control Algorithm." In: *AIAA Guidance, Navigation, and Control Conference and Exhibit*. American Institute of Aeronautics and Astronautics. DOI: 10.2514/6.2006-6054 (cit. on pp. 95, 217, 218).

Wildschek, Andreas et al. (2007). "Wind Tunnel Testing of an Adaptive Control System for Vibration Suppression on Aircraft." In: *AIAA Guidance, Navigation and Control Conference and Exhibit*. American Institute of Aeronautics and Astronautics. DOI: 10.2514/6.2007-6331 (cit. on pp. 95, 218).

Wildschek, Andreas et al. (2010). "Gust Load Alleviation on a Large Blended Wing Body Airliner." In: *27th International Congress of the Aeronautical Sciences* (cit. on pp. 95, 217).

Xiao, Y. Q. et al. (2019). "A Novel Framework for Parametric Loewner Matrix Interpolation." In: *IEEE Transactions on Components, Packaging and Manufacturing Technology* 9.12, pp. 2404–2417. DOI: 10.1109/TCPMT.2019.2948802 (cit. on p. 88).

Yılmaz, Burak et al. (2018). "A Randomized Algorithm for Parsimonious Model Identification." In: *IEEE Transactions on Automatic Control* 63.2, pp. 532–539. DOI: 10.1109/TAC.2017.2723959 (cit. on pp. 177, 231).

Zeng, Jie, Sunil L. Kukreja, and Boris Moulin (2012). "Experimental Model-Based Aeroelastic Control for Flutter Suppression and Gust-Load Alleviation." In: *Journal of Guidance, Control, and Dynamics* 35.5, pp. 1377–1390. DOI: 10.2514/1.56790 (cit. on pp. 96, 219).

Zeng, Jie et al. (2010). "Adaptive Feedforward Control for Gust Load Alleviation." In: *Journal of Guidance, Control, and Dynamics* 33.3, pp. 862–872. DOI: 10.2514/1.46091 (cit. on pp. 95, 218).

Zhang, Langwen, Jingcheng Wang, and Bohui Wang (2014). "A multi-step robust model predictive control scheme for polytopic uncertain multi-input systems." In: *IFAC Proceedings Volumes* 47.3, pp. 8540–8545 (cit. on pp. 96, 218).

Zhao, Yonghui, Chengyu Yue, and Haiyan Hu (2016). "Gust Load Alleviation on a Large Transport Airplane." In: *Journal of Aircraft* 53.6, pp. 1932–1946. DOI: 10.2514/1.c033713 (cit. on pp. 95, 217, 218).

Zimmermann, Helmut (1991). "Aeroservoelasticity." In: *Computer Methods in Applied Mechanics and Engineering* 90.1, pp. 719–735. ISSN: 0045-7825. DOI: https://doi.org/10.1016/0045-7825(91)90181-5 (cit. on p. 5).

FOLIO ADMINISTRATIF

THÈSE DE L'INSA LYON, MEMBRE DE L'UNIVERSITÉ DE LYON

NOM : Fournier
(avec précision du nom de jeune fille, le cas échéant)

DATE de SOUTENANCE : 2 juin 2023

Prénoms : Hugo, Charles, Romain

TITRE : Aeroelastic Reduced-Order Modeling and Active Control of Flexible Aircraft

NATURE : Doctorat

Numéro d'ordre : 2023ISAL0036

Ecole doctorale : Électronique, Électrotechnique, Automatique (n° 160)

Spécialité : Automatique

RÉSUMÉ :

Cette thèse porte sur la modélisation aéroélastique d'un avion, et à son contrôle actif. En utilisant les surfaces de contrôle de l'avion de manière appropriée, il est possible de réduire les charges dues aux rafales de vents et à la turbulence. Cela permet de réduire la masse des structures responsables de maintenir l'intégrité de l'avion, et donc d'améliorer les performances du design global. L'utilisation d'un lidar, un senseur permettant de mesurer la vitesse du vent plusieurs dizaines de mètres à l'avant de l'avion, est envisagée pour améliorer les capacités de réduction de charges. De plus, les futurs avions devraient avoir des ailes plus allongées et flexibles, ce qui réduit la traînée mais crée des effets aéroélastique néfastes. Le flottement est une instabilité pouvant amener à une destruction de l'aile, à haute vitesse. Il peut être annulé ou au moins déplacé en dehors de l'enveloppe de vol grâce au contrôle actif des surfaces de contrôle. Ces deux techniques ont été développées dans la thèse au moyen de diverses techniques de design de contrôleurs, principalement basées sur la synthèse robuste H-infini et ses variantes. Des techniques dédiées pour modéliser la dynamique aéroélastique de l'avion ont été développées. Pour obtenir des modèles d'états d'ordres réduits, avec des contraintes sur les pôles. Pour ce faire, une méthodologie basée directement sur la réponse fréquentielle aéroélastique de l'avion est employée, par opposition aux techniques classiques basées sur des équations mêlant l'aérodynamique et la dynamique structurelle, qui amènent en général à des modèles d'ordre importants, inutilisables par les techniques modernes de synthèse de contrôleurs.

MOTS-CLÉS :

Automatique, Aéronautique, Aéroélasticité, Aéroservoélasticité, Calcul de charges, Contrôle robuste, Identification de système, Systèmes dynamiques, Flottement

Laboratoire (s) de recherche : Laboratoire Ampère, UMR CNRS 5005

Directeur de thèse : Minh Tu PHAM

Président de jury : Emmanuelle VIDAL-SALLE

Composition du jury :

Daniel ALAZARD, Marco LOVERA, Rafael PALACIOS, Isabelle QUEINNEC, Emmanuelle VIDAL-SALLE, Minh Tu PHAM, Paolo MASSIONI, Laurent BAKO, Robin Vernay